EXPERIMENTAL AND NUMERICAL INVESTIGATION OF TURBULENT FLOW

AND HEAT (MASS) TRANSFER IN A TWO-PASS TRAPEZOIDAL CHANNEL

WITH TURBULENCE PROMOTERS

A Dissertation

by

SUNG HYUK OH

Submitted to the Office of Graduate Studies of
Texas A&M University
in partial fulfillment of the requirements for the degree of

DOCTOR OF PHILOSOPHY

December 2008

Major Subject: Mechanical Engineering

EXPERIMENTAL AND NUMERICAL INVESTIGATION OF TURBULENT FLOW

AND HEAT (MASS) TRANSFER IN A TWO-PASS TRAPEZOIDAL CHANNEL

WITH TURBULENCE PROMOTERS

A Dissertation

by

SUNG HYUK OH

Submitted to the Office of Graduate Studies of
Texas A&M University
in partial fulfillment of the requirements for the degree of

DOCTOR OF PHILOSOPHY

Approved by:

Chair of Committee,	S.C. Lau
Committee Members,	N.K. Anand
	W.M. Heffington
	Y.A. Hassan
Head of Department,	Dennis O'Neal

December 2008

Major Subject: Mechanical Engineering

ABSTRACT

Experimental and Numerical Investigation of Turbulent Flow and Heat (Mass) Transfer

in a Two-pass Trapezoidal Channel with Turbulence Promoters. (December 2008)

Sung Hyuk Oh, B.En., Inje University, Korea;

M.S., Texas A&M University

Chair of Advisory Committee: Dr. S.C. Lau

Experiments and numerical predictions were conducted to study heat (mass) transfer characteristics in a two-pass trapezoidal channel simulating the cooling passage of a gas turbine blade. Three different rib configurations were tested for the air entering the smaller cross section of the trapezoidal channel as well as the larger cross section of the trapezoidal channel at four different Reynolds numbers of 9,400, 16,800, 31,800, and 57,200. (+) 60º ribs, (–) 60º ribs and 60º V-shaped ribs were attached on both the top and bottom walls in parallel sequence. A naphthalene sublimation technique was used, and the heat and mass transfer analogy was applied to convert the mass transfer coefficients to heat transfer coefficients. Numerical predictions of three-dimensional flow and heat transfer also were performed for the trapezoidal channel with and without 90º ribs tested by Lee et al. (2007). Reynolds stress turbulence model (RSM) in the FLUENT CFD code was used to calculate the heat transfer coefficients and flow fields at Re = 31,800.

The results showed that the combined effects of the rib angle, rib orientation, and the sharp 180° turn significantly affected the heat (mass) transfer distributions. The secondary flows induced by the sharp 180° turn and the angled or V-shaped ribs played a very prominent role in heat (mass) transfer enhancements. The heat (mass) transfer enhancements and the pressure drops across the turn for 60° V-shaped ribs had the highest values, then came the case of (+) 60° ribs, and the heat (mass) transfer enhancements and the friction factor ratios for (–) 60º ribs was the lowest. However, comparing (–) 60º ribs with the 90º ribs, (–) 60º ribs produced higher heat (mass) transfer enhancements than the 90º ribs, as results of the secondary flow induced by the (–) 60º ribs. The overall average heat (mass) transfer for the larger inlet cases was always higher than that for the smaller inlet cases in the ribbed trapezoidal channel. Considering the thermal performance comparisons of the (+) 60° ribs, the (–) 60º ribs, and 60° V-shaped ribs for the smaller inlet cases, the highest thermal performance was produced by the (–) 60º ribs, and the 60° V-shaped ribs and the (+) 60° ribs had almost the same levels of the thermal performance since the 60° V-shaped ribs produced the highest heat (mass) transfer enhancement but also produced highest pressure drops. For the larger inlet cases, the (+) 60° ribs produced the highest values, then came the case of the 60° V-shaped ribs, and the thermal performance for the (–) 60º ribs was the lowest. The Reynolds stress model (RSM) showed well flow fields and heat transfer distributions but underpredicted average Nusselt number ratios.

DEDICATION

To my lovely wife, Soowon Kim

For her endless support and understanding

And

To my parents and parents-in-law

For their love, encouragement and prayer

ACKNOWLEDGEMENTS

First and foremost, all praise to Almighty God who gave me the courage, support and patience without which I could not have finished this work.

I would like to express my sincere appreciation to my advisors. Thanks to Dr. S.C. Lau for his patience and insightful guidance. I am also grateful to my academic committee members, Dr. N. K. Anand, Dr. W. M. Heffington and Dr. Y. A. Hassan, for their valuable time and helpful guidance.

Acknowledgements should also go to my colleagues from the heat (mass) transfer laboratory for their valuable discussions with me. Dr. Sang Won Lee and Dr. Hee Seok Ahn are my friends and my personal teachers. They spent countless time giving an advice and helping to conduct the experiments. Thank you so much Dr. Lee and Dr. Ahn.

I also would like to thank my friend, Dr. Tae Won Han, for his encouragement and help.

Finally, thanks to my father and mother for their encouragement and to my wife for her patience and love.

TABLE OF CONTENTS

Page

LIST OF FIGURES

LIST OF TABLES

NOMENCLATURE

A_c flow cross-sectional area at turn clearance, m^2

A_s surface area, m^2

D_h hydraulic diameter of flow cross section at turn clearance, m

f friction factor

f_0 reference friction factor for fully developed turbulent flow through smooth channel

$\bar{h}_m$ segmental or regional average mass transfer coefficient, m/s

L streamwise distance between pressure taps, m

$\dot{m}$ air mass flow rate, kg/s

$\dot{M}_n$ rate of total mass transfer from upstream naphthalene surfaces, kg/s

$\overline{Nu}$ segmental or regional average Nusselt number

Nu_0 reference Nusselt number for fully developed turbulent flow in smooth channel, equals to $0.023Re^{0.8}Pr^{0.4}$

P pressure, N/m^2

p_o absolute upstream pressure of the orifice, N/m^2

$P_{v,w}$ vapor pressure on naphthalene surface, N/m^2

P_w perimeter of flow cross section at turn clearance, m

R Universal gas constant for air of $287\,J/kg \cdot K$

Re Reynolds number

Sc Schmidt number

$\overline{Sh}$ segmental or regional average Sherwood number

Sh_0 reference Sherwood number for fully developed turbulent flow through smooth channel, equals to $0.023 Re^{0.8} Sc^{0.4}$

T_o orifice temperature, K

T_w naphthalene surface wall temperature, K

$\dot{V}$ volumetric flow rate of air, m^3/s

$\overline{V}$ average velocity, m/s

Greek Symbol

ΔM_n total mass transfer from naphthalene surface to air, kg

Δp pressure drop across sharp turn, N/m^2

Δp_o pressure drop through orifice, N/m^2

Δt duration of experiment, s

μ dynamic viscosity of air, $N \cdot s/m^2$

ρ density of air, kg/m^3

$\overline{\rho}_{v,b}$ average bulk vapor density of naphthalene, kg/m^3

$\rho_{v,w}$ vapor density of naphthalene on naphthalene surface, kg/m^3

σ mass diffusion coefficient of naphthalene vapor in air, m^2/s

CHAPTER I

INTRODUCTION

1.1 Background

Gas turbines have been dominant in the fields of power generation, aircraft propulsion, and mechanical drives for several decades. There have been considerable efforts directed toward increasing the turbine inlet temperature to achieve maximum efficiency and output power of gas turbines. The turbine inlet temperature in modern gas turbines is much higher than the melting point of the turbine blade material and causes excessive thermal stresses on turbine blades. In order to maintain safe and long operation of the gas turbines, higher thermal resistance materials and cooling techniques have been developed. Because higher thermal resistance materials still can not withstand excessive thermal stress, more effective and sophisticated cooling techniques should be employed.

One of the most widely used techniques for turbine blade cooling is to circulate coolant air through internal cooling passages within turbine blades and film cooling is used for surfaces of external turbine blades. Maximizing the cooling efficiency and attempting to accurately quantify the performance of these passages for parameters relevant to engine operating conditions have been the primary focus of researchers for several decades. Gas turbine blades are cooled internally and externally.

_____

The model journal is the ASME Journal of Heat Transfer.

Film cooling is external cooling. Film cooling protects the airfoil surface directly, compared to internal cooling techniques that remove heat from the inside surface. Film cooling also removes heat from the blade surface through the film hole by internal convection. Internal coolant air is ejected out through discrete holes to provide a coolant film to protect the outside surface of the blade from hot combustion gases.

The methods to enhance heat transfer in internal cooling passages are increasing the overall surface area of heat exchange, reducing the thickness of boundary layer, increasing the mixing within the cooling fluid, and raising turbulence levels which in turn reduce the thickness of the viscous sub-layer. In recent years, efforts directed at improving internal cooling have led to concepts that include the use of the rib turbulators, pin fins, dimpled surfaces, swirl chambers, and surface roughness. All of concepts provide increasing secondary flows and turbulence levels to enhance mixing, increasing secondary advection of heat away from surfaces, increasing three-dimensional turbulence production, and giving larger magnitudes of turbulence transport over larger portions of the flow fields. The overall objective of each internal cooling strategy is significant enhancement of turbulence transport and convective heat transfer coefficients, with minimal increases in streamwise pressure drop penalties and skin friction coefficients. Such heat transfer enhancements are needed for efficient heat load management, so that internal cooling air can remove the heat loads from turbine airfoil components. The best schemes give high cooling effectiveness with minimal coolant mass flow rates. Fig. 1.1 shows the common cooling technique with three major internal cooling zones in a turbine blade. The leading edge and trailing edge require the highest
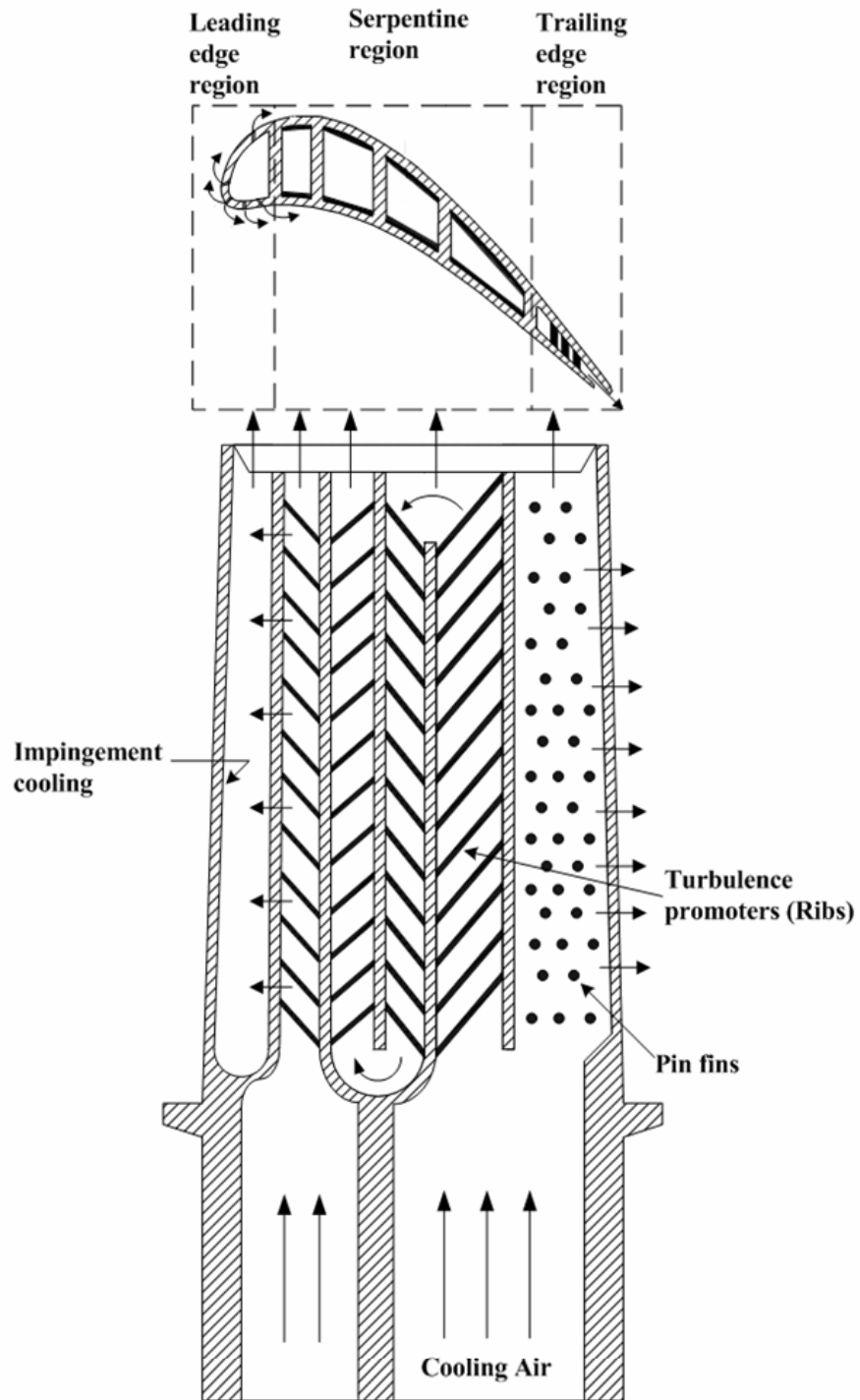
Fig. 1.1 Cooling concepts of a modern multi-pass turbine blade

heat transfer coefficients for a given flow rate. The leading edge geometry is characterized by a small coolant metal area to hot gas metal area ratio, while a thin trailing edge creates geometric constraints on passage sizes and accessibility for cooling air. For this reason, the leading edge of airfoil is cooled by jet impingement and swirl chamber, the trailing edge is cooled by pin-fins or dimples, and the middle portions of the airfoil are cooled by rib turbulators or turbulence promoters. Among these techniques, rib turbulated cooling in middle portion of the blades will be focused. The internal coolant passages in middle parts of the airfoil usually have either a rectangular or trapezoidal cross section and are roughened with ribs on two opposite walls. Normally, the pressure and suction sides are ribbed. In serpentine regions (rib roughened internal coolant passage), there are 180° sharp turns. A great number of experimental and numerical studies have been carried out to investigate the effects of ribs on heat transfer in internal channels. The factors considered in the studies include the rib geometry (the cross-sections of the ribs), the rib configuration in the channel (the angle of attack of the ribs and the relative distance between the ribs), the shape and the aspect ratio of the cross-section of the channel, the rotation of the channel, the turn or bend effects of the channel (multi-pass serpentine channels), and orientations of rotating channels with respect to the axis of rotation.

1.2 Literature Review

A large number of studies have been made both experimentally and numerically on the heat transfer enhancement in the internal channel. Most of these works deal with

square and rectangular cross sections, stationary and rotating channel, single and multi-pass channels, and with smooth and rib-roughened walls. These studies have examined heat transfer enhancement due to the effects of ribs of various configurations, channel aspect ratio, rib pitch-to-height, rib height-to-hydraulic diameter ratio, rotation, rib angle of attack, and 180° sharp turn. The results of these studies are useful in the design of serpentine cooling passages with turbulators in gas turbine. Many of the heat transfer enhancement and cooling issues related to turbine airfoils were introduced in Han et al. [1]. Heat transfer enhancement using turbulent promoters including ribs, pin-fins and impinging jets with or without rotation of channel has been studied by a number of researchers. Studies for heat transfer enhancement of internal channel flow installed with ribs with various configurations and parameters including channel aspect ratio, rib height-to-hydraulic diameter ratio, rib pitch-to-height ratio, rib height to width ratio, and rib angle of attack. The early investigations were focused primarily on straight, stationary, ribbed channels with a square or rectangular cross section. Han et al. [2] investigated the heat transfer and friction characteristics of rib roughened surfaces for various angle of attacks, rib profiles and P/e ratios in a square channel. It was found that ribs with an angle of attack of 45° at $P/e = 10$ had superior heat transfer performance for a given friction power when compared to that of ribs at an angle of attack of 90°. Han et al. [3] performed the experimental study of fully developed turbulent air flow in a square duct with two opposite rib-roughened walls. The effects of rib angle of attack and rib spacing on the heat transfer coefficients and friction factor also were investigated. Liou et al. [4] found that the rib pitch-to-height ratio of 10 resulted in the best heat transfer,

the heat transfer showed a periodic behavior between consecutive ribs, and both heat transfer and friction factor increased with decreasing rib spacing. Acharya et al. [5] experimentally investigated the flow and heat transfer in a rectangular channel with ribs attached along one wall. Their results also showed the periodic heat transfer profile induced by the ribs. The measured flow field revealed separation regions downstream the ribs followed by reattachment and redevelopment regions. Han et al. [6] and Park et al. [7] investigated the developing heat transfer in rectangular channels with rib turbulators for rib angles of attack, 90°, 60°, 45° and 30°. The combined effects of rib angle and channel aspect ratio on local heat transfer coefficient were studied. The results suggested that the low aspect ratio channels can give better heat transfer performance than the high aspect ratio channels, and the ribs with 60° angle of attack provide the highest heat transfer and pressure drop enhancement. The effect of rib configuration and Reynolds number on the local heat transfer distribution and pressure drop in a square channel with two opposite in-lined ribbed walls was studied by Han et al. [8]. The studies indicated that for V-shaped ribs the heat transfer augmentation was higher in comparison with other configurations and the reversed V-shaped ribs produced the maximum pressure drop. The heat transfer performance was found to decrease with increase in Reynolds number. Lau et al. [9] studied the effects of V-shaped ribs on two opposite walls on heat transfer enhancement in a square channel, compared to the effects of transverse or full angled ribs on two opposite walls. They concluded that V-shaped ribs, of 45º or 60º angle, on two opposite walls show better heat transfer enhancement than transverse or full angled ribs, of 45º or 60º angle, on two opposite walls which have

higher pressure drops. Ekkad and Han [10] performed a detailed study on heat transfer distributions in a non-rotating square ribbed channel using a liquid crystal technique. The results show that the 60º V-shaped ribbed channel produced more heat transfer enhancement than 60º and 90° angled ribbed channels. Taslim et al. [11] tested several different cases for straight, V-shaped, and discrete ribs with three different blockage ratios (ratios of rib height to channel height), and showed that low-blockage-ratio V-shaped ribs produce the highest heat transfer enhancement but with the highest pressure drop as well. Han et al. [12] studied local heat transfer distribution around a 180º turn in a two-pass square channel with smooth walls, and two opposing rib-roughened walls, by the naphthalene sublimation technique. They concluded that a considerable 180º turn effect with increased heat transfer after the turn. Chandra et al. [13] and Han and Zhang [14 and 15] studied the effect of rib angle orientation on local heat transfer distribution in a three-pass rib-roughened channel. They found that the rib angle and orientation and the sharp 180º turn significantly affected the local heat transfer and pressure drop distributions. The combined effects of these parameters increased or decreased the heat transfer coefficients after the sharp 180º turns. Cho et al. [16] presented mass transfer measurements in a one-pass non-rotating duct (AR=2.04:1) with different rib arrangements. Their results show that discrete 90º angled ribs have better heat transfer enhancement than non-discrete 90º angled ribs. However, the discrete and non-discrete 45° angled ribs have similar heat transfer enhancement. The local heat/mass transfer characteristics and friction loss were investigated for the 60º continuous V-shaped rib and the 45° discrete V-shaped rib configurations with various aspect ratios and Reynolds

number by Rhee et al. [17]. The average heat/mass transfer coefficients decrease as the aspect ratio increases for all the Reynolds numbers due to the decrease of local values at the centerline region with weakened secondary flow. All of the above studies are for non-rotating channels. It has been shown for non-rotating channels that the angled ribs have better heat transfer than normal ribs (90º), and the V-shaped ribs have better heat transfer than the angled ribs.

Experiments with rotation have been conducted to more closely model engine cooling environments. The interaction of the secondary flow induced by rotation and the rib turbulators results in different heat transfer trends, as in the stationary channels. In a rotating channel, heat transfer discrepancy between the leading and trailing surfaces is observed due to the Coriolis force and centrifugal buoyancy force. Taslim et al. [18] studied the effects of rotation, Reynolds number, and rib blockage ratio on heat transfer in these rib-roughened passages. Park et al. [19] measured local heat/mass transfer in a duct with rotation using a naphthalene sublimation method. They concluded that the Coriolis force does not affect heat transfer in a ribbed duct as much as in a smooth duct. Han et al. [20] and Parsons et al. [21] presented Nusselt number ratio distributions in rotating smooth and 90º ribbed two-pass square ducts. In their research, the changes of local heat transfer were observed when experimental conditions such as rib turbulators, rotational speed and thermal boundary condition were varied. Wright et al. [22] studied the heat transfer distributions in a one-pass rotating rectangular duct (AR=4:1) with angled, V-shaped, and W-shaped rib turbulators. They concluded that the discrete V-shaped and discrete W-shaped ribs have the best thermal performance in both rotating

and non-rotating cases. Lee et al. [23] investigated six different rib configurations in single-pass rectangular (AR=4:1) channels. They found that the V-shaped ribs produce the greatest heat transfer enhancement in both rotating and non-rotating channels.

To better understand the complex 3-D flow physics in the complicated blade internal coolant passage geometry, recent efforts also focus on the computational flow and heat transfer using the RANS (Reynolds-averaged Navier-Stokes) method with various turbulence models. Results indicate that the second-moment turbulence closure model (RSM) provides better flow and heat transfer predictions than the standard $k - \varepsilon$ model. The existing and modified CFD codes would become useful tools for rotor coolant passage heat transfer prediction and coolant flow optimization and management. Jang et al. [24] computed flow and heat transfer in two-pass, non-rotating square channels with 60º ribs with a near-wall second-order Reynolds stress (second-moment) closure model and a two-layer $k - \varepsilon$ model. The results show that the second-moment Reynolds stress model provides better heat transfer prediction than the two-layer $k - \varepsilon$ model. Jang et al. [25] also predicted flow and heat transfer in a rotating square channel with 45º angled ribs by Reynolds stress model. Their heat transfer coefficient prediction compares well with the experimental data. Benhoff et al. [26] numerically studied the flow characteristics in square channels with 45º angled ribs.

They compared the RSM model and $k - \varepsilon$ model. The comparison presented that the RSM results were more consistent with the experimental results than the $k - \varepsilon$ results with and without wall functions. Iacovides and Raisee [27] applied a number of turbulence models, EVM and second-moment type to predict the flow and heat transfer

through staggered ribbed-roughened passages with U-turn. They concluded that second-moment closures are necessary in order to correctly reproduce the regions of flow separation. Sleiti and Kapat [28] compared two-equation turbulence models ($k - \omega$ and $k - \varepsilon$) and RSM in predicting stationary and rotating flow and heat transfer in rib-roughened internal cooling channels. The results showed RSM is better than the two-equation models. Using the second-moment model, Al-Qahtani et al. [29] calculated flow and heat transfer in a rotating two-pass rectangular channel with 45º angled ribs and channel aspect ratio of 2:1. The focus was to investigate the effect of channel aspect ratio and channel orientation on the flow and heat transfer. The results compared reasonably with the experimental data for both stationary and rotating ribbed channels. Rigby [30] predicted fluid flow and heat transfer in a 90º ribbed rotating coolant passage with a 180º turn using a $k - \omega$ turbulence model. The results showed that the regional averaged heat transfer coefficient was overpredicted for the stationary case and underpredicted for the rotating case. Su et al. [31] computed flow and heat transfer in rotating rectangular channels with V-shaped ribs by using near wall second-moment closure model. The results predicted by second-moment model were in very good agreement with the experimental data for both the non-rotating and rotating cases. Many numerical investigations demonstrated that the advanced second-order RSMs (second-moment) are capable of providing detailed three dimensional velocity, pressure, temperature, Reynolds stresses, and turbulent heat fluxes that were not previously available in most of the experimental studies.

Most of the mentioned studies has been focused on heat transfer enhancement in smooth and rib-roughened walls, square and rectangular cross-sections, single and multi-pass channels with and without rotation. Experimental and numerical studies have modeled the serpentine region of the gas turbine airfoil mostly with square or rectangular cross-sectioned channels, with and without multi-pass with 180° sharp turns. However, the actual passages in the airfoil are all not exactly square or rectangular cross section and these shaped cooling passages often have irregular cross sections. Internal cooling passages of the serpentine region of turbine airfoils are rather trapezoidal-shaped channels. A few studies, such as Taslim et al. [32 and 33], Moon et al. [34], and Li et al. [35], have been conducted to investigate the effects of irregular geometries on heat transfer performance with and without turbulators in single and multi-pass internal cooling passages. Taslim et al. [32] conducted liquid crystal experiments to examine the effect of tapered ribs on heat transfer coefficients in trailing edge passages with and without bleed holes along the trailing edge. Nine different geometries and two passage aspect ratios were tested. The channel pressure losses were also measured. Heat transfer and friction factor results for various geometries were compared. They found that there was a large spanwise variation of heat transfer coefficients due to the non-uniform spanwise geometrical shape of the ribs and channels. Taslim et al. [33] measured heat transfer coefficient and friction factors in partially ribbed passages in two channels with square and trapezoidal cross sections by using a liquid crystal technique. They found that the half-length ribs significantly enhanced the heat transfer on the two walls with full ribs. Moon et al. [34] investigated local heat transfer distribution in a smooth two-pass

channel of trapezoidal cross section with the transient liquid crystal technique. The results showed that the heat transfer was much higher on the walls in the turn region and downstream of the turn than on the walls upstream of the turn. The turn caused high heat transfer in several distinct regions on the end wall, the outlet outer wall, and on the two opposite primary walls in the turn and downstream of the turn. The flow separated at the tip of the divider wall and reattached on the outlet inner wall in a location only a short distance from the turn. The heat transfer was the lowest on the inlet outer wall. Heat transfer enhancement due to the turn was the highest in the lowest Reynolds number case. The trends of the local heat transfer distributions on the various walls at the turn were relatively insensitive to varying the flow rate. Lee et al. [35] studied heat/mass transfer distribution in a two-pass trapezoidal channel with naphthalene sublimation method. Results were obtained for turbulent air flow through the channel with smooth walls, and with ribs on one wall and on two opposite walls, over a range of Reynolds numbers between about 10,000 and 60,000. The effect of ribs on the average heat transfer is higher when air enters larger straight section of the trapezoidal channel than when air enters smaller straight section of the channel. There was a very large variation of the local heat transfer distribution in the turn and downstream of the turn. In all cases studied, the average heat transfer was higher on the downstream half of the turn than on the upstream half of the turn. Immediately downstream of the turn, the regional average heat transfer in the larger exit section decreased abruptly, while the regional average heat transfer in the smaller exit section continued to increase and reached a maximum value before it decreased as the flow redeveloped. Immediately downstream of the turn, the

regional average heat transfer was lower in the larger exit section of the channel with ribs than in the exit section of the channel with smooth walls for air flow in either direction. Although Taslim et al. [32 and 33], Moon et al. [34] and Lee et al. [35] investigated the effects of irregular geometries, i.e. trapezoidal cross sectional channels, on heat transfer performance with and without turbulators, the effects of irregular geometries on heat transfer performance with 60º angled ribs and 60º V-shaped rib turbulators have not been studied. Most researches show that the 60º V-shaped ribbed channel produces more heat transfer enhancement than 60º and 90° angled ribbed channels that are idealized as square or rectangular cross-section. However, the flow conditions in the trapezoidal channel are different from square and rectangular channel and the effects of (+) 60º ribs, (–) 60º ribs and 60º V-shaped rib turbulators on the heat transfer enhancement may be different.

In this study, internal cooling channels in gas turbine airfoils were modeled as a channel with two straight trapezoidal sections with a sharp 180º turn. This study experimentally and numerically investigated the effect of rib configurations on the heat transfer enhancement, pressure penalty, and thus the overall thermal performance in cooling channels without rotation at four different Reynolds numbers of 9,400, 16,800, 31,800, and 57,200. (+) 60º ribs, (–) 60º ribs and 60º V-shaped ribs were attached on both the top and bottom walls in channels. Naphthalene sublimation experiments were conducted to obtain the mass transfer distributions and the heat and mass transfer analogy was used to convert the mass transfer distributions to heat transfer distributions. Numerical predictions of three-dimensional flow and heat transfer also were performed

for the trapezoidal channel with and without 90º ribs tested by Lee et al. [35]. Reynolds stress turbulence model (RSM) in the FLUENT CFD code was used to calculate the heat transfer coefficients and flow fields at Re = 34,500 for the square channel and at Re = 31,800 for the trapezoidal channel. The experimental and numerical results of this study will enable better understanding of the effect of ribs on the heat transfer distribution in a trapezoidal channel, validate computer codes, and help improve the design of cooling passages in gas turbine blades.

CHAPTER II

EXPERIMENTAL ANALYSIS

2.1 Experimental Apparatus

A schematic diagram of the experimental apparatus is presented in Fig. 2.1. It was operated in the suction mode to exclude the temperature rise caused by blowers. Two centrifugal blowers were connected in series in order to provide sufficient pressure below atmosphere to obtain Reynolds numbers based on the hydraulic diameter ($D_{h,turn}$ = 4.57 cm) of the cross section at the turn clearance in the test channel from 9,400 to 57,200.
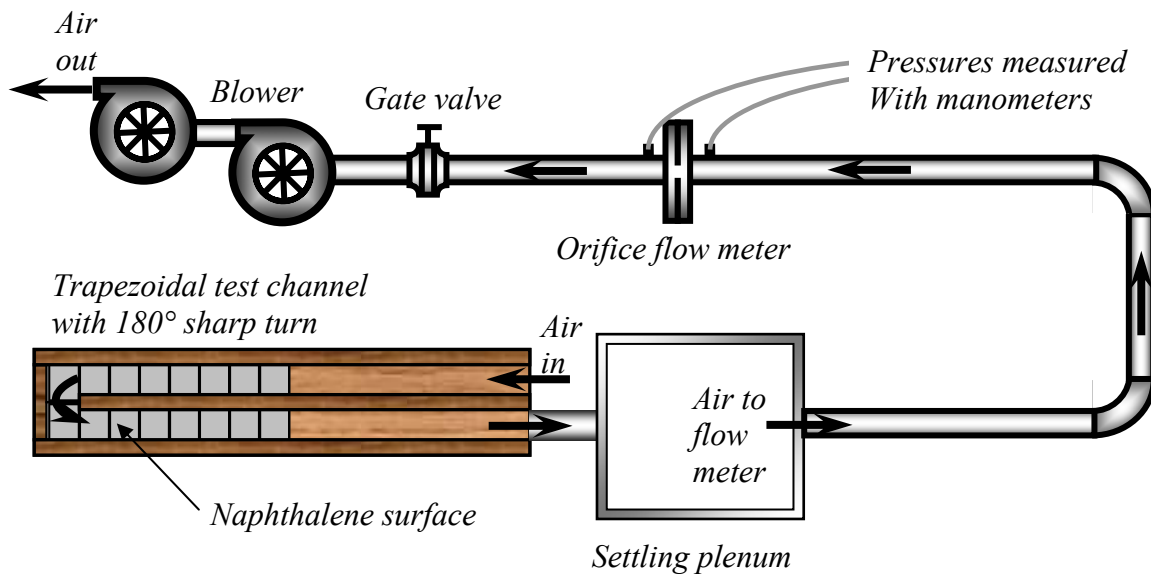
Fig. 2.1 Schematic of test apparatus

The main components of the test apparatus were the test section, a settling plenum, a calibrated orifice flow meter, a gate valve, and two blowers. The exiting air passing a gate valve and an orifice was vented through PVC pipe to the outside of the laboratory to prevent naphthalene molecule sublimated from mixing with inlet air. The test section was a two-pass channel with two straight sections of different trapezoidal cross sections ($D_{h,small}$ = 4.09 cm and $D_{h,large}$ = 4.83 cm), connected with a sharp 180° turn. The channel was constructed of 1.91 cm thick pine wood. As shown in Fig. 2.2, the length of each straight section with and without naphthalene surfaces was 30.5 cm, while the width of each section was 3.81 cm and the thickness of the divider wall between the two sections was 1.91 cm. The width of the clearance at the turn was also 3.81 cm.

13.3 cm

30.5 cm — 30.5 cm

(a) Top view of bottom wall of test channel

0.97 cm

1.91 cm

62.9 cm

(b) Side view of bottom wall of test channel
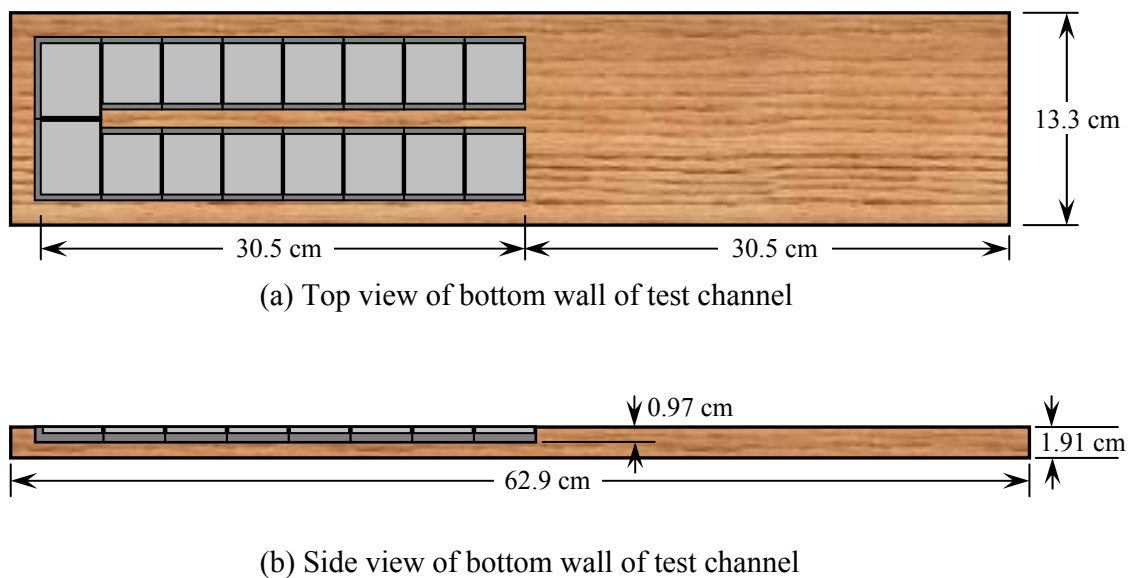
Fig. 2.2 Schematics of walls of trapezoidal test channel

1.91 cm thick divider wall

3.81 cm

3.81 cm

End wall

16 naphthalene cassettes

Side walls
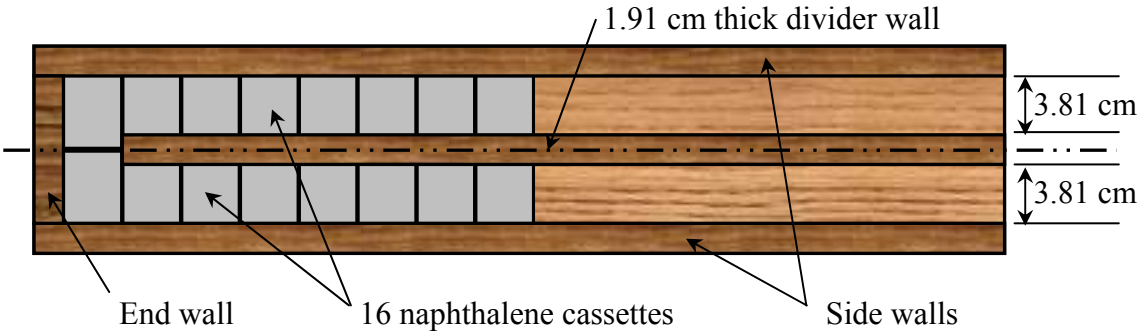
(c) Top view of test channel with top wall removed

Top wall

21.8°

Outer side wall

7.62 cm

3.81 cm

Outer side wall

Bottom wall

Divider side wall
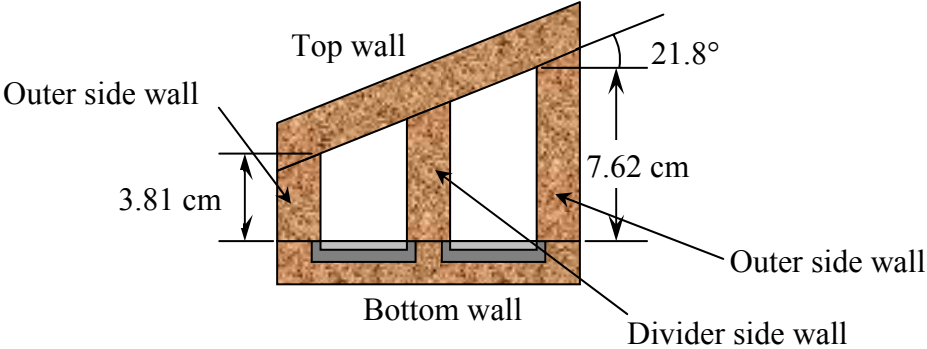
(d) Cutaway view of cross section of test channel

Fig. 2.2 (continued)

The included angle of trapezoidal cross section between the top wall and the bottom wall was 21.8°. The heights of the outer and inner vertical wall in small trapezoidal channel were 3.81 cm and 5.33 cm, and the height of the inner and outer vertical walls in large trapezoidal channel were 6.10 cm and 7.62 cm. All of these dimensions were for the inside surfaces of the channel walls.
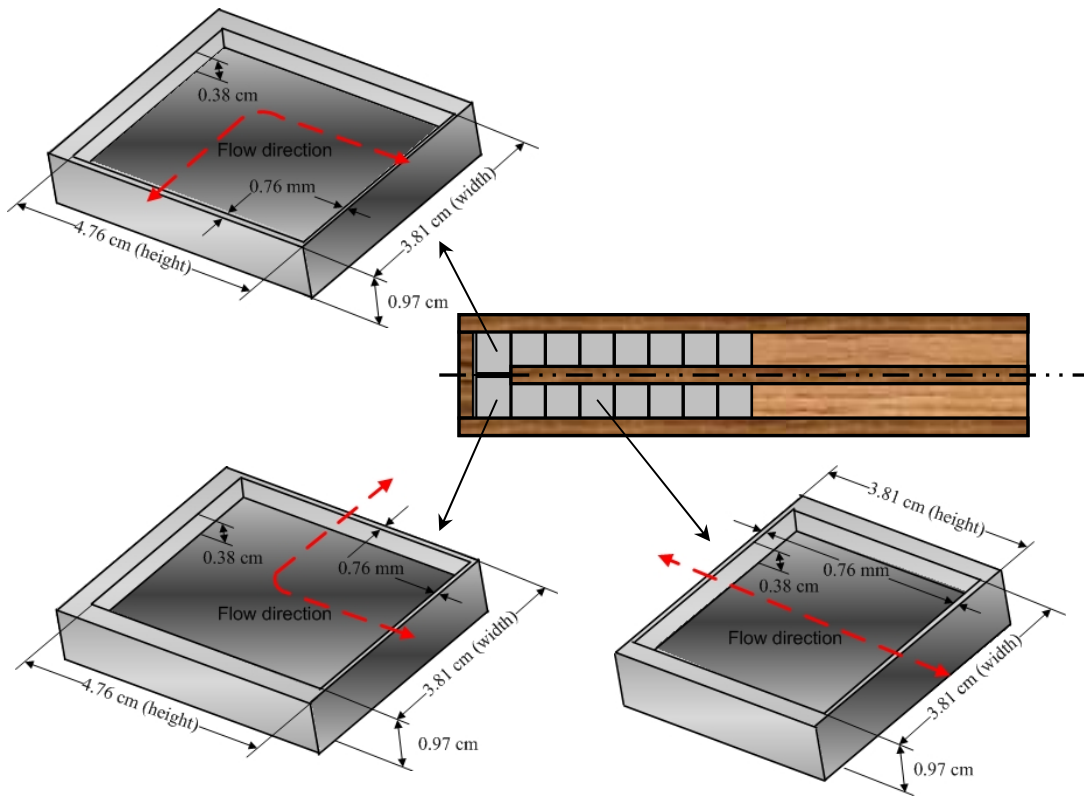
Fig. 2.3 Schematics of aluminum cassettes

As shown in Fig. 2.3, sixteen aluminum cassettes with 0.97 cm thick and 0.38 cm deep cavity were installed on the bottom wall to determine the streamwise variation of the regional mass transfer coefficient along the channel. The naphthalene surfaces on fourteen of the cassettes on the each straight section were 3.81 cm x 3.81 cm, and the naphthalene surfaces on two other cassettes at the turn were 3.81 cm x 4.76 cm. Once these sixteen cassettes were installed, the inner surface of the bottom wall was mass transfer active, except for the top of 0.76 mm wide rims of each cassette.

For six sets of experiments, (+) 60º ribs, (–) 60º ribs and 60º V-shaped ribs were attached with silicon adhesive on both the top and bottom walls, over the entire length of the test channel, with a spacing of 3.81 cm. These ribs were 3.2 mm by 3.2 mm square stripes of balsa wood. Thus, the rib height-to-hydraulic diameter ratio (e/ $D_{h,turn}$) was 0.07, and the rib pitch-to-rib height ratio (P/e) was 12. Regional average mass transfer coefficients were obtained for air flows through the test channel with (+) 60º ribs, (–) 60º ribs and 60º V-shaped ribs on two opposite walls. The inlet was small cross section or large cross section. Therefore, six experimental cases were conducted with four Reynolds numbers (9,400, 16,800, 31,800 and 57,200). Fig. 2.4 shows six experimental cases and rib configuration.

To obtain the pressure drop across the turn, two pressure taps were installed on the top wall and the outer side wall, respectively, in each of the two straight sections of the test channels [see Fig. 2.5]. These pressure taps were located on the center point between two ribs located 4th and 5th from the end wall. The difference in the static pressures at these two pairs of taps was measured with a micromanometer or an inclined

Case 1. 60 deg rib Smaller Inlet

Case 2. 60 deg rib Larger Inlet

Case 3. 60 deg rib Smaller Inlet

Case 4. 60 deg rib Larger Inlet

Case 5. 60 deg V-shaped Smaller Inlet

Case 6. 60 deg V-shaped Larger Inlet
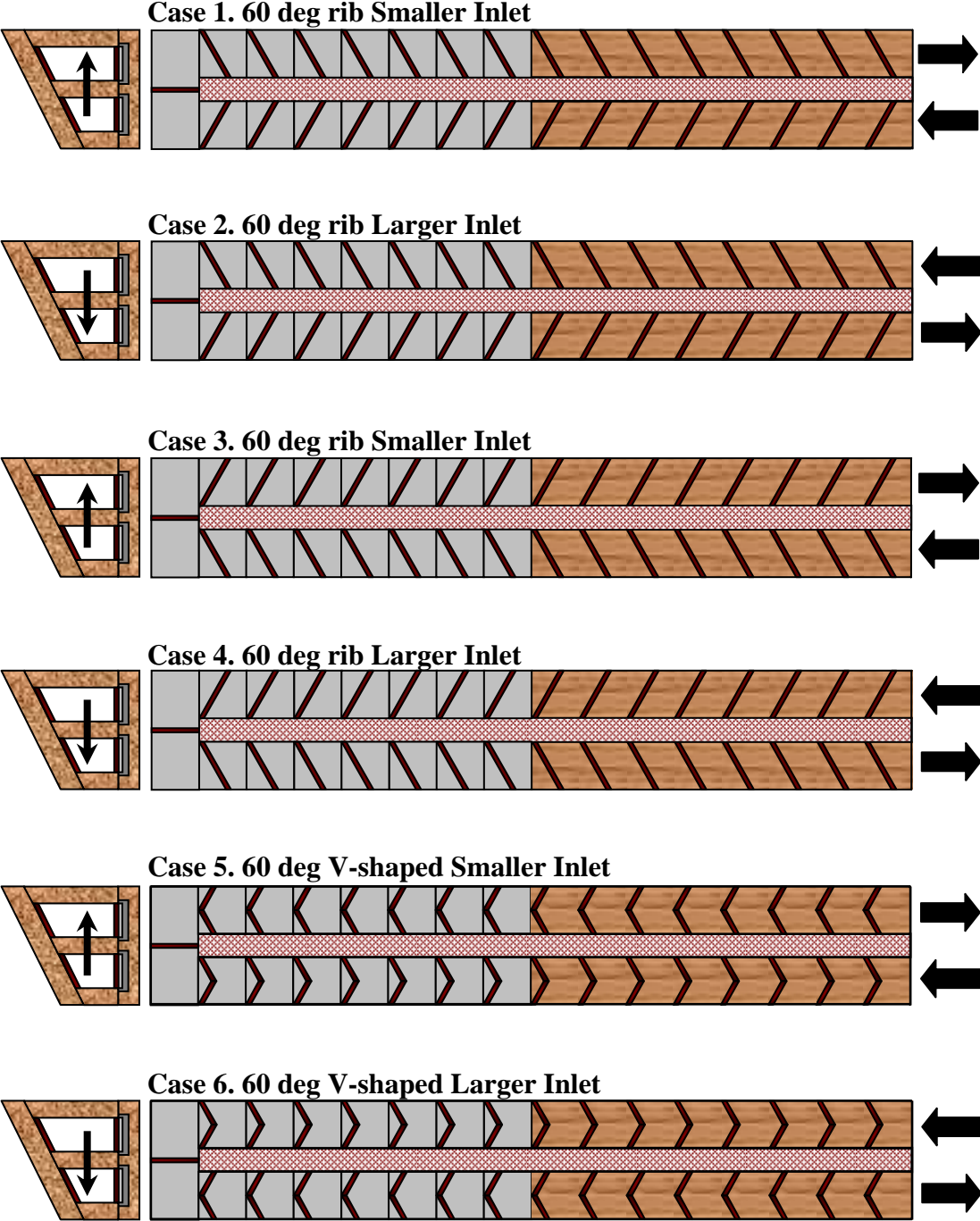
Fig. 2.4 Six experimental cases and rib configurations
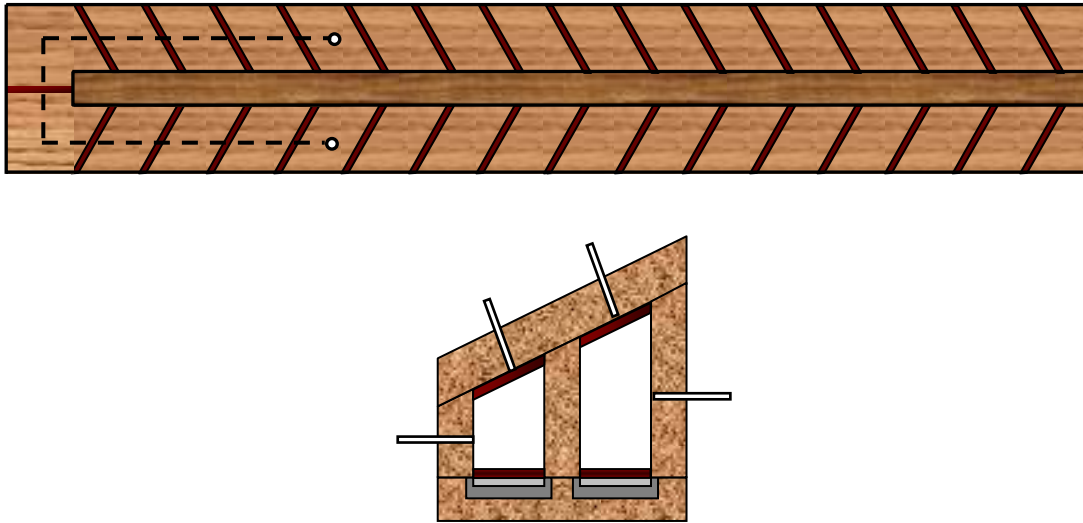
Fig. 2.5 Two pressure taps installed on both top and side wall of each passage

manometer, depending on the range, and was checked with a calibrated pressure transducer with a digital readout.

2.2 Naphthalene Molding

Naphthalene casting equipment included an electric heater, a beaker, aluminum plates or molds and base, alcohol, and some accessories. A sufficient amount of naphthalene pieces in a glass beaker were heated on an electric heater until they boil.

The melting point of naphthalene is 80.3°C, but superheating of the molten naphthalene is often needed to allow complete filing of the mold cavity prior to the occurrence of solidification. The naphthalene cassette was placed on a highly polished and flatted stainless steel plate with the rim of the cavity pressed against the surface of the stainless steel plate. A funnel for pouring naphthalene and two metal tubes for venting air were placed on holes of the backside of aluminum plate. The aluminum plate and the test specimen may need to be preheated to prevent naphthalene from forming wavy trace on surface. After the naphthalene was boiling, molten naphthalene was poured into the mold cavity and allowed to solidify at room temperature. The funnel and metal tubes were removed after solidification. The cassette was separated from the plate by tapping on one side with a hammer. The exposed surface of naphthalene on the cassette must be smooth and shiny corresponding to smoothness of the highly polished metal specimen. To ensure that the naphthalene in all of cassettes was in thermal equilibrium with the air in the air-conditioned laboratory, the cassettes were stored in a sealed plastic bag in the laboratory for approximately 12 hours before an experiment.

2.3 Experimental Procedure

The test section had two different sizes of trapezoidal straight sections with a divider wall in-between the two sections. The inlet was small cross section or large cross section. The experiments first used the smaller trapezoidal section as the inlet with the larger section as the outlet. Afterwards, the larger trapezoidal duct was used as the inlet

and the smaller duct served as the outlet. For each test configuration mentioned, four Reynolds numbers were considered. Regional average mass transfer coefficients were obtained for air flows through the test channel with (+) 60º ribs, (–) 60º ribs and 60º V-shaped ribs on two opposite walls. The analogy of heat and mass transfer was applied to convert the mass transfer coefficients to heat transfer coefficients.

The two-pass trapezoidal test channel was connected to a settling plenum and then to an open air flow loop. During an experiment, fresh air was drawn, by two centrifugal blowers connected in series, through the flow loop from the air-conditioned laboratory and the exhaust air that contained naphthalene vapor was ducted to the outside of the laboratory through a fume hood. The air mass flow rate was controlled with a valve and was calculated from measured pressure drop through an ASME sharp edge 3.81-*cm* hole-diameter orifice plate and absolute pressure upstream of the orifice plate. The pressure drop was measured with an inclined manometer and the upstream pressure was measured with a calibrated Cole Parmer pressure transducer with a digital TRMS multi-meter. The temperature of the air at the entrance of the test section was measured with two 30 gage T-type thermocouples, which were carefully calibrated with a NIST calibrated thermometer and a constant temperature bath, and was monitored continuously with a data acquisition system over the duration of the experiment. The data acquisition system consisted of a National Instrument's PCI-6024E board, a SCXI-1102 conditioner, a TC-2095 terminal block, and a computer on which Labview 7.0 was installed. To ensure that the naphthalene in all of the cassettes was in thermal equilibrium with the air in the air-conditioned laboratory, the cassettes were stored in

sealed plastic bags in the laboratory for approximately 12 hours before an experiment. After each experiment, the remaining naphthalene in all of the cassettes were melted and thrown away. All of the cassettes were cast with new melted naphthalene to ensure best results of regional average mass transfer experiments.

To obtain the pressure drop across the turn, two pressure taps were installed on the top wall and the outer side wall, respectively, in each of the two straight sections of the trapezoidal test channel. The difference in the static pressures at these two pairs of taps was measured with a Dwyer 1430 microtector electronic point gage that could measure up to a 5.08-*cm* water column with a resolution of $\pm 6.35 \times 10^{-3}$ *mm* or a calibrated Cole Parmer pressure transducer with a digital TRMS multi-meter that could measure up to a 25.40-*cm* water column with a resolution of $\pm 2.54 \times 10^{-2}$ *cm*, depending on the range of the measured pressure drops through the turn of the trapezoidal channel.

Before each regional average mass transfer experiment was conducted, pre-determined air flow rate, which gave turn-clearance based Reynolds number of 9,400 ~ 57,200, was carefully adjusted with a valve to minimize preparation time of each experiment and thus un-wanted mass transfer loss. To determine the variation of the sixteen regional average mass transfer coefficients along the two-pass test channel, the sixteen naphthalene cassettes were weighed and recorded five times for a statistical purpose, one at a time, with a Sartorious electronic balance that had a range up to 160.0 *g* with a resolution of 0.1 *mg* before and after the experiment. Each experiment was run for 60, 35, 25, and 15 minutes with corresponding turn clearance based Reynolds number of 9,400, 16,800, 31,800 and 57,200, respectively. Duration of each experiment

was carefully chosen such that amounts of the sublimated naphthalene for each cassette were comparable to each other for four different Reynolds numbers to minimize uncertainties of the experiments. Installation and un-installation of the sixteen cassettes in the test section were executed carefully and promptly to minimize un-wanted mass transfer loss to ambient. Every step in each experiment including weighing of the sixteen cassettes before and after the experiment, installation and un-installation of the sixteen cassettes in the test section, assembly and disassembly of the test channel, and turning on and off blowers was timed to account for an amount of the un-wanted mass transfer during the experiment. The difference between the weights of each of sixteen cassettes gave an amount of the mass transfer from the naphthalene surface of a cassette to airflow during the experiment, which was reduced to regional average mass transfer distribution along the test channel. Auxiliary experiments were conducted, after each experiment was performed, to account for mass transfer loss that was sublimed during the start and end of the suction pump(s) operation and the preparation of the experiment.

2.4 Data Reduction

With measured weight difference data of each specimen by high resolution balance, reduce the data to obtain the mass transfer coefficient or Sherwood number by following equations. Mass flow rates of air were calculated from pressure drop, Δp_o, through the orifice;

$$\dot{m} = \frac{\pi}{4} d_o^2 CY \left[\frac{2 p_o \Delta p_o}{RT_o (1 - \eta^4)} \right]^{\frac{1}{2}} \tag{1}$$

where d_o was the diameter of the orifice and is equal to 3.81cm, C was the discharge coefficient, Y was the expansion coefficient, p_o was the pressure at the tap upstream of the orifice, Δp_o was the pressure drop across the orifice, R was the universal gas constant for air ($287\,J/kg \cdot K$), T_o was the temperature at the orifice, and η was the orifice-diameter-to-pipe-diameter ratio and was equal to 0.6. The expansion coefficient, Y, and the discharge coefficient, C, were calculated, respectively, with the following equations:

$$Y = 1.0 - \frac{(0.41 + 0.35\eta^4)\Delta p_o}{1.4 p_o} \tag{2}$$

and

$$C = 0.5959 + 0.0312\eta^{2.1} + \frac{91.71\eta^{2.5}}{Re_{dp}^{0.75}} - 0.01584\eta^3 + \frac{0.0390\eta^4}{1 - \eta^4} - 0.1840\eta^8 \tag{3}$$

where the pipe Reynolds number based on the pipe diameter, Re_{Dp}, was given by

$$Re_{Dp} = \frac{4\dot{m}}{\pi d_p \mu} \tag{4}$$

where d_p was the diameter of the pipe at the orifice and was equal to 6.35cm, and μ was based on the orifice temperature, T_o. Mass flow rates were calculated iteratively, because the equations were in tangles each other. Reynolds numbers based on the channel hydraulic diameter, D_h, Re_{Dh} was calculated from the mass flow rates;

$$\text{Re}_{Dh} = \frac{\rho \bar{V} D_h}{\mu} = \frac{4\dot{m}}{P\mu} \tag{5}$$

where μ was based on the inlet temperature, T_i, and the perimeter of the test channel, P, was the rectangular flow cross section between the tip of the divider wall and the end wall. For the same air mass flow rate, the two Reynolds numbers based on the hydraulic diameters of the trapezoidal cross section of the two straight sections of the test channel were 10.5% smaller and 13.5% larger than this Reynolds number based on the hydraulic diameter of the cross section at the turn clearance.

The regional average mass transfer coefficients was defined as

$$\bar{h}_m = \frac{\Delta M_n / \Delta t}{A_s (\rho_{v,w} - \bar{\rho}_{v,b})} \tag{6}$$

where ΔM_n was the total mass transfer from a naphthalene surface to the air. As for natural convection, while naphthalene sublimation occurred before and after experiment and these additional weight losses were not negligible, it compensated the error. The correction values were obtained from natural convection with 1 hour weight loss data under room temperature. The consideration was calculated by

$$\Delta M_n = M_i - M_f - M_{conv,ave} \tag{7}$$

where ΔM_n was the total sublimation weight difference due to experiment, M_i was the initial weight of aluminum molds, M_f was the final weight of aluminum molds, and $M_{conv,ave}$ was the average convection sublimation weight during measurement and experiment process. Δt was the duration of the experiment. $\rho_{v,w}$ was the local vapor density of naphthalene at the wall, and was evaluated using the ideal gas law.

$$\rho_{v,w} = \frac{P_{v,w}}{RT_w} \qquad (8)$$

The vapor pressure, $P_{v,w}$, was determined using the vapor pressure-temperature correlation for naphthalene by Ambrose et al. [36].

$$T_w \log(P_{v,w}) = \frac{a_0}{2} + \sum_{s=1}^{3} a_s E_s(x)$$

$$\text{with } E_1(x) = x, E_2(x) = 2x^2 - 1, \text{ and } E_3(x) = 4x^3 - 3x \qquad (9)$$

where a_0=301.6247, a_1=791.4937, a_2= −8.2536, a_3=0.4043, and $x = (2T_w-574)/114$. T_w was in [K] and $p_{v,w}$ was in [N/m^2].

The average bulk vapor density of naphthalene in Eq. (6), $\overline{\rho}_{v,b}$ was the average of the vapor densities at the upstream and downstream edges of the naphthalene surface being considered, and was calculated as

$$\overline{\rho}_{v,b} = \frac{1}{2} \left[\left(\frac{\dot{M}_n}{\dot{V}} \right)_{upstream} + \left(\frac{\dot{M}_n}{\dot{V}} \right)_{downstream} \right] \qquad (10)$$

where $\dot{M}_n$ was the rate of total mass transfer from the upstream naphthalene surfaces, and $\dot{V}$ was the volumetric flow rate of air. The bulk vapor density was zero upstream of the first blockage since there was no naphthalene vapor in the air at the test channel inlet. The average Sherwood numbers was defined, as

$$\overline{Sh}_{Dh} = \frac{\overline{h}_m D_h}{\sigma} \qquad (11)$$

where σ was the mass diffusion coefficient for naphthalene vapor in the air. A correlation given by Goldstein and Cho [37] was used to determine the mass diffusion coefficient.

$$\sigma = 0.0681 \left(\frac{T}{298.16} \right)^{1.93} \left(\frac{1.013 \times 10^5}{P} \right) \times 10^{-4} \tag{12}$$

where σ was in [m²/s], T was in [K], and p was in [N/m²]. According to the analogy between heat transfer and mass transfer described in Eckert [38],

$$\frac{\overline{Nu}}{Nu_0} = \frac{\overline{Sh}}{Sh_0} \tag{13}$$

where the reference Nusselt number and Sherwood number were based on the Dittus–Boelter correlations for a fully developed turbulent flow at the same Reynolds number through a smooth channel with the same hydraulic diameter as the test channel.

$$Nu_0 = 0.023 \, \mathrm{Re}_{Dh}^{0.8} \, \mathrm{Pr}^{0.4} \tag{14}$$

$$Sh_0 = 0.023 \, \mathrm{Re}_{Dh}^{0.8} \, Sc^{0.4} \tag{15}$$

In Eqs. (14) and (15), Pr was the Prandtl number, defined as 0.69 for air, and Sc was the Schmidt number, defined as

$$Sc = 2.28 \left(T_{air} \Big/ 298.16 \right)^{-0.1526} \tag{16}$$

The friction factor was determined as

$$f = \frac{(\Delta p/L) D_h}{\rho \overline{V}^2 / 2} = 2\rho \left(\frac{\Delta p}{L} \right) \left(\frac{A_c}{\dot{m}} \right)^2 D_h \tag{17}$$

where Δp was the pressure drop across the sharp turn, L was the streamwise distance between the locations of the pressure taps along the centerline of the test channel, and A_c was the channel flow cross-sectional area at the turn clearance. The experimental friction factor was normalized by the friction factor for fully developed turbulent flow in a smooth channel, f_0, which was given as

$$f_0 = \left[0.79\ln(\mathrm{Re}_{Dh}) - 1.64\right]^{-2} \tag{18}$$

The relative thermal performance to compare the heat transfer per unit pumping power for the test channel with that for a smooth channel was given by

$$TP = \left(\frac{\overline{Nu}_{Dh}}{Nu_{Dh,0}}\right) \cdot \left(\frac{f}{f_0}\right)^{-\frac{1}{3}} \tag{19}$$

2.5 Uncertainty Analysis

The calculations of uncertainty values were based on a confidence level of 95% and the relative uncertainty analysis method of Coleman and Steele [39]. In all uncertainty calculations, uncertainty values of $\pm 1.0\%$ for all properties of air and ± 0.25 mm for all physical dimensions were used. The maximum uncertainty of the air mass flow rate was calculated from the maximum uncertainties of the measured pressures at the orifice flow meter, and was found to be $\pm 3.1\%$. The corresponding maximum uncertainty of the Reynolds number was $\pm 3.3\%$.

Based on the uncertainty values of $\pm4.9\%$ for ΔM_n, $\pm5.5\%$ for $\rho_{v,w}$, and $\pm5.8\%$ for $\rho_{v,b}$, the maximum uncertainty of the average mass transfer coefficient was estimated to be $\pm7.7\%$. According to Goldstein and Cho [37], the diffusion coefficient of naphthalene vapor in air had an uncertainty of about $\pm2.0\%$. With this value, the estimated value of the maximum uncertainty for the average Sherwood numbers was $\pm8.0\%$.

Using the maximum uncertainty values of $\pm5.8\%$ for the measured pressure drops and $\pm3.1\%$ for the air mass flow rate, the maximum value of the uncertainty of the friction factor was estimated to be $\pm8.8\%$.

CHAPTER III

NUMERICAL MODEL AND PROCEDURE

Numerical predictions provide the details that are difficult to obtain by experimental means. Moreover, the increase in computation power in desktop computers has made it economical to optimize the design parameters based on numerical analyses. Based on the number of equations to be solved, turbulence modeling approaches can be broadly classified as one-equation, two-equation, and second-moment closure models. The accurate prediction of heat transfer in high-pressure turbine stages has long been recognized as a key to improve gas turbine performance and engine life. Development of faster computers with more memory makes it feasible to compute more details of heat transfer analysis. The main difficulties in predictions are proper turbulence models.

Numerical analysis was conducted to better understanding the three dimensional flow and heat transfer distribution in a two-pass trapezoidal channel with (+) 60º ribs, (–) 60º ribs and 60º V-shaped ribs at Re = 31,800. The square channel with smooth walls and the trapezoidal channel with and without 90º ribs tested by Lee et al. [35] were also simulated at Re = 34,500 for the square channel and at Re =31,800 for the trapezoidal channel. The Reynolds stress model (RSM) with enhanced wall treatment in FLUENT code was used to perform the calculations. Three dimensional numerical simulations were compared with experimental results.

3.1 Governing Equations

In Reynolds averaging, the solution variables in the instantaneous Navier-Stokes equations are decomposed into the mean and fluctuating components. For the velocity components: $u_i = \overline{u_i} + u'_i$ where $\overline{u_i}$ and u'_i are the mean and fluctuating velocity components. Likewise, for pressure and other scalar quantities: $\phi = \overline{\phi} + \phi'$ where ϕ denotes a scalar such as pressure, energy, or species concentration. Taking a time average to the instantaneous Navier-Stokes equations and dropping the over bar yield the ensemble-averaged equations. The continuity and momentum equations can be written in Cartesian tensor form as:

$$\frac{\partial \rho}{\partial t} + \frac{\partial}{\partial x_i}(\rho u_i) = 0 \tag{1}$$

$$\frac{\partial}{\partial t}(\rho u_i) + \frac{\partial}{\partial x_j}(\rho u_i u_j) = -\frac{\partial P}{\partial x_i} + \frac{\partial}{\partial x_j}\left[\mu\left(\frac{\partial u_i}{\partial x_j} + \frac{\partial u_j}{\partial x_i} - \frac{2}{3}\delta_{ij}\frac{\partial u_l}{\partial x_l}\right)\right] + \frac{\partial}{\partial x_j}\left(-\rho\overline{u'_i u'_j}\right) \tag{2}$$

Turbulent heat transfer is modeled using the concept of Reynolds' analogy to turbulent momentum transfer. Thus, the modeled energy equation is given as follow:

$$\frac{\partial}{\partial t}(\rho E) + \frac{\partial}{\partial x_i}[u_i(\rho E + p)] = \frac{\partial}{\partial x_i}\left[\left(k + \frac{c_p \mu_t}{Pr_t}\right)\frac{\partial T}{\partial x_i} + u_j\left(\tau_{ij}\right)_{eff}\right] \tag{3}$$

where E is the total energy, k is the thermal conductivity and $\left(\tau_{ij}\right)_{eff}$ is the deviatoric stress tensor, given by

$$\left(\tau_{ij}\right)_{eff} = \mu_{eff}\left(\frac{\partial u_j}{\partial x_i} + \frac{\partial u_i}{\partial x_j}\right) - \frac{2}{3}\mu_{eff}\frac{\partial u_i}{\partial x_i}\delta_{ij} \tag{4}$$

The viscous heating is represented by the term $(\tau_{ij})_{eff}$. Pr_t is the turbulent Prandtl number with a value of 0.85. Equations (1) and (2) are called Reynolds-averaged Navier-Stokes (RANS) equations. Additional terms now appear that represent the effects of turbulence. These Reynolds stresses, $-\rho\overline{u_i' u_j'}$ must be modeled in order to close Eq. (2).

3.2 Reynolds Stress Model (RSM)

The Reynolds stress model (RSM) is also known as a second-moment closure model. Reynolds stresses are solved directly with transport equations avoiding isotropic viscosity assumption of other models. The RSM avoids the isotropic eddy viscosity assumption. In other words, the individual Reynolds stresses, $\overline{u_i' u_j'}$, are calculated by using differential transport equations. Thus RSM takes into account the directional effects of the Reynolds stress field, which is not the case for two-equation models. The RSM is suitable for complex 3D flows with strong streamline curvature and severe pressure gradients, highly swirling flows and rotation like curved duct, rotating flow passages, swirl combustors with very large inlet swirl, and rotation. The RSM is a physically most complete model because it is tightly coupled momentum and turbulence equations. The history, transport, and anisotropy of turbulent stresses are all accounted for. However, it is tougher to converge due to close coupling of equations and the RSM requires more memory, computational effort and time. The exact transport equations for the transport of the Reynolds stresses, $\rho\overline{u_i' u_j'}$, are written as follows:

$$\frac{\partial}{\partial t}\left(\rho \overline{u_i' u_j'}\right) + C_{ij} = D_{T,ij} + D_{L,ij} + P_{ij} + G_{ij} + \phi_{ij} - \varepsilon_{ij} + F_{ij} \tag{5}$$

where $\dfrac{\partial}{\partial t}\left(\rho \overline{u_i' u_j'}\right)$: The local time derivative $\tag{6}$

$$C_{ij} = \frac{\partial}{\partial x_k}(\rho u_k \overline{u_i' u_j'}) \quad :\text{Convection} \tag{7}$$

$$D_{T,ij} = -\frac{\partial}{\partial x_k}\left[\rho \overline{u_i' u_j' u_k'} + \overline{p'(\delta_{kj} u_i' + \delta_{ik} u_j')}\right]: \text{Turbulent diffusion} \tag{8}$$

$$D_{L,ij} = \frac{\partial}{\partial x_k}\left[\mu \frac{\partial}{\partial x}(\overline{u_i' u_j'})\right]: \text{Molecular diffusion} \tag{9}$$

$$P_{ij} = -\rho\left(\overline{u_i' u_k'}\frac{\partial u_j}{\partial x_k} + \overline{u_j' u_k'}\frac{\partial u_i}{\partial x_k}\right): \text{Stress production} \tag{10}$$

$$G_{ij} = -\rho\beta\left(g_i \overline{u_j' \theta} + g_j \overline{u_i' \theta}\right): \text{Buoyancy production} \tag{11}$$

$$\phi_{ij} = \overline{p'\left(\frac{\partial u_i'}{\partial x_j} + \frac{\partial u_j'}{\partial x_i}\right)} : \text{Pressure strain} \tag{12}$$

$$\varepsilon_{ij} = -2\mu\overline{\frac{\partial u_i'}{\partial x_k}\frac{\partial u_j'}{\partial x_k}} : \text{Dissipation} \tag{13}$$

$$F_{ij} = -2\rho\Omega_k\left(\overline{u_j' u_m'}\varepsilon_{ikm} + \overline{u_i' u_m'}\varepsilon_{jkm}\right): \text{Production by system rotation} \tag{14}$$

Of the above terms the convection (C_{ij}), molecular diffusion ($D_{L,ij}$), stress production (P_{ij}) and production by system rotation (F_{ij}) terms do not need any modeling, thus are solved exactly. However, the turbulent diffusion ($D_{T,ij}$), buoyancy production (G_{ij}), pressure strain (ϕ_{ij}) and dissipation (ε_{ij}) terms all need to be modeled to close the equations.

The simplified turbulent diffusion ($D_{T,ij}$) can be modeled as follows:

$$D_{ij}^T = \frac{\partial}{\partial x_k}\left(\frac{\mu_t}{\sigma_k}\frac{\partial \overline{u_i' u_j'}}{\partial x_k}\right)$$

(15)

The buoyancy production (G_{ij}) is modeled as

$$G_{ij} = \beta \frac{\mu_t}{\mathrm{Pr}_t}\left(g_i \frac{\partial T}{\partial x_j} + g_j \frac{\partial T}{\partial x_i}\right)$$

(16)

where Pr_t is the turbulent Prandtl number for energy, with a default value of 0.85.

The dissipation (ε_{ij}) is modeled as

$$\varepsilon_{ij} = \frac{2}{3}\delta_{ij}\left(\rho\varepsilon + Y_M\right)$$

(17)

where $Y_M = 2\rho\varepsilon M_t^2$ is an additional dilatation dissipation term.

The pressure strain (ϕ_{ij}) can be written as follows:

$$\phi_{ij} = \phi_{ij,1} + \phi_{ij,2} + \phi_{ij,w}$$

(18)

$$\phi_{ij,1} = -C_1 \rho \frac{\varepsilon}{k}\left[\overline{u_i' u_j'} - \frac{2}{3}\delta_{ij}k\right]$$

(19)

$$\phi_{ij,2} = -C_2\left[\left(P_{ij} + F_{ij} + G_{ij} - C_{ij}\right) - \frac{1}{3}\delta_{ij}\left(P_{kk} + G_{kk} - C_{kk}\right)\right]$$

(20)

$$\phi_{ij,w} = C_1' \frac{\varepsilon}{k}\left(\overline{u_k' u_m'}n_k n_m \delta_{ij} - \frac{3}{2}\overline{u_i' u_k'}n_j n_k - \frac{3}{2}\overline{u_j' u_k'}n_i n_k\right)\frac{k^{3/2}}{C_{l\varepsilon d}}$$

$$+ C_2'\left(\phi_{km,2}n_k n_m \delta_{ij} - \frac{3}{2}\phi_{ik,2}n_j n_k - \frac{3}{2}\phi_{jk,2}n_i n_k\right)\frac{k^{3/2}}{C_{l\varepsilon d}}$$

(21)

where $C_1 = 1.8$, $C_2 = 0.6$, $C_1' = 0.5$, $C_2' = 0.3$, n_k is the x_k component of the unit normal

to wall, d is the normal distance to the wall, and $C_l = C_\mu^{3/4}/\kappa$, where $C_\mu = 0.09$ and κ

is the von *Ka'rma'n* constant (=0.4187). The equation for the scalar dissipation rate (ε)

is as follow:

$$\frac{\partial}{\partial t}(\rho\varepsilon) + \frac{\partial}{\partial x_i}(\rho\varepsilon u_i) = \frac{\partial}{\partial x_j}\left[\left(\mu + \frac{\mu_t}{\sigma_\varepsilon}\right)\frac{\partial\varepsilon}{\partial x_j}\right] + C_{\varepsilon 1}\frac{1}{2}[P_{ii} + C_{\varepsilon 3}G_{ii}]\frac{\varepsilon}{k} - C_{\varepsilon 2}\rho\frac{\varepsilon^2}{k} \tag{22}$$

where $\sigma_\varepsilon = 1.0$, $C_{\varepsilon 1} = 1.44$, $C_{\varepsilon 2} = 1.92$, $C_{\varepsilon 3}$ is evaluated as a function of the local flow

direction relative to the gravitational vector. Turbulent kinetic energy can be written as

$$k = \frac{1}{2}\overline{u_i' u_j'} \tag{23}$$

The turbulent viscosity, μ_t, is computed from:

$$\mu_t = \rho C_\mu \frac{k^2}{\varepsilon} \tag{24}$$

with $C_\mu = 0.09$, where k is the turbulent kinetic energy and ε is its turbulent

dissipation rate.

3.3 Near Wall Modeling

The turbulence models are primarily valid for turbulent core flows. The accurate

representation of the flow in the near wall region determines successful predictions of

wall bounded turbulent flows because the presence of wall affects significantly turbulent

flows. In the turbulent boundary layer, there are three different regions. Viscous sublayer

is the innermost layer and the flow is almost laminar. The transport is dominated by diffusion and the velocity profile is nearly linear. There is an adjoining buffer layer in which diffusion and turbulent mixing are comparable, and in the outer layer, there is the fully turbulent layer which transport is dominated by turbulent mixing.

There are two ways for modeling the near wall region. In the first model, the viscous sublayer and buffer layer are not resolved. Instead, semi-empirical formulas (wall function) are used to link the viscosity affected region between the wall and the fully-turbulent region. The second model is enhanced wall treatment that combines a two-layer model with enhanced wall functions. The near wall mesh must be fine enough to be able to resolve the laminar sublayer. In the two-layer model, viscosity affected near wall region is completely resolved all the way to the viscous sublayer. These two approaches are described schematically in Fig. 3.1.

turbulent core

buffer &
sublayer

?

Wall Function Approach

Near-Wall Model Approach
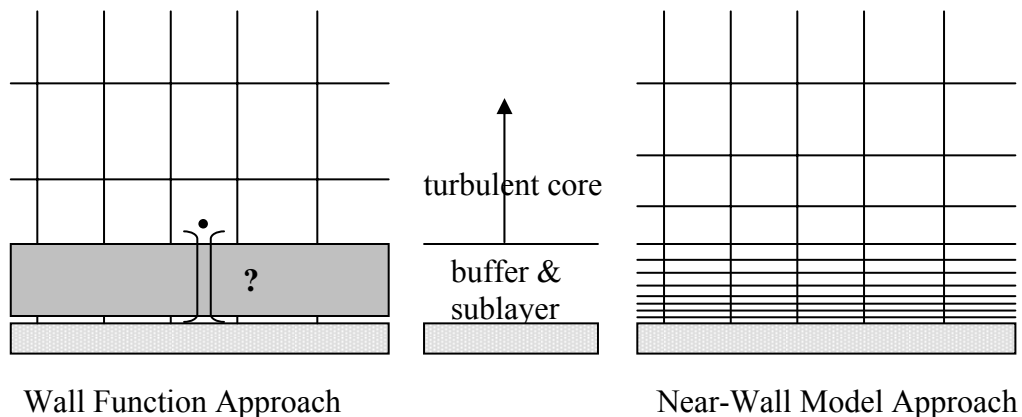
Fig. 3.1 Near-Wall Treatments in FLUENT

The two-layer model subdivides the near wall region into a viscosity-affected region and a fully-turbulent region. In the viscosity-affected region, one equation by Wolfstein is solved, while in the fully turbulent flow the Reynolds stress equations are computed. The turbulent viscosity (μ_t) and turbulent dissipation (ε) are computed from:

$$\mu_{t,2layer} = \rho C_\mu l_\mu \sqrt{k} \tag{25}$$

$$\varepsilon = \frac{k^{3/2}}{l_\varepsilon} \tag{26}$$

where the length scales can be expressed as

$$l_\mu = c_l y \left[1 - \exp\left(-\frac{\mathrm{Re}_y}{A_\mu} \right) \right] \tag{27}$$

$$l_\varepsilon = c_l y \left[1 - \exp\left(-\frac{\mathrm{Re}_y}{A_\varepsilon} \right) \right] \tag{28}$$

where y is the normal distance from the wall, $c_l = \kappa C_\mu^{-3/4}$, $A_\mu = 70$, $A_\varepsilon = 2c_l$ and turbulent Reynolds number, Re_y, is defined as

$$\mathrm{Re}_y = \frac{\rho \sqrt{k} y}{\mu} \tag{29}$$

3.4 Boundary Conditions

The test channel in the computation had the same dimensions as the test section in the experiments described in previous section. The Reynolds numbers were fixed at

34,500 for the square channel and at 31,800 for the trapezoidal channel. The mass flow

rates at the channel inlet were specified with 2.42×10^{-2} kg/s for Re = 34,500 and with

2.79×10^{-2} kg/s for Re = 31,800. The turbulence intensity of 4% and the coolant

temperature of 300K were imposed on the inlet of the channel. At the outlet of the

channel, boundary condition was defined as outflow. Because the boundary condition of

naphthalene coated surfaces corresponds to a uniform wall temperature condition and

that of inactive surfaces to an adiabatic wall condition in heat transfer experiment, only

bottom wall was heated to a constant temperature except the entrance of duct and the

ribs. No-slip boundary conditions were enforced at all walls and rib sides. Properties of

air were calculated by piecewise linear functions.

3.5 Numerical Method of Solution

In this numerical study, the control-volume-based finite difference method was

used to convert the governing equations to algebraic equations that could be solved

numerically. The FLUENT 6.2 program was applied to integrate the governing equations

for each control volume and to yield discrete equations conserving each quantity. The

segregated and explicit solver was chosen to solve flow, energy, turbulence and

Reynolds stresses equations in three dimensions. For the pressure-velocity coupling

discretization, the SIMPLE (Semi-Implicit Method for Pressure-Linked Equation)

algorithm was used to solve the continuity equation. For the pressure interpolation, the

PRESTO! (PREssure Staggering Option) scheme was chosen, which showed better

results for the cases where the pressure profile had a high gradient at the cell face. The equations for the momentum, turbulent dissipation, turbulent kinetic energy, Reynolds stresses and energy were discretized spatially with a second-order upwind scheme. The convergence criteria are 10^{-8} for energy and 10^{-4} for others. The commercial software package GAMBIT grid generator was used to generate the 3-D structured grid. The grid distributions were effectively controlled by clustering the mesh towards the walls in such a way that the employed near wall treatment was properly applied. For enhanced wall treatment, y^+ the first cell next to a wall was maintained below 1. The gravitational effect on the geometry was neglected in this study.

CHAPTER IV

FLOW AND HEAT TRANSFER IN A TWO-PASS SQUARE CHANNEL

WITH SMOOTH WALLS

In chapter IV, computations were performed for a two-pass square channel with smooth walls as tested by Lee et al. [35] using the Reynolds stress model (RSM) with enhanced wall treatment in FLUENT.

4.1 Description of Problem

The simulated geometry was the same as the experimental geometry by Lee et al. [35]. Figure 4.1 & 4.2 show the geometry and the numerical grids for the two-pass square channel with the 180º sharp turn. The length of the duct was 61 cm. The length of each straight section with and without heating surfaces was 30.5 cm, while the width of each section was 3.81 cm and the divider wall thickness was 1.91 cm. The length from the divider wall tip to the end wall in the turn was 3.81 cm. Only bottom wall was heated to a constant temperature since the mass transfer experiment can simulate uniform wall temperature boundary condition. The Reynolds number based on channel hydraulic diameter was fixed at 34,500.
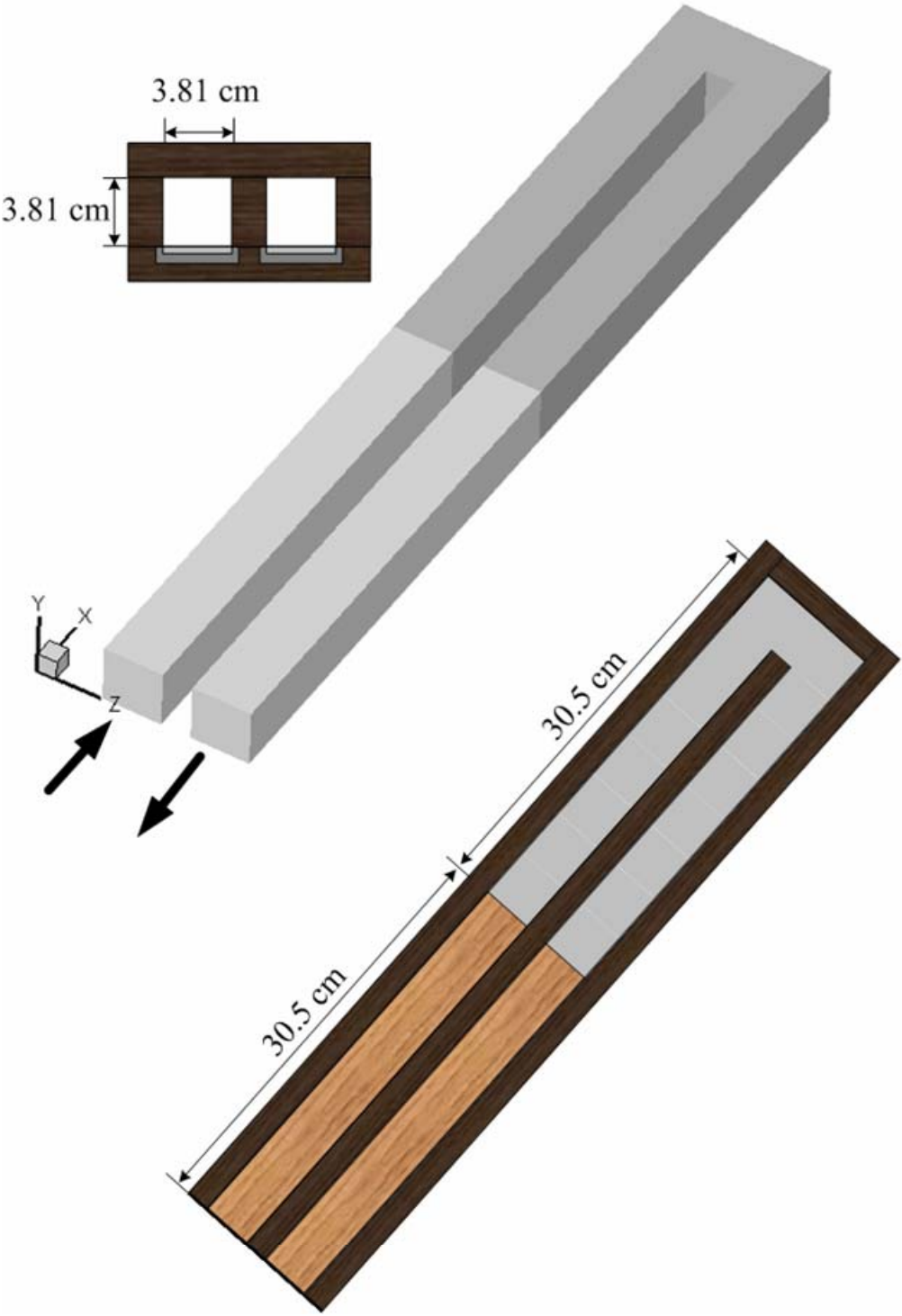
Fig. 4.1 Geometry for square channel with smooth walls
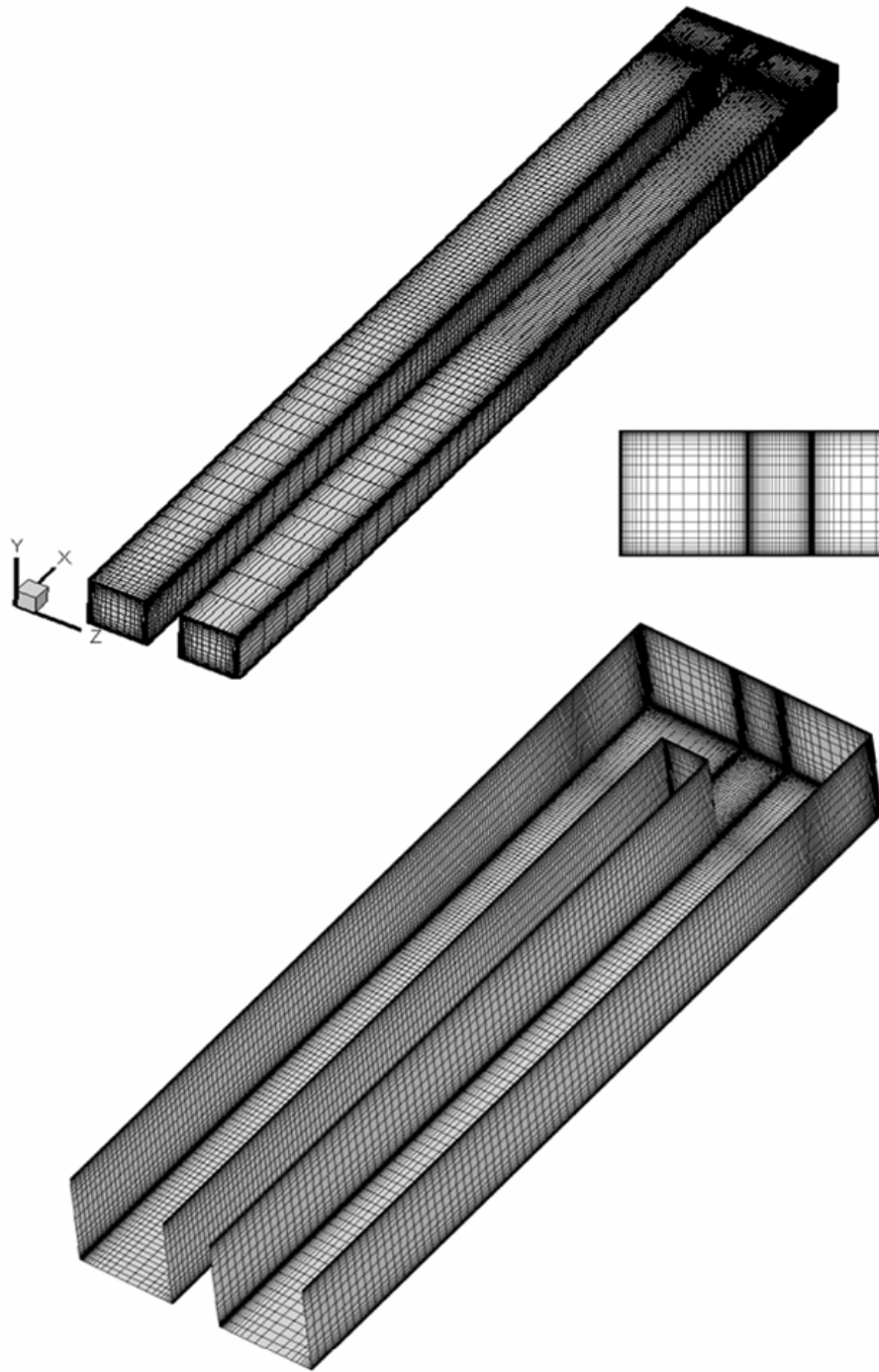
Fig. 4.2 Numerical grid for square channel with smooth walls

4.2 Grid Independence Study

Fig. 4.2 gives the numerical grid generated using Gambit for this simulation. Fig 4.3 shows a comparison of the calculated Nusselt number ratios for a grid refinement study. The grid independent study was performed for three different cross sectional grids of $34 \times 34 \times 520$, $44 \times 44 \times 520$ and $54 \times 54 \times 520$, and one streamwise $44 \times 44 \times 620$ grid with mesh refined in the near wall regions. A comparison between $34 \times 34 \times 520$ and $44 \times 44 \times 520$ grid points showed 7.8% maximum changes in the Nusselt number ratio. The maximum difference in Nusselt number ratio was less than 2.8% between $44 \times 44 \times 520$ and $54 \times 54 \times 520$ grid points. Further increase of the number of grid points in streamwise direction of the channel produced only minor changes of the Nusselt number ratios. Therefore, it was determined that grid independence was achieved with $44 \times 44 \times 520$ grid points and all results were based on the $44 \times 44 \times 520$ grid points, which resulted in 1,006,720 grid points. The y^+ values were less than unity in all test runs of grid independent study for the very fine mesh.

4.3 Velocity Fields

The streamwise velocity vector distributions at the middle plane between the top and bottom surfaces in the heated section are shown in Fig. 4.4(a). In the first passage before the turn, the flow was fully developed and the velocity distributions were constant. As the flow approached the turn region, the turn caused a streamwise flow acceleration

near the divider wall and flow deceleration near the outer wall. Due to the streamwise curvature of the flow in the turn, a radial pressure gradient developed across the turn
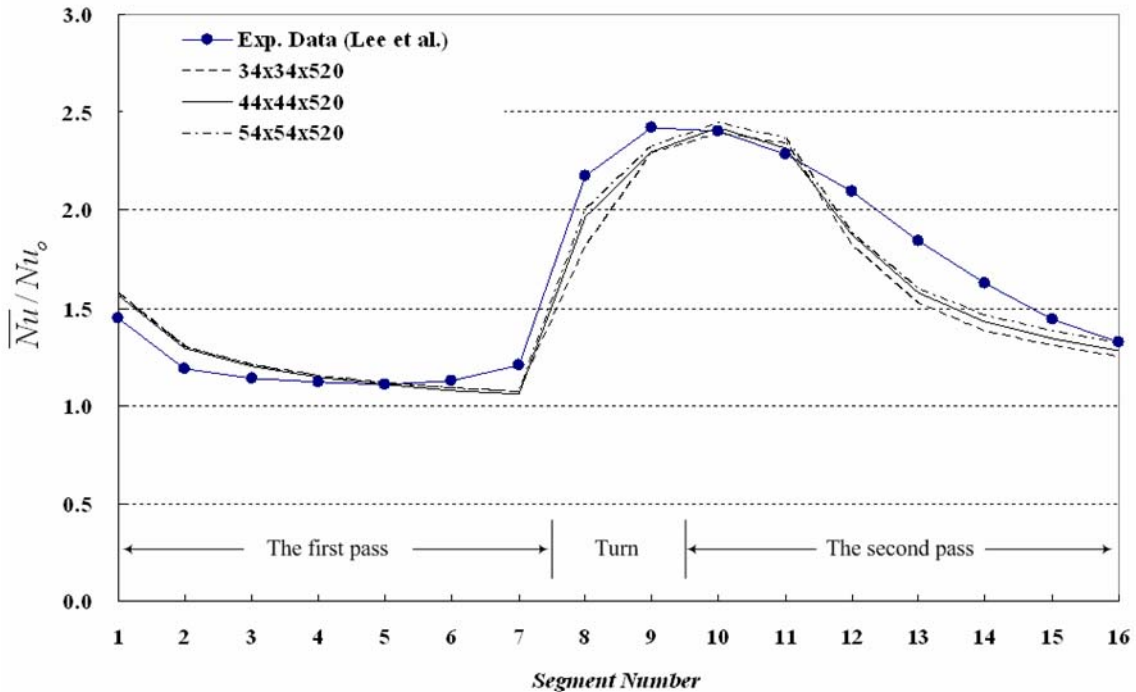
Fig. 4.3 Grid independent study for square channel with smooth walls

region with lower pressure near the divider wall and higher pressure near the outer wall. In other words, the favorable pressure gradient existed near the divider wall and the adverse pressure gradient existed near the outer wall. The sharp tip of the divider wall drove an abrupt change of the flow direction with pressure reduction that made a separation bubble at the tip. The 180º sharp turning pushed the flow outward creating adverse pressure gradient near the divider wall and created a large flow recirculation along the divider wall in the second pass. It was not seen any reattachment to the divider
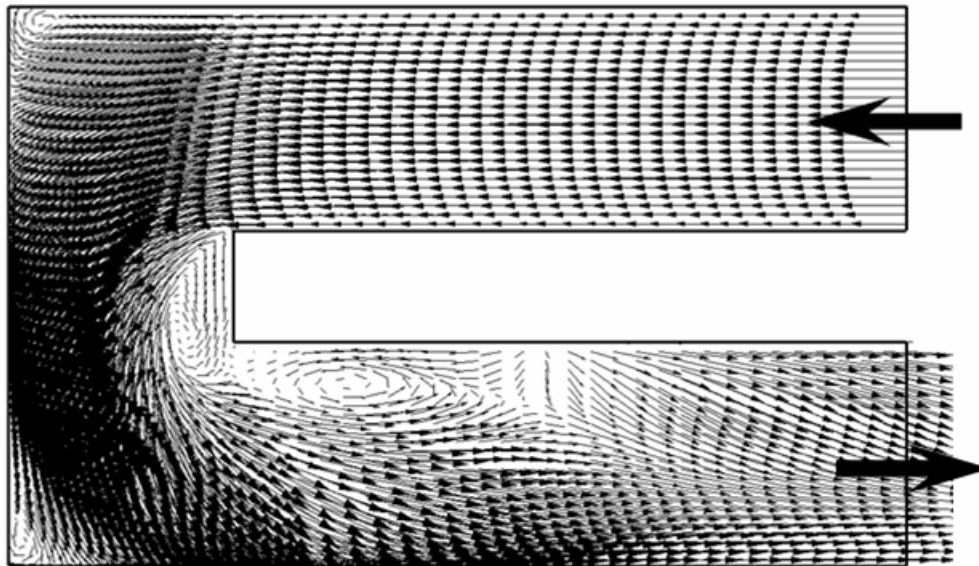
(a) Streamwise velocity vector at y = 0.5D$_h$
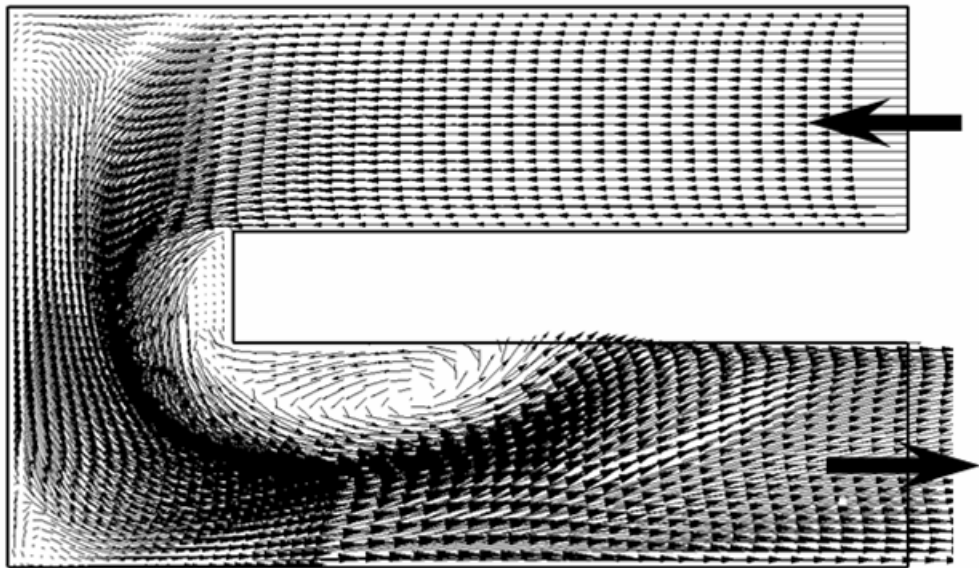
(b) Streamwise velocity vector at y = 0.125D$_h$

Fig. 4.4 Streamwise velocity vector for square channel with smooth walls at Re = 34,500

wall in the recirculation bubble zone on the middle plane. The small recirculation bubble existed at the upstream corner and at the downstream corner. Two flow impingement zones were observed. The high momentum flow entering the turn impinged onto the end wall. This impingement flow divided up and down, and contributed to the secondary flow formation. The other impingement location was on the outer wall at the turn exit due to strong flow acceleration induced by secondary flows and the pressure filed changes. Figure 4.4(b) shows the averaged main flow velocity, which were calculated near the bottom wall. It can be seen that stronger flow recirculation developed near the tip of divider wall reattached to the divider wall after the turn in second pass. It seems that the stronger flow recirculation reattached to the divider wall surface location off the middle plane and two reattached flows from top and bottom walls merged into the middle plane to create the bifurcating flow.

4.4 Secondary Flow Development

Fig. 4.5 shows the mean secondary flow development of the counter-rotating vortices. In the first passage, small secondary corner vortices were generated as a result of the Reynolds stress anisotropy. The magnitude of these vortices, which was very small, cannot be seen clearly. In the turn region, the centrifugal forces and the associated pressure gradients produced two counter-rotating vortices which transported cooler fluid from the core toward the outer surface, resulting in a steeper temperature gradient and thus a higher heat transfer on the outer wall. The relatively faster inner flow carries a
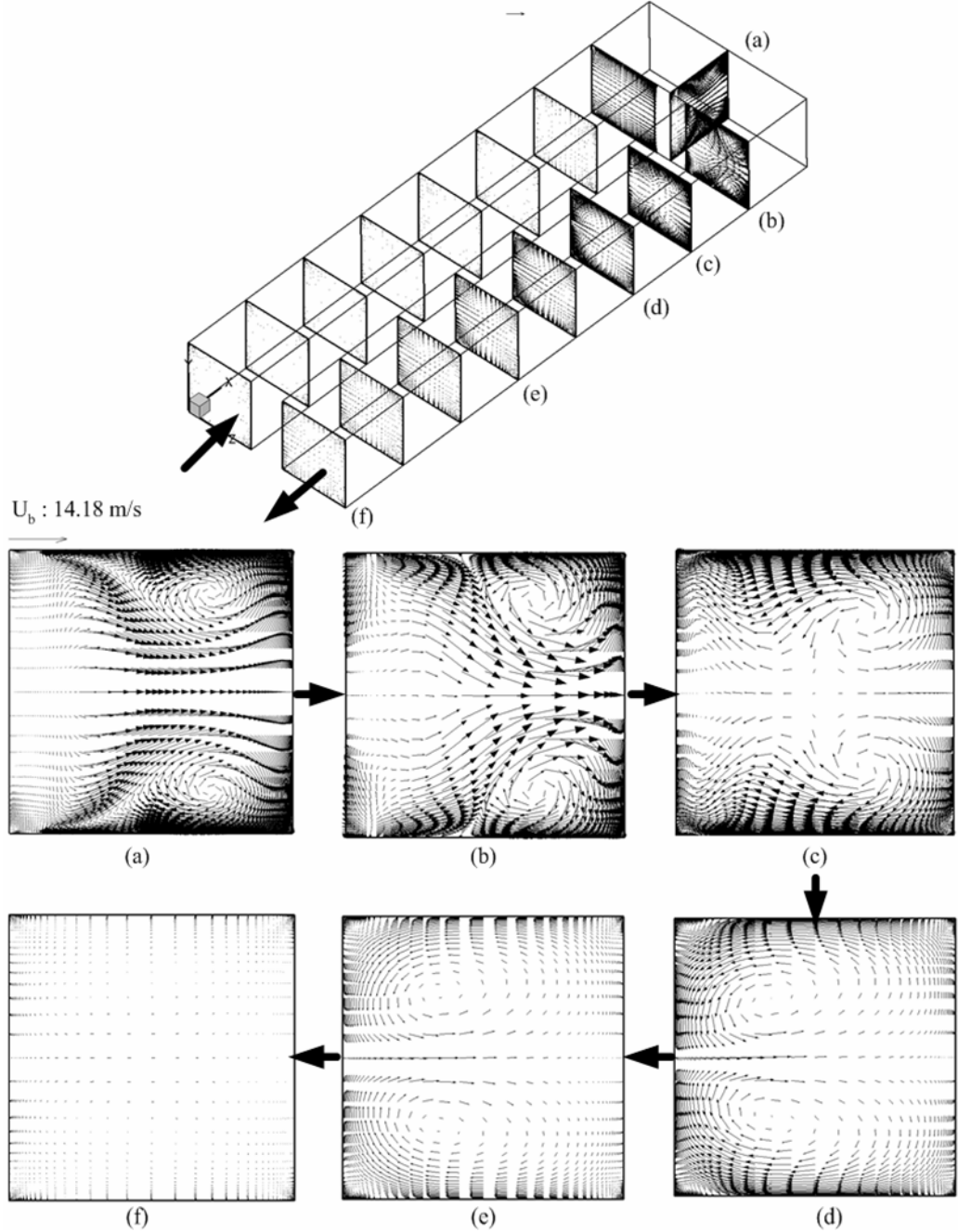
Fig. 4.5 Secondary flow developments for square channel with smooth walls

at Re = 34,500

larger centrifugal force than the outer flow and this leads to the emergence of the secondary flow directing outwards in the center and inwards near the surface. This secondary flow started to decrease in the second passage and diminished almost completely at the end of the second passage. The strong vortex pair appeared at the 90° turning plane from the incident flow direction (Fig. 4.5(a)) due to the centrifugal force action. Through the turn, the vortex strength further increase with more flow turning at the 180° turning plane. The counter-rotating vortex pair was pushed toward the outer wall as shown in Fig. 4.5(b) &(c) and occupied only half of the cross section due to the large separating bubble that occurred immediately downstream the turn near the inner wall. Downstream of the separation bubble (Fig. 4.5(d)), the counter-rotating vortex pair was pushed toward the divider wall since the pressure gradient was recovered on the inner surface (divider wall) and then gradually diminished in second passage channel cross sections (Fig. 4.5(e) and (f)).

4.5 Heat Transfer Distribution

Fig. 4.6 & 4.7 show the Nusselt number ratio contour plots and regional average Nusselt number ratios on the bottom wall at Re = 34,500. Comparisons were made between calculations and experiment data of Lee et al (2007). The entrance and exit regions were cut off to focus on the bend effect. In the first passage, as the flow approached the 180° turn, the flow was fully developed and the Nusselt number ratios were low and almost constant. In the turn region, the turn effect was attributed to
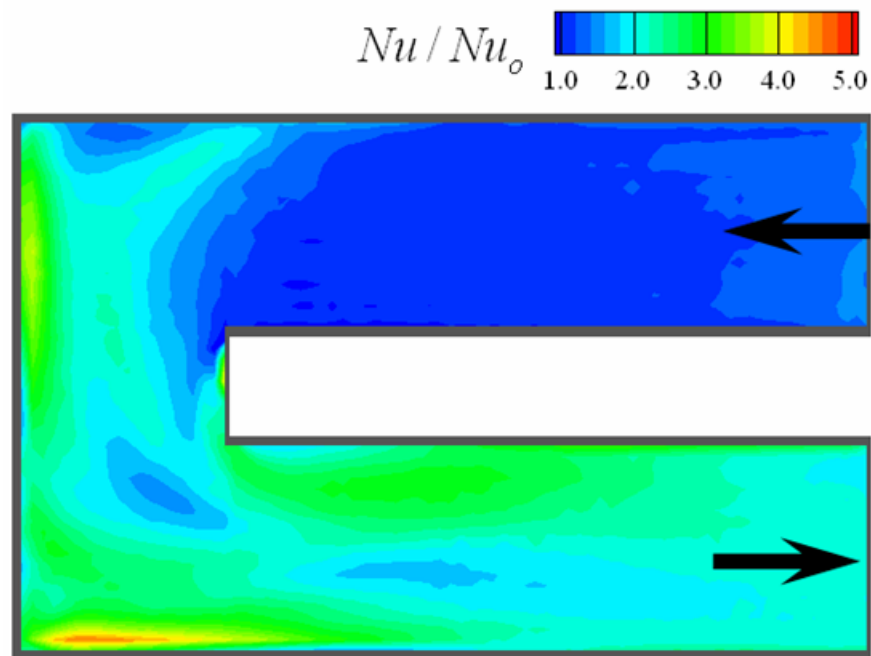
(a) Experimental Data by Lee et al (2007)
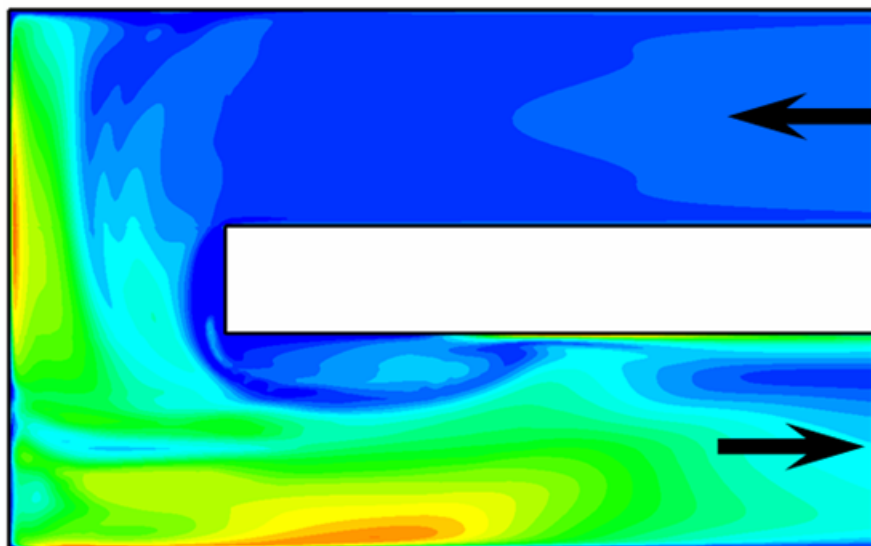
(b) Numerical Data by RSM

Fig. 4.6 Detailed Nusselt number ratio distributions for square channel with smooth walls at Re = 34,500
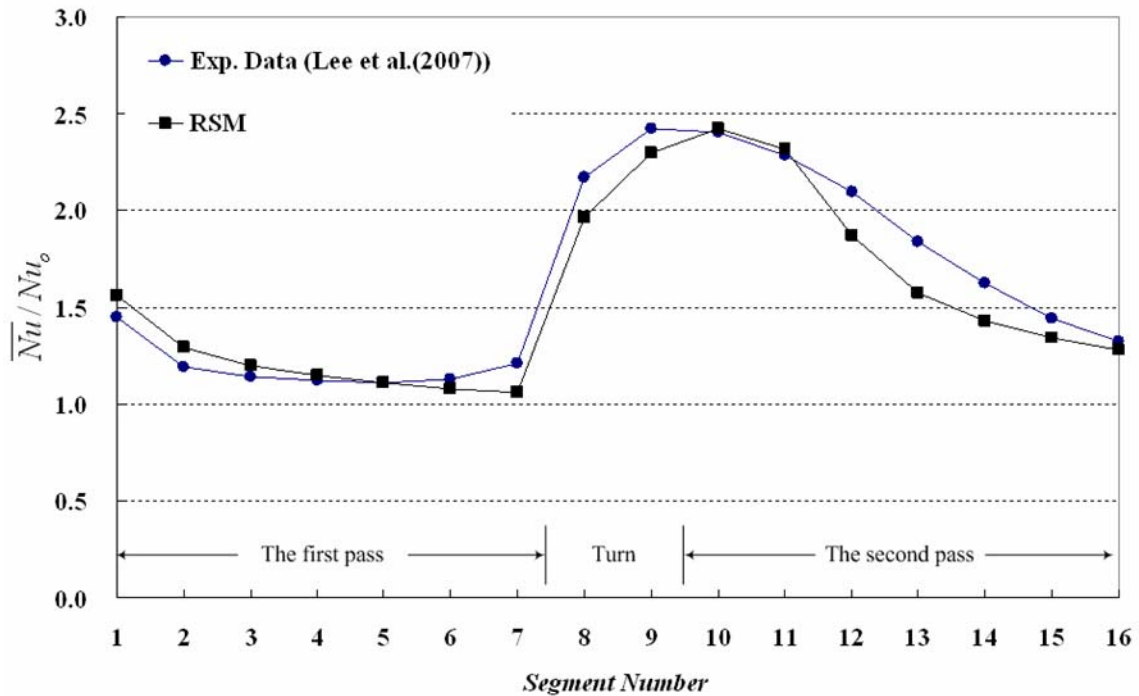
Fig. 4.7 Calculated and measured regional average Nusselt number ratios

for square channel with smooth walls at Re = 34,500

secondary flows induced by the centrifugal force. Thus, high heat transfer was observed

near the end wall due to the flow impingement. As the flow entered the second passage,

another flow impingement was observed near the outer surface caused by the centrifugal

force created by the 180º sharp turn. When the flow impinges the surface, the boundary

layer thickness diminishes near the stagnation point, thus heat transfer enhancement was

expected due to the high temperature gradient. Another relatively higher heat transfer

region was near divider wall in second passage due to reattachment of flow after the turn.

Farther downstream in the second passage, the Nusselt number ratio decreased as the effect of the turn reduced. There were relatively low heat transfer regions in the first outer corner due to corner flow entrapment.

In the regional average Nusselt number ratios (Fig. 4.7), the Nusselt number ratio decreased gradually in first passage. This continuous decrease was due to the developing thermal boundary layer. As the flow approached the turn, the Nusselt number ratio increased due to the secondary flows induced by the turn. The Nusselt number ratio reached the peak value at the entrance of the second passage due to the flow impingement onto the bottom wall and then decreased as the flow moved to the exit of the second passage. This was due to the diminishing of secondary flow induced by the turn.

The predicted Nusselt number ratios by the Reynolds stress model (RSM) were closed to the experimental data of Lee et al (2007). It can show well flow field and heat transfer distribution. However, the Reynolds stress model (RSM) slightly underpredicted the steep increase of the heat transfer in the turn region and the Nusselt number ratios in after the turn in second passage. The maximum relative error was 13.3% and the average relative error was 6.1%. The relative error is defined by normalizing the difference between the experimental and numerical values with respect to the experimental values.

CHAPTER V

FLOW AND HEAT TRANSFER IN A TWO-PASS TRAPEZOIDAL

CHANNEL WITH SMOOTH WALLS

In chapter V, computations were performed for a two-pass trapezoidal channel with smooth walls as tested by Lee et al. [35] using the Reynolds stress model (RSM) with enhanced wall treatment in FLUENT.

5.1 Description of Problem

The simulated geometry was the same as the experimental geometry by Lee et al. [35]. Fig. 5.1 & 5.2 show the geometry and the numerical grids for the two-pass trapezoidal channel with the 180º sharp turn. The length of the duct was 61 cm. The length of each straight section with and without heating surfaces was 30.5 cm, while the width of each section was 3.81 cm and the divider wall thickness was 1.91 cm. The length from the divider wall tip to the end wall in the turn was 3.81 cm. Only bottom wall was heated to a constant temperature since the mass transfer experiment can simulate uniform wall temperature boundary condition. The included angle of trapezoidal cross section between the top wall and the bottom wall was 21.8°. The heights of the outer and inner vertical wall in small trapezoidal channel were 3.81 cm and 5.33 cm, and the height of the inner and outer vertical walls in large trapezoidal channel were 6.10 cm and 7.62 cm, respectively. Therefore, when the average values of
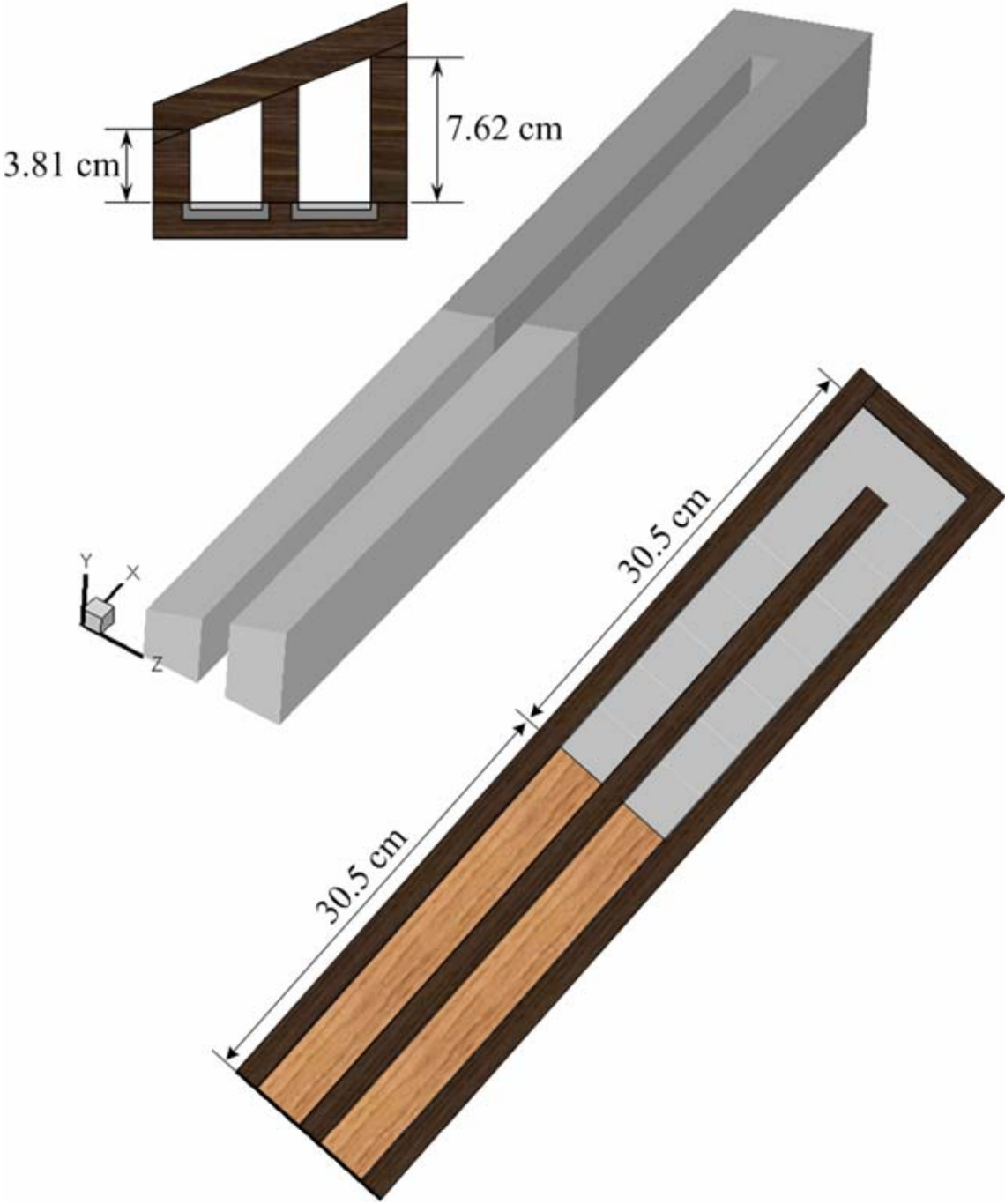
Fig. 5.1 Geometry for trapezoidal channel with smooth walls
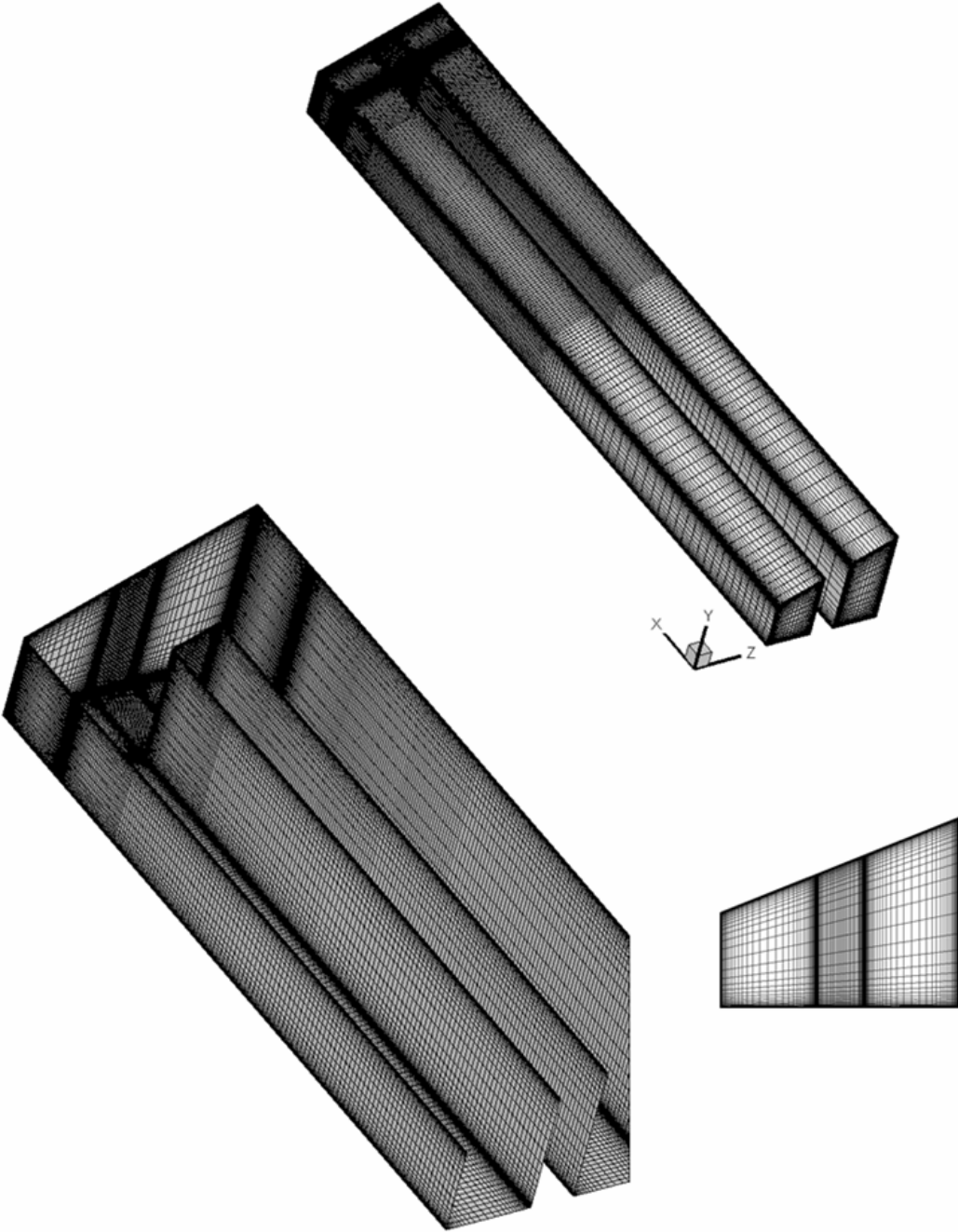
Fig. 5.2 Numerical grid for trapezoidal channel with smooth walls

channel width and height were considered, the channel aspect ratios (W/H) were 1:1.16 for smaller cross section and 1:1.73 for larger cross section. The hydraulic diameters of the small trapezoidal cross section ($D_{h,small}$) was 4.09 cm and the hydraulic diameter of the large trapezoidal crosses section ($D_{h,large}$) was 4.83 cm. For the same air mass flow rate, the Reynolds number was based on the hydraulic diameter of the cross section at the turn clearance ($D_{h,turn}$ = 4.57 cm) because the channel height in the trapezoidal channel was varied in the turn region. The Reynolds numbers were fixed at 31,800.

Experiments were performed for the air entering the trapezoidal channel through the straight section with the smaller cross section as well as entering through the straight section with the larger cross section. Therefore, there were two inlet velocity conditions. The velocities in channel inlet in smaller cross section and in larger cross section were 13.61 m/s and 9.08 m/s, respectively.

5.2 Grid Independence Study

Fig. 5.2 gives the numerical grid generated using Gambit for this simulation. The grid independent study was made by performing the simulations for three different cross sectional grids of $34 \times 54 \times 520$, $44 \times 64 \times 520$ and $54 \times 74 \times 520$, and one streamwise $44 \times 64 \times 620$ grid with mesh refined in the near wall regions (Fig. 5.3). For the smaller inlet case (Fig. 5.3(a)), a comparison between $34 \times 54 \times 520$ and $44 \times 64 \times 520$ grid points showed 7.4% maximum changes in the Nusselt number ratio. The maximum difference
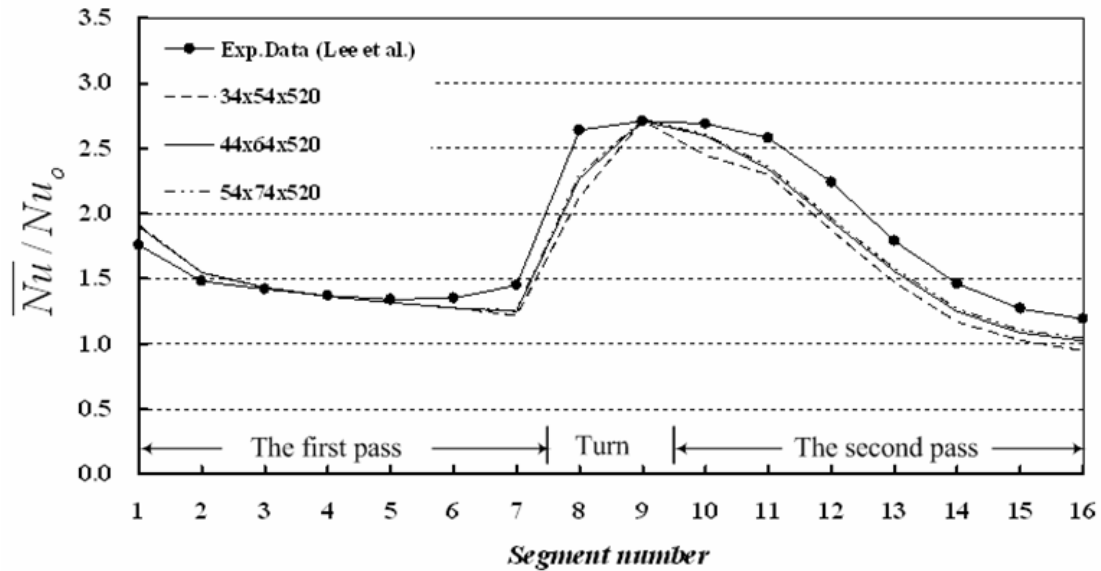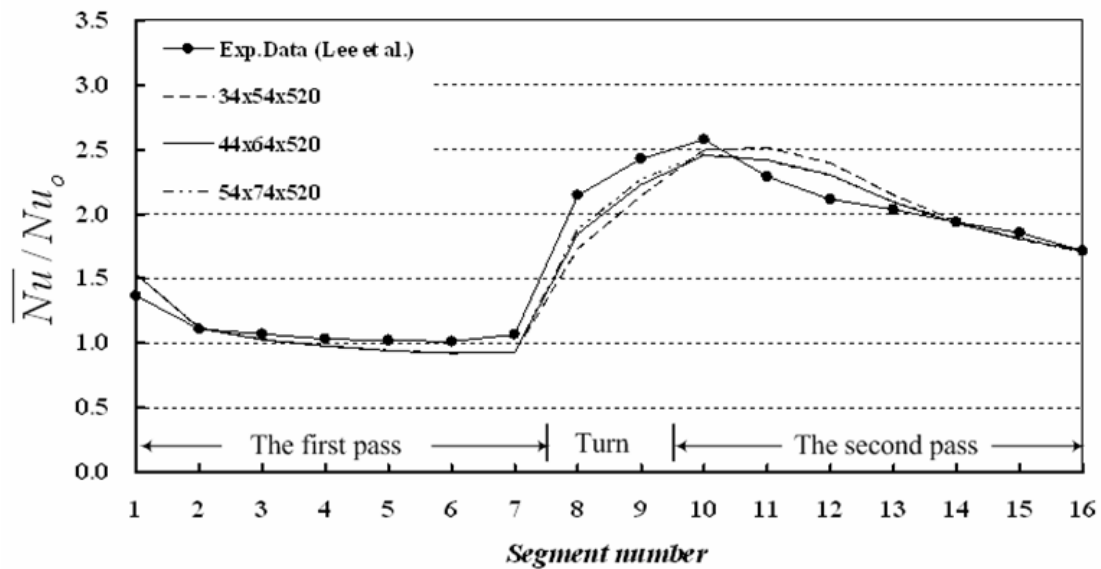
Fig. 5.3 Grid independent study for trapezoidal channel with smooth walls

in Nusselt number ratio was less than 1.9% between $44 \times 64 \times 520$ and $54 \times 74 \times 520$ grid points. For the larger inlet case (Fig. 5.3(b)), a comparison between $34 \times 54 \times 520$ and $44 \times 64 \times 520$ grid points showed 6.3% maximum changes in the Nusselt number ratio. The maximum difference in Nusselt number ratio was less than 1.8% between $44 \times 64 \times 520$ and $54 \times 74 \times 520$ grid points. Further increase of the number of grid points in streamwise direction of the channel produced only minor changes of the Nusselt number ratios for the both cases. Therefore, it was determined that grid independence was achieved with $44 \times 64 \times 520$ grid points and all results were based on the $44 \times 64 \times 520$ grid points, which resulted in 1,464,320 grid points for both the smaller inlet and larger inlet cases. The y^{+} values were less than unity in all test runs of grid independent study.

5.3 Velocity Fields

For the inlet at smaller cross section, the streamwise velocity vector distributions at the middle plane between the top and bottom walls and near bottom wall are shown in Fig. 5.4. In the first passage before the turn, the flow was fully developed and the velocity distributions were constant. As the flow approached the turn region, the turn caused a streamwise flow acceleration near the divider wall and flow deceleration near the outer wall. Due to the streamwise curvature of the flow in the turn, a radial pressure gradient developed across the turn region with lower pressure near the divider wall and higher pressure near the outer wall.
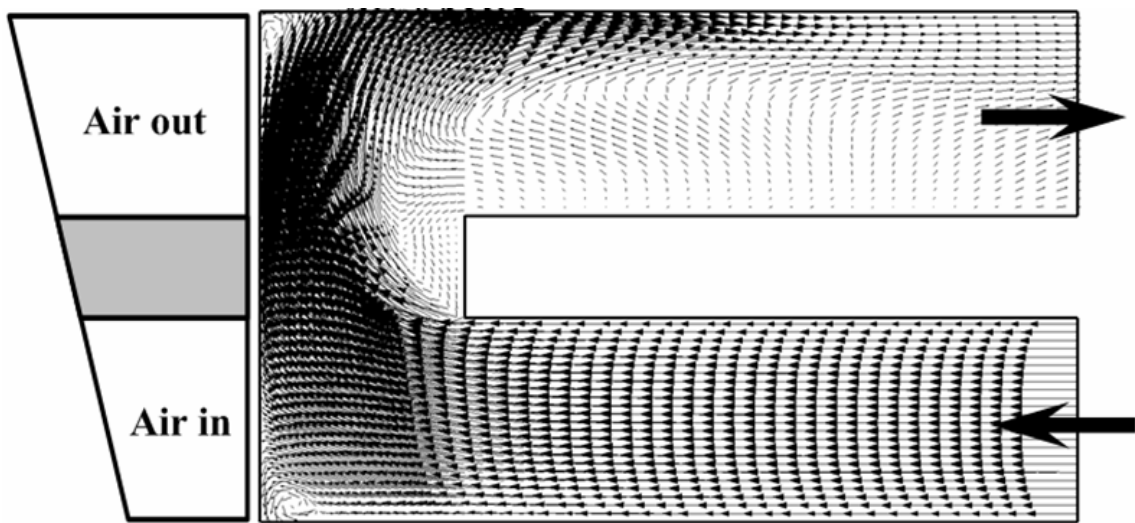
(a) Streamwise velocity vector at y = 0.5D$_h$
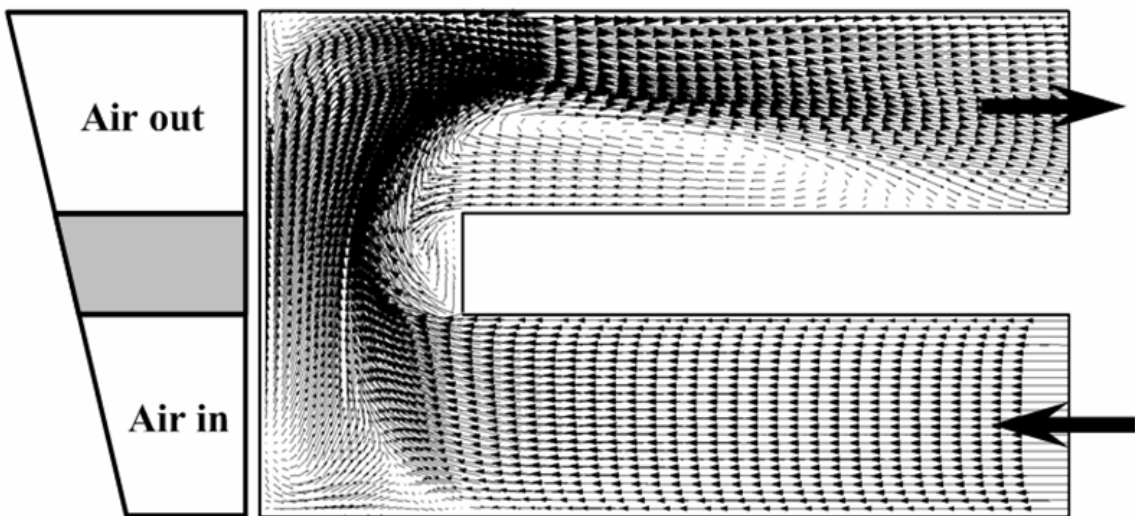
(b) Streamwise velocity vector at y = 0.125D$_h$

Fig. 5.4 Streamwise velocity vector of trapezoidal channel with smooth walls

for inlet at smaller cross section at Re = 31,800
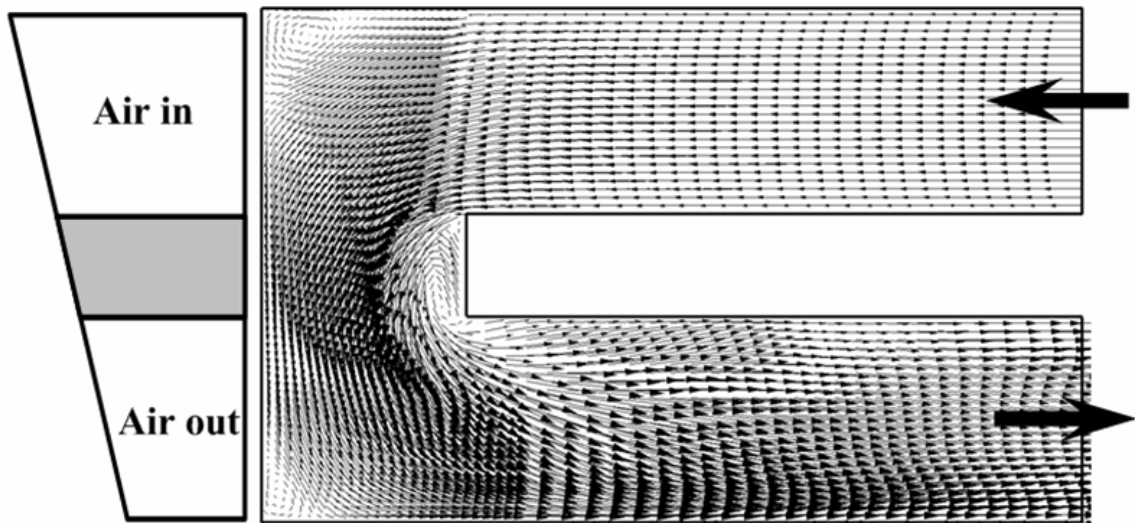
(a) Streamwise velocity vector at y = 0.5D$_h$
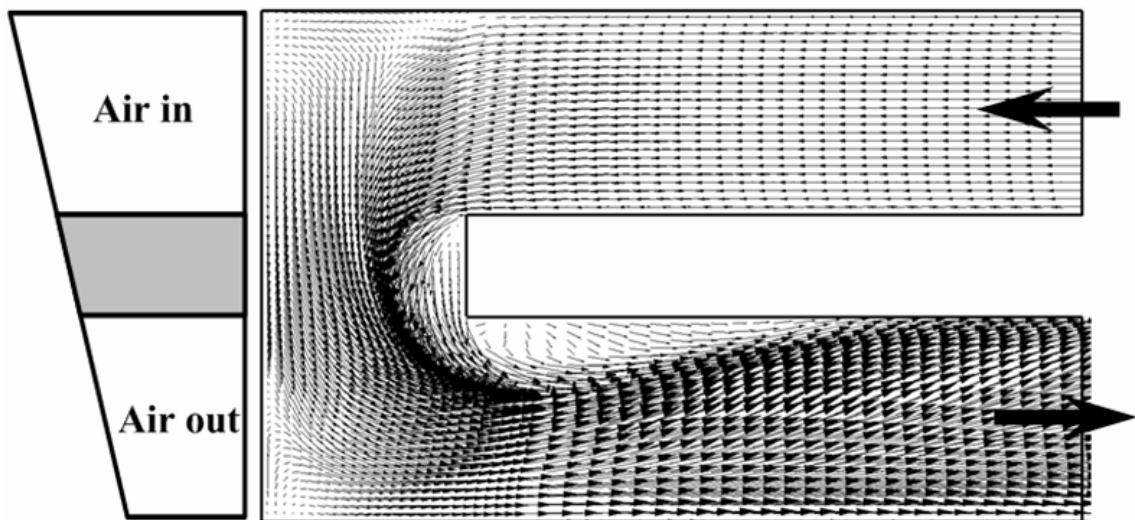
(b) Streamwise velocity vector at y = 0.125D$_h$

Fig. 5.5 Streamwise velocity vector of trapezoidal channel with smooth walls

for inlet at larger cross section at Re = 31,800

The sharp tip of the divider wall drove an abrupt change of the flow direction with pressure reduction that made a separation bubble at the tip. Unlike the square channel, the large flow recirculation along the divider wall in the second passage was not observed midway between the top and bottom walls. Instead of the recirculation there was a large bifurcating zone along the divider wall. Due to increasing flow cross section in the turn, the flow was decelerated and centrifugal force was weakened. The main flow was pushed by centrifugal force at the turn toward outer wall and was then deflected onto the top wall. However there were seen the recirculation bubble zone and the reattachment to the divider wall near the bottom wall (Fig. 5.4(b)). The small recirculation bubble existed at the upstream corner and at the downstream corner. Two flow impingement zones were observed. The high momentum flow entering the turn impinged onto the end wall. The other impingement location was on the outer wall at the turn exit due to still large momentum of the flow from the smaller inlet section. Fig. 5.5 shows streamwise velocity vector for inlet at larger cross section. The flow approached the turn from the larger inlet section with relatively lower velocity and accelerates through the turn as the flow cross section was decreased in the turn region. Unlike the smaller inlet case, the separation bubble at the tip of the divider wall was smaller due to the accelerated flow through the turn. The large bifurcating zone along the divider wall was not observed. However there were seen the small bifurcating zone along the divider wall near the bottom wall due to the secondary flow induced by the turn (Fig. 5.5(b)).
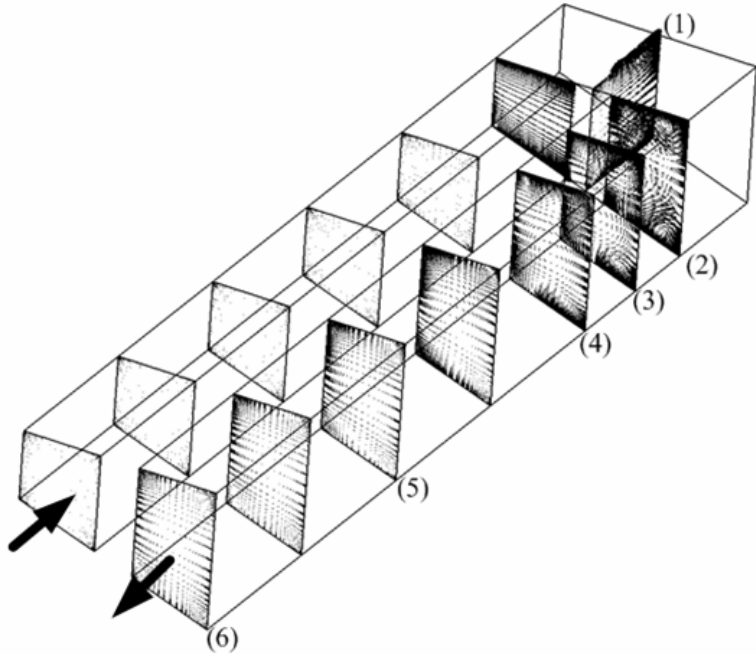
(a) Smaller inlet case
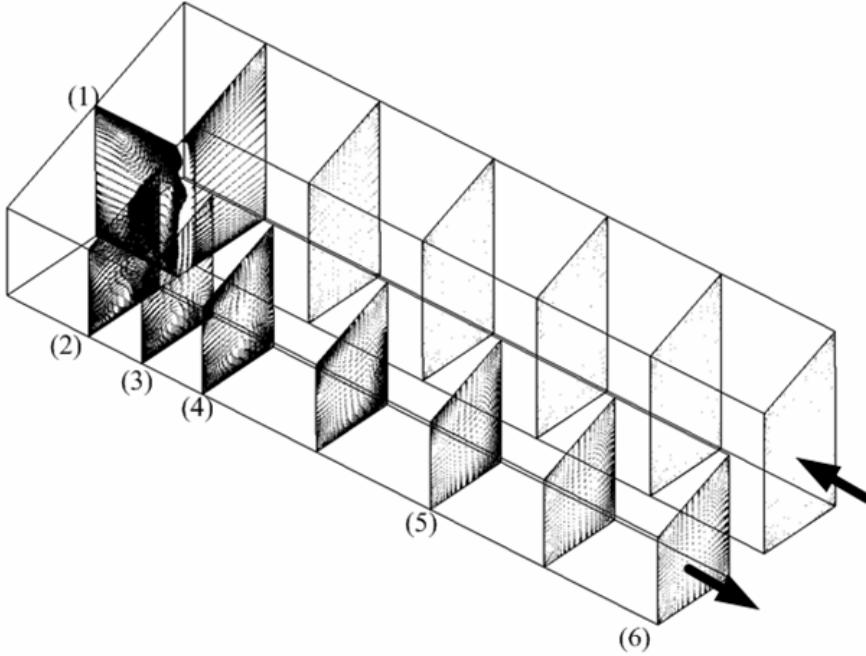
(b) Larger inlet case

Fig. 5.6 Secondary flow location for trapezoidal channel with smooth walls
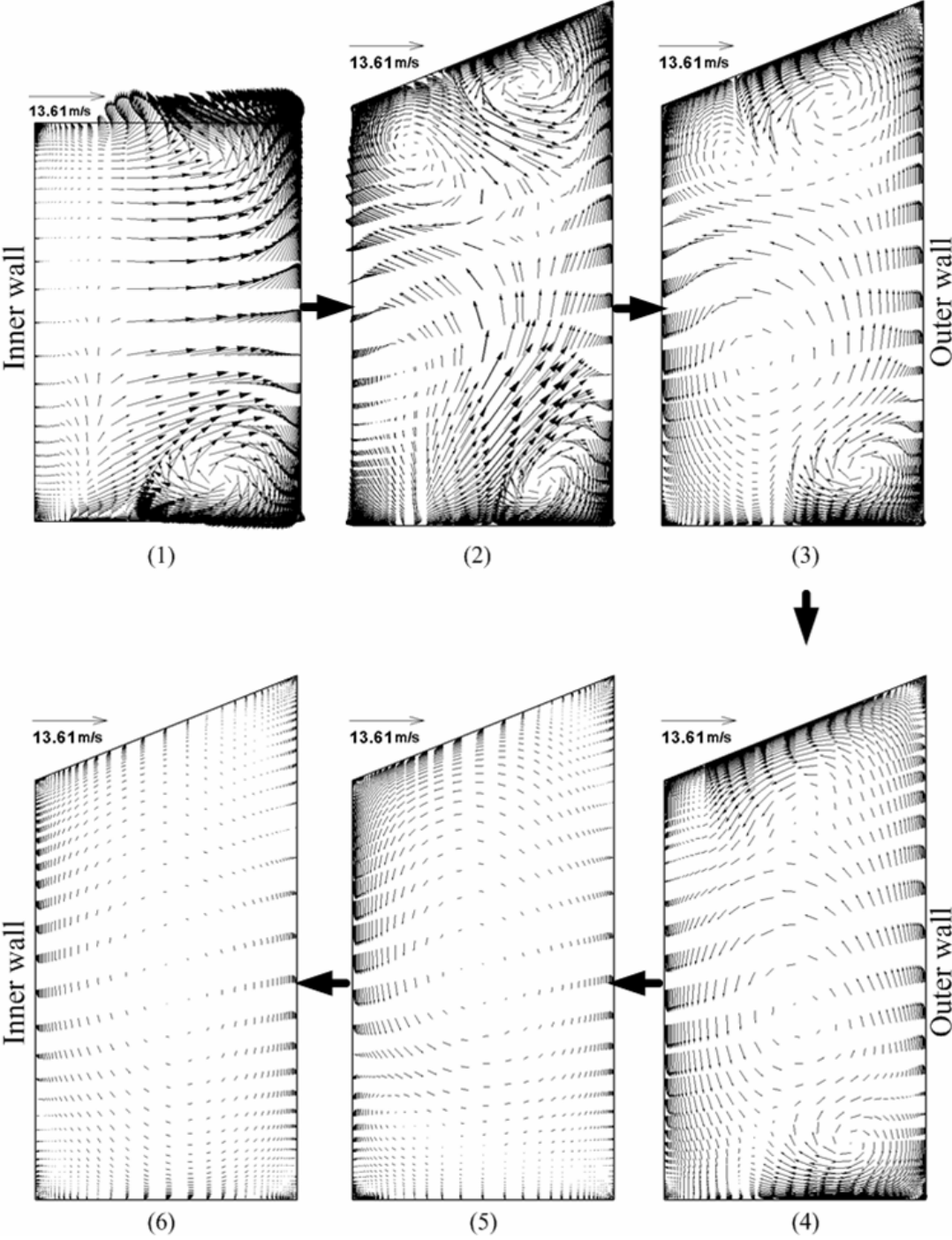
Fig. 5.7 Secondary flow developments of trapezoidal channel with smooth walls

for inlet at smaller cross section
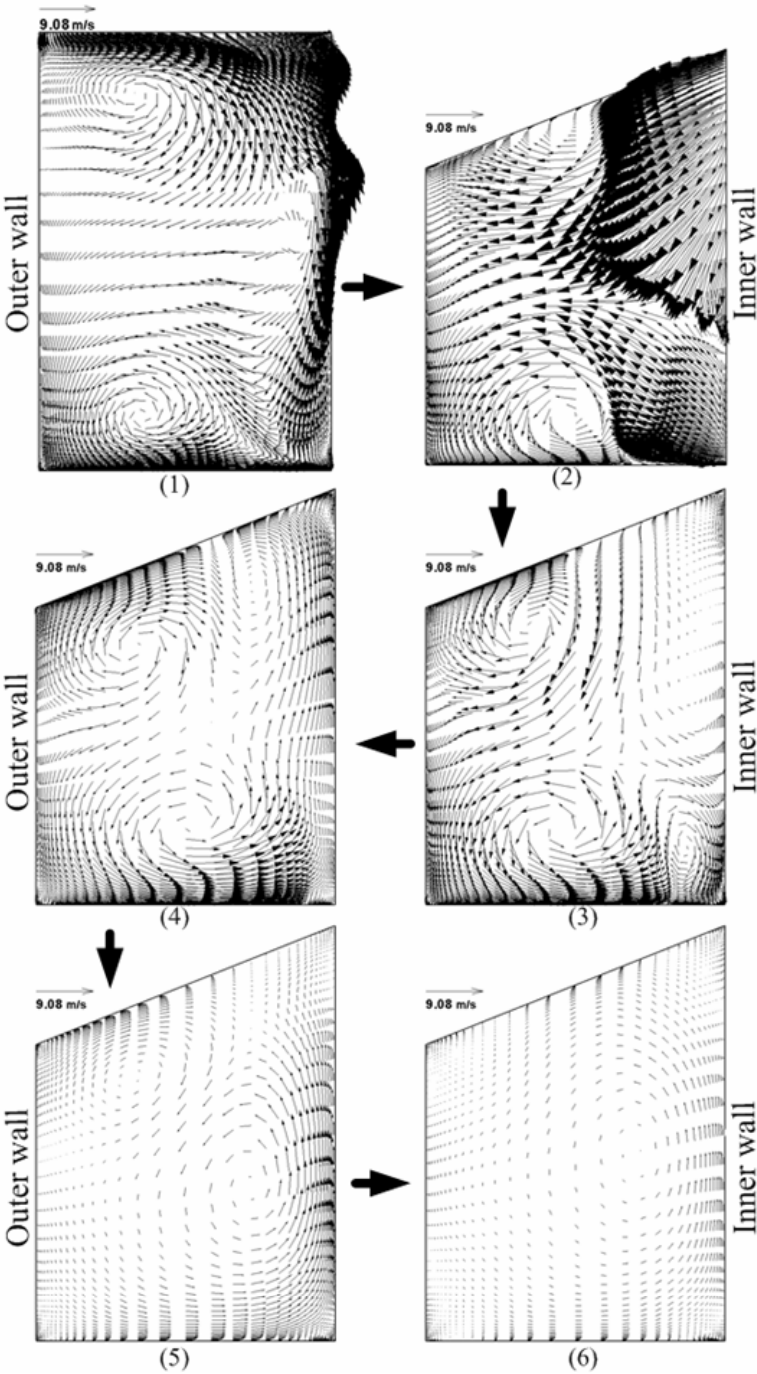
Fig. 5.8 Secondary flow developments of trapezoidal channel with smooth walls

for inlet at larger cross section

5.4 Secondary Flow Development

To facilitate a more detailed understanding of the three-dimensional flow field, secondary flow fields were presented. Fig. 5.7 and 5.8 show the calculated secondary flow vectors at several streamwise locations denoted in Fig. 5.6 for the smaller inlet and larger inlet cases. It was seen from Fig. 5.6 that the anisotropy of the turbulent Reynolds stresses produced small secondary corner vortices in the first passage. The magnitude of those vortices was so small and it cannot be clearly seen in this figure. For the smaller inlet case (Fig. 5.7), two counter-rotating vortices were produced in the turn as shown in Fig. 5.7. (1), which transported flow from core toward the end (outer) wall since the relatively faster inner flow carries a larger centrifugal force than the outer flow and this leads to the emergence of a secondary flow directing outward in the center and inward near the top and bottom walls. The secondary flow near the bottom wall was large and well formed a vortex flow but the secondary flow near the top wall was smaller and slightly distorted. At the 180° turning plane (Fig. 5.7. (2)), the vortex near the bottom wall was pushed toward the outer wall and two counter-rotating vortices were formed near the top wall due to the vertically extended cross sectional area. At the location (3), four counter-rotating vortices were observed. One large counterclockwise rotating vortex occupied in the center of the channel. Two small vortices existed near the top wall and one small vortex existed near the outer and bottom wall (Fig. 5.7. (3)). After the effects of the turn were decreased, the vortices near the top wall disappeared and the vortex near the bottom wall was weakened (Fig. 5.7. (4)). Further downstream of the turn, only one

large counterclockwise rotating vortex was left and other vortices were diminished (location (5) and (6)). For the larger inlet case (Fig. 5.8), two counter-rotating vortices were produced in the turn as shown in Fig. 5.8. (1), which transported flow from core toward the end (outer) wall. The upper vortex was slightly bigger than a lower vortex. The vertical downward velocity was very strong due to the flow acceleration. At the 180° turning plane (Fig. 5.8. (2)), the two vortices were pushed toward the outer wall due to the strong centrifugal force. Downstream of the turn, two large strong vortices occupied almost entire cross sectional area and a small vortex near the inner and bottom wall was observed (location (3)). Further downstream (location (4)), the small vortex was diminished and the two large vortices predominated entire cross sectional area. Finally the weaker vortices were merged into one large counterclockwise vortex and relatively weaker vortex occupied the whole cross section (location (5) and (6)).

5.5 Heat Transfer Distribution

The Nusselt numbers presented here were normalized with a smooth tube correlation by Dittus-Boelter for fully developed turbulent non-rotating tube flow:

$$Nu_0 = 0.023 \, \mathrm{Re}_{Dh}^{0.8} \, \mathrm{Pr}^{0.4}$$

Fig. 5.9 shows the detailed Nusselt number ratio distributions on the bottom wall in a two-pass trapezoidal channel with smooth walls at Re = 31,800. Comparisons were made between calculations and experiment data of Lee et al (2007). The entrance and exit regions were cut off to focus on the turn effect. For the smaller inlet case (Fig. 5.9),

in the first passage, as the flow approached the 180º turn, the flow was fully developed and the Nusselt number ratio was low and almost constant. In the turn region, the turn effect was attributed to secondary flows induced by the centrifugal force. Thus, high heat transfer was observed near the end wall due to the flow impingement. As the flow entered the second passage, another flow impingement was observed near the outer surface caused by the centrifugal force created by the 180º sharp turn. When the flow impinges the surface, the boundary layer thickness diminishes near the stagnation point, thus heat transfer enhancement is expected due to the high temperature gradient. Further downstream in the second passage, the Nusselt number ratio decreased as the effect of the turn reduced. The Nusselt number ratios gradually decreased along the outer wall due to the secondary flow and the lowest heat transfer enhancement was observed along the downstream side of the divider wall. There was relatively low heat transfer region in the tip of the divider wall due to the flow separation. For the larger inlet case (Fig. 5.10), the heat transfer enhancement was higher near the downstream outer wall in the turn than near the end wall. The flow entered the turn from the larger inlet section with relatively low velocity and accelerated through the turn as the flow cross section was reduced in the turn. After the turn the high Nusselt number ratios were along the two side walls and relatively low ratios were in the middle of the bottom wall since the accelerated flow through the turn strengthened a pair of counter-rotating vortices over the bottom wall.

The regional average Nusselt number ratios on the bottom wall for the two-pass trapezoidal channel with smooth walls at Re = 31,800 are shown in Fig. 5.11.

Nu/Nu_o
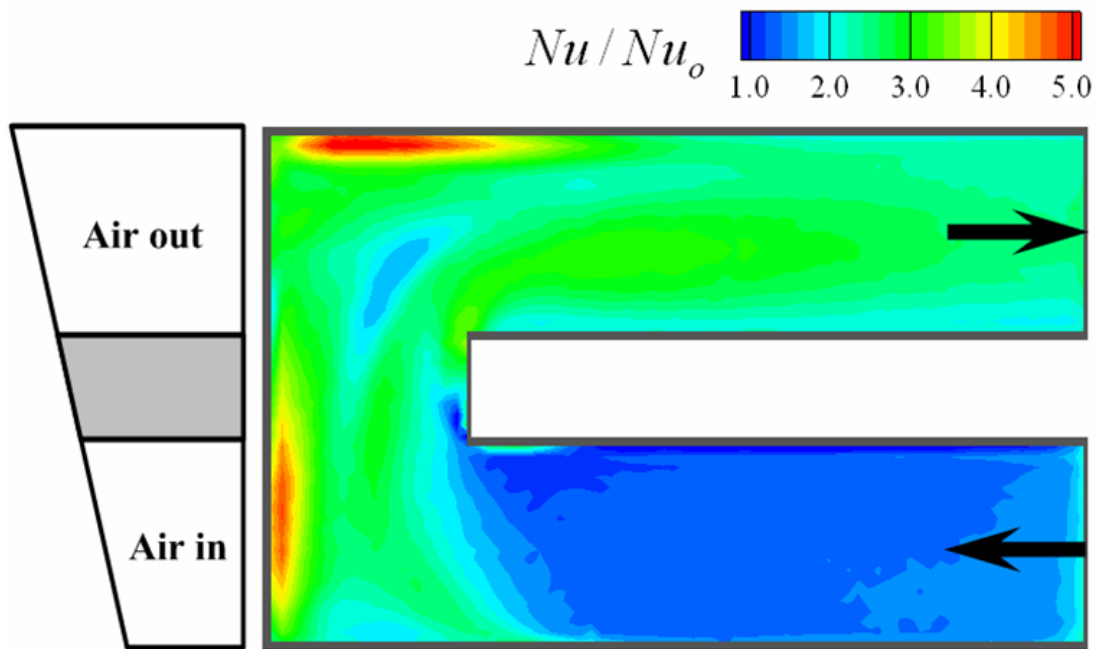
(a) Experimental Data by Lee et al (2007)
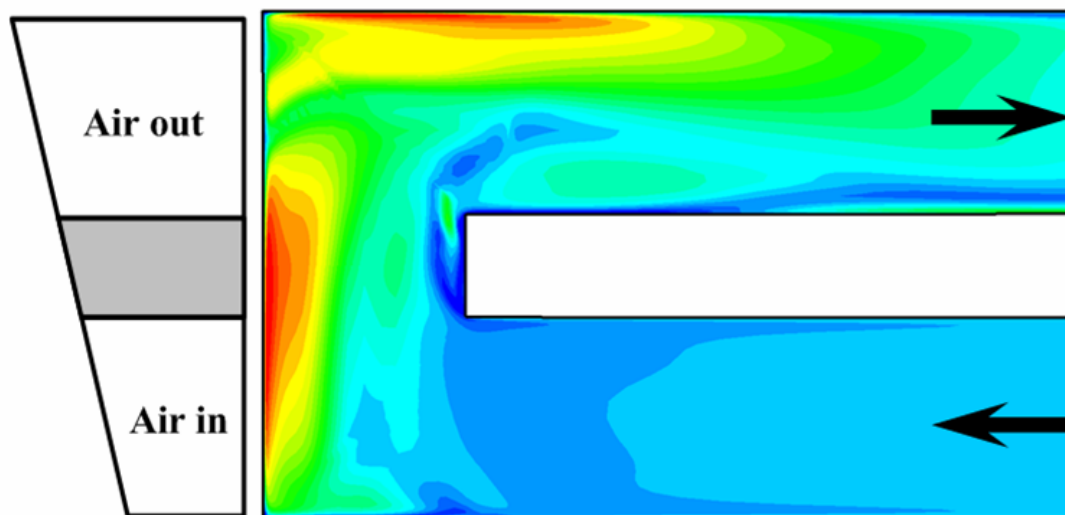
(b) Numerical Data by RSM

Fig. 5.9 Detailed Nusselt number ratio distributions of trapezoidal channel with

smooth walls for smaller inlet case at Re = 31,800

Nu / Nu_o

1.0   2.0   3.0   4.0   5.0

Air in

Air out

(a) Experimental Data by Lee et al (2007)

Air in

Air out
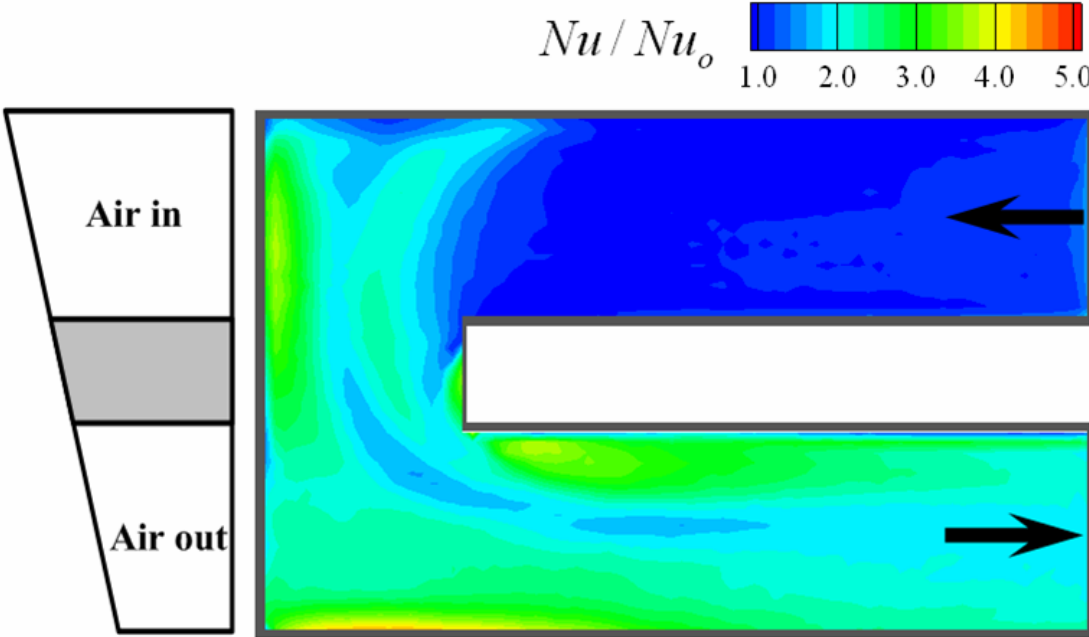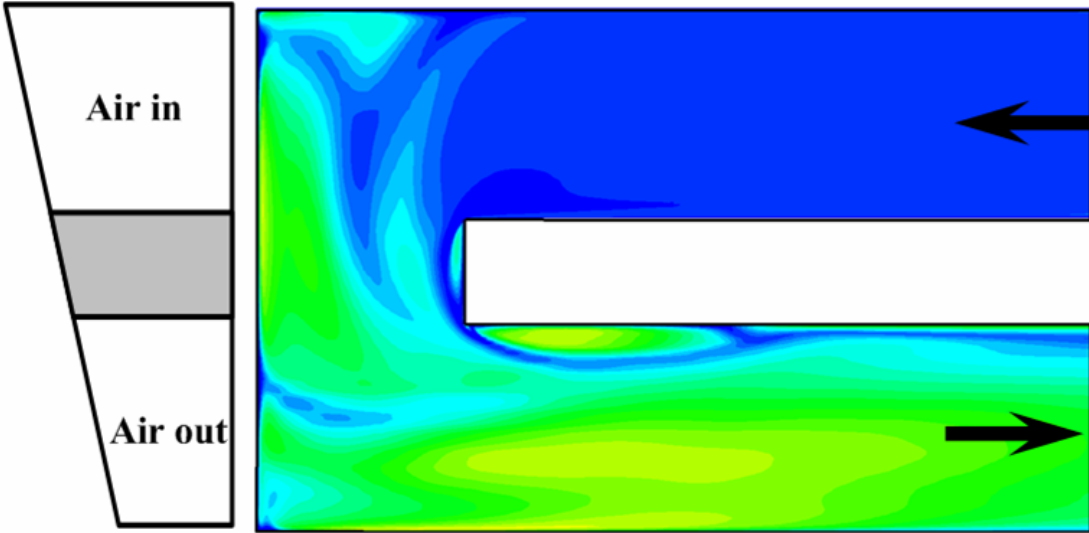
(b) Numerical Data by RSM

Fig. 5.10 Detailed Nusselt number ratio distributions of trapezoidal channel with

smooth walls for larger inlet case at Re = 31,800

In the first passage, as the flow approached the turn, the Nusselt number ratios gradually decreased. This continuous decrease is due to the developing thermal boundary layer. The Nusselt number ratio reached the peak value at the entrance of the second passage due to the flow impingement onto the bottom wall and then decreased as the flow moved to the exit of the second passage. This is due to the diminishing of secondary flow induced by the turn.

Trapezoidal Channel
Smooth Walls : Re = 31,800
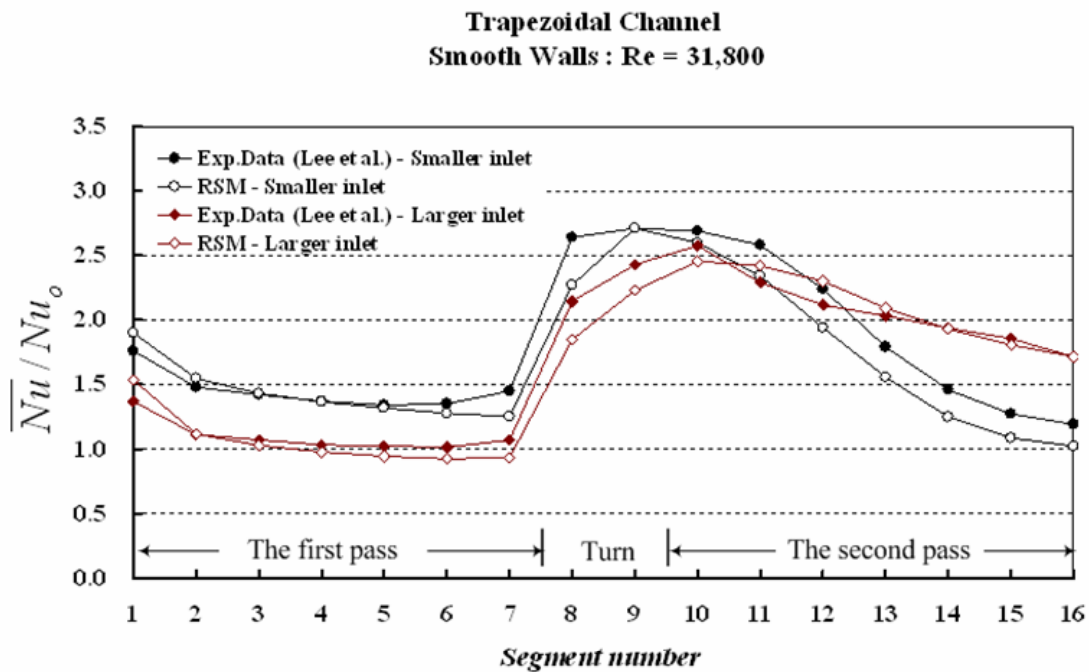
Fig. 5.11 Regional average measured and calculated Nusselt number ratio for trapezoidal channel with smooth walls at Re = 31,800

The Nusselt number ratios before the turn were higher for smaller inlet case than for larger inlet case because of the higher velocity of the flow in the inlet section with the

smaller flow cross sectional area. However, after the turn, the heat transfer enhancements were higher in the larger inlet case than in the smaller inlet case.

The predicted Nusselt number ratios by the Reynolds stress model (RSM) were closed to the experimental data of Lee et al. [35]. It can show well flow field and heat transfer distribution. However, the Reynolds stress model (RSM) slightly underpredicted the steep increase of the heat transfer in the turn region and the Nusselt number ratios in after the turn in second passage. The maximum relative error was 14.7% and the average relative error was 8.2% for the smaller inlet case. The relative error is defined by normalizing the difference between the experimental and numerical values with respect to the experimental value. The maximum relative error was 13.9% and the average relative error was 6.2% for the larger inlet case.

CHAPTER VI

FLOW AND HEAT TRANSFER IN A TWO-PASS TRAPEZOIDAL

CHANNEL WITH 90° RIBS ON TWO OPPOSITE WALLS

In chapter VI, computations were performed for a two-pass trapezoidal channel with 90º ribs on the two opposite walls as tested by Lee et al. [35] using the Reynolds stress model (RSM) with enhanced wall treatment in FLUENT.

6.1 Description of Problem

The simulated geometry was the same as the experimental geometry by Lee et al. [35]. Fig. 6.1 & 6.2 show the geometry and the numerical grids for the two-pass trapezoidal channel with 90° ribs on two opposite walls. The top and bottom walls were roughened by thirty two equally-spaced 90° angled ribs. Therefore, the total of sixty four 90° angled ribs was attached on both the top and bottom walls in parallel sequence so that they were directly opposite each other. These ribs were 3.2 mm by 3.2 mm and rib-to-rib spacing (P) was 3.81 cm. Thus, the rib height-to-hydraulic diameter ratio (e/ $D_{h,turn}$) was 0.07, and the rib pitch-to-rib height ratio (P/e) was 12. The actual rib height-to-hydraulic diameter ratio (e/ $D_{h,small}$) in the smaller cross section was 0.078 and the
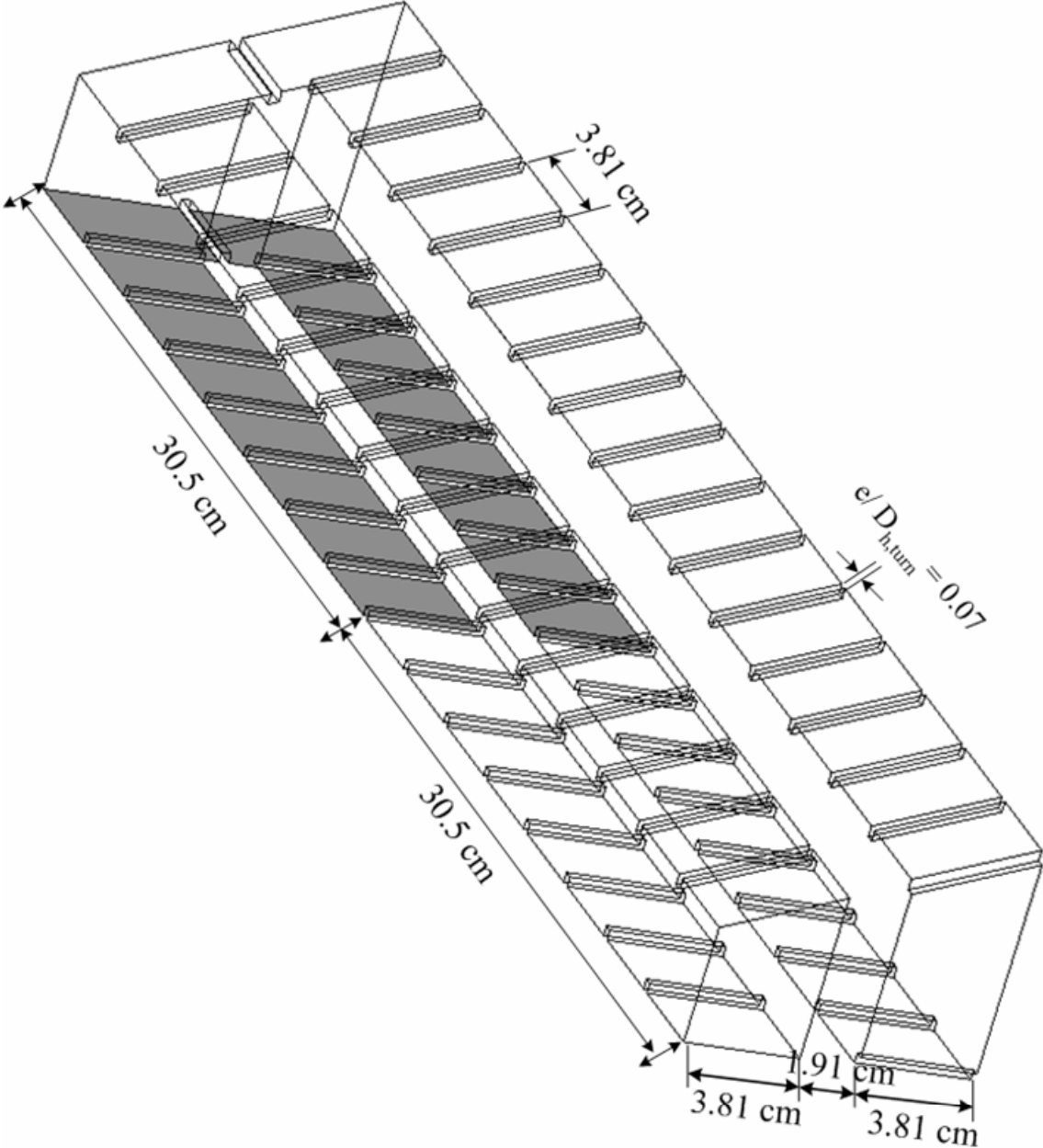
Fig. 6.1 Geometry for trapezoidal channel with 90º ribs
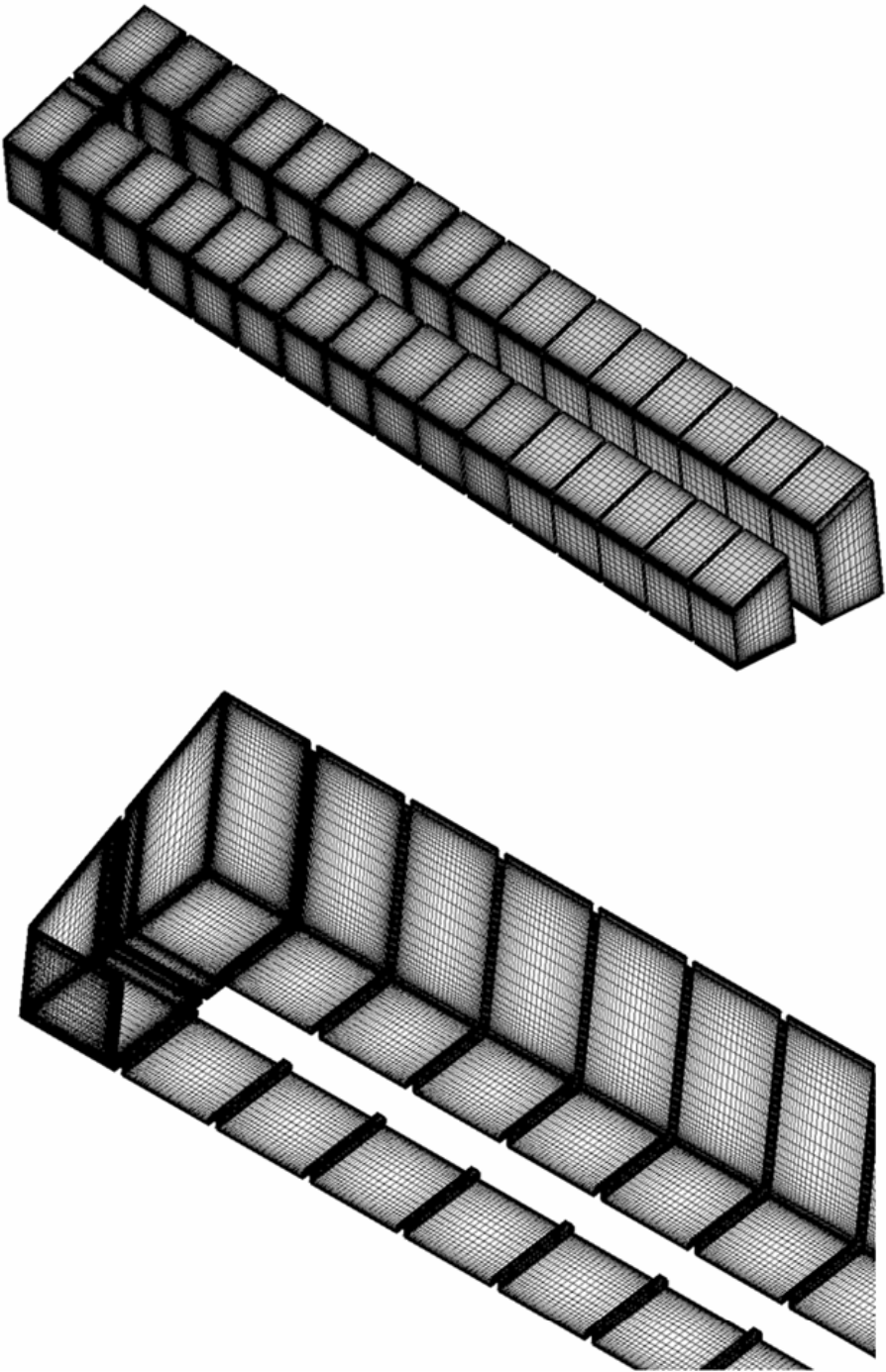
Fig. 6.2 Numerical grid for trapezoidal channel with 90º ribs

actual rib height-to-hydraulic diameter ratio (e/ $D_{h,large}$) in the larger cross section was 0.066. The Reynolds numbers were fixed at 31,800.

6.2 Grid Independence Study

Fig. 6.2 gives the numerical grid generated using Gambit for this simulation. The grid independent study was made by performing the simulations for three different cross sectional grids of $34 \times 64 \times 650$, $44 \times 74 \times 650$ and $54 \times 84 \times 650$, and one streamwise $44 \times 74 \times 750$ grid with mesh refined in the near wall regions (Fig. 6.2). For the smaller inlet case (Fig. 6.3(a)), a comparison between $34 \times 64 \times 650$ and $44 \times 74 \times 650$ grid points showed 7.8% maximum changes in the Nusselt number ratio. The maximum difference in Nusselt number ratio was less than 1.9% between $44 \times 74 \times 650$ and $54 \times 84 \times 650$ grid points. For the larger inlet case (Fig. 6.3(b)), a comparison between $34 \times 64 \times 650$ and $44 \times 74 \times 650$ grid points showed 5.9% maximum changes in the Nusselt number ratio. The maximum difference in Nusselt number ratio was less than 1.8% between $44 \times 74 \times 650$ and $54 \times 84 \times 650$ grid points. Further increase of the number of grid points in streamwise direction of the channel produced only minor changes of the Nusselt number ratios for the both cases. Therefore, it was determined that grid independence was achieved with $44 \times 74 \times 650$ grid points and all results were based on the $44 \times 74 \times 650$ grid points, which resulted in 2,116,400 grid points for both the smaller inlet and larger inlet cases. The y^{+} values were less than unity in all test runs of grid independent study.

(a) Trapezoidal Channel, Inlet at Smaller Section, 90° ribs : Re = 31,800
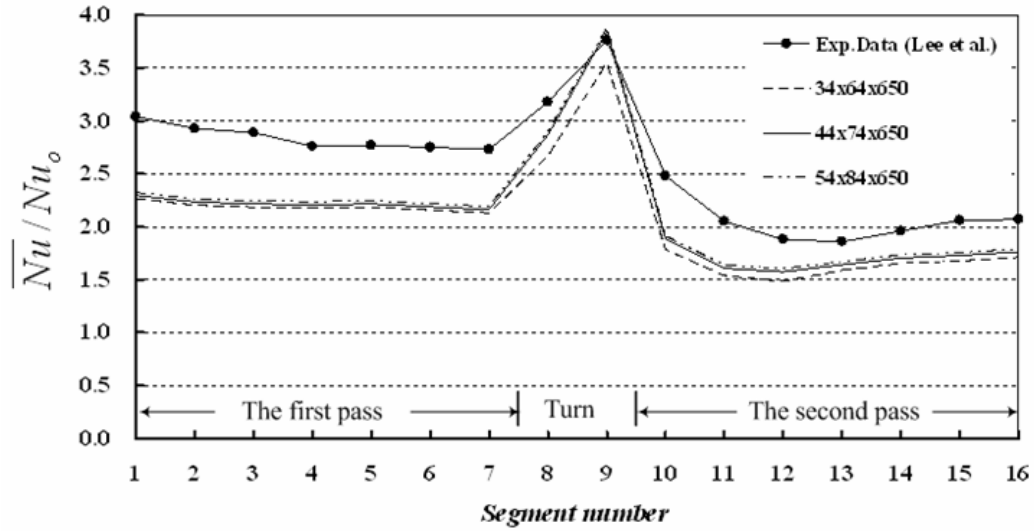
(b) Trapezoidal Channel, Inlet at Larger Section, 90° ribs : Re = 31,800
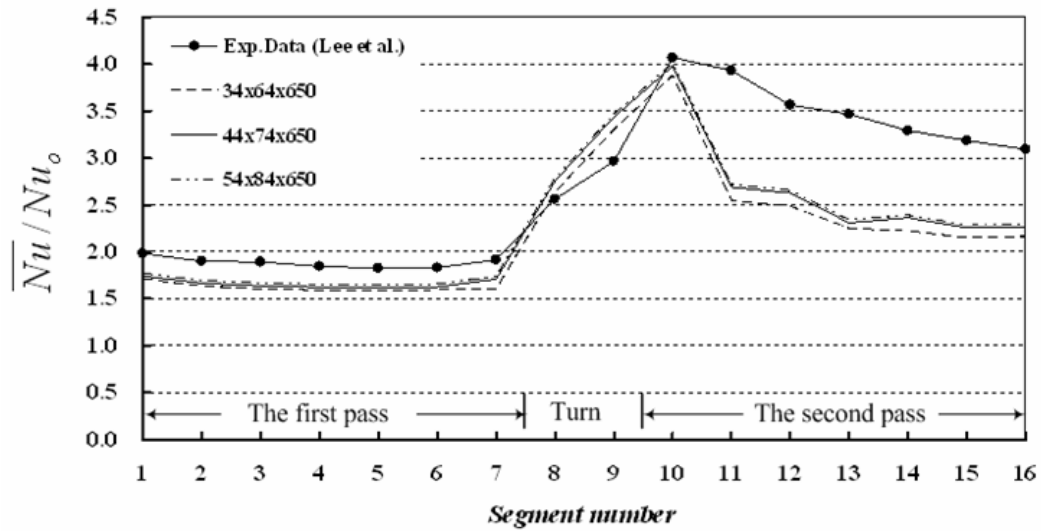
Fig. 6.3 Grid independent study for trapezoidal channel with 90° ribs

6.3 Velocity Fields

Fig. 6.4 shows the velocity vector distributions at the mid-plane between the top and bottom walls with 90° ribs at Re = 31,800 for inlet at smaller cross section and for inlet at larger cross section. For inlet at smaller cross section (Fig. 6.4(a)), the velocity profiles were flat before the turn. As the flow approached the turn region, flow accelerations occurred near the divider wall and a flow deceleration occurred near the outer wall due to the favorable and adverse pressure gradients along the divider and outer wall, respectively. Flow deceleration took place at the outer wall and was followed by flow separation, which results in a zone of recirculating flow in the upstream corner in the first passage. Unlike the smooth channel case, flow separation did not occur in the turn at the tip of divider wall due to the presence of ribs on both the top and bottom walls. Downstream of the turn exit the large separation also did not exist due to the fact that the centrifugal effect was reduced resulted from the deceleration flow through the turn and the presence of the ribs in the second passage. For the inlet at larger cross section (Fig. 6.4(b)), flow patterns were similar. The flow was accelerated through though the turn. Unlike the inlet at smaller case two separation zones were observed in the both of the outer corners in the turn. Fig. 6.5 & 6.6 show streamwise velocity and turbulence intensity in the planes midway between the inner (divider) and outer walls with 90° ribs at Re = 31,800 for inlet at smaller cross section and for inlet at larger cross section in the first passage. The reversal flow occurred immediately downstream and upstream of the ribs.
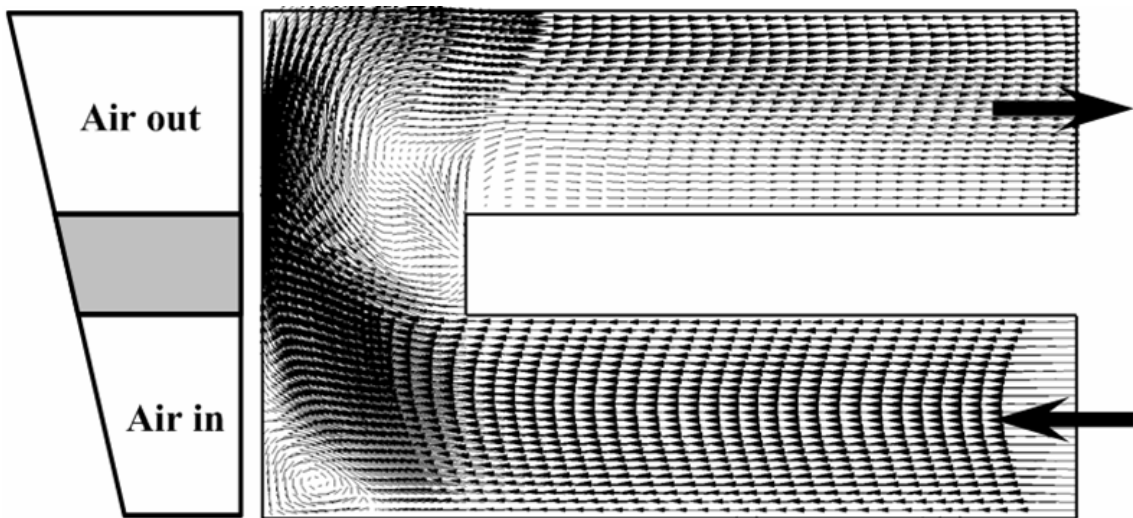
(a) Streamwise velocity vector for inlet at smaller section
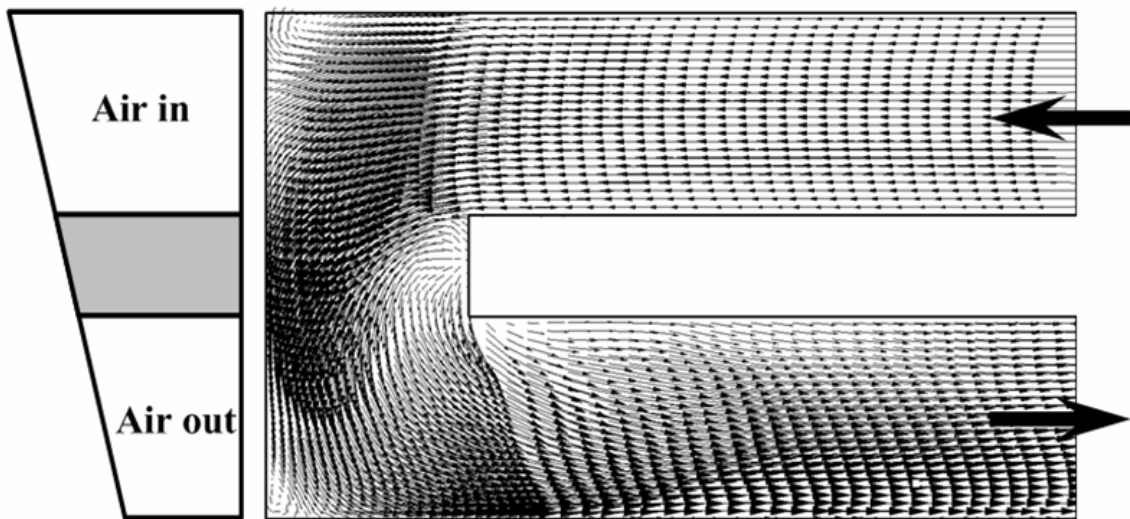
(b) Streamwise velocity vector for inlet at larger section

Fig. 6.4 Streamwise velocity vector midway between the top and bottom walls

with 90° ribs at Re = 31,800

As the flow near the top and bottom wall passes over the ribs, the flow separates from the walls. This separation results in relatively low heat transfer, due to a relatively hot cell being trapped in the recirculation. However, when the flow reattaches to the wall between the ribs, this is an area of relatively high heat transfer. This pattern of separation and recirculation continues through the channel with a pattern of repeating ribs. In fact, the existence of the rib reduces the cross sectional area of the channel, which leads to higher pressure region before the rib and the main flow is accelerated when it passes rib midsection. The ribs also increase turbulent mixing. The relatively hot flow near the wall is continuously mixing with the relatively cooler core flow near the center of the channel. This mixing also serves to increase the heat transfer from the channel. As the overall characteristics of the Reynolds stress in the ribbed channel, the ribs strongly intensify the turbulence level on both the top and bottom walls. The turbulence intensities were as high as 25% immediately downstream of the ribs on the top and the bottom wall, and diminished gradually toward the center of the channel (Fig. 6.5(b)). High level of turbulence intensity (32%) was observed near the end wall due to flow impingements. Fig 6.6(b) shows the streamwise velocity and turbulence intensity at the first passage in the planes midway between the inner and outer wall for inlet at larger cross section. Since the velocity magnitude and rib height-to-hydraulic diameter ratio (e/ $D_{h,large}$) were smaller than those of the smaller inlet case, the effects of the ribs were less. The turbulence intensities were as high as 21% immediately downstream of the ribs on the top and the bottom wall, and near the end wall, turbulence intensity was 25%. The flow is seen to impinge on the end wall and one large strong secondary flow is created near

the bottom wall. However, near the top wall a secondary flow can not be formed since the flow merges on the corner of the top wall and there is not enough room to form the vortex. In general, when the flow impinges on the end wall double vortex is formed due to symmetry of the wall in square or rectangular channel.

Fig. 6.7 & 6.8 show streamwise velocity and turbulence intensity in the planes midway between the inner (divider) and outer walls with 90° ribs at Re = 31,800 for inlet at smaller cross section and for inlet at larger cross section in the second passage. For the inlet at smaller cross section, after the turn, there were no flow reattachments between ribs 10 and 11 due to a large flow separation on the rib 9 (Fig. 6.7(a)). The main flow was shifted toward the top wall and then a strong flow impingement occurred on the top wall. The flow reattachments were observed after rib 12 when the turn effects were decreased. Near the bottom wall, turbulence intensity also was low about 8% - 10%. However, near the top wall high levels of turbulence intensity (24% - 32%) were observed due to strong flow impingements (Fig. 6.7(b)). For the inlet at larger cross section, after the turn, the strong flow impingement occurred on the bottom walls unlike the smaller inlet case. As the flow goes through the turn, the flow is accelerated by decreasing the cross section area. Therefore, a larger momentum of the flow from the larger inlet makes the strong flow impingements on the walls and increases turbulence intensities in the second passage of the channel. In the second passage, the levels of turbulence intensity were about 43% - 54% near the bottom walls and 36% - 43% near the bottom walls.
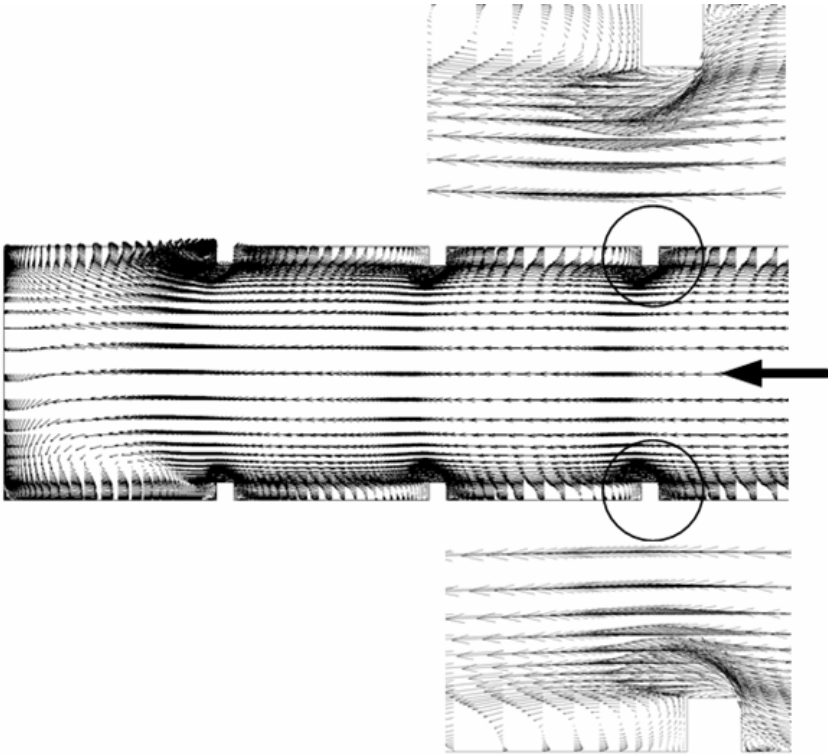
(a) Streamwise velocity
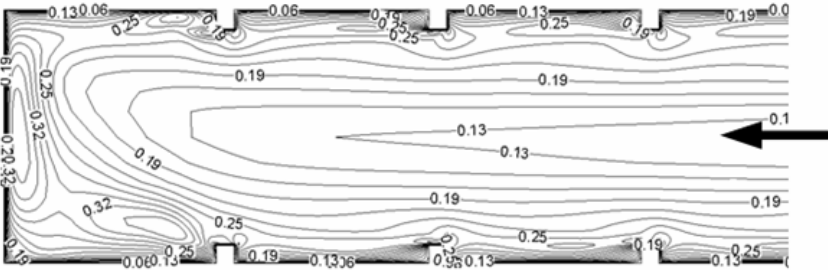
(b) Turbulence intensity

Fig. 6.5 Streamwise velocity and turbulence intensity midway between the inner and
outer walls with 90° ribs in the first passage for inlet at smaller cross section
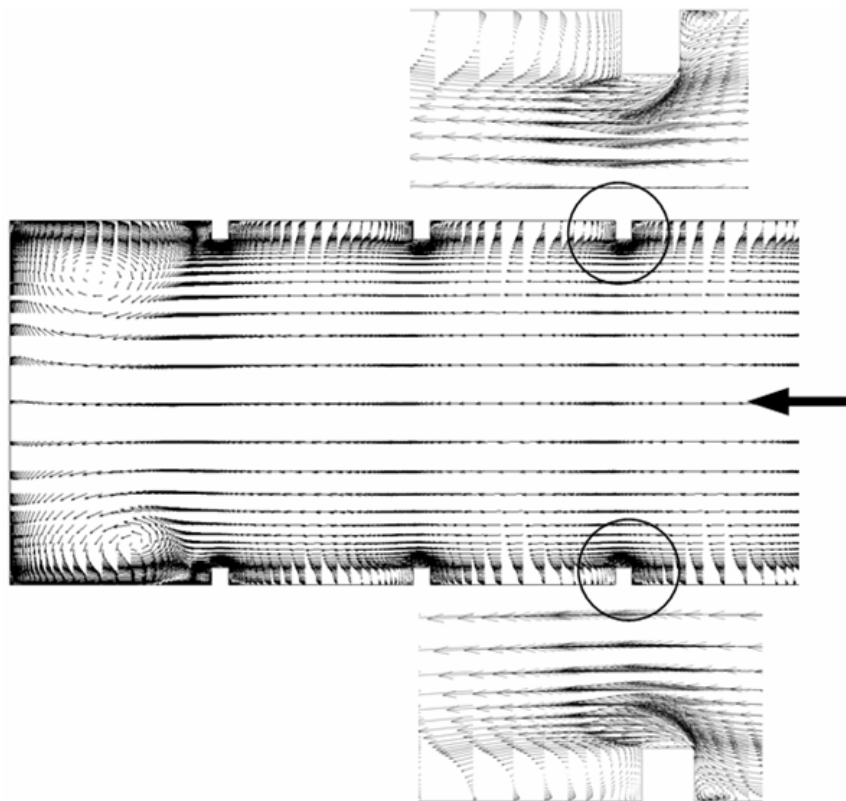
(a) Streamwise velocity
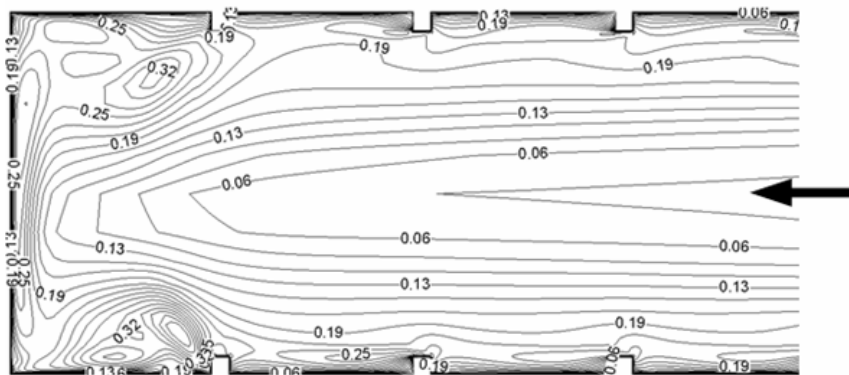
(b) Turbulence intensity

Fig. 6.6 Streamwise velocity and turbulence intensity midway between the inner and

outer walls with 90° ribs in the first passage for inlet at larger cross section
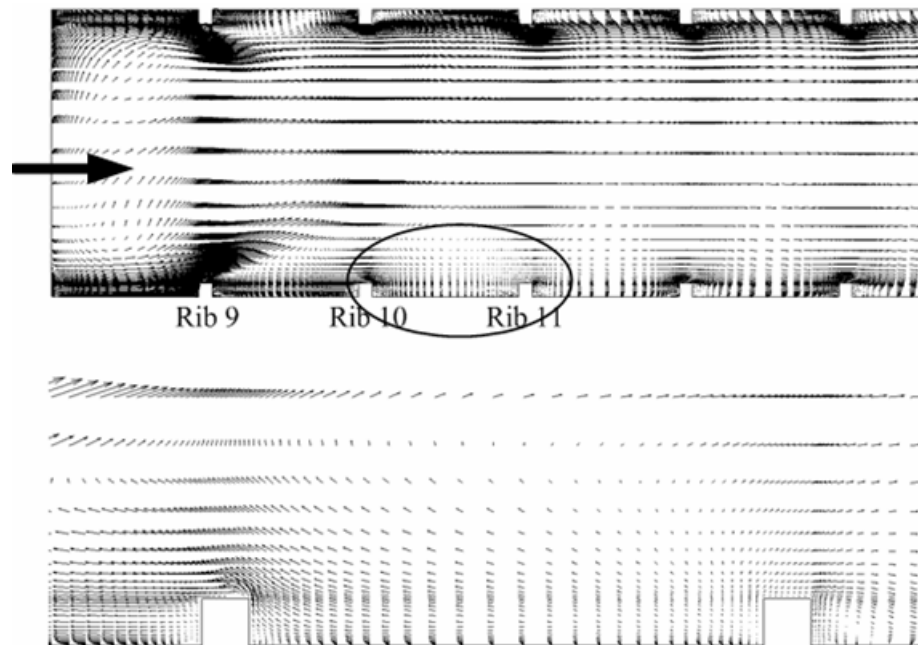
(a) Streamwise velocity
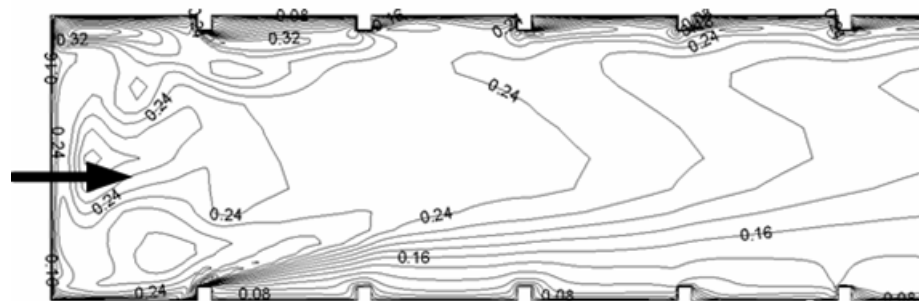
(b) Turbulence intensity

Fig. 6.7 Streamwise velocity and turbulence intensity midway between the inner and outer walls with 90° ribs in the second passage for inlet at smaller cross section
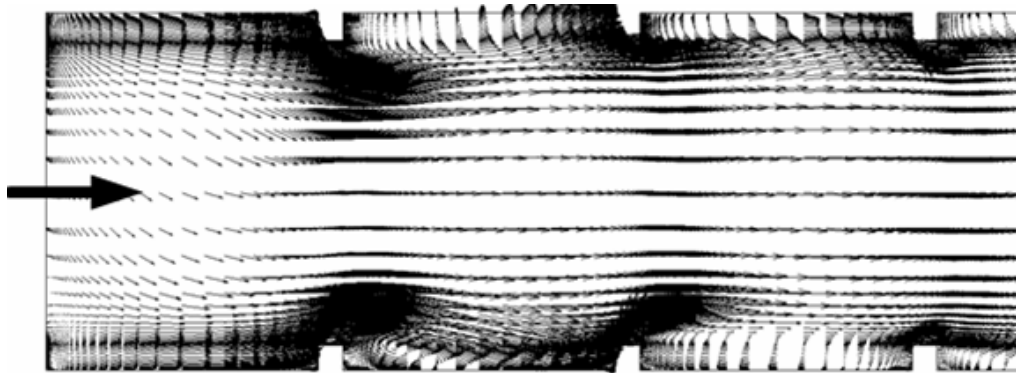
(a) Streamwise velocity
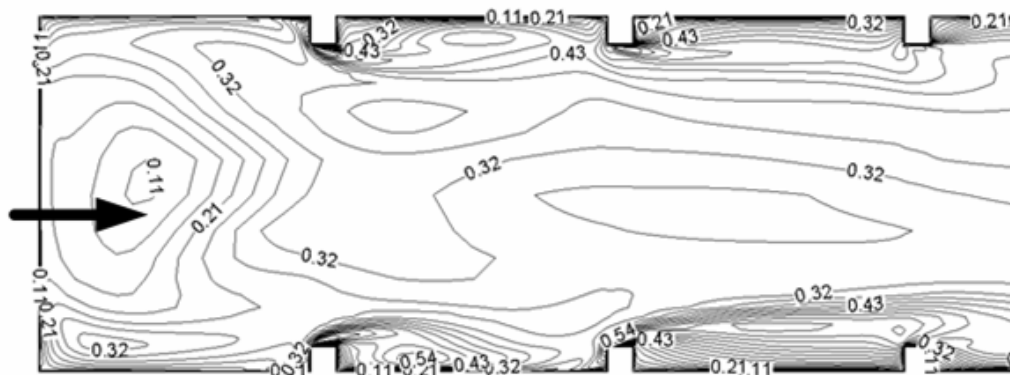
(b) Turbulence intensity

Fig. 6.8 Streamwise velocity and turbulence intensity midway between the inner and
outer walls with 90° ribs in the second passage for inlet at larger cross section

6.4 Secondary Flow Development

Fig. 6.9 & 10 show the secondary flow developments at selected streamwise locations. In the first passage, small secondary corner vortices were generated as a result of the Reynolds stress anisotropy. The magnitude of these vortices, which was very small, cannot be seen clearly. As shown in Fig. 6.9(a), 90° parallel ribbed channel produced periodically up and down flow movement in the first passage and simultaneously generated the small vortices near the corners on the top and bottom walls. These small vortices were generated by the anisotropic of the turbulent Reynolds stress. At the rib location (a), the vertical velocity component leaving from the rib was clearly seen. Near the inner and outer walls, the existence of the rib induced the flow going from the rib-roughened wall to the center of the channel. In the plane between the ribs (b), the flows directing to the top and bottom walls were seen. These flows composed the reattachment of the separated flow occurring around the midpoint between ribs. The flow then changed its direction to the inner and outer walls, although the flow directing to opposite direction was also seen in the region very close to rib-roughened wall. Higher heat transfer enhancements are expected near the inner and outer wall due to more flow impingements. The flow pattern in the location (c) was completely different with location (a) and (b) due to the turn effect. The flows were faster and directed slightly to the inner wall, and the upward vertical velocity component was strong near the inner wall. In the 90° turn (d), a strong vortex was generated near the top of the rib on the bottom wall, and smaller and slightly distorted one occurred the near the top of rib
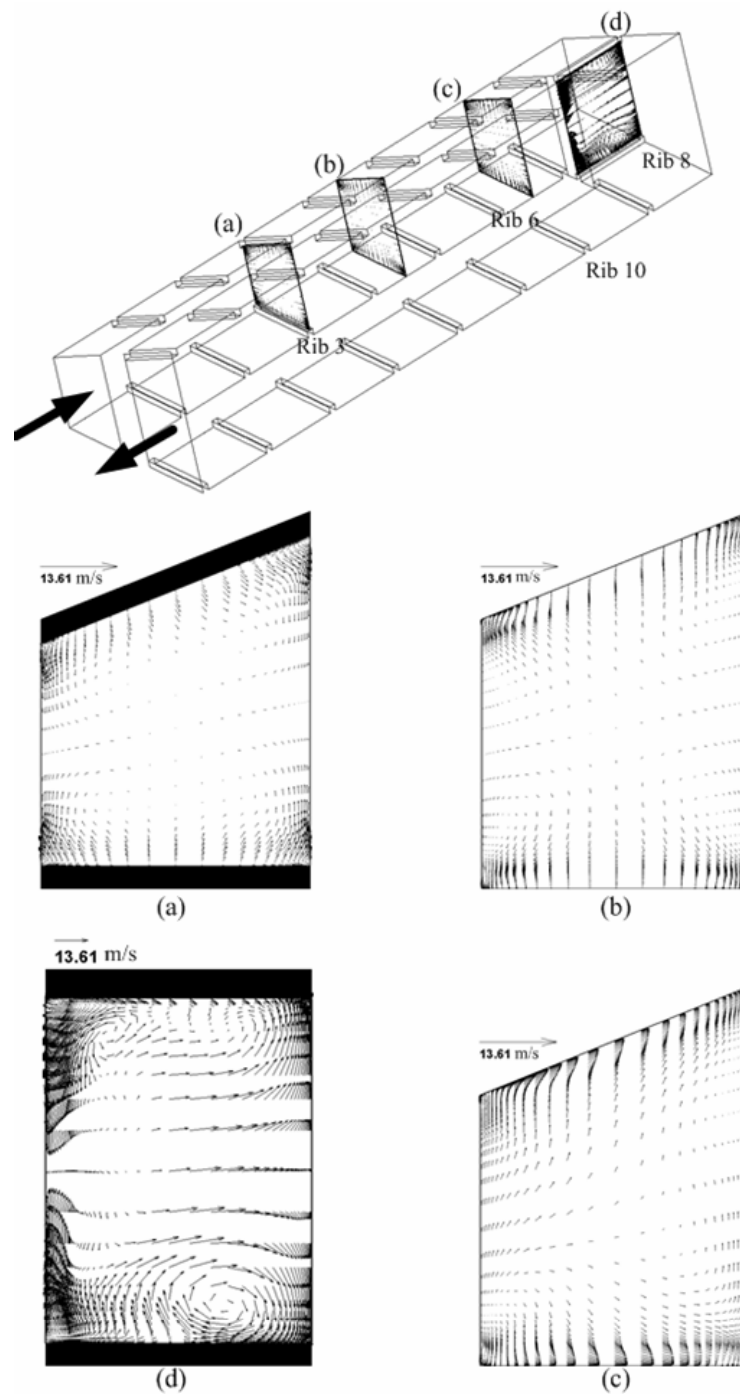
Fig. 6.9(a) Secondary flow developments with 90° ribs in the first passage for inlet at smaller cross section
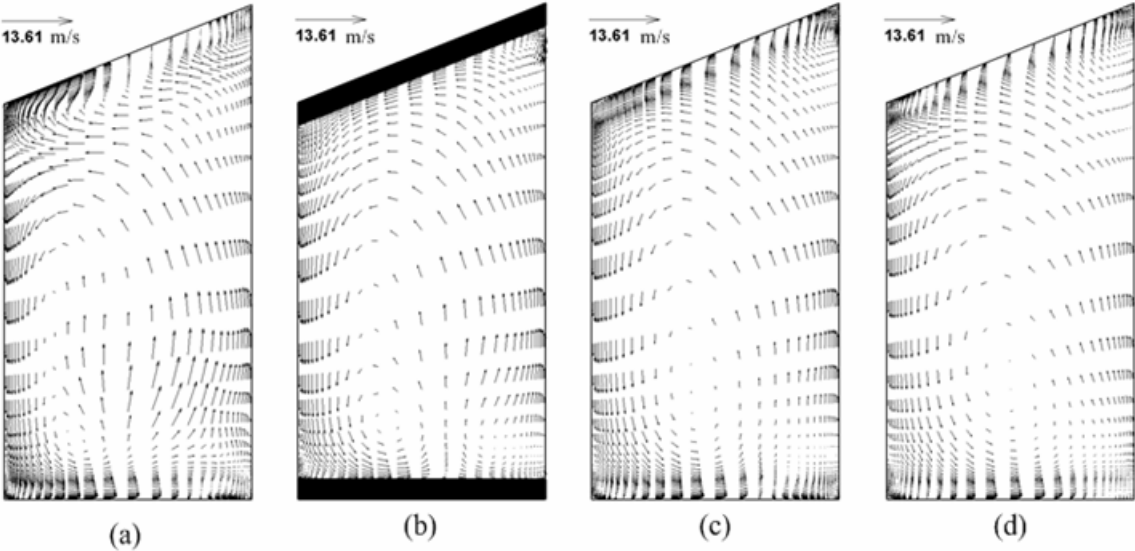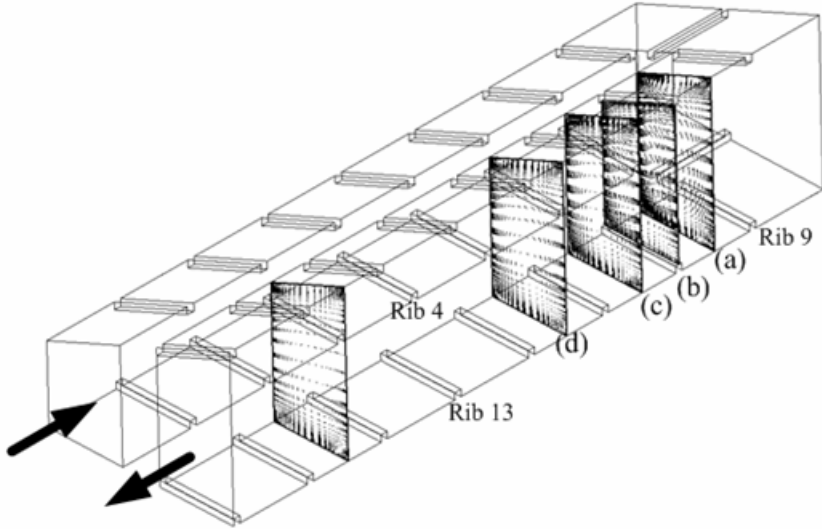
Fig. 6.9(b) Secondary flow developments with 90° ribs in the second passage for inlet at

smaller cross section
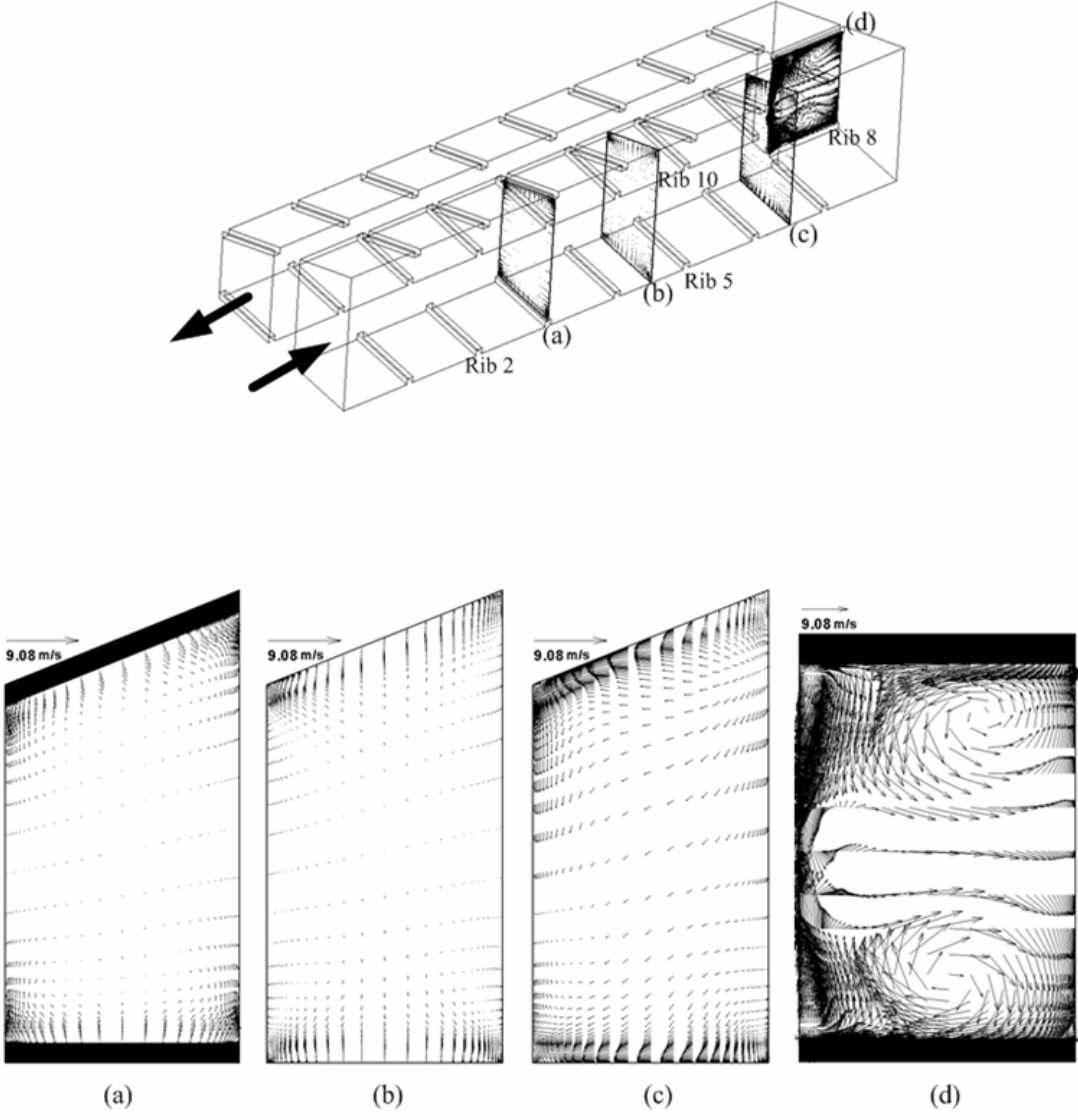
Fig. 6.10(a) Secondary flow developments with 90° ribs in the first passage for inlet at

larger cross section
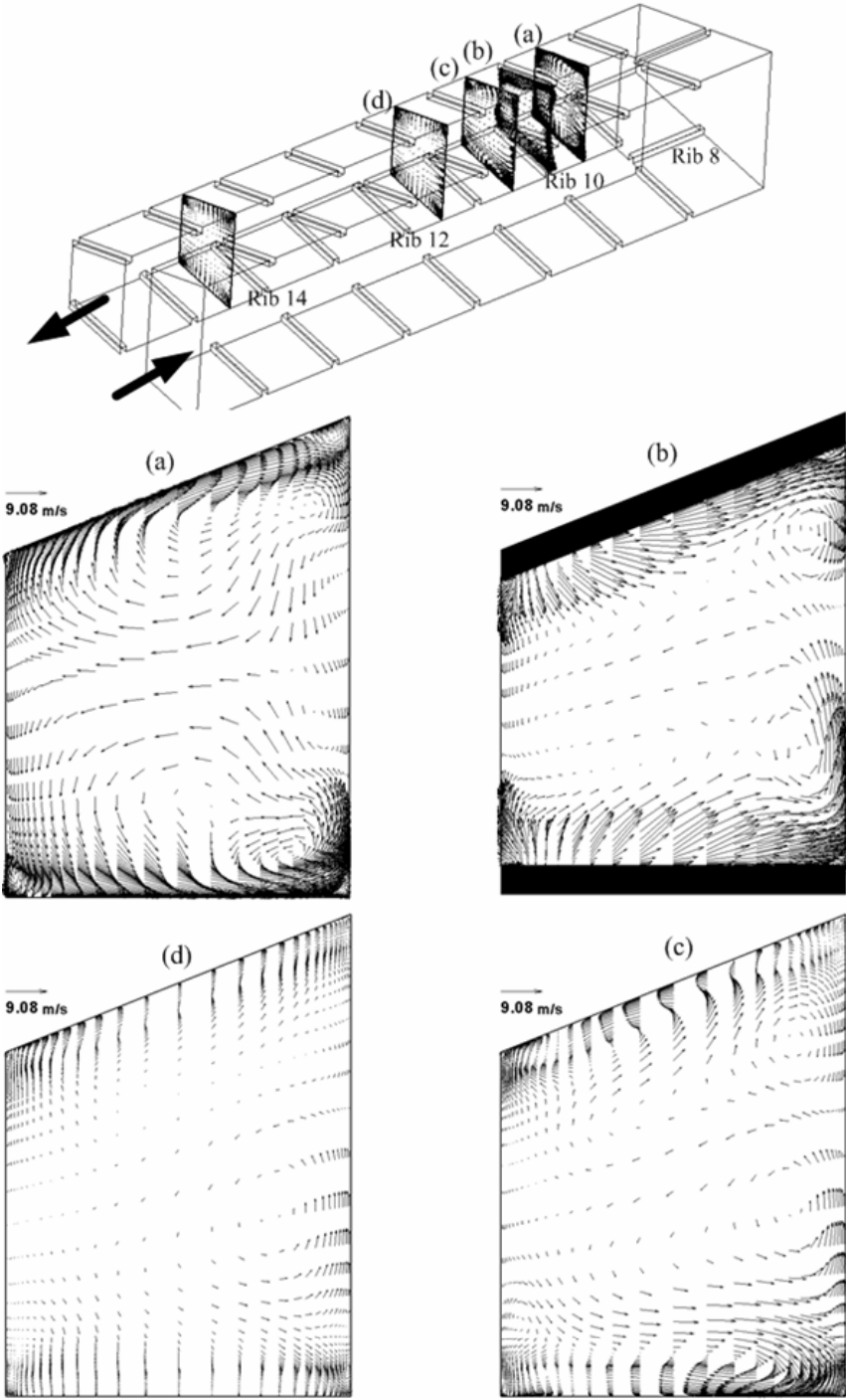
Fig. 6.10(b) Secondary flow developments with 90° ribs in the second passage for inlet

at larger cross section

on the top wall due to the combined effect of centrifugal induced vortex in the turn and rib induced vortex in the upstream. However, these vortices maintained their counter rotating directions. The strong flow impingements were observed near the end wall, and high heat transfer enhancements were expected at this location. The secondary flow pattern in the second passage was more complicated due to the combined effect of the turn and ribs (Fig. 6.9(b)). In locations (a), (b) and (c), one large counterclockwise rotating vortex occupied almost entire cross area and smaller clockwise rotating vortex was seen near outer and bottom wall. The velocity magnitudes were not high compared to those in the first passage because the flow was decelerated through the turn. In the second passage, the bulk mean velocity was decreased from 13.61 m/s to 9.08 m/s. The rib height-to-hydraulic diameter ratio (e/ $D_{h,large}$) was also decreased since the same ribs were installed but channel height was increased. Therefore, the effect of the ribs on the flow of channel was mush less and the secondary flow induced by the turn was dominant in the second passage. The flow impingements mostly occurred near the inner and outer wall. In the location (d), the small vortex was diminished and one large counterclockwise rotating vortex occupied entire cross area. The most flow impingements were located near the inner wall.

Fig. 6.10 shows the secondary flow developments at selected streamwise locations for the inlet at larger cross section. In the first passage, the flow patterns were similar with smaller inlet case (Fig. 6.10(a)) and location (a), (b) and (c)). In the 90° turn (d), the strong vortex pair appeared due to the centrifugal force action. These vortices were not distorted unlike smaller inlet case. The upper vortex was a little bit bigger than

down vortex since as cross section area was decreased with upper area, upper flow velocity was slightly faster than down flow. The secondary flow in the second passage was much strong due to the acceleration of the flow. In the second passage at location (a), two large counter-rotating vortices were generated and four small corner vortices were observed (Fig. 6.10(b)). The velocity magnitudes were very high. Due to the ribs, the counter-rotating vortices were severely distorted in their sizes, strengths and locations (location (b) and (c)). In the location (d), two large counter-rotating vortices were almost diminished and only weak vortex occupied half cross section near the inner wall. Unlike smaller inlet case, the turning effect was short and the effects of the ribs were dominant after secondary flow disappeared.

6.5 Heat Transfer Distribution

Fig. 6.11 and 6.12 show the detailed Nusselt number ratio distributions on the bottom wall with 90° ribs at Re = 31,800. Comparisons were made between the calculations and the experimental data of Lee et al (2007). The entrance and exit regions were cut off to focus on the turn effect. The 90° ribs gave substantially higher heat transfer compared with smooth wall case. Significant effects of the 90° ribs were evident in the first passage. Heat transfer distributions between ribs appeared periodic because the ribs periodically interrupted the boundary layers on the bottom wall. Therefore, the Nusselt number ratios were larger than 1.0 everywhere along the straight sections of the channel. The streamwise Nusselt number ratio variations between consecutive ribs in the

first passage were larger than the spanwise variations. In the 90° rib, the spanwise variations of the Nusselt number ratios are generally small since the 90° ribs can not produce secondary flows like the angled ribs do. The heat transfer enhancement was high in the middle region between two ribs due to the flow reattachments and thinner boundary layer and very low immediately before and after the ribs due to the flow recirculation. In the turn region, heat transfer enhancements were very high due to the combination of the sharp 180° turn and the 90° rib. Near the end wall heat transfer was high due to flow impingements and immediately downstream of the 90° rib the highest heat transfer was observed due to the combination of strong flow reattachments and flow impingements on the end wall. Unlike smooth wall case, near outer wall in the turn region heat transfer enhancement was mush less because the presence of the 90° rib and the flow deceleration reduced the effect of centrifugal forces on the secondary flow, and caused lesser impingement on the outer wall. In the second passage the periodic heat transfer patterns were not seen due to the turning effect. Downstream of the turn, heat transfer enhancements were higher near the inner and outer walls, and were lower in the middle of the bottom due to secondary flow induced by the turn. Every Nusselt number ratio was lower than one in the first passage because bulk mean velocity was relatively lower.

For the larger inlet case, the highest heat transfer enhancement was observed near outer wall after the turn unlike at the turn for smaller inlet case. Through the cross section that was decreased, the flow was accelerated and the main flow velocity radially
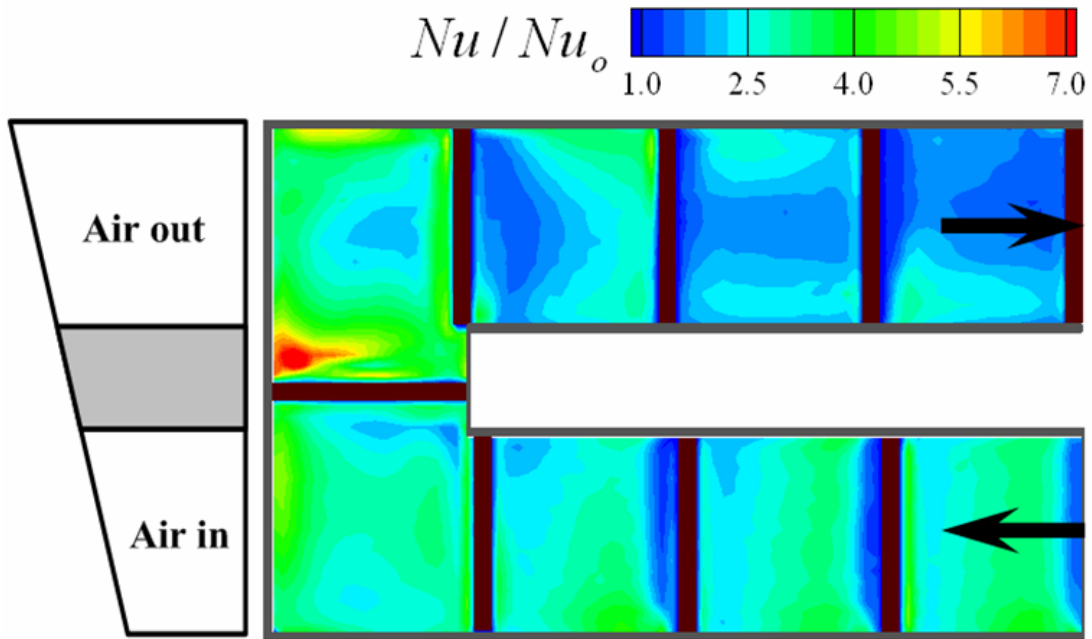
(a) Experimental Data by Lee et al (2007)
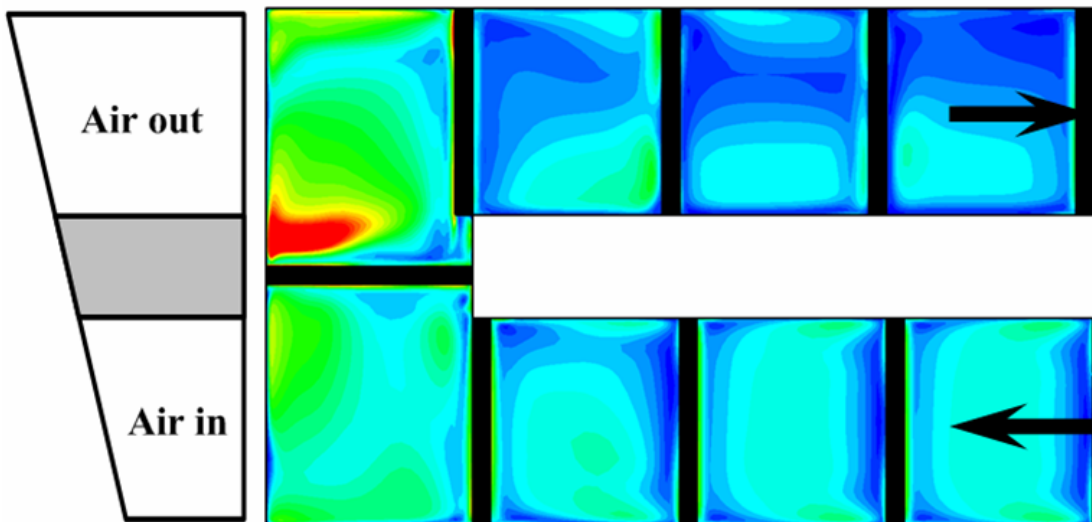
(b) Numerical Data by RSM

Fig. 6.11 Detailed Nusselt number ratio distributions of trapezoidal channel with 90° ribs for smaller inlet case at Re = 31,800
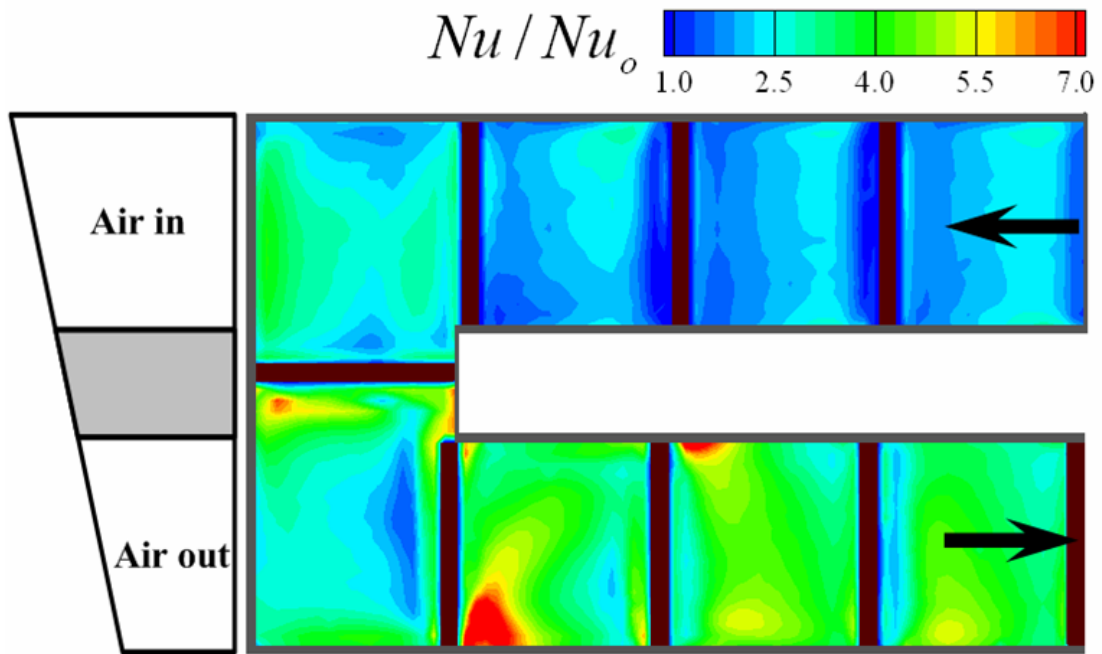
(a) Experimental Data by Lee et al (2007)
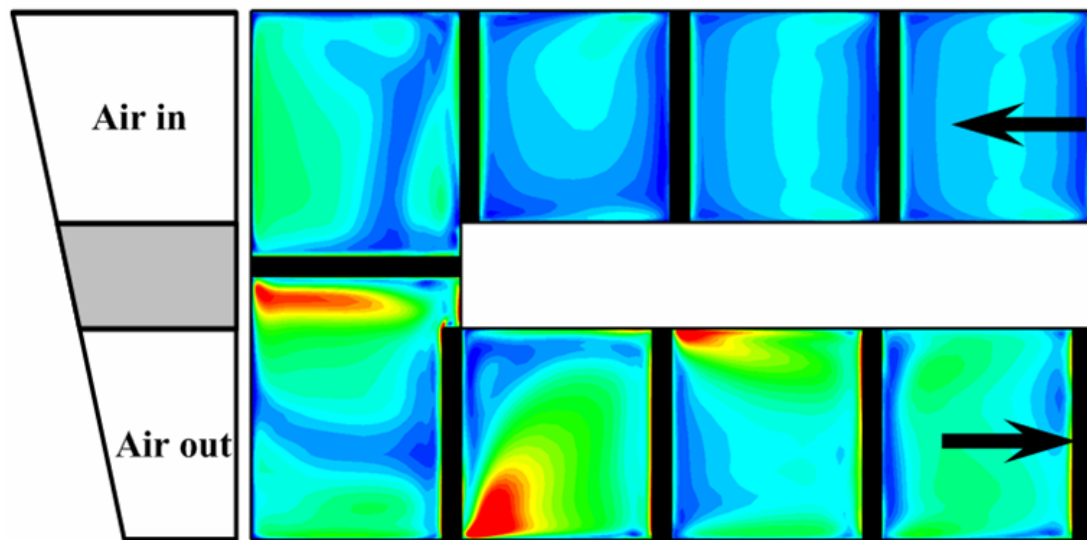
(b) Numerical Data by RSM

Fig. 6.12 Detailed Nusselt number ratio distributions of trapezoidal channel with

90° ribs for larger inlet case at Re = 31,800

Trapezoidal Channel
90° ribs : Re = 31,800
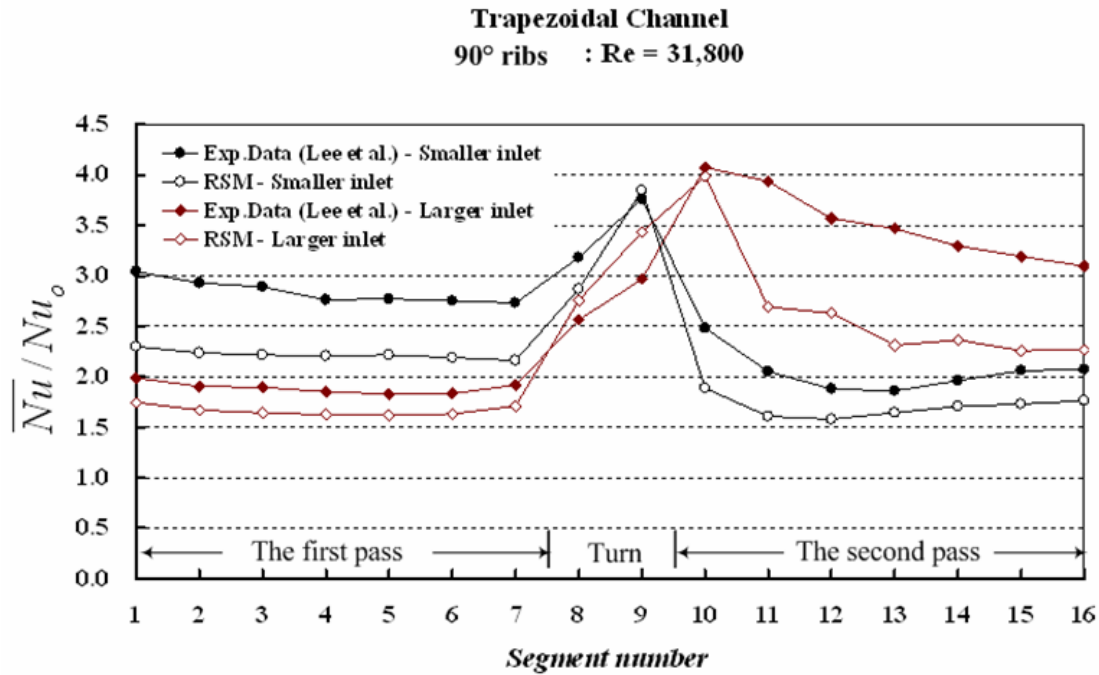
Fig. 6.13 Regional average measured and calculated Nusselt number ratio for trapezoidal channel with 90° ribs at Re = 31,800

increased. Therefore, most strong flow impingements occurred near the outer wall just after the turn region rather at the turn. Heat transfer enhancements were higher near the inner and outer walls, and were lower in the middle of the bottom due to secondary flow induced by the turn like smaller inlet case.

The regionally averaged Nusselt number ratios on the bottom wall with 90° ribs at Re = 31,800 are shown in Fig. 6.13. For the smaller inlet case, the Nusselt number ratio gradually decreased before the turn in the first passage. In the turn, Nusselt number ratio was highest. Downstream of the turn in the second passage Nusselt number ratio

abruptly decreased and then gradually increased. The values of Nusselt number ratio were even lower than those in the first passage due to relatively lower mean velocity. For the larger inlet case, as flow approached the turn with relatively lower values of Nusselt number ratio, Nusselt number ratio gradually decreased. Nusselt number ratio was highest just after the turn, and then gradually decreased in the second passage.

The predicted Nusselt number ratio distributions by the Reynolds stress model (RSM) were closed to the experimental data of Lee et al (2007). It can show well flow field and heat transfer distribution. However, when the comparison between the numerical prediction and measured regional average were considered, the prediction can not agree well with the experimental data. The maximum relative error was 24.5% and the average relative error was 17.7% for the smaller inlet case. The relative error is defined by normalizing the difference between the experimental and numerical values with respect to the experimental value. The maximum relative error was 33.3% and the average relative error was 17.8% for the larger inlet case.

CHAPTER VII

FLOW AND HEAT TRANSFER IN A TWO-PASS TRAPEZOIDAL CHANNEL

WITH (+) 60° RIBS ON TWO OPPOSITE WALLS

In chapter VII, an experimental study was performed to measure the regionally averaged heat (mass) transfer in a two-pass trapezoidal channel with (+) 60° ribs on two opposite walls by Naphthalene sublimation technique and an numerical study also was performed using the Reynolds stress model (RSM) with enhanced wall treatment in FLUENT.

7.1 Description of Problem

Fig. 7.1 & 7.2 show the experimental test section and the numerical grids for the two-pass trapezoidal channel with (+) 60° ribs on two opposite walls. The simulated geometry was the same as the experimental geometry. The length of the duct was 61 cm. Only the bottom wall was coated with naphthalene, which is analogous to the one-side heating condition of heat transfer experiment. The length of each straight section with and without mass transfer active surfaces was 30.5 cm, while the width of each section was 3.81 cm and the divider wall thickness was 1.91 cm. The length from the divider wall tip to the end wall in the turn was 3.81 cm. For the numerical study, only bottom wall except the ribs was heated to a constant temperature since the mass transfer experiment can simulate uniform wall temperature boundary condition. The included

angle of trapezoidal cross section between the top wall and the bottom wall was 21.8°. The heights of the outer and inner vertical wall in small trapezoidal channel were 3.81 cm and 5.33 cm, and the height of the inner and outer vertical walls in large trapezoidal channel were 6.10 cm and 7.62 cm, respectively. The hydraulic diameters of the small trapezoidal cross section ($D_{h,small}$) is 4.09 cm and the hydraulic diameter of the large trapezoidal crosses section ($D_{h,large}$) is 4.83 cm. For the same air mass flow rate, the Reynolds number was based on the hydraulic diameter of the cross section at the turn clearance ($D_{h,turn}$ = 4.57 cm) because the channel height in the trapezoidal channel is varied in the turn region. The top and bottom walls were roughened by thirty equally-spaced (+) 60° angled ribs and one 90° rib in the turn region. Therefore, the total of sixty (+) 60° angled ribs and two 90° ribs was attached on the top and bottom walls in parallel sequence so that they were directly opposite each other. The ribs in the first passage are angled away from the divider wall and the ribs in the second passage are angled towards the divider wall. These ribs were 3.2 mm by 3.2 mm square stripes of balsa wood and rib-to-rib spacing (P) was 3.81 cm. Thus, the rib height-to-hydraulic diameter ratio (e/ $D_{h,turn}$) was 0.07, and the rib pitch-to-rib height ratio (P/e) was 12. The actual rib height-to-hydraulic diameter ratio (e/ $D_{h,small}$) in the smaller cross section was 0.078 and the actual rib height-to-hydraulic diameter ratio (e/ $D_{h,large}$) in the larger cross section was 0.066. The regional average mass transfer experiment was conducted with Re = 9,400, 16,800, 31,800 and 57,200 but the Reynolds number was fixed at 31,800 for the numerical study.
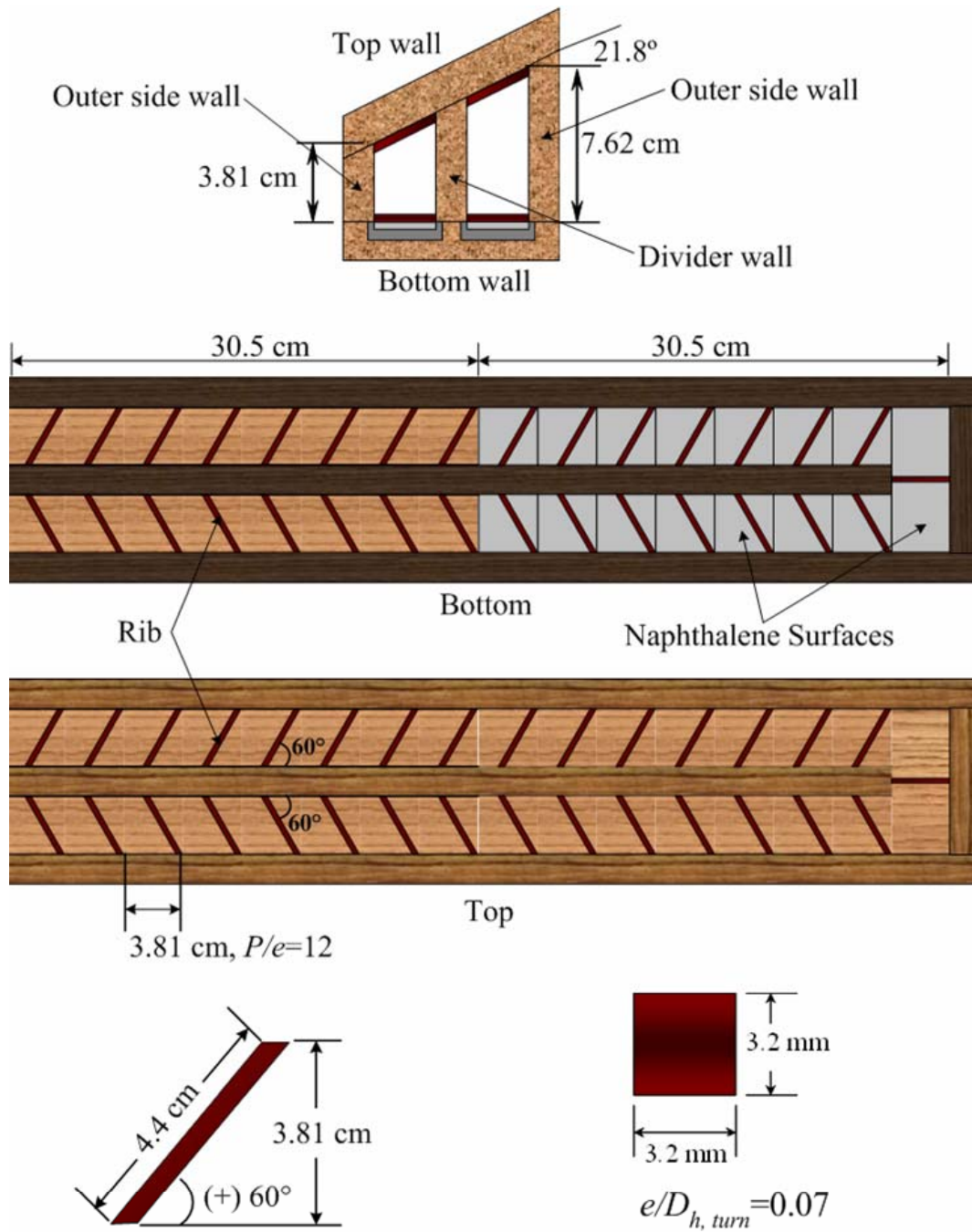
Fig. 7.1 Geometry for trapezoidal channel with (+) 60° ribs
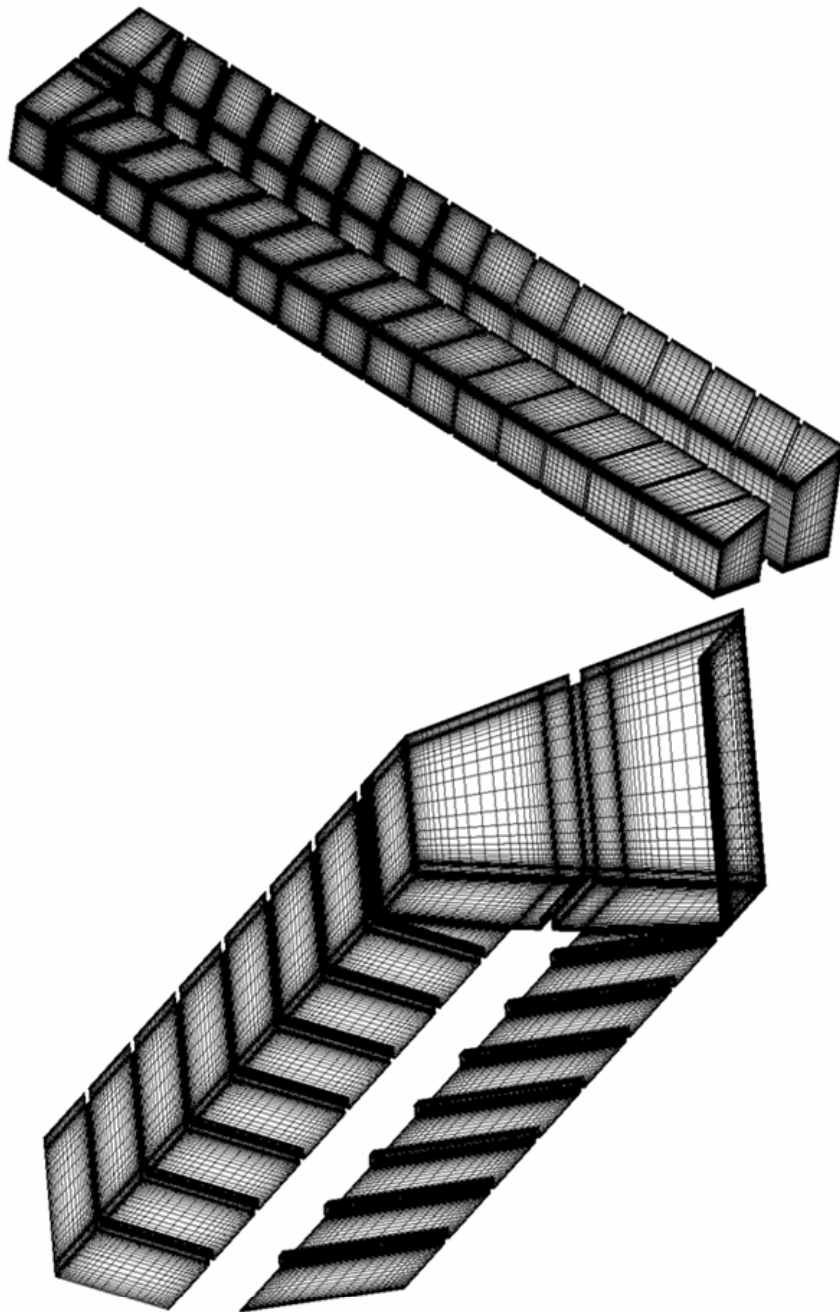
Fig. 7.2 Numerical grid for trapezoidal channel with (+) 60° ribs

Experiments were performed for the air entering the trapezoidal channel through the straight section with the smaller cross section as well as entering through the straight section with the larger cross section. Therefore, there were two inlet velocity conditions. The velocities in channel inlet in smaller cross section and in larger cross section were 13.61 m/s and 9.08 m/s, respectively.

7.2 Grid Independence Study

Fig. 7.2 gives the numerical grid generated using Gambit for this simulation. The grid independent study was made by performing the simulations for three different cross sectional grids of $32 \times 62 \times 640$, $42 \times 72 \times 640$ and $52 \times 82 \times 640$, and one streamwise $42 \times 72 \times 740$ grid with mesh refined in the near wall regions (Fig. 7.2). For the smaller inlet case (Fig. 7.3(a)), a comparison between $32 \times 62 \times 640$ and $42 \times 72 \times 640$ grid points showed 7.8% maximum changes in the Nusselt number ratio. The maximum difference in Nusselt number ratio was less than 1.9% between $42 \times 72 \times 640$ and $52 \times 82 \times 640$ grid points. For the larger inlet case (Fig. 7.3(b)), a comparison between $32 \times 62 \times 640$ and $42 \times 72 \times 640$ grid points showed 5.8% maximum changes in the Nusselt number ratio. The maximum difference in Nusselt number ratio was less than 1.7% between $42 \times 72 \times 640$ and $52 \times 82 \times 640$ grid points. Further increase of the number of grid points in streamwise direction of the channel produced only minor changes of the Nusselt number ratios for the both cases. Therefore, it was determined that grid independence was achieved with $42 \times 72 \times 640$ grid points and all results were
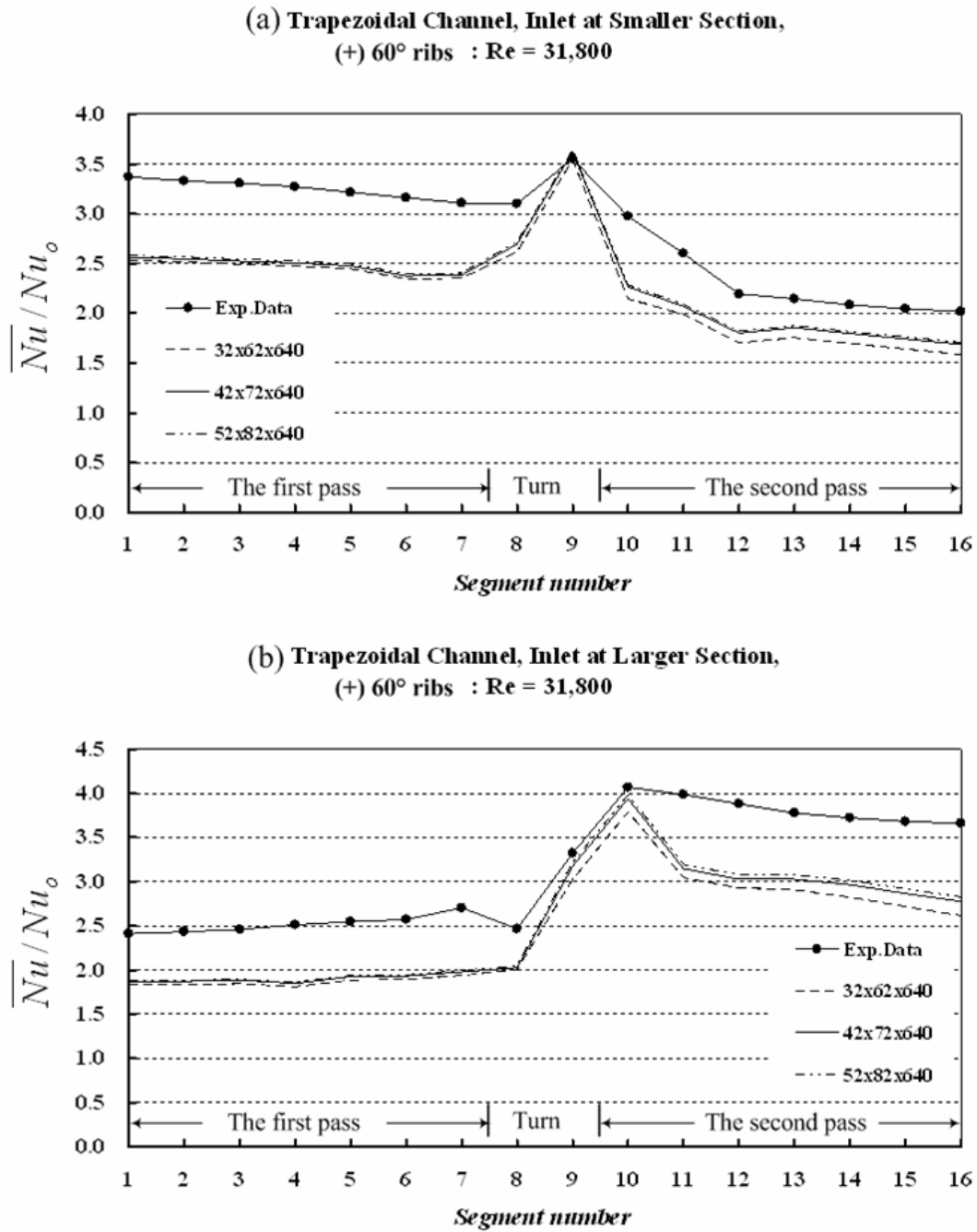
Fig. 7.3 Grid independent study for trapezoidal channel with (+) 60° ribs

based on the $42 \times 72 \times 640$ grid points, which resulted in 1,935,360 grid points for both the smaller inlet and larger inlet cases. The y^+ values were less than unity in all test runs of grid independent study.

7.3 Velocity Fields

Unlike 90° ribs, angled ribs induce the secondary flow. As the flow approaches the ribs, the angled ribs guide the near wall flow to move parallel to the rib from inner (divider) wall to the outer wall. The secondary flow follows the ribs until it hits on the outer wall. After hitting on the outer wall, the secondary flow induced by the rib returns back to the inner wall and a vortex is created. This behavior is similar on the top and bottom wall, therefore, two counter-rotating vortices form in the trapezoidal channel (Fig. 7.4). Fig. 7.5 shows the velocity vector distributions at the mid-plane between the top and bottom walls with (+) 60° ribs at Re = 31,800 for inlet at smaller cross section and for inlet at larger cross section. For the inlet at the smaller cross section (Fig. 7.5(a)), the velocity profiles were flat before the turn. As the flow approached the turn region, flow accelerations occurred near the divider wall and a flow deceleration occurred near the outer wall due to the favorable and adverse pressure gradients along the divider and outer wall, respectively. Flow deceleration took place at the outer wall and was followed by flow separation, which results in a zone of recirculating flow in the upstream corner in the first passage. There were no separation bubbles near the divider wall tip in the turn region. However, a large bifurcating zone existed near the divider wall in the second
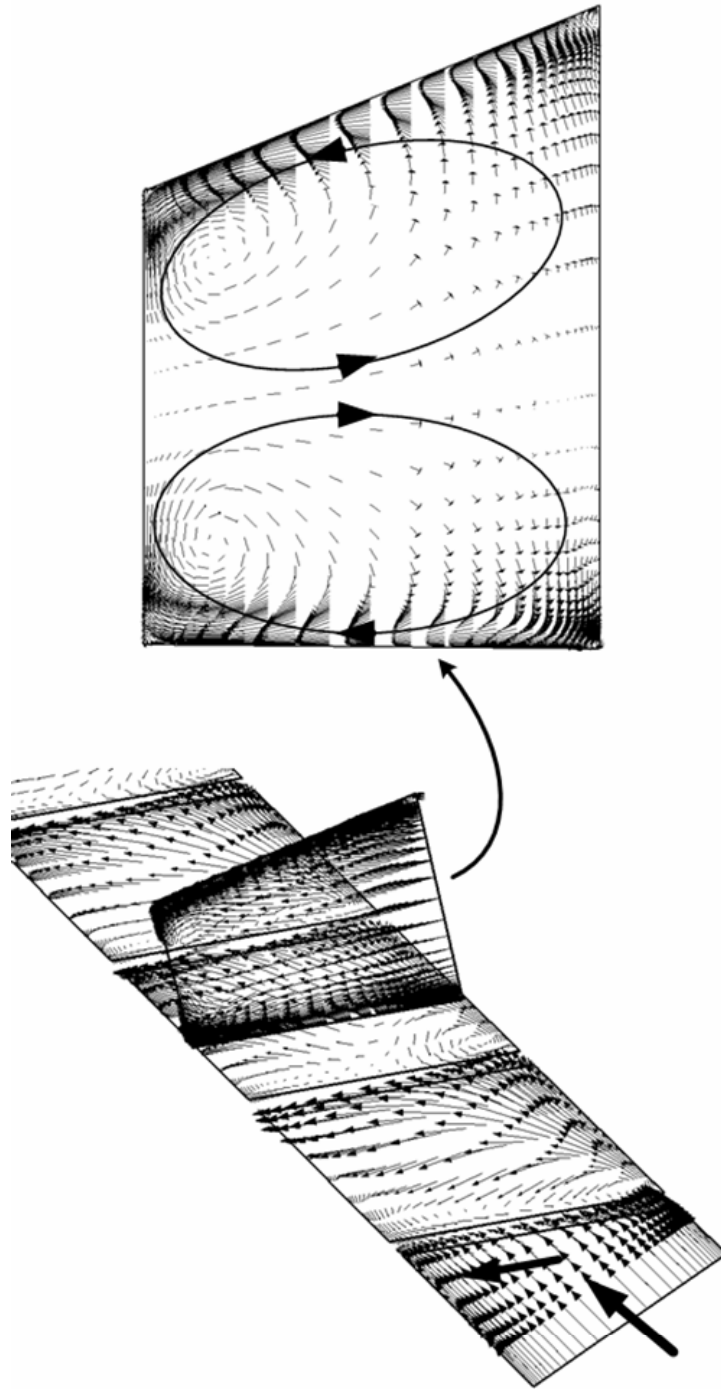
Fig. 7.4 Secondary flow vortices induced by (+) 60° rib
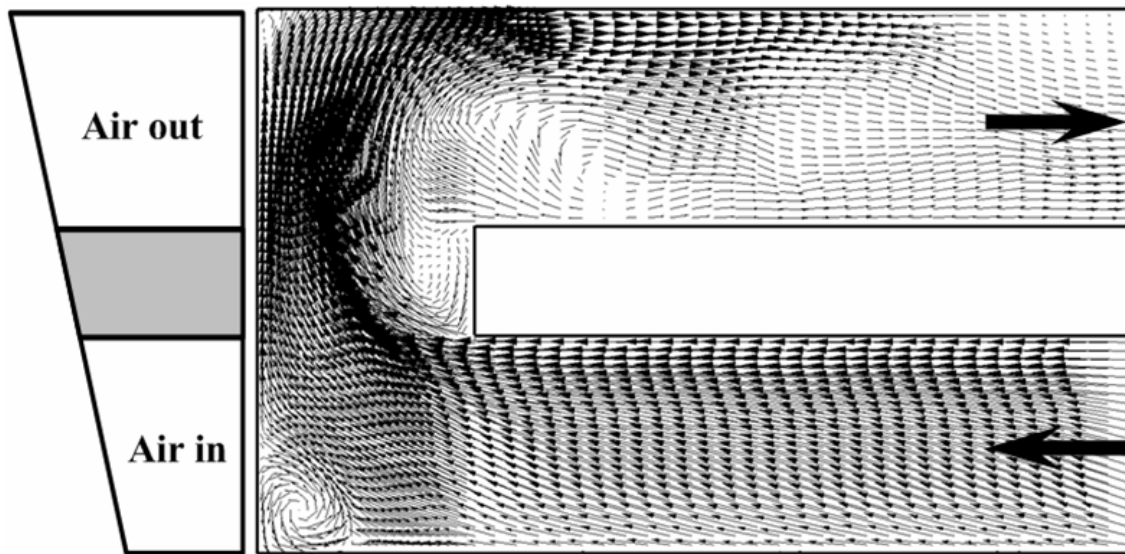
(a) Streamwise velocity vector for inlet at smaller section
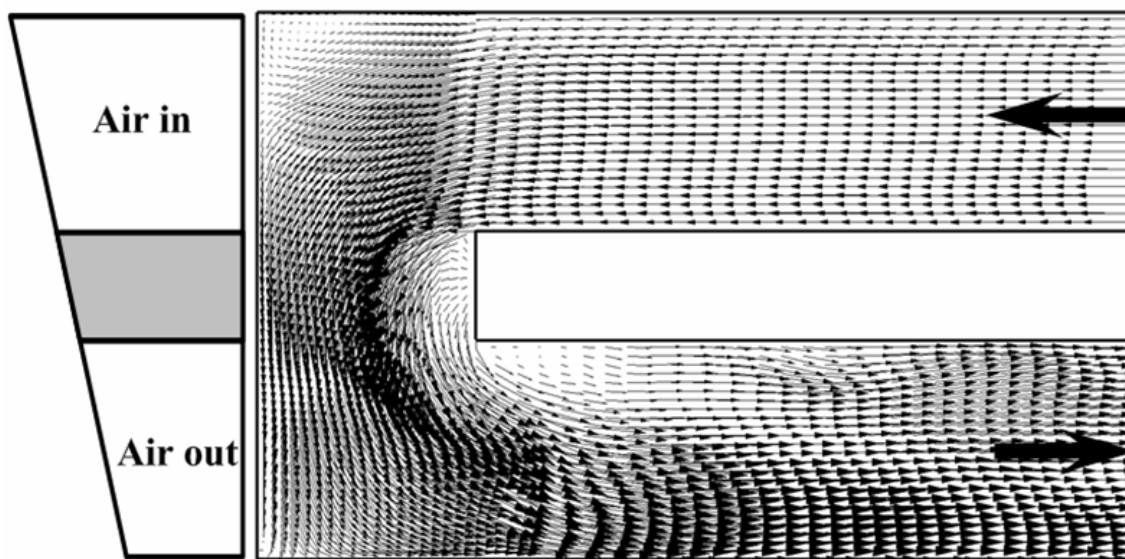
(b) Streamwise velocity vector for inlet at larger section

Fig. 7.5 Streamwise velocity vector midway between the top and bottom walls

with (+) 60° ribs

passage. For the inlet at the larger cross section (Fig. 7.5(b)), the flow had a similar pattern but bifurcating zone was smaller. Because the flow was accelerated by decreasing cross area through the turn, the streamwise velocity was much faster than the vertical velocity. In both case, there were weak flow impingements onto the end wall due to the secondary flow induced by angled ribs because the secondary flow pushed the flow in the core toward the divider wall. However, still high momentum flow after the turn impinged onto the outer wall in the second passage.

Figures 7.6, 7.7, 7.8 and 7.9 show streamwise velocity and turbulence intensity in the planes midway between the inner (divider) and outer walls with (+) 60° ribs at Re = 31,800 for inlet at smaller cross section and for inlet at larger cross section. As the flow near the top and bottom wall passes over the ribs, the flow separates from the walls. This separation results in relatively low heat transfer, due to a relatively hot cell being trapped in the recirculation. However, when the flow reattaches to the wall between the ribs, this is an area of relatively high heat transfer. This pattern of separation and recirculation continues through the channel with a pattern of repeating (+) 60° ribs. The reversal flow occurred immediately downstream of the ribs on both the top and bottom walls. However, immediately upstream of the ribs there were no separations, such as that generally found in a 90° ribbed channel case. In the (+) 60° ribs case, the flows near the inner and outer walls were different from each other due to the secondary flow induced by the angled ribs. For the smaller inlet case (Fig. 7.6(a)) near the inner wall the flows beyond ribs and directing to rib-roughened wall to reattach were intense and near the outer wall these flows become weaker in the first passage. In the turn, one large vortex

occurred near the bottom, and a small vortex was observed near the top wall. It was also observed that the flow over the ribs near the top wall was faster than the one near the bottom wall. The reason was that the rib induced secondary flow near the top wall was much stronger than the one near the bottom wall. Since the top and bottom walls are at an angle of 21.8° with respect to each other, the flows along the ribs moved fast down the slop due to the acceleration. Fig. 7.6(b) shows the turbulence intensity distributions in the first passage for the smaller inlet case. The turbulence intensities were as high as 34% immediately downstream of the ribs on the top wall and 29% immediately downstream of the ribs on the bottom wall, and diminished gradually toward the center of the channel around 12%. The highest turbulence intensity was 42% immediately downstream of the rib on the top wall just before the turn. Near the end wall the turbulence intensity was relatively low about 32% due to less flow impingement. Due to the same reason mentioned above, the higher turbulence intensity occurred near the top wall. Fig 7.7 shows the streamwise velocity and turbulence intensity in the second passage in the planes midway between the inner and outer wall for inlet at smaller cross section. Through the turn, the flow was decelerated due to increase of the cross section area. Since the velocity magnitude and rib height-to-hydraulic diameter ratio (e/ $D_{h,large}$) were smaller than those in the first passage, the effects of the angled ribs were much less. After the turn, there no flow reattachments between ribs due to a large flow separation on the rib just after the turn (Fig. 7.7(a)). The main flow was shifted toward the top wall and then a strong flow impingement occurred on the top wall. The highest turbulence intensity was 39% on the top wall in and just after the turn.

(a) Streamwise velocity

(b) Turbulence intensity
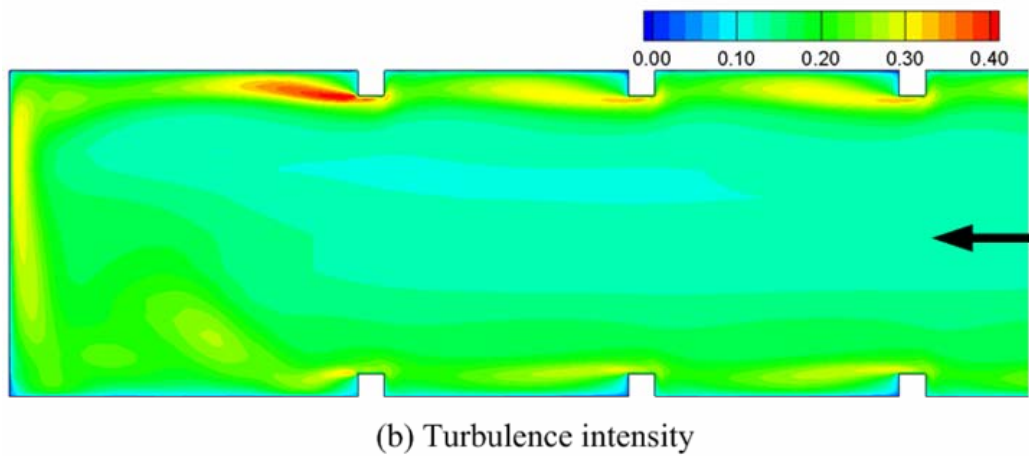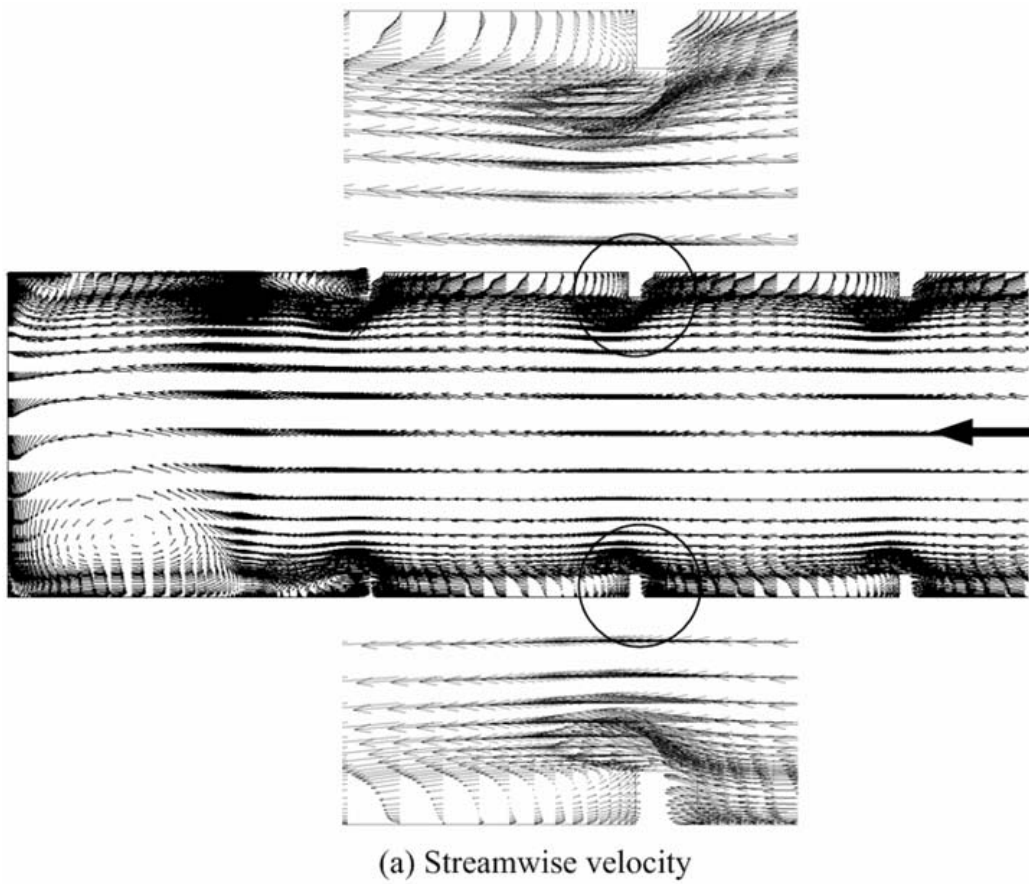
Fig. 7.6 Streamwise velocity and turbulence intensity midway between the inner and

outer walls with (+) 60° ribs in the first passage for inlet at smaller cross section
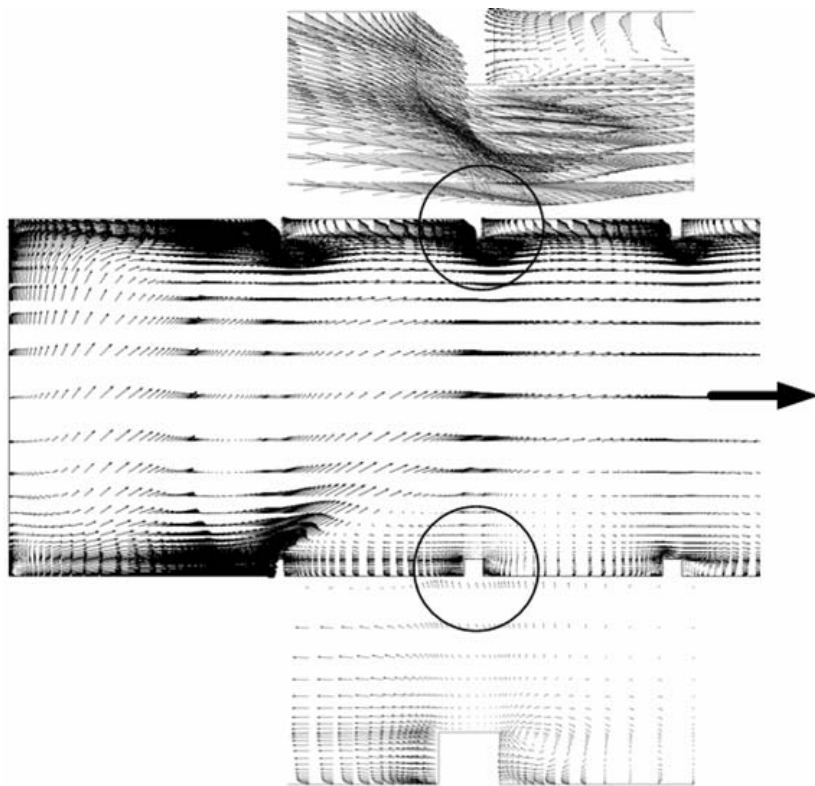
(a) Streamwise velocity
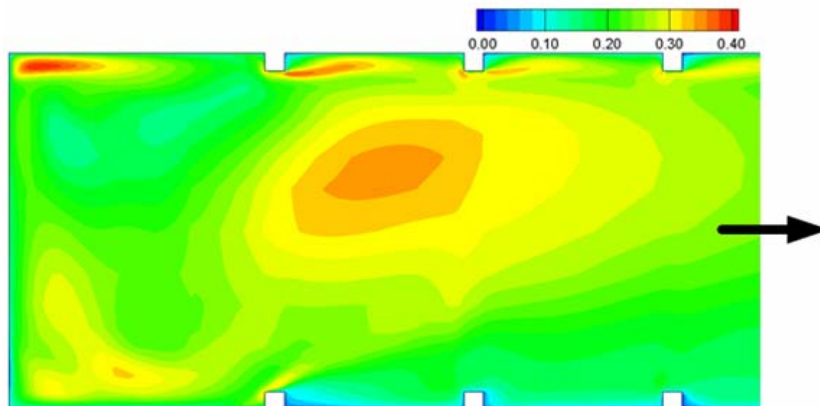
(b) Turbulence intensity

Fig. 7.7 Streamwise velocity and turbulence intensity midway between the inner and

outer walls with (+) 60° ribs in the second passage for inlet at smaller cross section

However, the turbulence intensity had low values in the second passage. The turbulence intensities were as high as 30% immediately downstream of the ribs on the top wall and 19% immediately downstream of the ribs on the bottom wall.

Figure 7.8 and 7.9 show streamwise velocity and turbulence intensity for the larger inlet case. Since the velocity magnitude and rib height-to-hydraulic diameter ratio (e/ $D_{h,large}$) were smaller than those of the smaller inlet case, the effects of the ribs were much less. In the turn, two small vortices occurred near the bottom and the top wall due to weak impingements (Fig. 7.8 (a)). Unlike the smaller inlet case, the flow over the ribs near the bottom wall was a little faster than the one near the top wall. The reason was that the rib induced secondary flow near the bottom wall was slightly stronger than the one near the top wall. The turbulence intensities were as high as 20% immediately downstream of the ribs on the bottom wall and 18% immediately downstream of the ribs on the top wall, and diminished gradually toward the center of the channel around 6% (Fig. 7.8(b)). In the second passage (Fig. 7.9), after the turn, the strong flow impingement occurred on the bottom walls unlike the smaller inlet case (Fig. 7.9 (a)). As the flow goes through the turn, the flow is accelerated by decreasing the cross section area. Therefore, a larger momentum of the flow from the larger inlet makes the strong flow impingements on the walls and increases turbulence intensities in the second passage of the channel. The level of turbulence intensity was about 40% near the bottom wall. Near the top wall 40% turbulence intensity only on the two ribs just after the turn was observed and farther downstream turbulence intensity level decreased to 20% (Fig. 7.9 (b)).
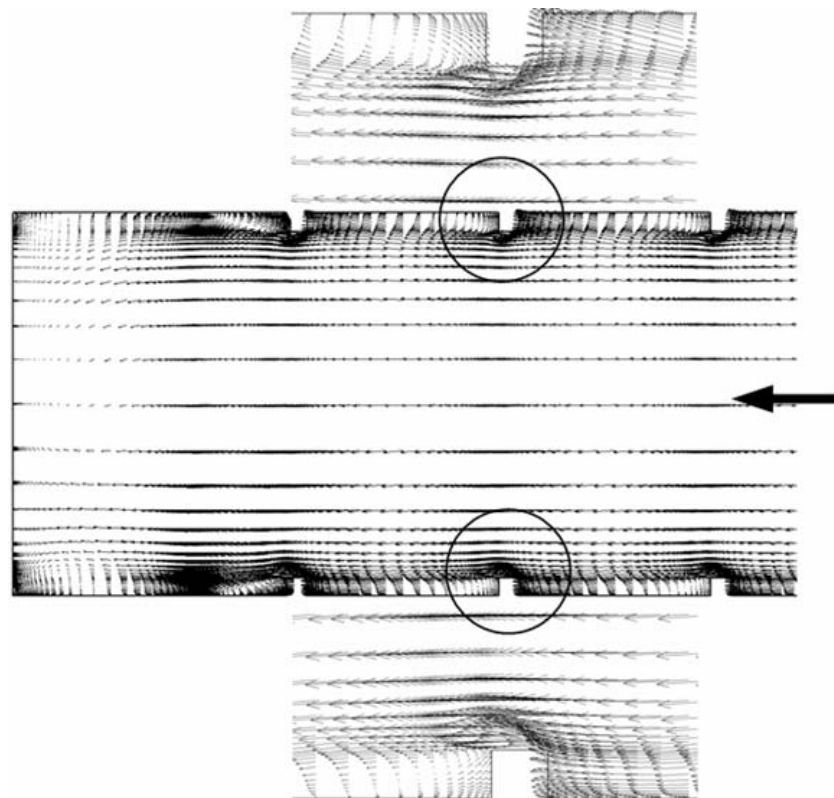
(a) Streamwise velocity
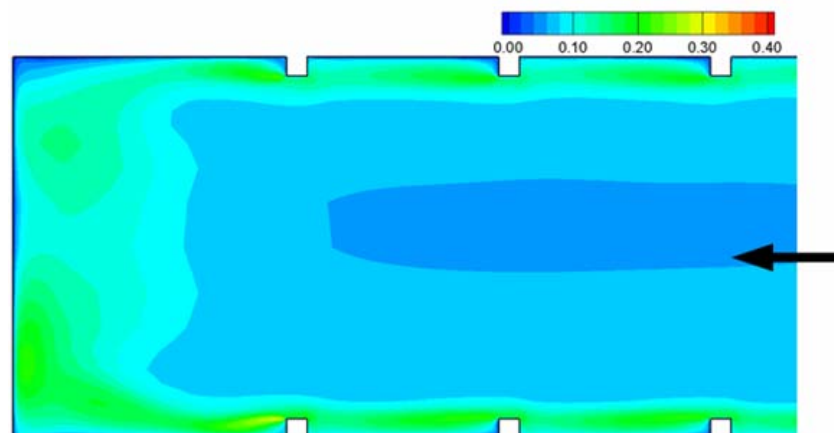
(b) Turbulence intensity

Fig. 7.8 Streamwise velocity and turbulence intensity midway between the inner and

outer walls with (+) 60° ribs in the first passage for inlet at larger cross section
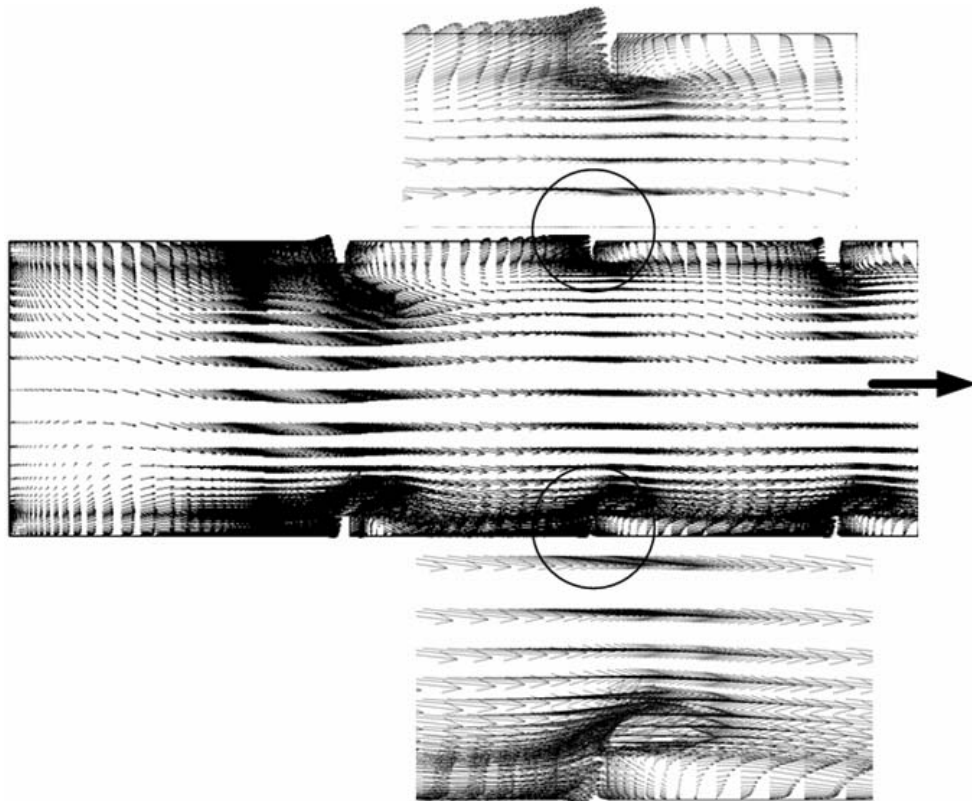
(a) Streamwise velocity
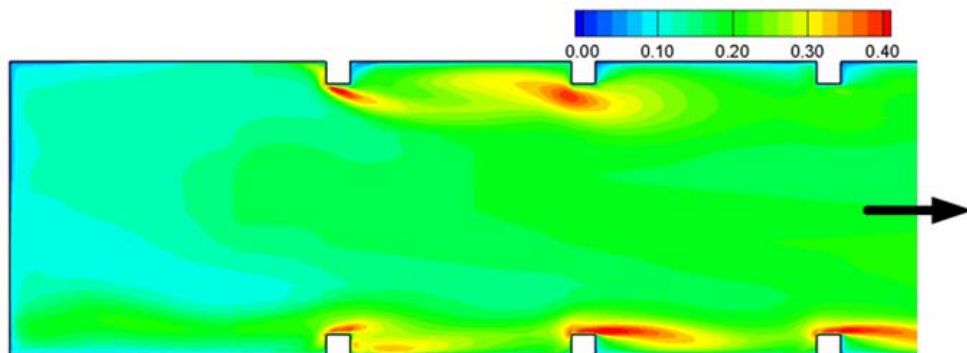
(b) Turbulence intensity

Fig. 7.9 Streamwise velocity and turbulence intensity midway between the inner and

outer walls with (+) 60° ribs in the second passage for inlet at larger cross section

7.4 Secondary Flow Development

To better understand the complex three-dimensional flow fields in the trapezoidal channel with (+) 60° ribs, the secondary flow was presented here. Fig. 7.11, 7.12, 7.13 and 7.14 show the secondary flow vectors at selected planes as denoted in Fig. 7.10. The secondary flow vectors of Fig. 7.11 and 7.13 were viewed from the inlet, while the secondary flow vectors of Fig. 7.12 and 7.14 were viewed from the outlet. As mentioned earlier, angled ribs induced the fast secondary flow that moved parallel to the ribs from the inner wall to outer wall. Because the ribs are oriented at a (+) 60° angle, the flow adjacent to the inner wall will reach the ribs first and move along the ribbed wall toward the outer wall. It then returns back to the inner wall along the centerline of the channel. The secondary flow near the inner wall was much stronger than the one near the outer wall. For the smaller inlet case (Fig. 7.11 & 12), one can clearly see that the ribs induced two counter-rotating vortices that impinge on the inner wall in the first passage (Fig. 7.11). One can also notice that along the streamwise direction, the size of two vortices oscillated from the largest in the middle of each inter-rib distance to the smallest on the ribs. From the Fig. 7.4, near the inlet two vortices were initially almost same in the size and strength. However, the upper secondary flow near the top wall became stronger than the lower secondary flow near the bottom and had a bigger size along the streamwise direction. The reason was that the magnitude of the vertical component velocity of the upper secondary flow was bigger than the one of the lower secondary flow due to the geometry of the cross section.
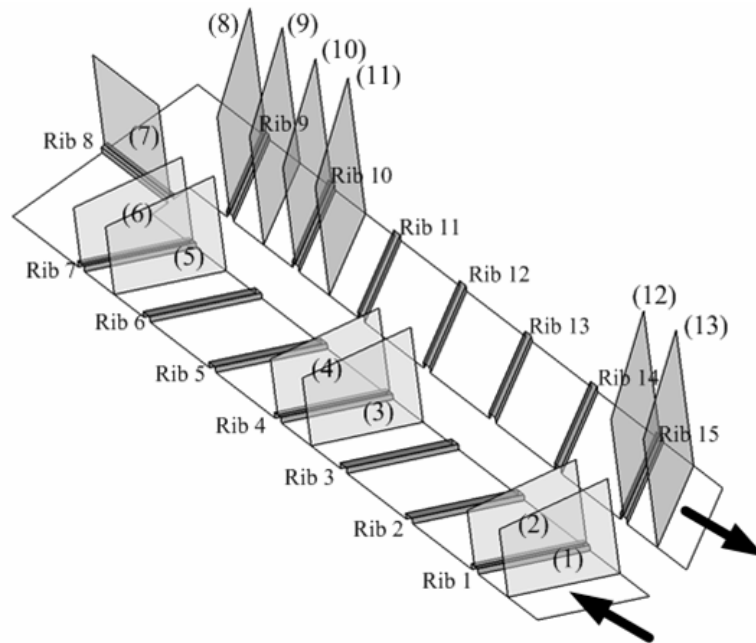
(a) Secondary flow location for smaller inlet
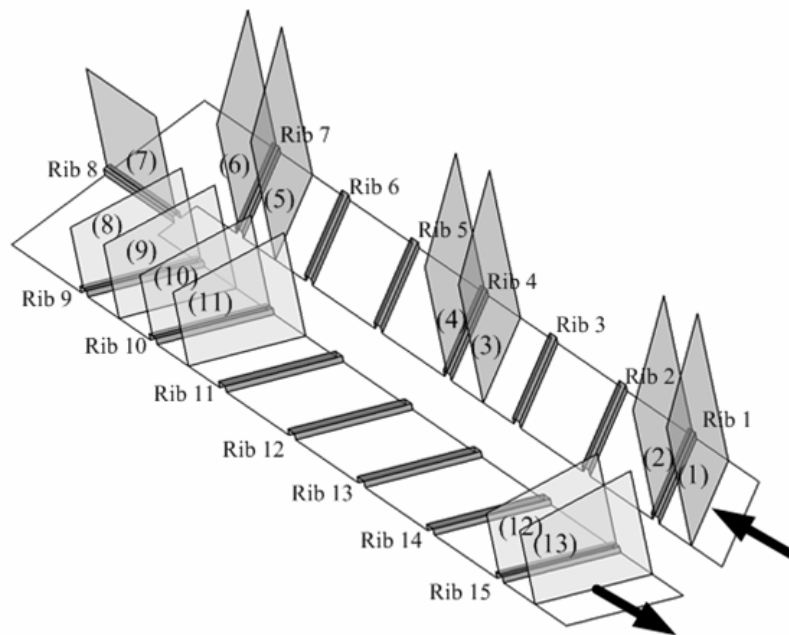
(b) Secondary flow location for larger inlet

Fig. 7.10 Secondary flow locations for trapezoidal channel with (+) 60° ribs
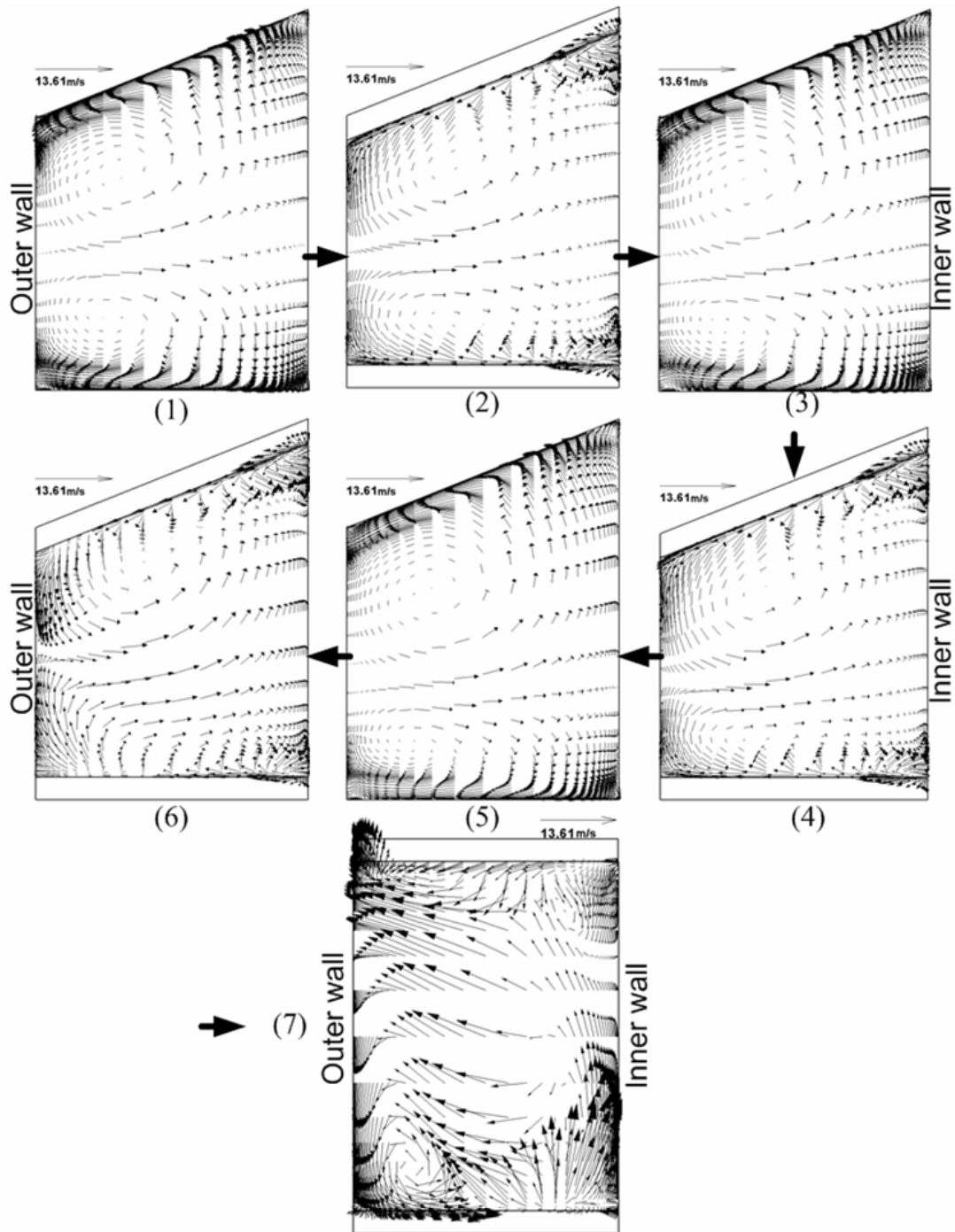
Fig. 7.11 Secondary flow developments of trapezoidal channel with (+) 60° ribs

in the first passage for inlet at smaller cross section
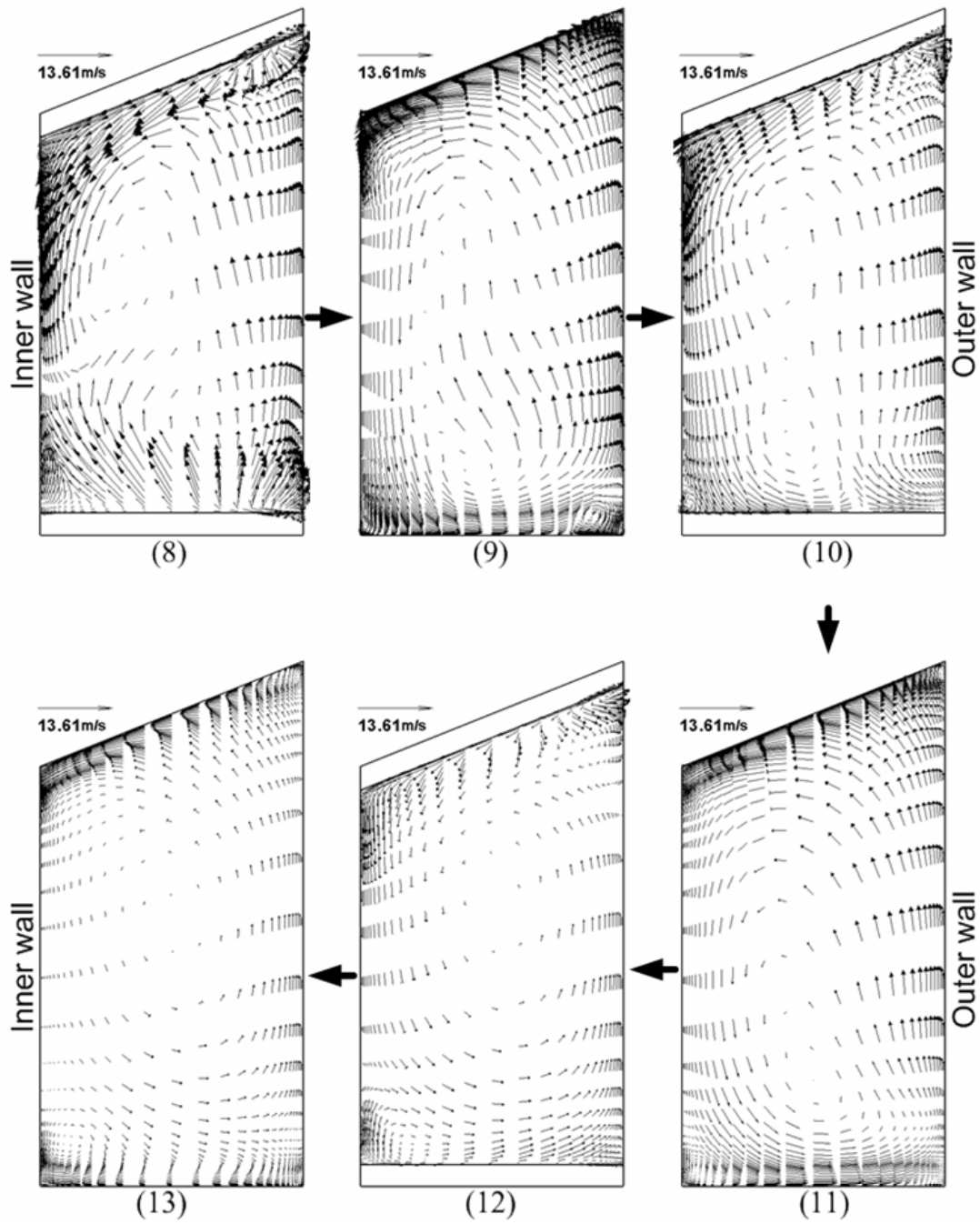
Fig. 7.12 Secondary flow developments of trapezoidal channel with (+) 60° ribs

in the second passage for inlet at smaller cross section
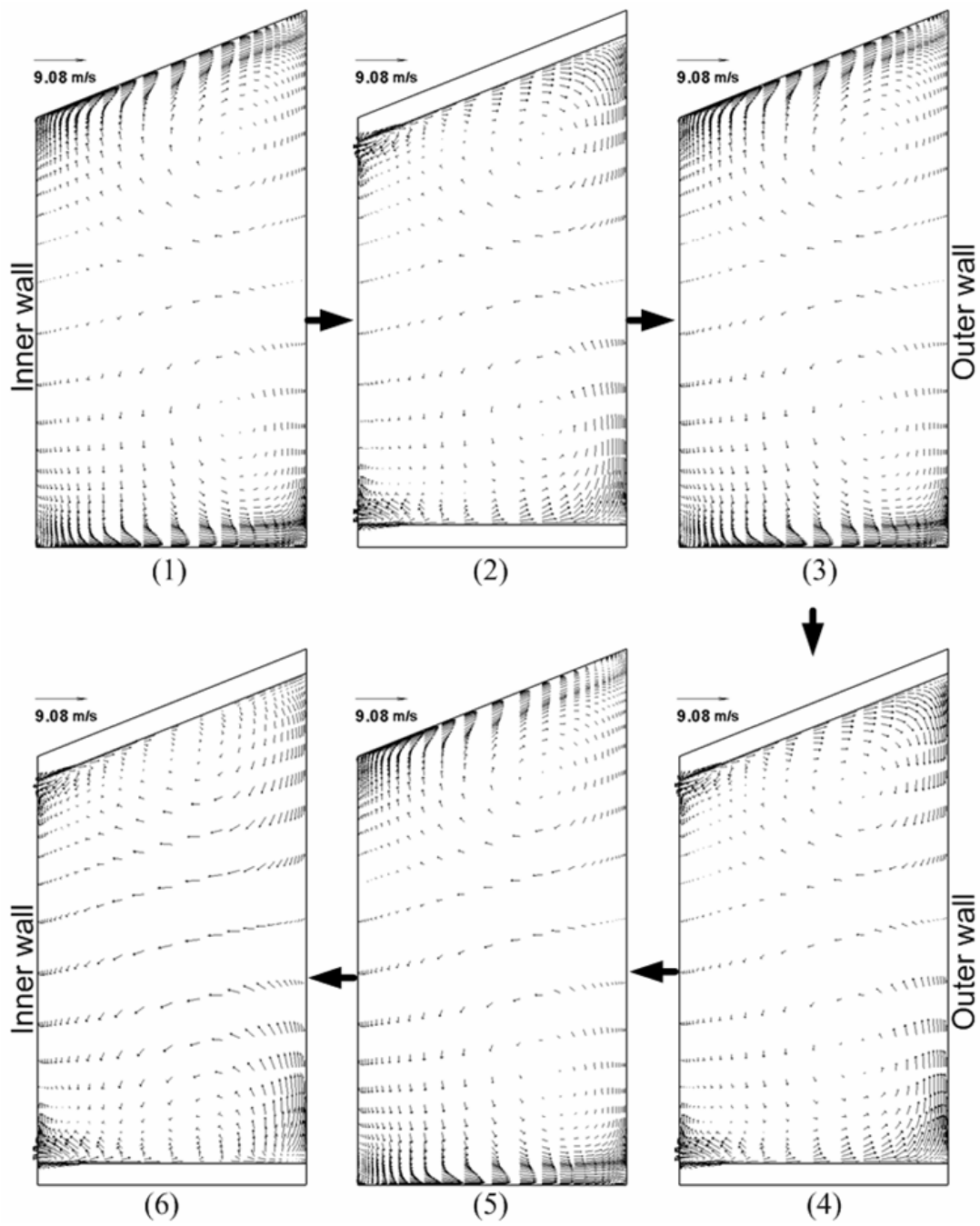
Fig. 7.13 Secondary flow developments of trapezoidal channel with (+) 60° ribs

in the first passage for inlet at larger cross section
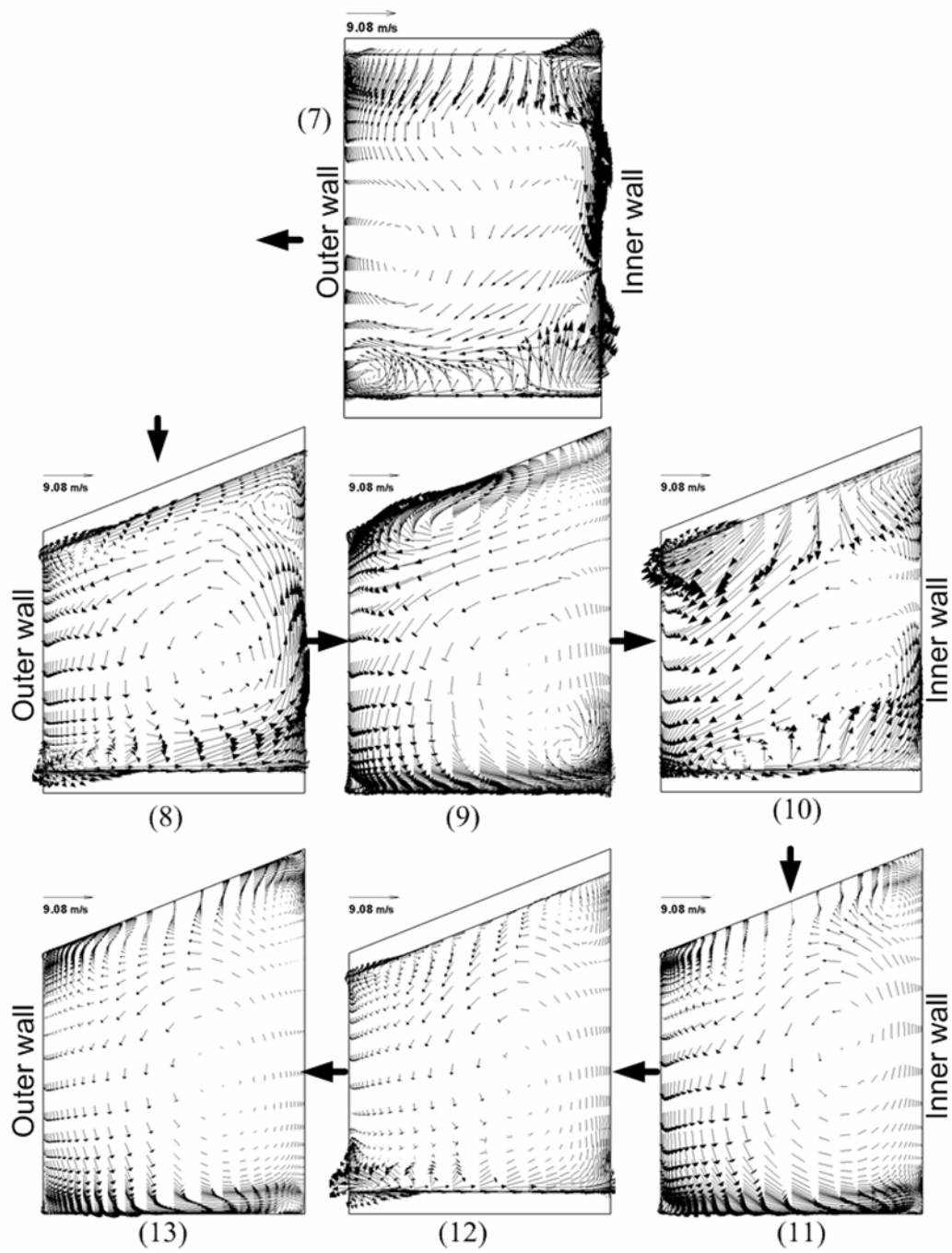
Fig. 7.14 Secondary flow developments of trapezoidal channel with (+) 60° ribs

in the second passage for inlet at larger cross section

On the rib 7 (Fig. 7.11(6)), the secondary flow became strong flow motion from the outer to the inner wall due to the turn effects. Upon entering the turn, the curvature induced secondary flow which pushed flow from the inner to outer wall overcame the secondary flow induced by the ribs, and the direction of the secondary flow was reversed and became from the inner to outer wall (Fig. 7.11(7)). Only one vortex was observed on the bottom rib and was distorted by the combined effects of centrifugal induced vortex and rib-induced vortex upstream. In the second passage (Fig. 7.12), the rib induced fast flow was reversed in direction due to the opposite rib angle compared to the first passage. One large counterclockwise rotating vortex occupied almost entire cross area and smaller clockwise rotating vortex was seen near outer and bottom wall (Fig. 7.12(9)). The velocity magnitudes were not high compared to those in the first passage because the flow was decelerated through the turn. In the second passage, the bulk mean velocity was decreased from 13.61 m/s to 9.08 m/s. The rib height-to-hydraulic diameter ratio (e/$D_{h,large}$) was also decreased since the same ribs were installed but channel height was increased. Therefore, the effect of the ribs on the flow of channel was mush less and the secondary flow induced by the turn was dominant in the second passage. Since the direction of the vortex circulation near the top wall coincided with that of the secondary flow formed by the turn, while that created near the bottom wall gave the opposite circulation to the secondary flow induced by the turn, the magnitude of flow velocity near the top wall was bigger than that near the bottom wall. Therefore, strong impingements were observed on the top wall.

Fig. 7.13 and 7.14 show secondary flow developments for the larger inlet case. Unlike the smaller inlet case, in the first passage (Fig. 7.13) the two vortices induced by the ribs were almost symmetric due to the enough space to maintain rotating shapes, while the two vortices were squashed in the vertical direction due to the tight spacing between the top and bottom walls in the smaller inlet case. It seemed that two vortices were less interacted with each other. In the turn (Fig. 7.14(7)), a small vortex was observed on the bottom rib and was less strong due to a relatively low velocity from the large cross section. Downward flow from the top wall was strong along the inner (tip of the divider) wall. In the second passage (Fig. 7.14), the secondary flow induced by the turn was dominant in the second passage due to the flow acceleration through the decrease of cross sectional area. Therefore, the downward flow along the outer wall was much strong and a large counterclockwise rotating vortex was created. In location (9) between rib 9 and rib 10, one large vortex occupied over half of the channel and a small one observed near the top wall (Fig. 7.14 (9)). However, the small vortex disappeared at location 11. Since the direction of the vortex circulation near the bottom wall coincided with that of the secondary flow formed by the turn, while that created near the top wall gave the opposite circulation to the secondary flow induced by the turn, the magnitude of flow velocity near the top wall was lower than that near the bottom wall. Therefore, the small vortex near the top wall could not overcome the strong secondary flow by the turn and disappeared. Strong impingements were observed on the bottom and near outer wall.

7.5 Heat (Mass) Transfer Distribution

The experiments were conducted to measure the regional average heat (mass) transfer in a two-pass trapezoidal channel with (+) 60° ribs on two opposite walls by naphthalene sublimation technique, and the analogy of heat and mass transfer was applied to convert the mass transfer coefficients to heat transfer coefficients. The regional average Sherwood number ratios were determined for four Reynolds numbers of 9,400, 16,800, 31,800 and 57,200. Also the numerical study was performed to compare the experimental results and the numerical predictions at Re = 31,800.

Fig. 7.15 shows calculated Nusselt number ratio distributions by the RSM. Significant effects of the 60° ribs were evident in the first passage. The 60° ribs gave substantially higher heat transfer compared with 90° ribs since the vigorous mixing between the main flow and secondary flows enhances the heat transfer on the ribbed wall more than 90° ribs. The 60° angled ribs generated secondary flows parallel to the rib axes over the top and bottom walls between two adjacent ribs from the inner wall toward the outer wall. It hit the outer wall, then, circulated across the inner wall. The two vortices were induced. These circulated flows across the inner wall pushed down the separated flow from a rib near the inner wall, shortening the reattachment length with consequent high heat transfer due to the large angle of reattachment. The secondary flow on the wall between ribs was strong enough to sweep the separated flow toward the outer wall, preventing flow reattachment near the outer wall. The secondary flow moved away from the divider wall towards the outer wall in the first passage. Nusselt number

ratios decreased from the inner wall to outer wall in the spanwise direction for both cases. Heat transfer distributions between ribs appeared periodic because the ribs periodically interrupted the boundary layers on the bottom wall. For the smaller inlet case (Fig. 7.15 (a)), in the turn region, Nusselt number ratios were very high due to the combination of the 180° sharp turn and the 90° rib. The 90° rib in the turn region produced high heat transfer enhancement immediately downstream of the rib. The large vortex impinged on the end wall resulting in the high heat transfer. Due to the presence of the rib and deceleration of the flow, the centrifugal effect was reduced. The contracted but strengthened vortex in the turn region pressed down the separated flow by the rib, causing strong reattachment immediate downstream of the rib in the turn. Unlike smooth wall case, near outer wall in the turn region heat transfer enhancement was mush less because the presence of the 90° rib and the flow deceleration reduced the effect of centrifugal forces, and caused lesser impingement on the outer wall. Unlike in the first passage, the enhancement of heat transfer by the 60° angled ribs was not evident after the turn but by the secondary flow induced by the turn in the second passage. Just after the turn, heat transfer enhancements were higher near the inner and outer walls, and were lower in the middle of the bottom due to secondary flow induced by the turn. As the small vortex near the outer wall disappeared, heat transfer enhancements were intense near the inner wall. Further downstream heat transfer enhancements were slightly increasing near the outer wall and were decreasing near the inner wall since the turning effects were reduced and the secondary flow induced by the bottom ribs seemed to overcome the secondary flow by the turn.
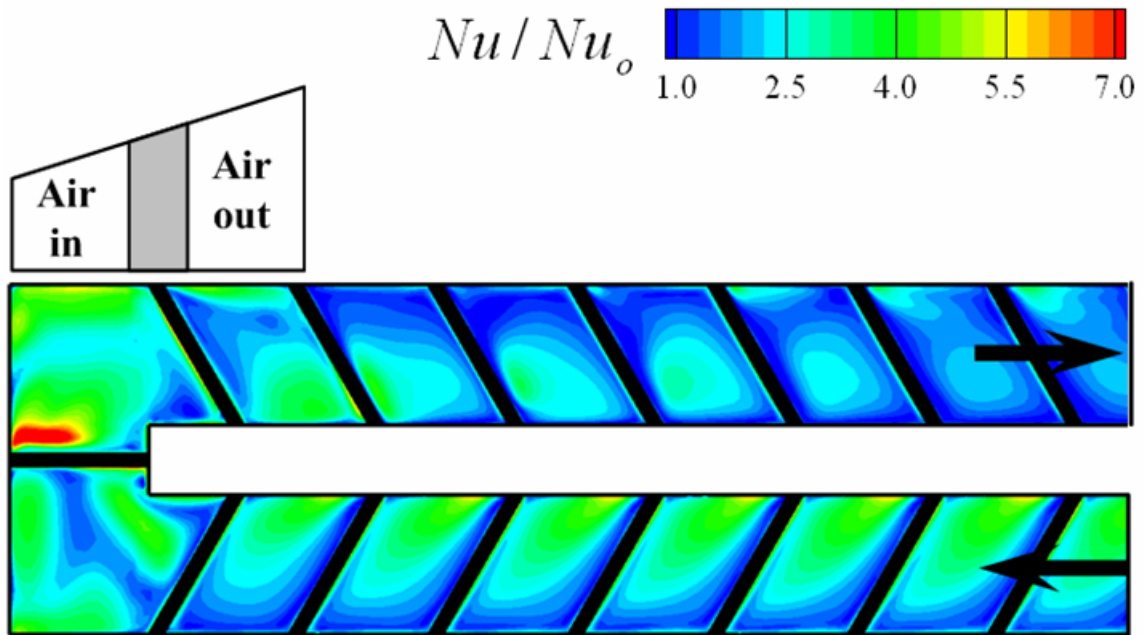
(a) Smaller inlet case
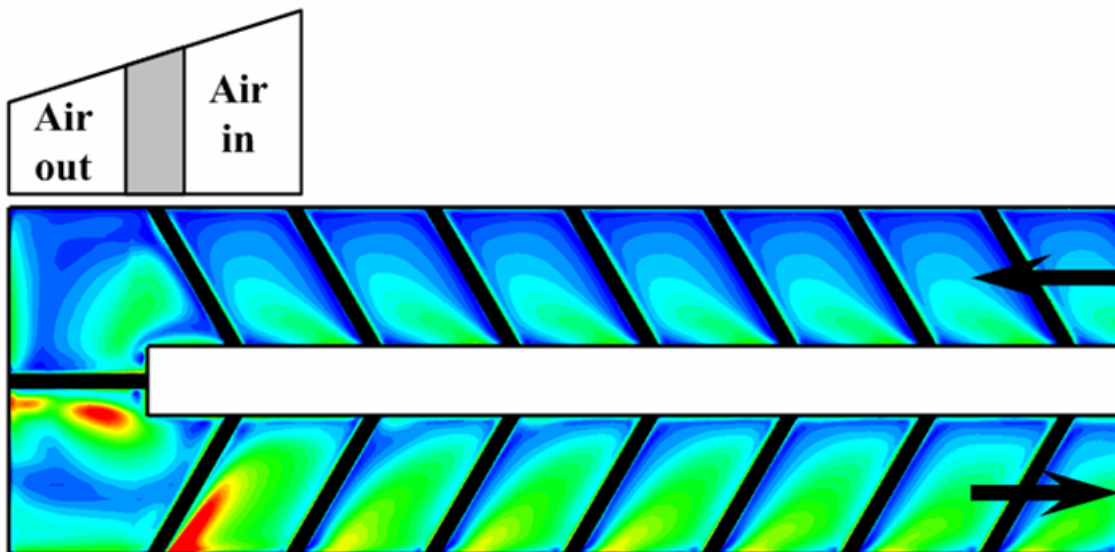
(b) Larger inlet case

Fig. 7.15 Detailed Nusselt number ratio distributions of trapezoidal channel with

(+) 60° ribs at Re = 31,800 by RSM

Every Nusselt number ratio was lower than that in the first passage because bulk mean velocity was relatively lower. For the larger inlet case (Fig. 7.15 (b)), heat transfer distribution between the ribs in the first passage was periodic, and the Nusselt number ratios were higher near the inner wall and decreased toward the outer wall in the spanwise direction. In the turn region, the heat transfer enhancements near the tip of divider wall were higher than those near the end wall downstream of the 90° rib due to strong downward flow impingements along the tip of the divider wall. In the second passage, just after the turn the highest heat transfer was occurred due to very strong flow impingement with high magnitude of the flow velocity that was accelerated through the turn. The Nusselt number ratio distributions were reverse in the spanwise direction. The Nusselt number ratios near the outer wall were higher than those near the inner wall. As the effect of the turn on the flow field vanished gradually, heat transfer enhancement decreased gradually.

Fig. 7.16 shows the streamwise distributions of the regional average Sherwood number ratios ($\overline{Sh}/Sh_0$) along the trapezoidal channel for air flow entering the smaller straight section and those for air flow entering the larger straight section. It is clear that the greatest mass transfer enhancement occurred at the lowest Reynolds number of 9,400. As the Reynolds number increased, the mass transfer coefficients increased, but the Sherwood number ratios decreased, as the Dittus-Boelter correlation absorbed the effect of the Reynolds number. The general trends of Sherwood number ratios were similar for all four Reynolds numbers. For the smaller inlet case, Sherwood number ratios gradually decreased before the turn in the first passage.
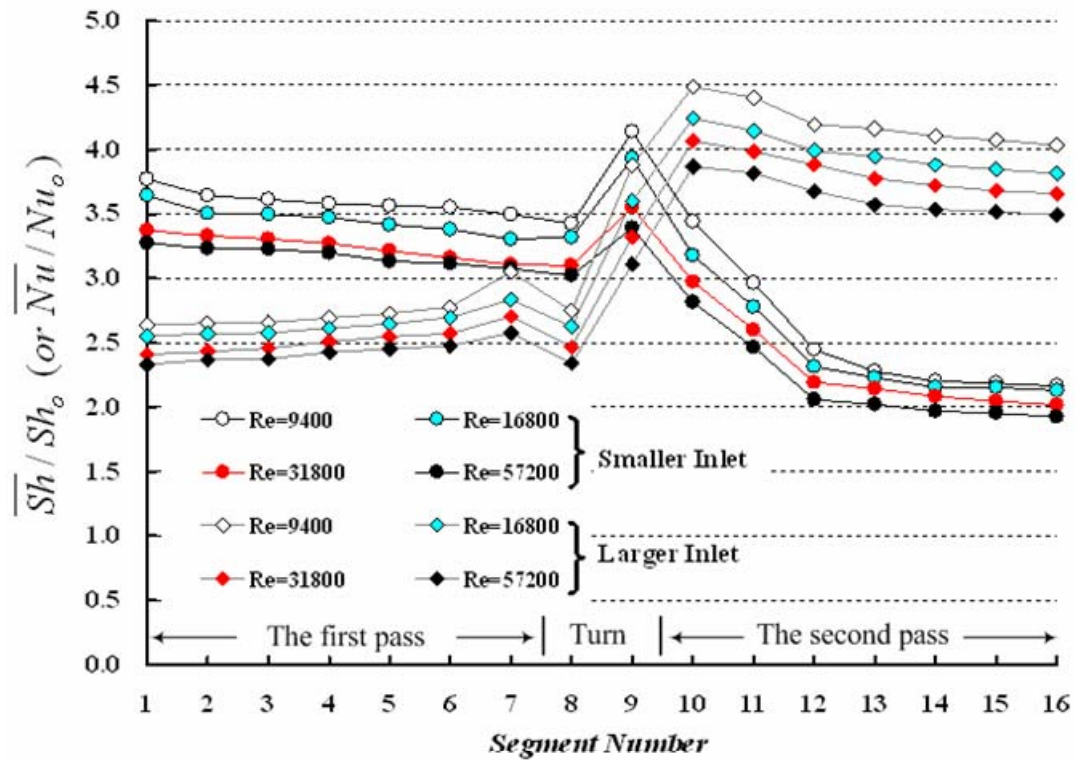
Fig. 7.16 Segmental average mass transfer distributions along the trapezoidal channel

with (+) 60° ribs

The $\overline{Sh}/Sh_0$ value was still low on wall segment no. 8. Usually in the turn region, mass

transfer enhancement is high since the flow impinges on the end wall and is deflected

onto the bottom wall near end wall. However, the secondary flow induced by the ribs

interrupted the main flow and the less impingement occurred on the end wall. Moreover,

the secondary flow was distorted by the turn effects and it did not impinge on the bottom

wall in the turn. On wall segment no.9 in the turn in the second passage, the $\overline{Sh}/Sh_0$ value was highest due to the secondary flow impingements induced by the turn. In the second passage, after the turn, mass transfer enhancement abruptly decreased due to the lower magnitude of the flow velocity. After that, the $\overline{Sh}/Sh_0$ value gradually decreased. For the larger inlet case, unlike the smaller inlet case, Sherwood number ratios gradually increased before the turn in the first passage. The reason was that the secondary flow induced by the ribs was growing near the bottom along the streamwise direction of the channel and the flow was already fully developed. It is clear that the mass transfer was the highest downstream of the turn, as the flow that left the turn with very high turbulence entered the smaller exit section. The highest mass transfer enhancement occurred on wall segment no. 10. After that, Sherwood number ratios gradually decreased since the turning effects were diminished.

The Reynolds stress model (RSM) showed well flow field and heat transfer distribution. However, when the comparison between the numerical prediction and measured regional average were considered, the prediction can not agree well with the experimental data (Fig.7.3). The RSM underpredicted heat (mass) transfer enhancements for the both cases. The maximum relative error was 24.9% and the average relative error was 18.9% for the smaller inlet case. The relative error is defined by normalizing the difference between the experimental and numerical values with respect to the experimental value. The maximum relative error was 26.9% and the average relative error was 20.4% for the larger inlet case.

CHAPTER VIII

FLOW AND HEAT TRANSFER IN A TWO-PASS TRAPEZOIDAL CHANNEL

WITH (–) 60º RIBS ON TWO OPPOSITE WALLS

In chapter VIII, an experimental study was performed to measure the regionally averaged heat (mass) transfer in a two-pass trapezoidal channel with (–) 60º ribs on two opposite walls by Naphthalene sublimation technique and an numerical study also was performed using the Reynolds stress model (RSM) with enhanced wall treatment in FLUENT.

8.1 Description of Problem

Fig. 8.1 & 8.2 show the experimental test section and the numerical grids for the two-pass trapezoidal channel with (–) 60º ribs on two opposite walls. The simulated geometry was the same as the experimental geometry. Fig 8.1 shows the rib orientation is reversed to that of (+) 60° rib case in the chapter VII. For the numerical study, only bottom wall except the ribs was heated to a constant temperature since the mass transfer experiment can simulate uniform wall temperature boundary condition. The top and bottom walls were roughened by thirty equally-spaced (–) 60º angled ribs and one 90° rib in the turn region. Therefore, the total of sixty (–) 60º angled ribs and two 90° rib was

Top wall

21.8º

Outer side wall

Outer side wall

7.62 cm

3.81 cm

Divider wall

Bottom wall

30.5 cm

30.5 cm

Bottom

Rib

Naphthalene Surfaces

60°

60°

Top

3.81 cm, *P/e*=12

3.81 cm

4.4 cm

(-) 60°

3.2 mm

3.2 mm

$e/D_{h, turn}$=0.07
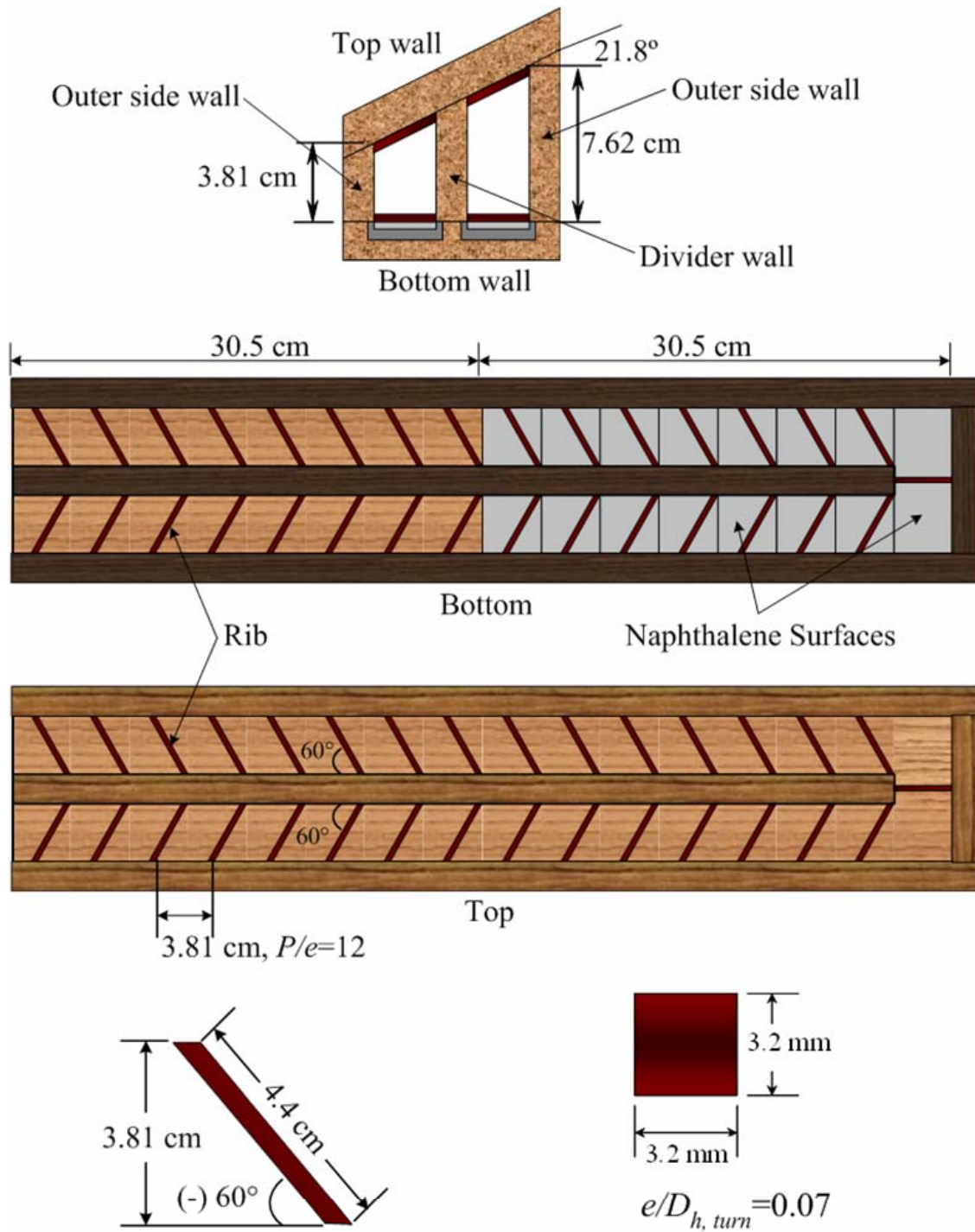
Fig. 8.1 Geometry for trapezoidal channel with (–) 60º ribs
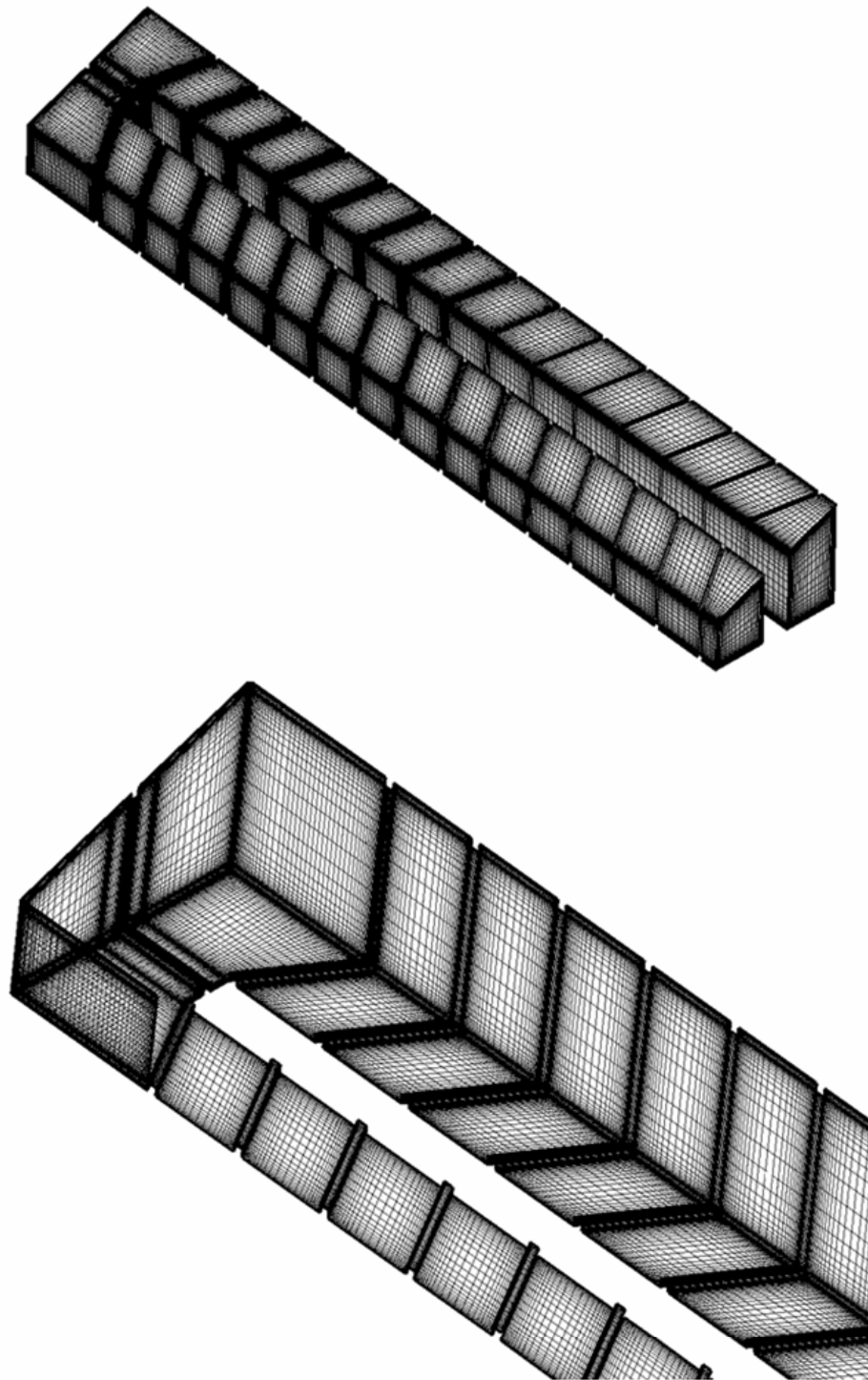
Fig. 8.2 Numerical grid for trapezoidal channel with (–) 60º ribs

attached on the top and bottom walls in parallel sequence so that they were directly opposite each other. The ribs in the first passage were angled towards the divider wall and the ribs in the second passage were angled away from the divider wall. These ribs were 3.2 mm by 3.2 mm square stripes of balsa wood and rib-to-rib spacing (P) was 3.81 cm. Thus, the rib height-to-hydraulic diameter ratio (e/ $D_{h,turn}$) was 0.07, and the rib pitch-to-rib height ratio (P/e) was 12. The regional average mass transfer experiment was conducted with Re = 9,400, 16,800, 31,800 and 57,200 but the Reynolds number was fixed at 31,800 for the numerical study.

8.2 Grid Independence Study

Fig. 8.2 gives the numerical grid generated using Gambit for this simulation. The grid independent study was made by performing the simulations for three different cross sectional grids of $32 \times 62 \times 620$, $42 \times 72 \times 620$ and $52 \times 82 \times 620$, and one streamwise $42 \times 72 \times 720$ grid with mesh refined in the near wall regions (Fig. 8.2). For the smaller inlet case (Fig. 8.3(a)), a comparison between $32 \times 62 \times 620$ and $42 \times 72 \times 620$ grid points showed 6.5% maximum changes in the Nusselt number ratio. The maximum difference in Nusselt number ratio was less than 2.5% between $42 \times 72 \times 620$ and $52 \times 82 \times 620$ grid points. For the larger inlet case (Fig. 8.3(b)), a comparison between $32 \times 62 \times 620$ and $42 \times 72 \times 620$ grid points showed 4.6% maximum changes in the Nusselt number ratio. The maximum difference in Nusselt number ratio was less than 1.5% between $42 \times 72 \times 620$ and $52 \times 82 \times 620$ grid points.

(a) Trapezoidal Channel, Inlet at Smaller Section,
(-) 60° ribs : Re = 31,800

(b) Trapezoidal Channel, Inlet at Larger Section,
(-) 60° ribs : Re = 31,800
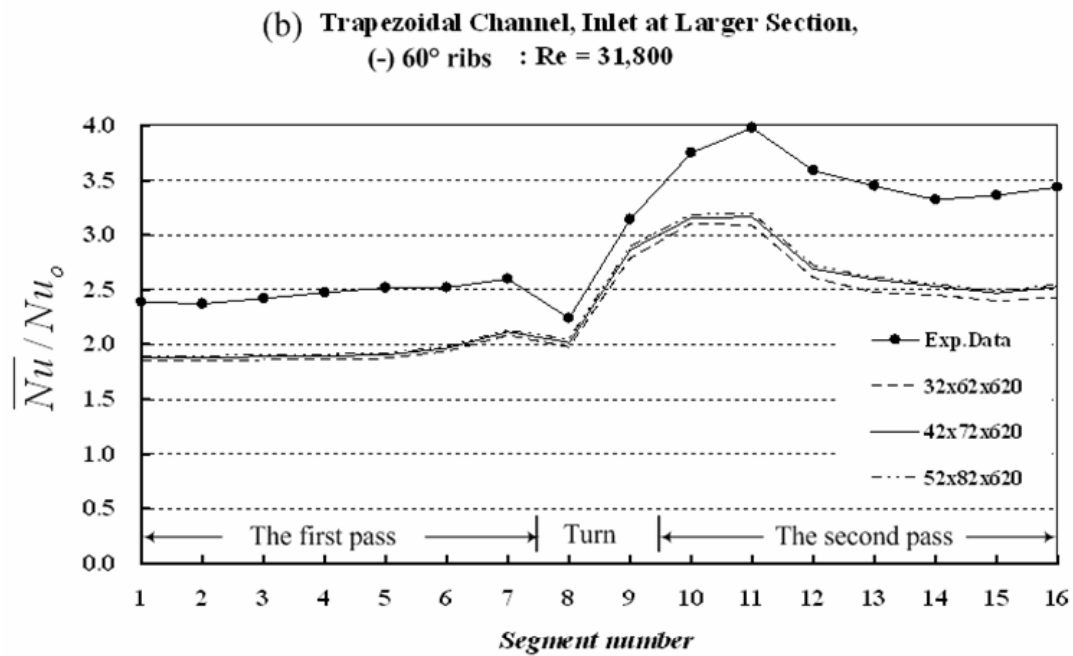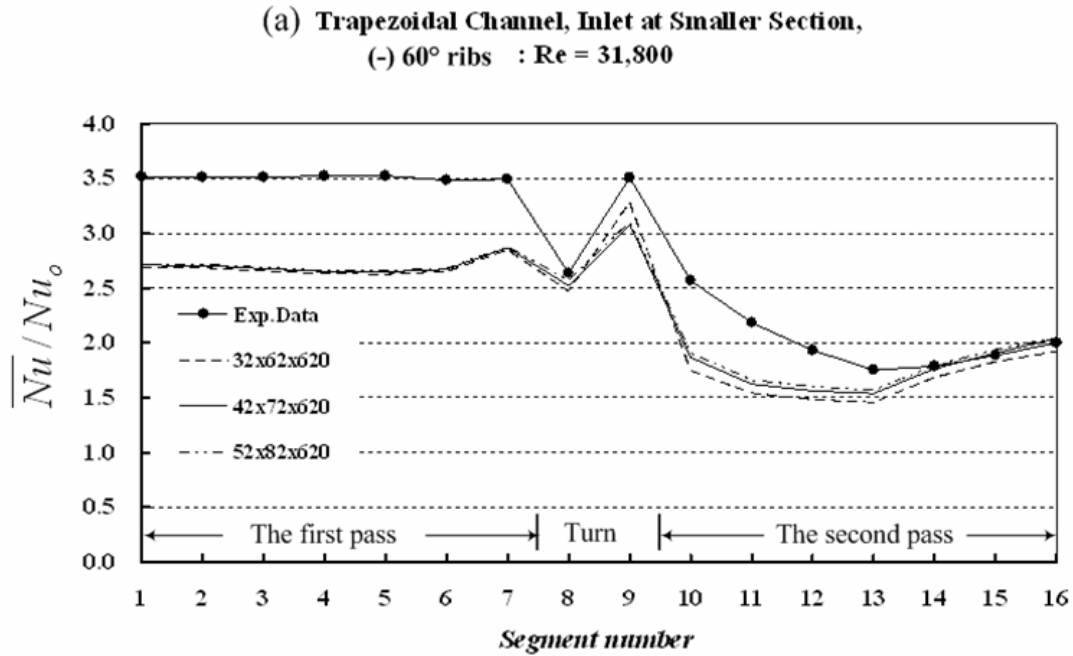
Fig. 8.3 Grid independent study for trapezoidal channel with (–) 60º ribs

Further increase of the number of grid points in streamwise direction of the channel produced only minor changes of the Nusselt number ratios for the both cases. Therefore, it was determined that grid independence was achieved with $42 \times 72 \times 620$ grid points and all results were based on the $42 \times 72 \times 620$ grid points, which resulted in 1,874,880 grid points for both the smaller inlet and larger inlet cases. The y^+ values were less than unity in all test runs of grid independent study.

8.3 Velocity Fields

For this case, the ribs are just in the contrary orientation compared with the case of (+) 60° ribs. As the flow approaches the ribs, the angled ribs guide the near wall flow to move along the ribs. The secondary flow follows the ribs until it hits on the divider (inner) wall. After hitting on the inner wall, the secondary flow induced by the rib returns to the outer wall and a vortex is created. This behavior is similar on the top and bottom wall, therefore, two counter-rotating vortices form in the trapezoidal channel (Fig. 8.4). Fig. 8.5 shows the streamwise velocity vector distributions at the mid-plane between the top and bottom walls with (–) 60º ribs at Re = 31,800 for inlet at smaller cross section and for inlet at larger cross section. For the inlet at the smaller cross section (Fig. 8.5(a)), the velocity profiles were flat before the turn. The magnitude of the flow velocity along the outer wall seemed to be higher than that along the inner wall due to the rib orientation which the ribs were angled towards the inner wall. As the flow approached the turn region, flow accelerations occurred near the divider wall and flow
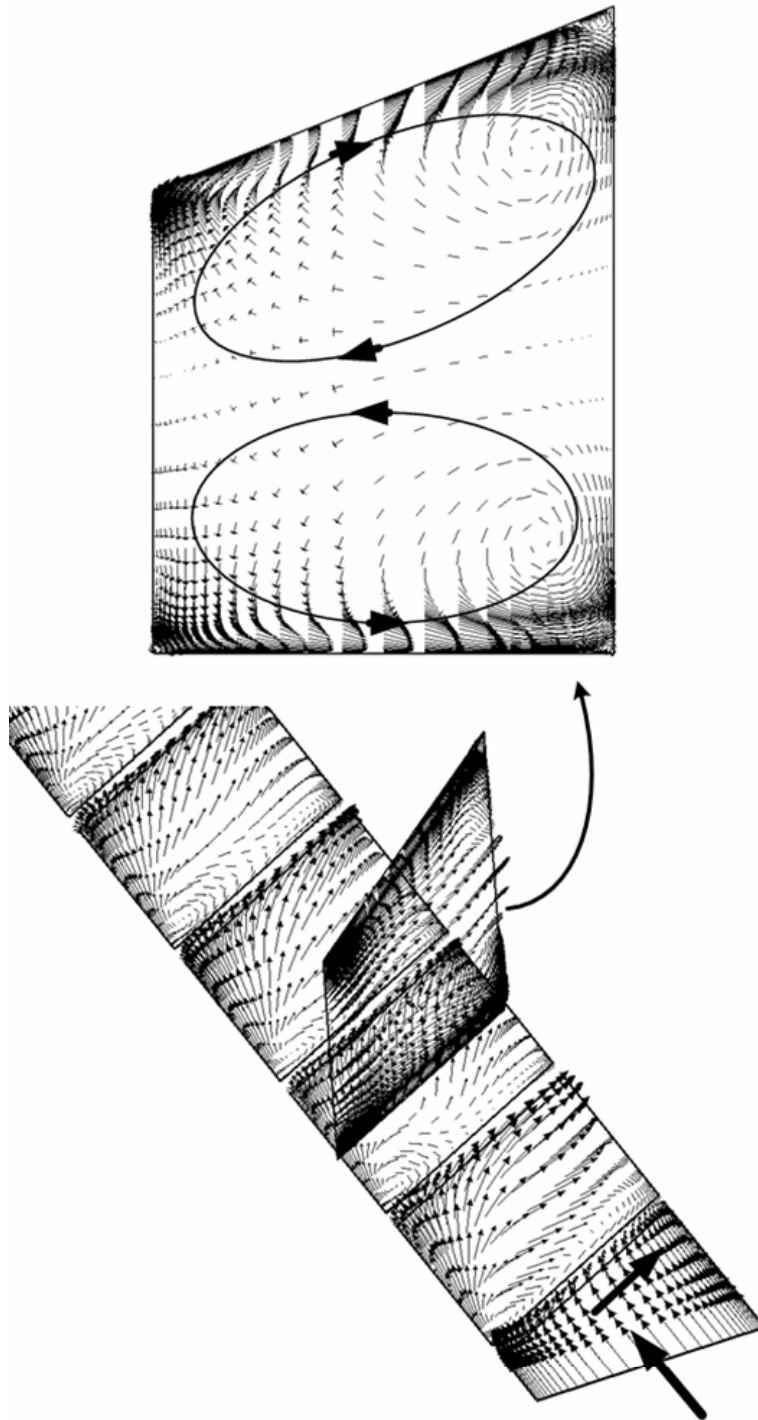
Fig. 8.4 Secondary flow vortices induced by (–) 60º rib
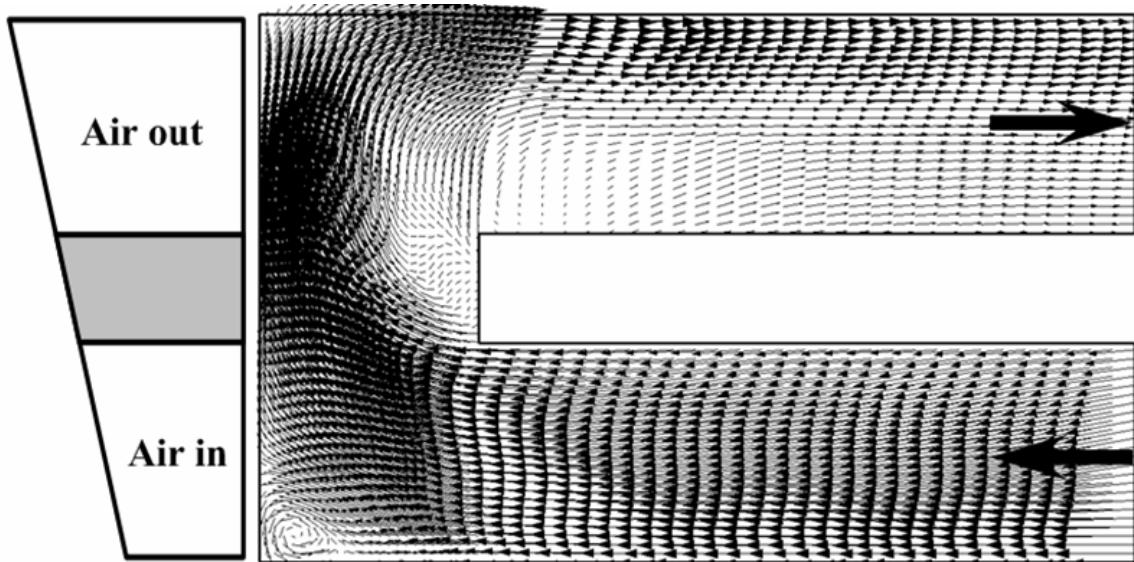
(a) Streamwise velocity vector for inlet at smaller section
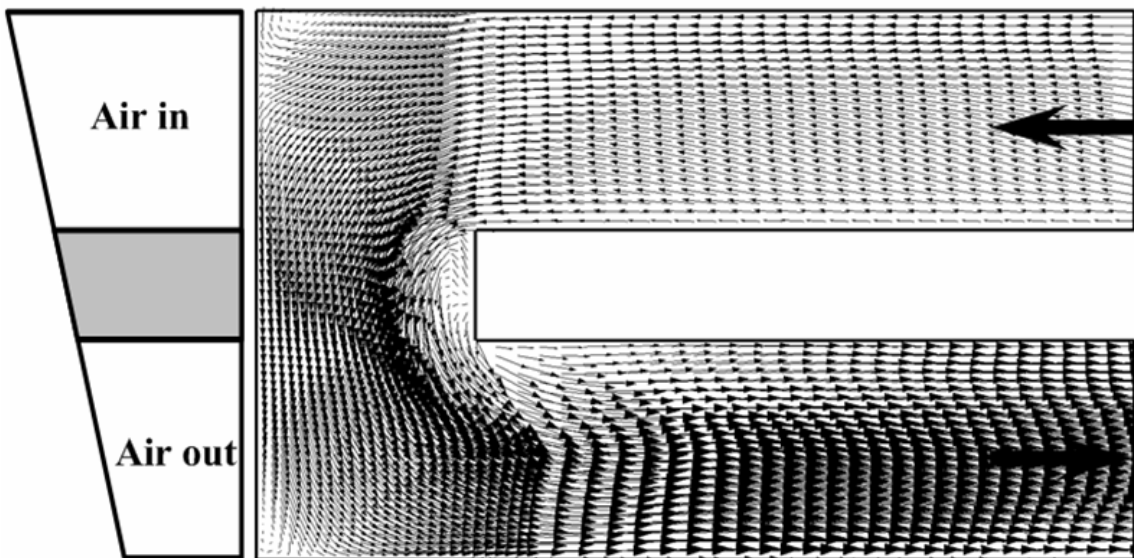
(b) Streamwise velocity vector for inlet at larger section

Fig. 8.5 Streamwise velocity vector midway between the top and bottom walls

with (−) 60º ribs

decelerations occurred near the outer wall due to the favorable and adverse pressure gradients along the divider and outer wall, respectively. Flow deceleration took place at the outer wall and was followed by flow separation, which results in a zone of recirculating flow in the upstream corner in the first passage. This recirculation zone was slightly smaller than that of (+) 60° rib case since the secondary flow induced by the ribs pushed the main flow in the core toward the outer wall and thus, the separation bubble was squashed. There were no separation bubbles near the divider wall tip in the turn region. However, a large bifurcating zone existed near the divider wall in the second passage. For the inlet at the larger cross section (Fig. 8.5(b)), the flow had a similar pattern but bifurcating zone did not existed. Because the flow was accelerated by decreasing cross area through the turn, the streamwise velocity was much faster than the vertical velocity. In both case, there were weak flow impingements onto the end wall in the turn due to the secondary flow induced by angled ribs because the secondary flow pushed the flow in the core toward the outer wall. Just after the turn the high momentum flow impinged onto the outer wall in the second passage.

Fig. 8.6, 8.7, 8.8 and 8.9 show streamwise velocity and turbulence intensity in the planes midway between the inner and outer walls with (–) 60º ribs at Re = 31,800 for inlet at smaller cross section and for inlet at larger cross section. The reversal flow occurred immediately downstream of the ribs on both the top and bottom walls. However, immediately upstream of the ribs there were no separations, such as that generally found in a 90° ribbed channel case. In the 60° ribs case, the flows near the inner and outer walls were different from each other due to the secondary flow induced

by the angled ribs. For the smaller inlet case (Fig. 8.6(a)) near the outer wall the flows beyond ribs and directing to rib-roughened wall to reattach were intense and near the inner wall these flows become weaker in the first passage. In the turn, one large vortex occurred near the bottom, and a small vortex was observed near the top wall. It was also observed that the flow over the ribs near the bottom wall was faster than the one near the top wall. The reason was that the rib induced secondary flow near the bottom wall was much stronger than the one near the top wall. As the overall characteristics of the Reynolds stress in the ribbed channel, the ribs strongly intensify the turbulence level on both the top and bottom walls. The ribs also increase turbulent mixing. The relatively hot flow near the wall is continuously mixing with the relatively cooler core flow near the center of the channel. This mixing also serves to increase the heat transfer from the channel. Fig. 8.6(b) shows the turbulence intensity distributions in the first passage for the smaller inlet case. The turbulence intensities were as high as 33% immediately downstream of the ribs on the bottom wall and 25% immediately downstream of the ribs on the top wall, and diminished gradually toward the center of the channel around 10%. Near the end wall the turbulence intensity was relatively low about 26% due to less flow impingement. Due to the stronger secondary flow, the higher turbulence intensity occurred near the bottom wall. Fig 8.7 shows the streamwise velocity and turbulence intensity in the second passage in the planes midway between the inner and outer wall for inlet at smaller cross section. Through the turn, the flow was decelerated due to increase of the cross section area. Since the velocity magnitude and rib height-to-hydraulic diameter ratio (e/ $D_{h,large}$) were smaller than those in the first passage, the

effects of the angled ribs were much less. After the turn, there no flow reattachments between ribs due to a large flow separation on the rib just after the turn (Fig. 8.7(a)). The main flow was shifted toward the top wall and then a strong flow impingement occurred on the top wall. The highest turbulence intensity was 36% on the first rib on the top wall just after the turn. However, the turbulence intensity had low values in the second passage. The turbulence intensities were as high as 26% immediately downstream of the ribs on the top wall and 11% immediately downstream of the ribs on the bottom wall.

Fig. 8.8 and 8.9 show streamwise velocity and turbulence intensity for the larger inlet case. Since the velocity magnitude and rib height-to-hydraulic diameter ratio (e/$D_{h,large}$) were smaller than those of the smaller inlet case, the effects of the ribs were much less. In the turn, only one small vortex occurred near the bottom due to weak impingements with relatively low velocity (Fig. 8.8 (a)).

Unlike the smaller inlet case, the flow over the ribs near the top wall was a little faster than the one near the bottom wall. The reason was that the rib induced secondary flow near the top wall was slightly stronger than the one near the top wall. The turbulence intensities were as high as 30% immediately downstream of the ribs on the top wall and 28% immediately downstream of the ribs on the top wall, and diminished gradually toward the center of the channel around 10% (Fig. 8.8(b)). In the second passage (Fig. 8.9), after the turn, the strong flow impingement occurred on the bottom walls unlike the smaller inlet case (Fig. 8.9 (a)). As the flow goes through the turn, the flow is accelerated by decreasing the cross section area. Therefore, a larger momentum of the flow from the larger inlet makes the strong flow impingements on the walls and

(a) Streamwise velocity

(b) Turbulence intensity
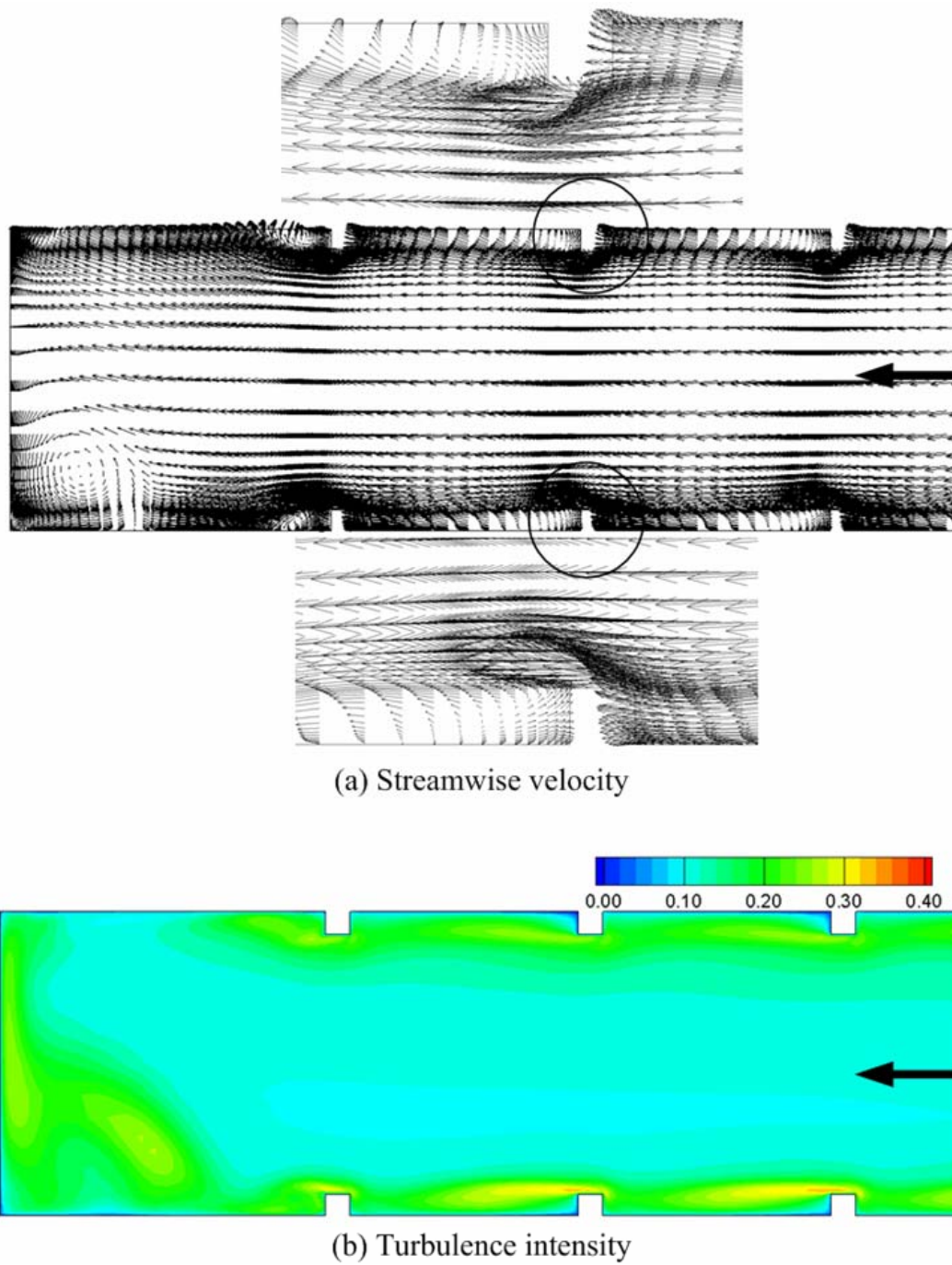
Fig. 8.6 Streamwise velocity and turbulence intensity midway between the inner and

outer walls with (–) 60º ribs in the first passage for inlet at smaller cross section
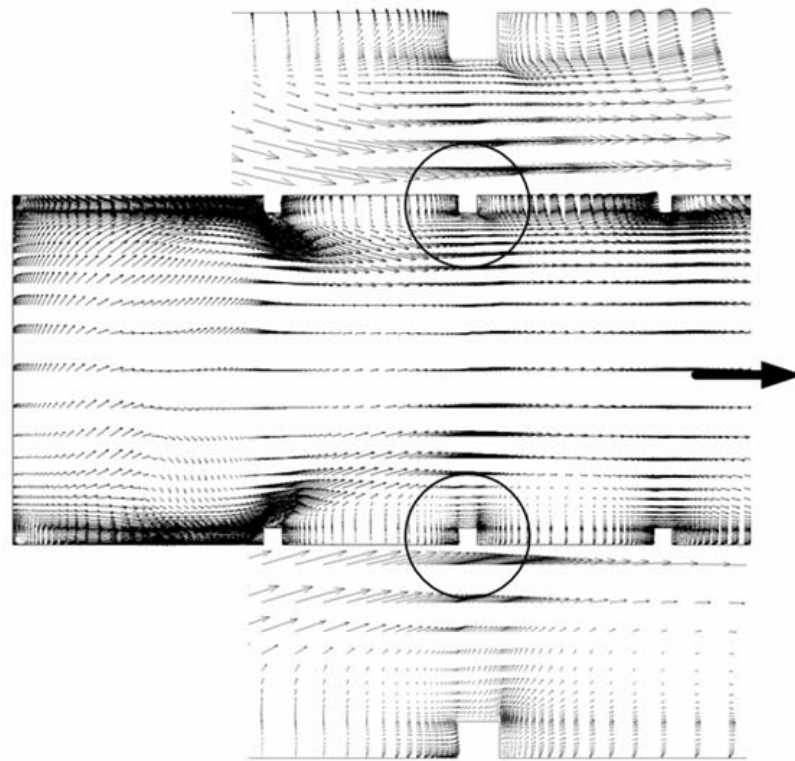
(a) Streamwise velocity
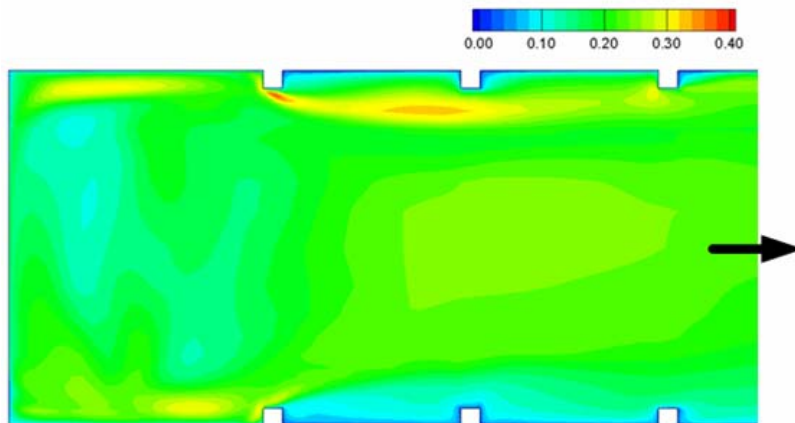
(b) Turbulence intensity

Fig. 8.7 Streamwise velocity and turbulence intensity midway between the inner and

outer walls with (−) 60º ribs in the second passage for inlet at smaller cross section
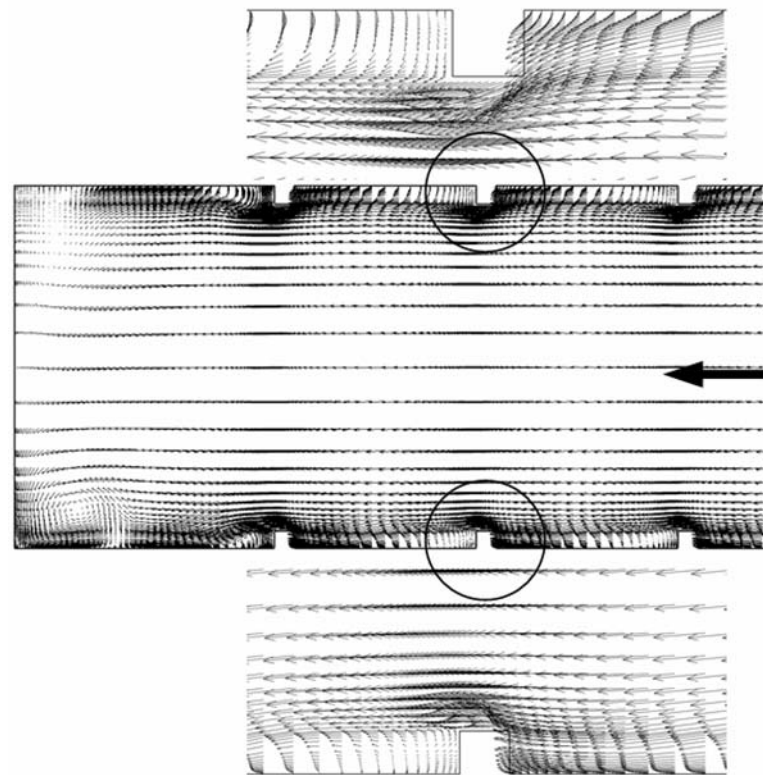
(a) Streamwise velocity
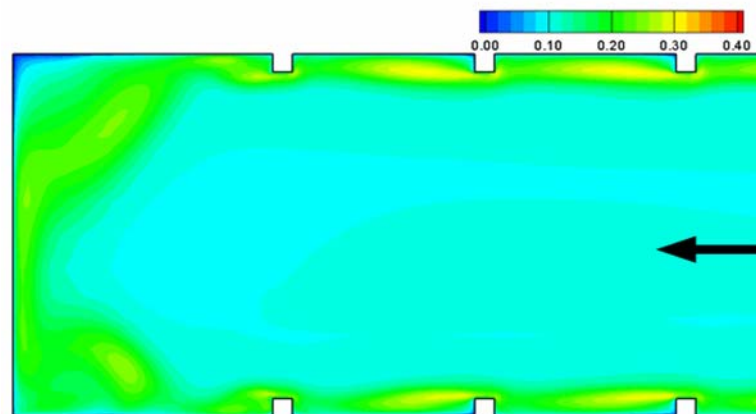
(b) Turbulence intensity

Fig. 8.8 Streamwise velocity and turbulence intensity midway between the inner and outer walls with (–) 60º ribs in the first passage for inlet at larger cross section
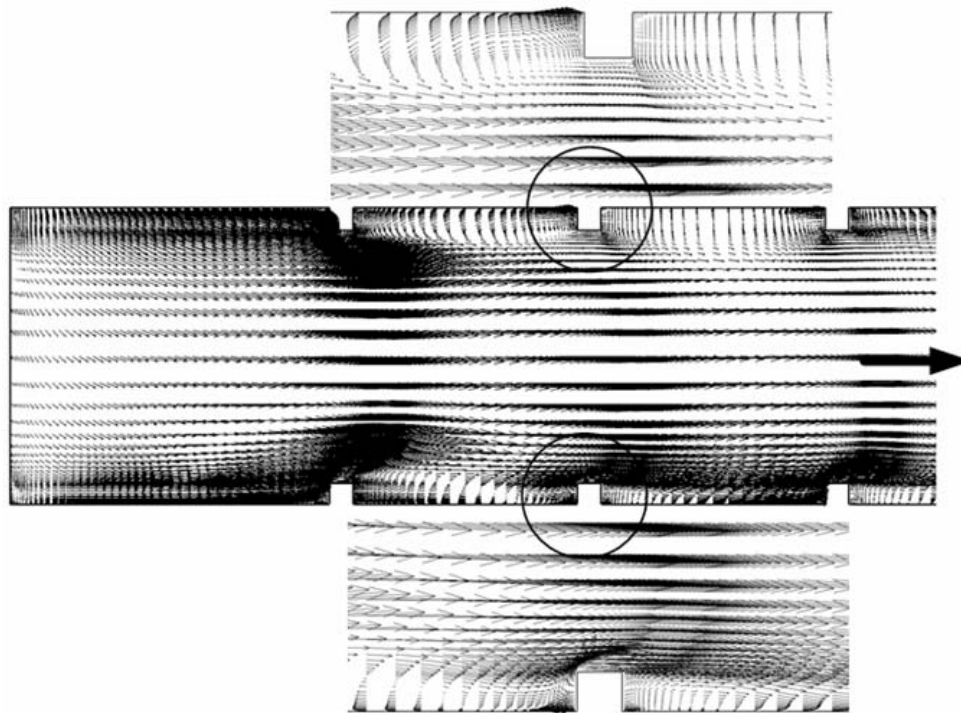
(a) Streamwise velocity
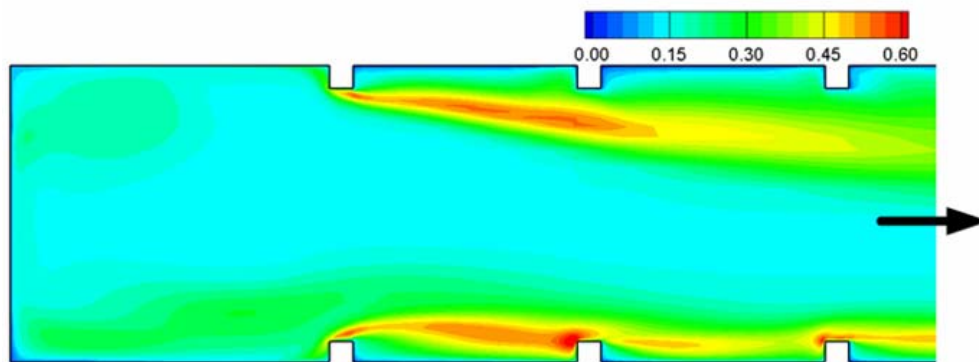
(b) Turbulence intensity

Fig. 8.9 Streamwise velocity and turbulence intensity midway between the inner and

outer walls with (–) 60º ribs in the second passage for inlet at larger cross section

increases turbulence intensities in the second passage of the channel. The level of turbulence intensity was about 59% near the bottom wall. Near the top wall 54% turbulence intensity only on the two ribs just after the turn was observed and further downstream turbulence intensity level decreased to 25% (Fig. 8.9 (b)).

8.4 Secondary Flow Development

To better understand the complex three-dimensional flow fields in the trapezoidal channel with (–) 60º ribs, the secondary flow was presented here. Fig. 8.11, 8.12, 8.13 and 8.14 show the secondary flow vectors at selected planes as denoted in Fig. 8.10. The secondary flow vectors of Fig. 8.11 and 8.13 were viewed from the inlet, while the secondary flow vectors of Fig. 8.12 and 8.14 were viewed from the outlet. As mentioned earlier, angled ribs induced the fast secondary flow that moves parallel to the ribs from the outer wall to inner wall. Because the ribs were oriented at a (–) 60º angle, the flow adjacent to the outer wall will reach the ribs first and move along the ribbed wall toward the inner wall. It then returns back to the outer wall along the centerline of the channel. The secondary flow near the outer wall was much stronger than the one near the inner wall. For the smaller inlet case (Fig. 8.11 & 12), one can clearly see that the ribs induced two counter-rotating vortices that impinge on the outer wall in the first passage (Fig. 8.11). One can also notice that along the streamwise direction, the size of two vortices oscillated from the largest in the middle of each inter-rib distance to the smallest on the ribs.
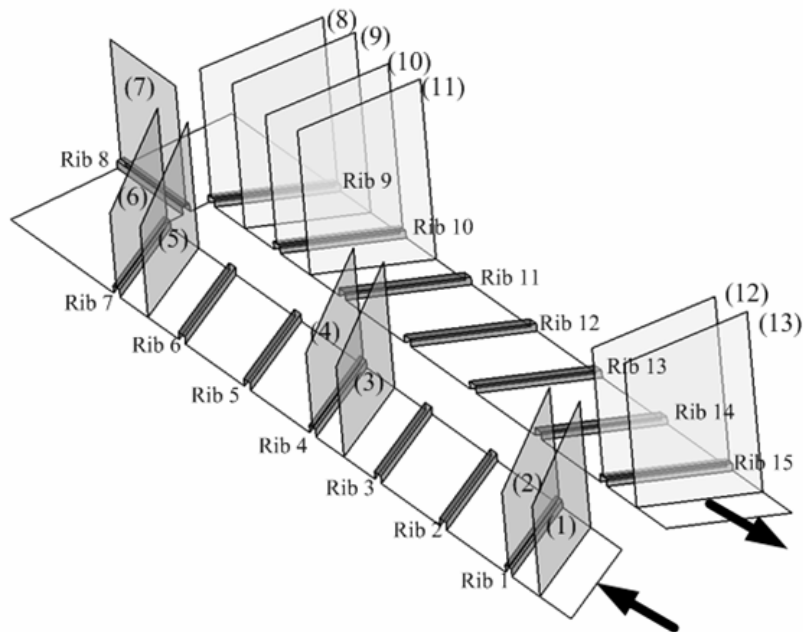
(a) Secondary flow location for smaller inlet
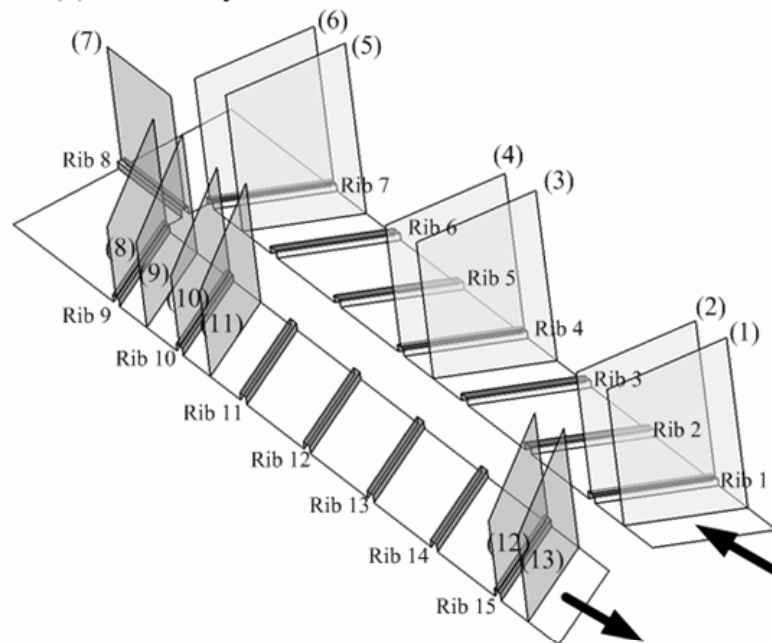
(b) Secondary flow location for larger inlet

Fig. 8.10 Secondary flow locations for trapezoidal channel with (−) 60º ribs
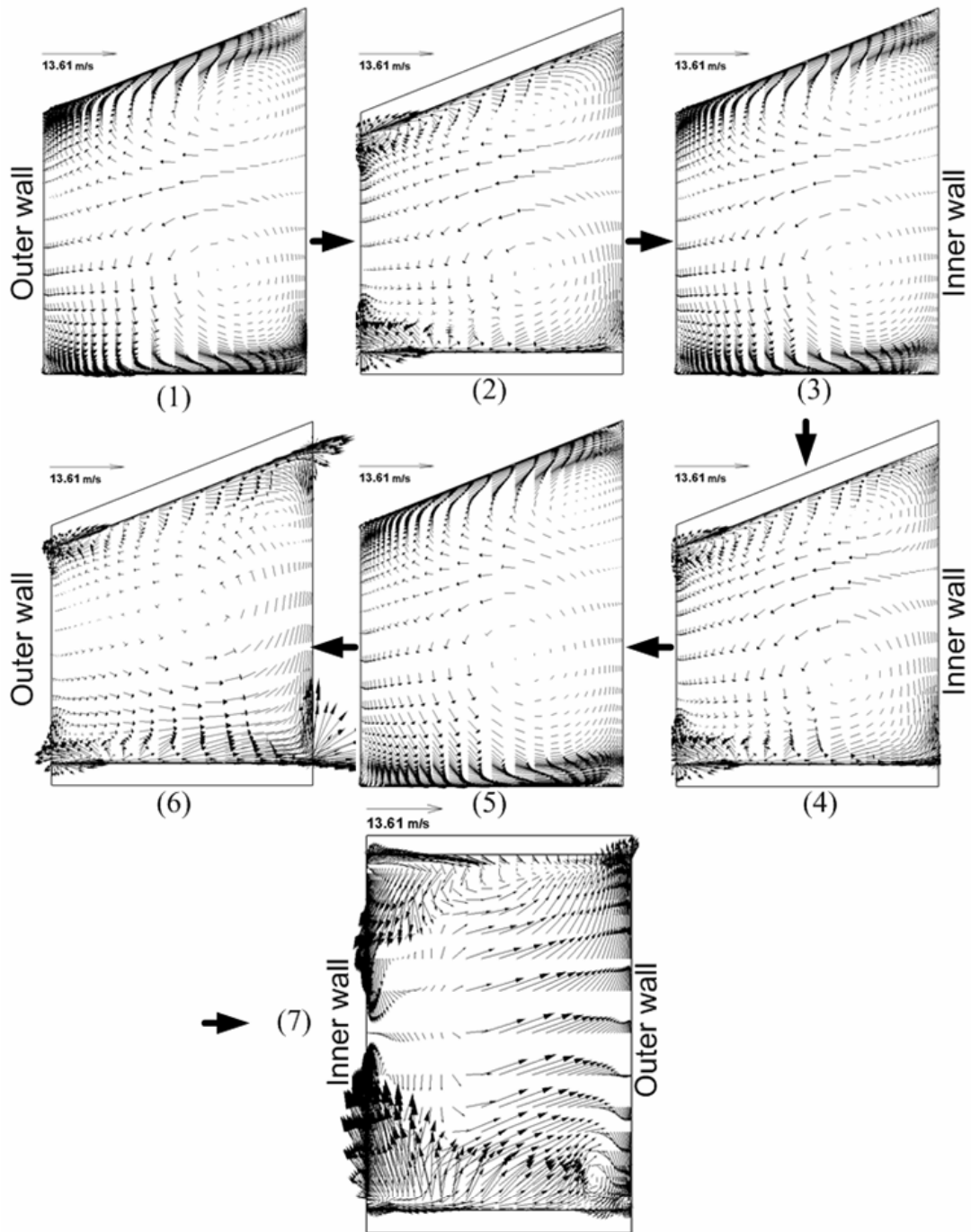
Fig. 8.11 Secondary flow developments of trapezoidal channel with (–) 60º ribs

in the first passage for inlet at smaller cross section
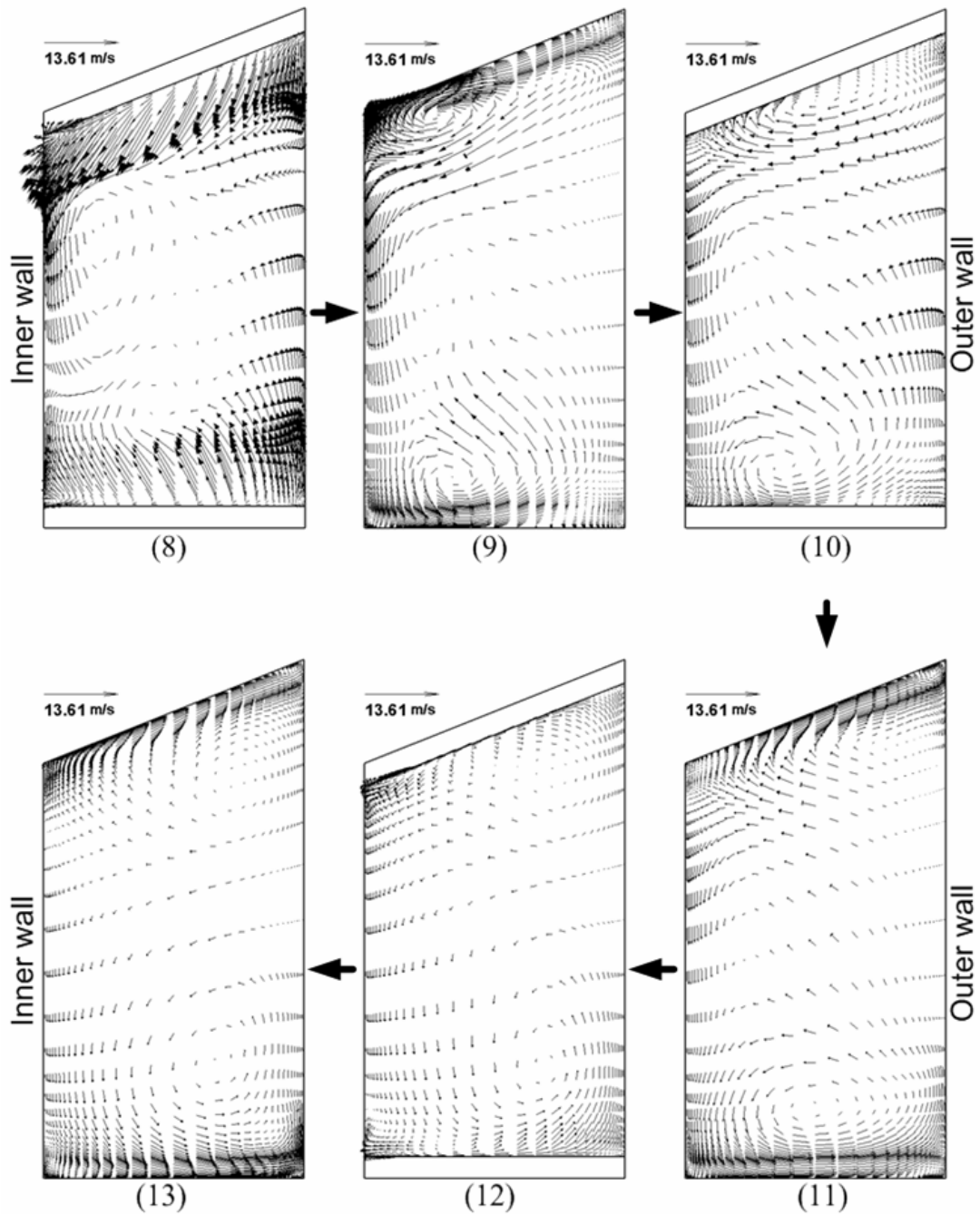
Fig. 8.12 Secondary flow developments of trapezoidal channel with (–) 60º ribs

in the second passage for inlet at smaller cross section
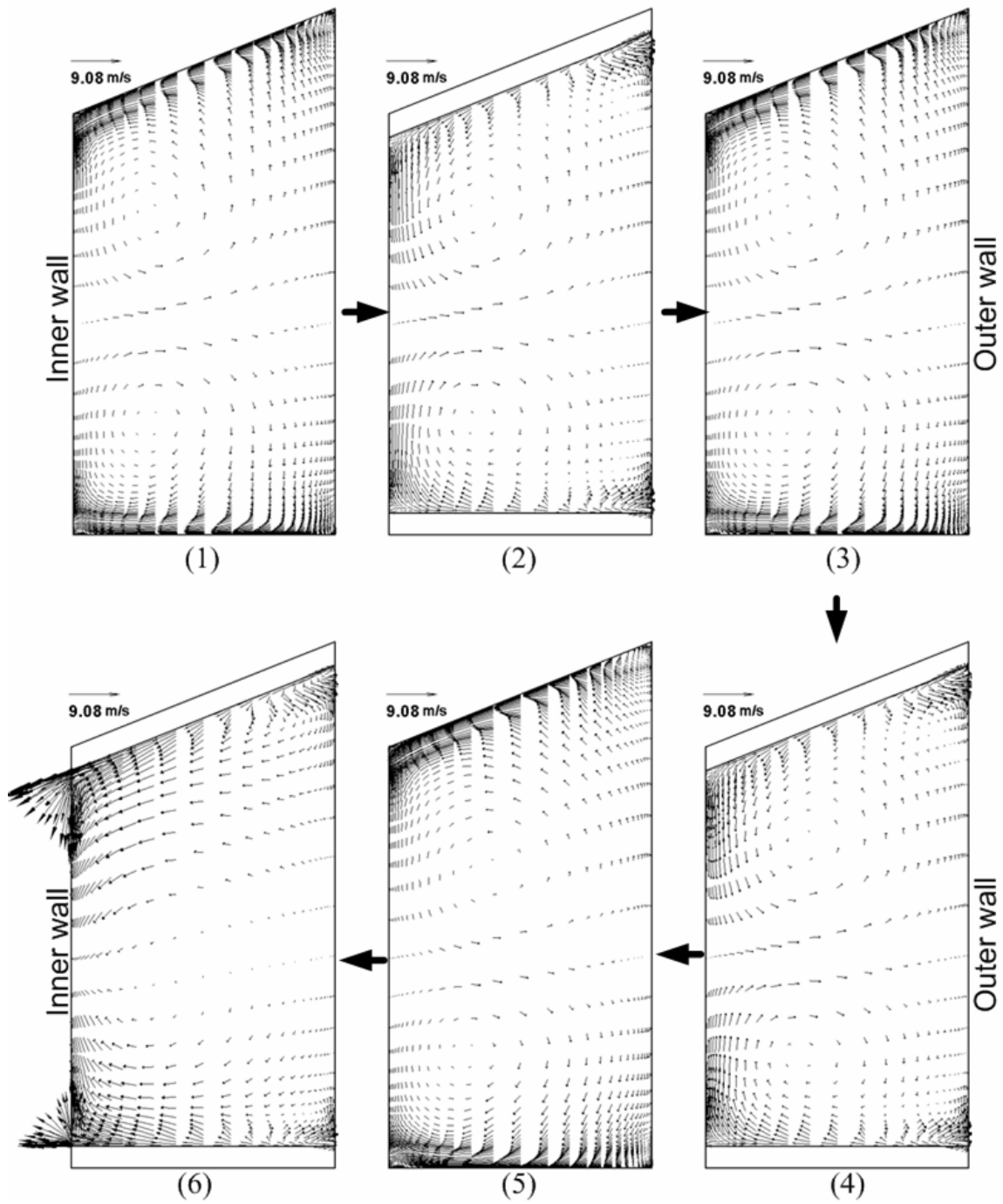
Fig. 8.13 Secondary flow developments of trapezoidal channel with (–) 60º ribs

in the first passage for inlet at larger cross section
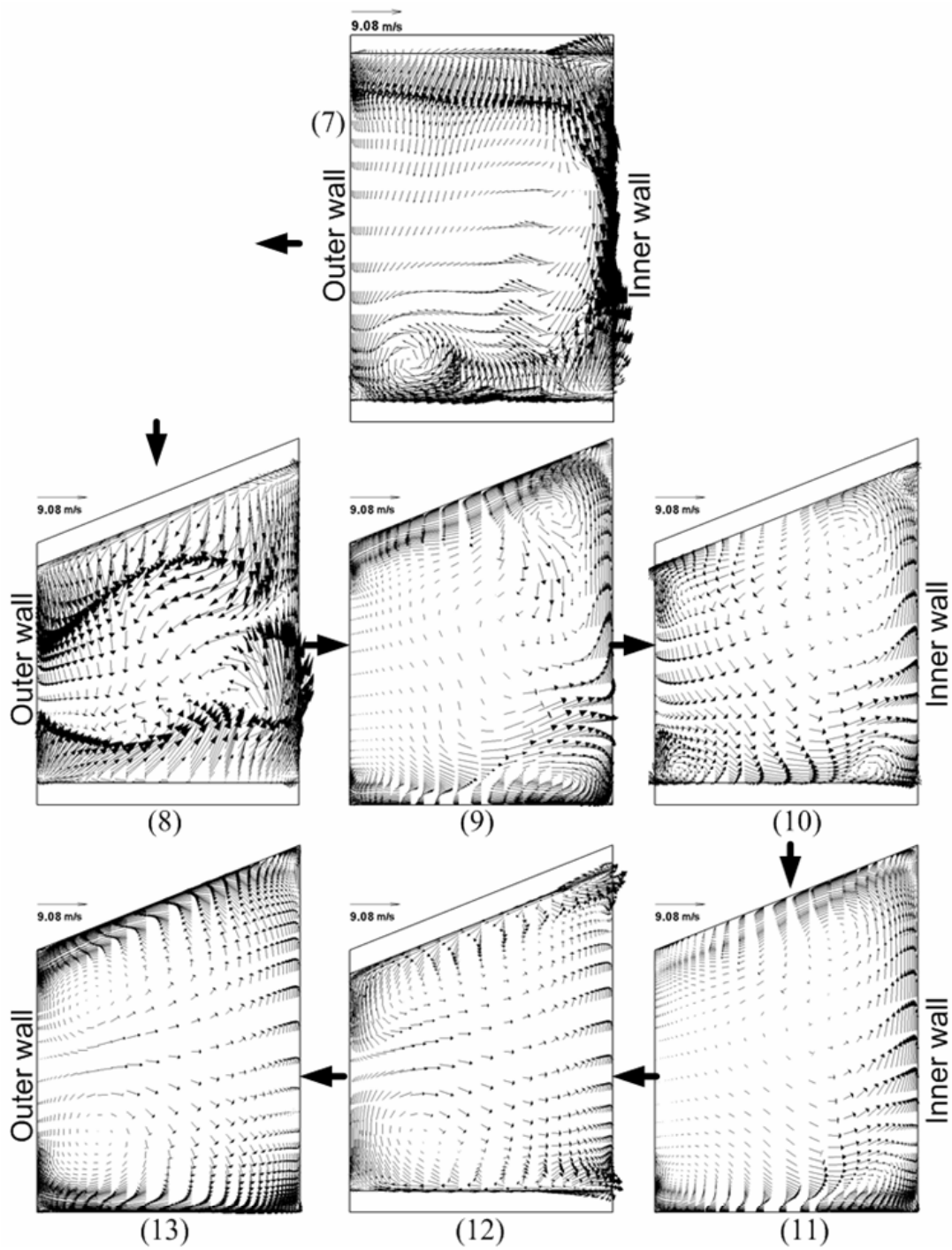
Fig. 8.14 Secondary flow developments of trapezoidal channel with (−) 60º ribs

in the second passage for inlet at larger cross section

From the Fig. 8.4, near the inlet two vortices were almost same in the size and strength. However, the lower secondary flow near the top wall became stronger than the upper secondary flow near the bottom and had a bigger size along the streamwise direction. The reason was that the magnitude of the vertical component velocity of the lower secondary flow was bigger than the one of the upper secondary flow due to the geometry of the cross section. On the rib 7 (Fig. 8.11(6)), the secondary flow became s strong flow motion from the outer to the inner wall due to the turn effects. Upon entering the turn, the curvature induced secondary flow which pushed flow from the inner to outer wall had the same direction of the vortex circulation induced by the ribs. Only one vortex was observed on the bottom rib and was distorted by the combined effects of centrifugal induced vortex and rib-induced vortex upstream (Fig. 8.11(7)). In the second passage (Fig. 8.12), the rib induced fast flow was reversed in direction due to the opposite rib angle compared to the first passage. Two counter-rotating vortices occupied near top and bottom wall, and the downward flow seemed to be very strong (Fig. 8.12(9)). The velocity magnitudes were not high compared to those in the first passage because the flow was decelerated through the turn. In the second passage, the bulk mean velocity was decreased from 13.61 m/s to 9.08 m/s. The rib height-to-hydraulic diameter ratio (e/ $D_{h,large}$) was also decreased since the same ribs were installed but channel height was increased. Therefore, the effect of the ribs on the flow of channel was mush less and the secondary flow induced by the turn was dominant in the second passage. Since the direction of the vortex circulation near the bottom wall coincided with that of the secondary flow formed by the turn, while that created near the top wall gave the opposite

circulation to the secondary flow induced by the turn, the magnitude of flow velocity near the bottom wall was bigger than that near the top wall. Therefore, strong impingements were observed on the bottom wall. The lower vortex became stronger and the upper vortex became weaker along the streamwise direction.

Fig. 8.13 and 8.14 show secondary flow developments for the larger inlet case. Unlike the smaller inlet case, in the first passage (Fig. 8.13) the two vortices induced by the ribs were almost symmetric due to the enough space to maintain rotating shapes, while the two vortices were squashed in the vertical direction due to the tight spacing between the top and bottom walls in the smaller inlet case. It seemed that two vortices were less interacted with each other. In the turn (Fig. 8.14(7)), a small vortex was observed on the bottom rib and was less strong due to a relatively low velocity from the large cross section. Downward flow from the top wall was strong along the inner (tip of the divider wall) wall. In the second passage (Fig. 8.14), the secondary flow induced by the turn was dominant in the second passage due to the flow acceleration through the decrease of cross sectional area. Therefore, the downward flow along the outer wall was much strong and a large counterclockwise rotating vortex was created. In location (9) between rib 9 and rib 10, one large vortex occupied over half of the channel and a small one observed near the top wall (Fig. 8.14 (9)). However, the size of small vortex decreased at location 11. The direction of the vortex circulation near the top wall coincided with that of the secondary flow formed by the turn, while that created near the bottom wall gave the opposite circulation to the secondary flow induced by the turn. However, the magnitude of flow velocity near the top wall was lower than that near the

bottom wall. Therefore, the small vortex near the bottom wall with high magnitude of the flow velocity overcame the secondary flow by the turn. Near the end of the heating section, two counter-rotating vortices were observed since the effects of the turn were diminished and the secondary flow induced the ribs started to develop (Fig. 8.14 (13)).

8.5 Heat (Mass) Transfer Distribution

The experiments were conducted to measure the regional average heat (mass) transfer in a two-pass trapezoidal channel with (–) 60º ribs on two opposite walls by naphthalene sublimation technique, and the analogy of heat and mass transfer was applied to convert the mass transfer coefficients to heat transfer coefficients. The regional average Sherwood number ratios were determined for four Reynolds numbers of 9,400, 16,800, 31,800 and 57,200. Also the numerical study was performed to compare the experimental results and the numerical predictions at Re = 31,800.

Fig. 8.15 shows calculated Nusselt number ratio distributions by the RSM. Significant effects of the (–) 60º angled ribs were evident in the first passage. The (–) 60º angled ribs gave substantially higher heat transfer compared with 90° ribs. The (–) 60º angled ribs generated secondary flows parallel to the rib axes over the top and bottom walls between two adjacent ribs from the outer wall toward the inner wall. It hit the inner wall, then, circulated across the outer wall. The two vortices were induced. These circulated flows across the outer wall pushed down the separated flow from a rib near the outer wall, shortening the reattachment length with consequent high heat transfer due

to the large angle of reattachment. The secondary flow on the wall between ribs was strong enough to sweep the separated flow toward the inner wall, preventing flow reattachment near the inner wall. The secondary flow moved away from the outer wall towards the inner wall in the first passage. Nusselt number ratios decreased from the outer wall to inner wall in the spanwise direction for both cases. Heat transfer distributions between ribs appeared periodic because the ribs periodically interrupted the boundary layers on the bottom wall. For the smaller inlet case (Fig. 8.15 (a)), just before the turn, the high heat transfer enhancement was observed immediately downstream of the last rib in the first passage. Since the direction of the vortex circulation created by the rib coincided with that of the secondary flow formed in the turn, the secondary flow induced by the last rib became stronger. In the turn region, Nusselt number ratios were very high due to the combination of the 180° sharp turn and the 90° rib. The 90° rib in the turn region produced high heat transfer enhancement immediately downstream of the rib. The large vortex impinged on the end wall resulting in the high heat transfer. Due to the presence of the rib and deceleration of the flow, the centrifugal effect was reduced. The contracted but strengthened vortex in the turn region pressed down the separated flow by the rib, causing strong reattachment immediate downstream of the rib in the turn. Unlike smooth wall case, near outer wall in the turn region heat transfer enhancement was mush less because the presence of the 90° rib and the flow deceleration reduced the effect of centrifugal forces, and caused lesser impingement on the outer wall. Unlike in the first passage, the enhancement of heat transfer by the (–) 60º angled ribs was not evident after the turn but by the secondary flow induced by the turn in the second

(a) Smaller inlet case

(b) Larger inlet case

Fig. 8.15 Detailed Nusselt number ratio distributions of trapezoidal channel with

(–) 60º ribs at Re = 31,800 by RSM

passage. In the second passage the periodic heat transfer patterns were not seen at the first half of downstream of the turn due to the turning effect. As the effects of the turn were diminished, the periodic heat transfer patterns were observed. Just after the turn, heat transfer enhancements were higher near the inner and outer walls, and were lower in the middle of the bottom due to secondary flow induced by the turn. As the small vortex near the outer wall disappeared, heat transfer enhancements were intense near the inner wall. Further downstream heat transfer enhancements were slightly increasing near the inner wall since the turning effects were reduced and the secondary flow induced by the bottom ribs seemed to overcome the secondary flow by the turn. Every Nusselt number ratio was lower than that in the first passage because bulk mean velocity was relatively lower. For the larger inlet case (Fig. 8.15 (b)), heat transfer distribution between the ribs in the first passage was periodic, and the Nusselt number ratios were higher near the outer wall and decreased toward the outer wall in the spanwise direction. In the turn region, the heat transfer enhancements near the tip of divider wall were higher than those near the end wall downstream of the 90° rib due to strong downward flow impingements along the tip of the divider wall. In the second passage, just after the turn the high heat transfer was occurred due to very strong flow impingement with high magnitude of the flow velocity that was accelerated through the turn. The Nusselt number ratio distributions were reverse in the spanwise direction. The Nusselt number ratios near the inner wall were higher than those near the outer wall. As the effect of the turn on the flow field vanished gradually, heat transfer enhancement decreased gradually. Near the exit of the heating section heat transfer enhancements were slightly increasing since the

turning effects were reduced and the secondary flow induced by the bottom ribs seemed

to start to develop.
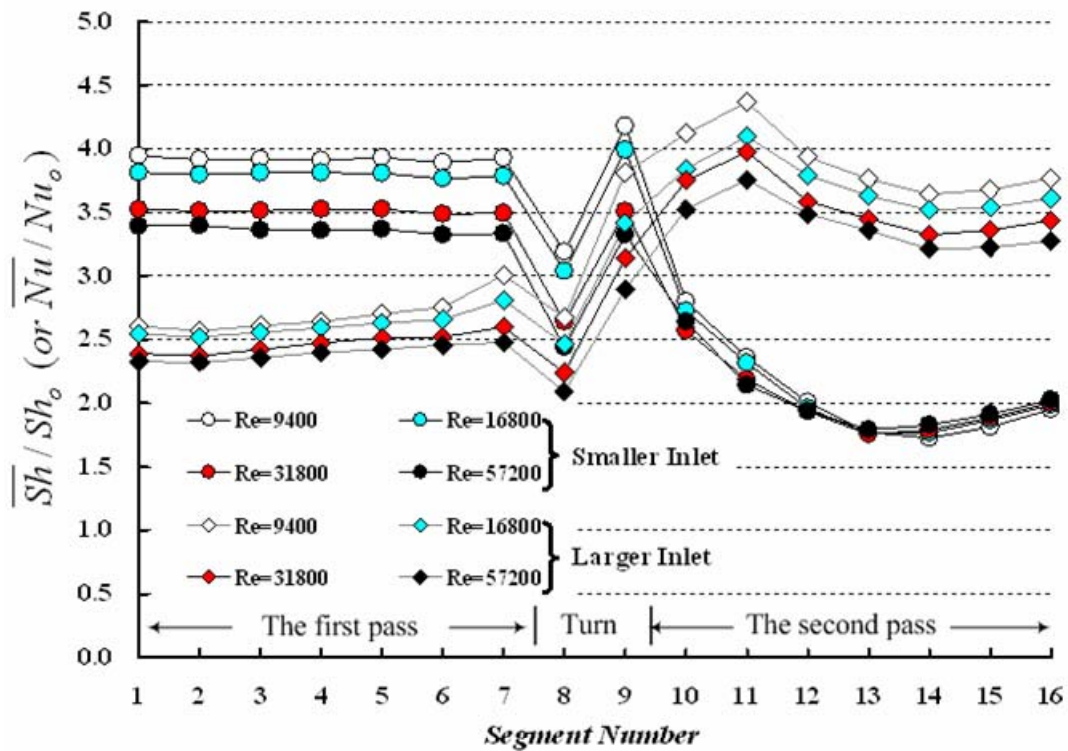
Fig. 8.16 Segmental average mass transfer distributions along the trapezoidal channel

with (−) 60º ribs

Fig. 8.16 shows the streamwise distributions of the regional average Sherwood

number ratios ($\overline{Sh}/Sh_0$) along the trapezoidal channel for air flow entering the smaller

straight section and those for air flow entering the larger straight section. It is clear that the greatest mass transfer enhancement occurred at the lowest Reynolds number of 9,400. As the Reynolds number increased, the Sherwood number ratios decreased. The general trends of Sherwood number ratios were similar for all four Reynolds numbers. For the smaller inlet case, Sherwood number ratios were almost constant before the turn in the first passage since the angled rib-induced secondary flow near the bottom wall was developed and became strong along the channel. The $\overline{Sh}/Sh_0$ value was abruptly dropped on wall segment no.8 since much less impingements onto the end wall. Usually in the turn region, mass transfer enhancement is high since the flow impinges on the end wall and is deflected onto the bottom wall near end wall. However, the secondary flow induced by the ribs interrupted the main flow and the less impingement occurred on the end wall. Moreover, the secondary flow was distorted by the turn effects and it did not impinge on the bottom wall in the turn. On wall segment no.9 in the turn in the second passage, the $\overline{Sh}/Sh_0$ value was highest due to the secondary flow impingements induced by the turn. In the second passage, after the turn, mass transfer enhancement abruptly decreased due to the lower magnitude of the flow velocity. After that, the $\overline{Sh}/Sh_0$ value gradually decreased. However, from the wall segment no.13, the $\overline{Sh}/Sh_0$ value was slightly increasing by developing the secondary flow induced by the angled ribs. For the larger inlet case, unlike the smaller inlet case, Sherwood number ratios gradually increased before the turn in the first passage. The reason was that the secondary flow induced by the ribs was growing near the bottom along the streamwise direction of the

channel and the flow was already fully developed. It is clear that the mass transfer was the highest downstream of the turn, as the flow that left the turn with very high turbulence entered the smaller exit section. The highest mass transfer enhancement occurred on wall segment no.11. After that, Sherwood number ratios gradually decreased since the turning effects were diminished. However, from the wall segment no.14, the $\overline{Sh}/Sh_0$ value was slightly increasing by developing the secondary flow induced by the angled ribs.

The Reynolds stress model (RSM) showed well flow field and heat transfer distribution. However, when the comparison between the numerical prediction and measured regional average were considered, the prediction can not agree well with the experimental data (Fig.8.3). The RSM underpredicted heat (mass) transfer enhancements for the both cases. The maximum relative error was 27.3% and the average relative error was 16.6% for the smaller inlet case. The relative error is defined by normalizing the difference between the experimental and numerical values with respect to the experimental value. The maximum relative error was 26.6% and the average relative error was 20.8% for the larger inlet case.

CHAPTER IX

FLOW AND HEAT TRANSFER IN A TWO-PASS TRAPEZOIDAL CHANNEL

WITH 60° V-SHAPED RIBS ON TWO OPPOSITE WALLS

In chapter IX, an experimental study was performed to measure the regionally averaged heat (mass) transfer in a two-pass trapezoidal channel with 60° V-shaped ribs on two opposite walls by Naphthalene sublimation technique and an numerical study also was performed using the Reynolds stress model (RSM) with enhanced wall treatment in FLUENT.

9.1 Description of Problem

Figure 9.1 & 9.2 show the experimental test section and the numerical grids for the two-pass trapezoidal channel with 60° V-shaped ribs on two opposite walls. The simulated geometry was the same as the experimental geometry. For the numerical study, only bottom wall except the ribs was heated to a constant temperature since the mass transfer experiment can simulate uniform wall temperature boundary condition. The top and bottom walls were roughened by thirty equally-spaced 60° V-shaped ribs and one 90° rib in the turn region. Therefore, the total of sixty 60° V-shaped ribs and two 90° ribs was attached on the top and bottom walls in parallel sequence so that they were directly opposite each other. The 60° V-shaped ribs point upstream of the main flow direction both in the first and second passage. These ribs were 3.2 mm by 3.2 mm square

stripes of balsa wood and rib-to-rib spacing was 3.81 cm. Thus, the rib height-to-hydraulic diameter ratio (e/ $D_{h,turn}$) was 0.07, and the rib pitch-to-rib height ratio (P/e) was 12. The regional average mass transfer experiment was conducted with Re = 9,400, 16,800, 31,800 and 57,200 but the Reynolds number was fixed at 31,800 for the numerical study.

9.2 Grid Independence Study

Fig. 9.2 gives the numerical grid generated using Gambit for this simulation. The grid independent study was made by performing the simulations for three different cross sectional grids of $34 \times 62 \times 640$, $44 \times 72 \times 640$ and $54 \times 82 \times 640$, and one streamwise $44 \times 72 \times 740$ grid with mesh refined in the near wall regions (Fig. 9.2). For the smaller inlet case (Fig. 9.3(a)), a comparison between $34 \times 62 \times 640$ and $44 \times 72 \times 640$ grid points showed 7.2% maximum changes in the Nusselt number ratio. The maximum difference in Nusselt number ratio was less than 1.2% between $44 \times 72 \times 640$ and $54 \times 82 \times 640$ grid points. For the larger inlet case (Fig. 9.3(b)), a comparison between $34 \times 62 \times 640$ and $44 \times 72 \times 640$ grid points showed 6.4% maximum changes in the Nusselt number ratio. The maximum difference in Nusselt number ratio was less than 2.0% between $44 \times 72 \times 640$ and $54 \times 82 \times 640$ grid points. Further increase of the number of grid points in streamwise direction of the channel produced only minor changes of the Nusselt number ratios for the both cases.

Fig. 9.1 Geometry for trapezoidal channel with 60° V-shaped ribs

30.5 cm   30.5 cm

Bottom

Naphthalene Surfaces

Rib

Top

3.81 cm, *P/e*=12

2.2 cm

60°
60°   3.81 cm

3.2 mm

3.2 mm

$e/D_{h, turn}$=0.07
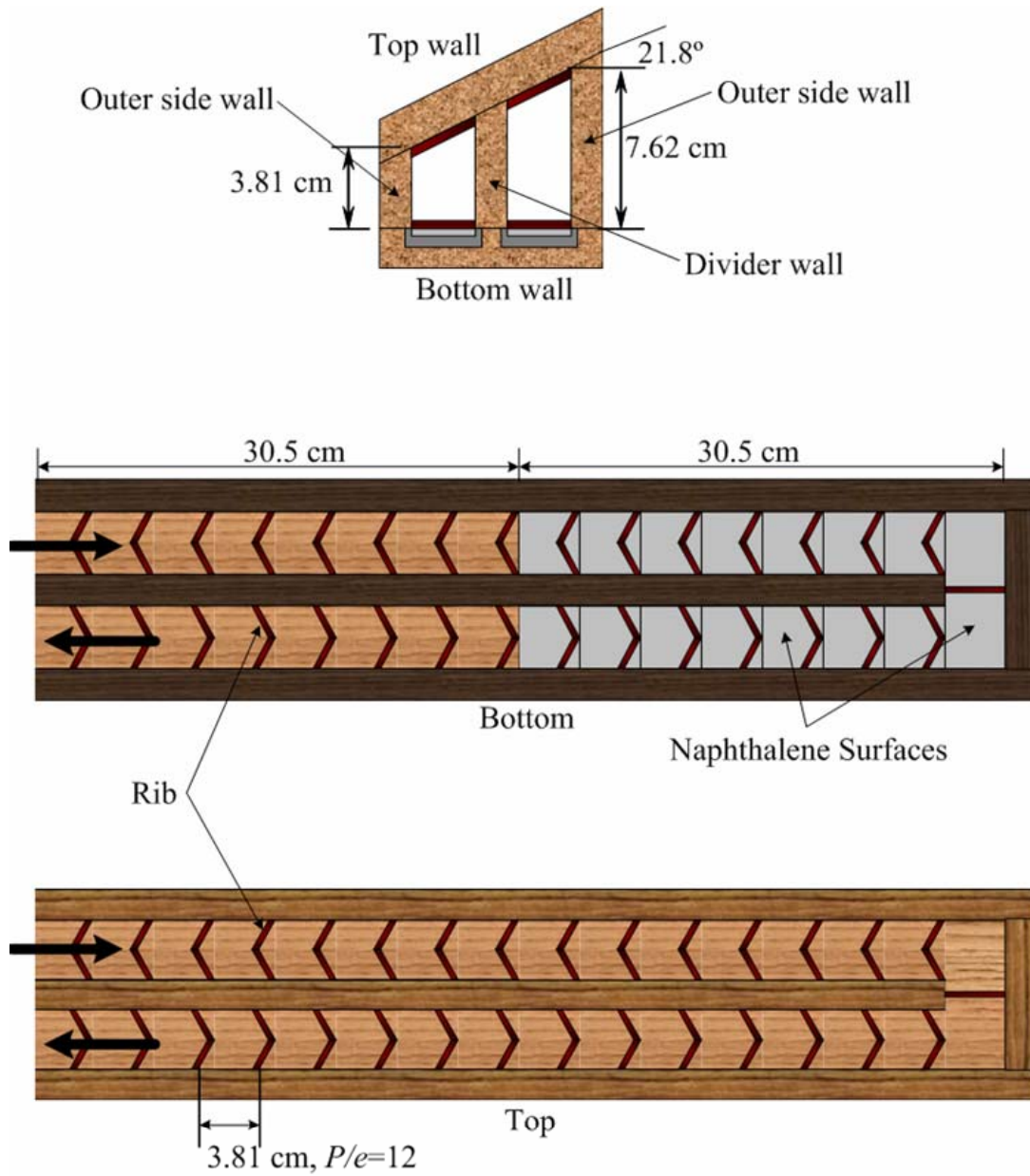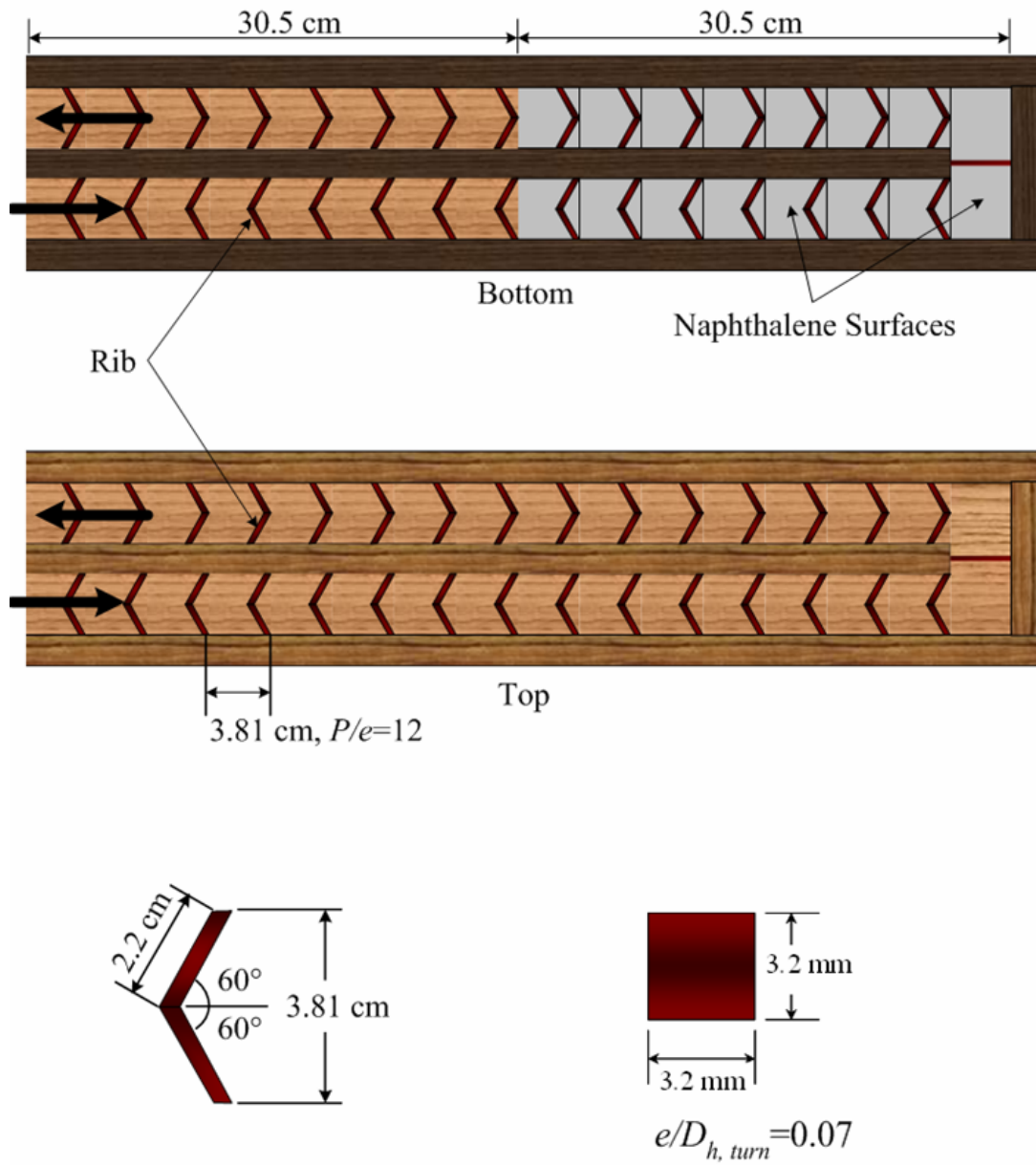
Fig. 9.1 (continued)
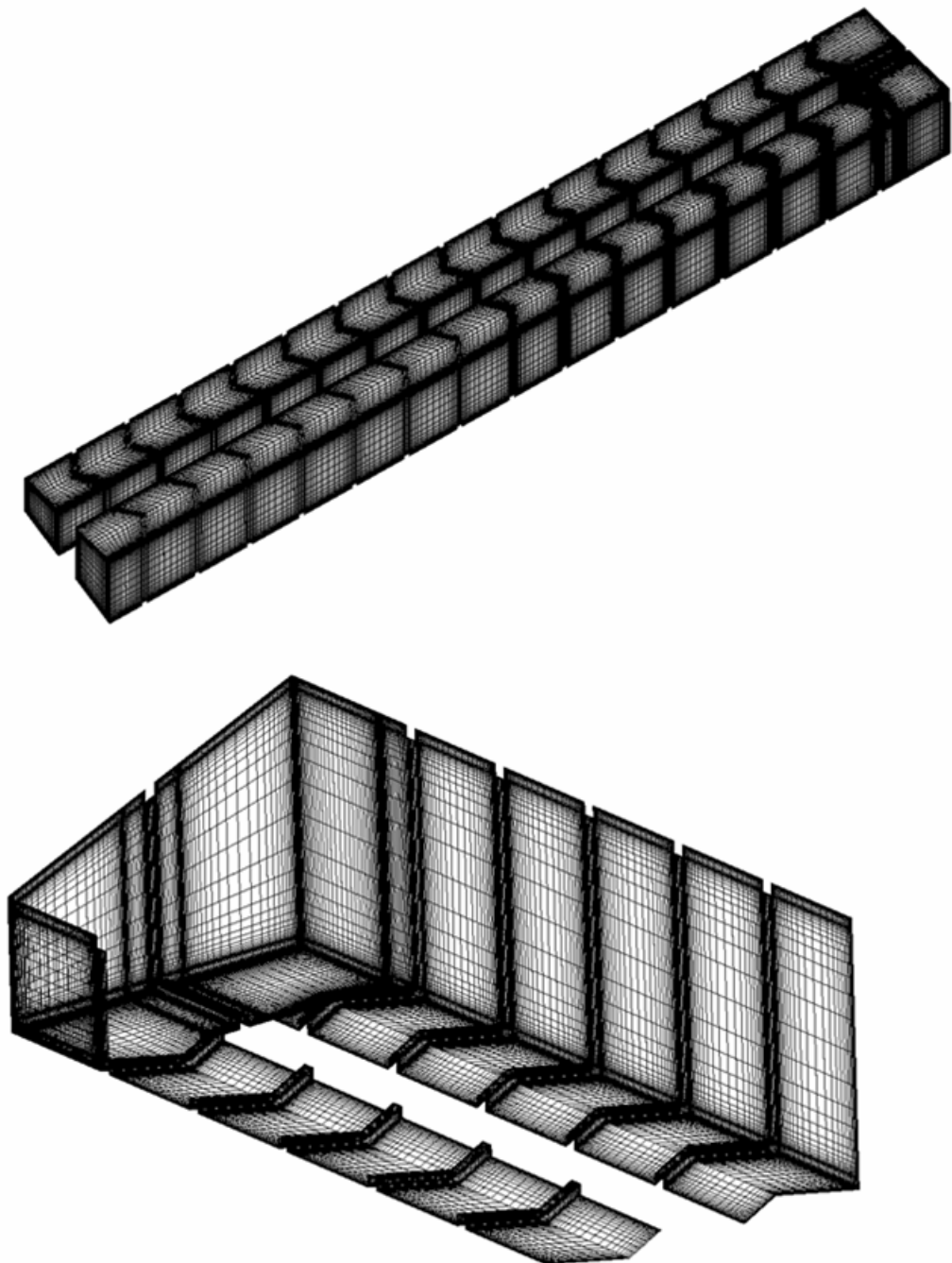
Fig. 9.2 Numerical grid for trapezoidal channel with 60° V-shaped ribs
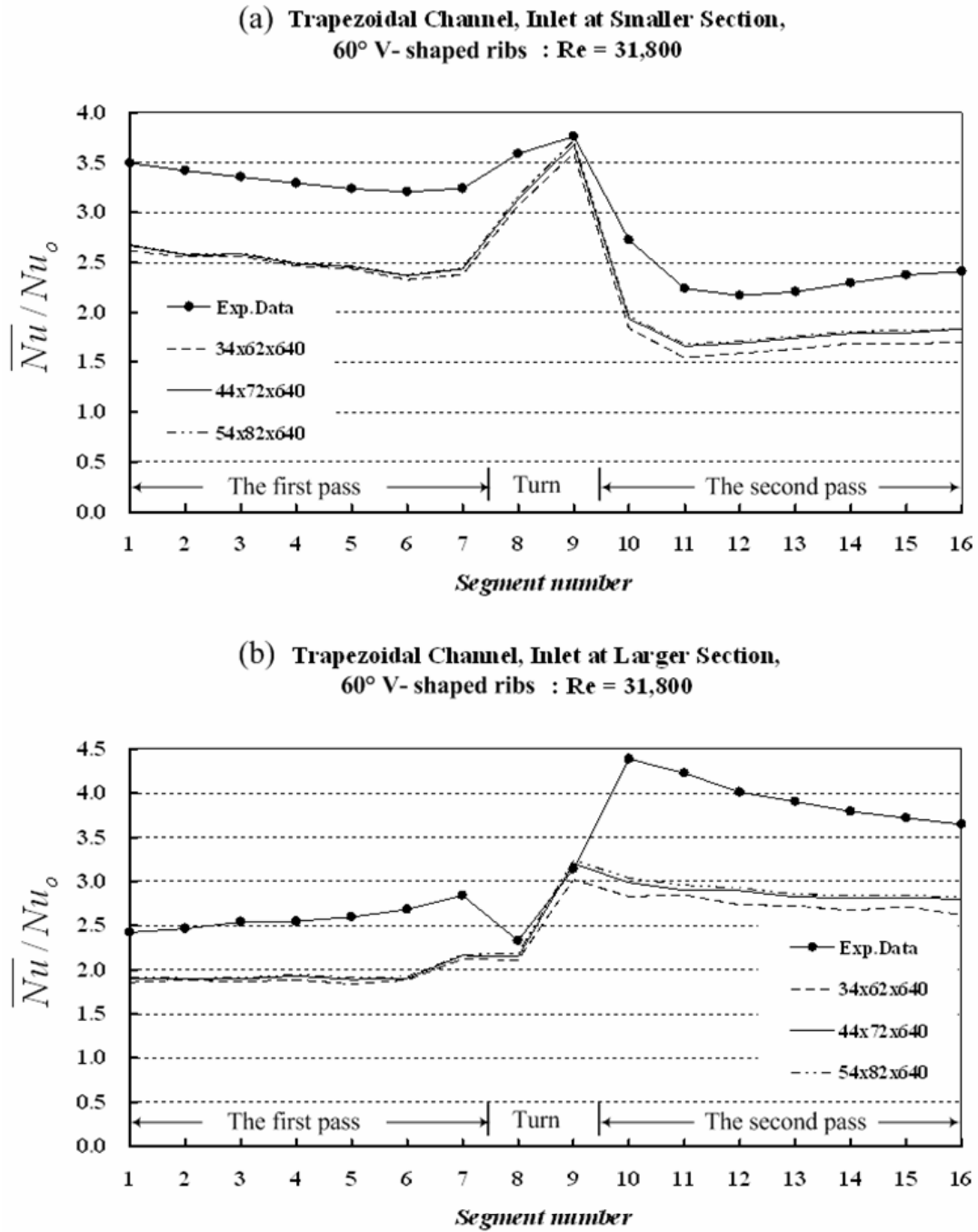
Fig. 9.3 Grid independent study for trapezoidal channel with 60° V-shaped ribs

Therefore, it was determined that grid independence was achieved with $44 \times 72 \times 640$ grid points and all results were based on the $44 \times 72 \times 640$ grid points, which resulted in 2,027,520 grid points for both the smaller inlet and larger inlet cases. The y^+ values were less than unity in all test runs of grid independent study.

9.3 Velocity Fields

In the near ribbed surfaces (Fig. 9.4), the flow in the center of the channel approached the V-shaped ribs first and the flow separated into two streams since the ribs were oriented at a 60° angle pointing upstream of the main flow direction. Each flow moved almost parallel to the ribs from the centerline to the outer and inner (divider) walls which were side walls. In addition, the 60° V-shaped ribs created four counter-rotating vortices parallel to the ribs. Due to the existence of the outer and inner wall, each separated flow along the ribs hit the wall and returned to the centerline making a counter-rotating vortex. Since the 60° V-shaped rib was half of the 60° angled rib, the boundary layer thickness for the flow that moves parallel to one side of the 60° V-shaped rib was thinner than that produced by the 60° angled rib. Therefore, higher heat transfer enhancements were expected compared to the 60° angled rib since the 60° V- shaped rib produced four counter-rotating vortices that promoting more mixing in the core main stream and simultaneously produced thinner boundary layer near the heated wall. Because the ribs periodically interrupt the boundary layers of the flow, the repeated flow separations behind the ribs and reattachment between the ribs in the streamwise direction
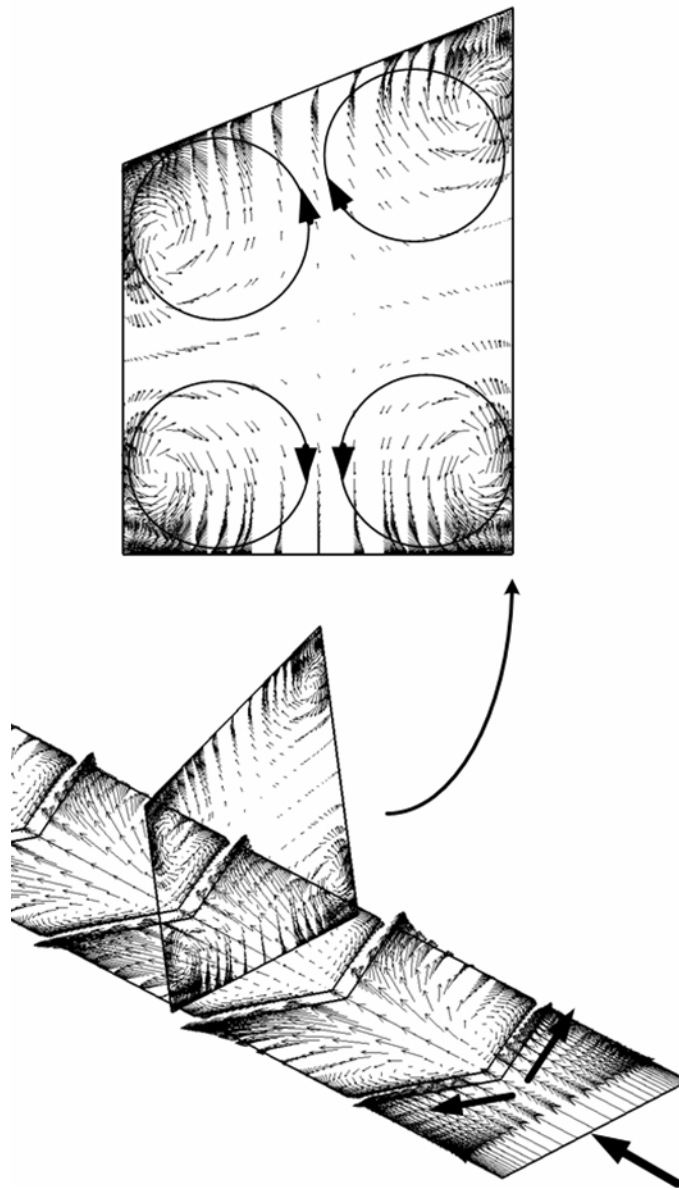
Fig. 9.4 Secondary flow vortices induced by 60° V-shaped ribs
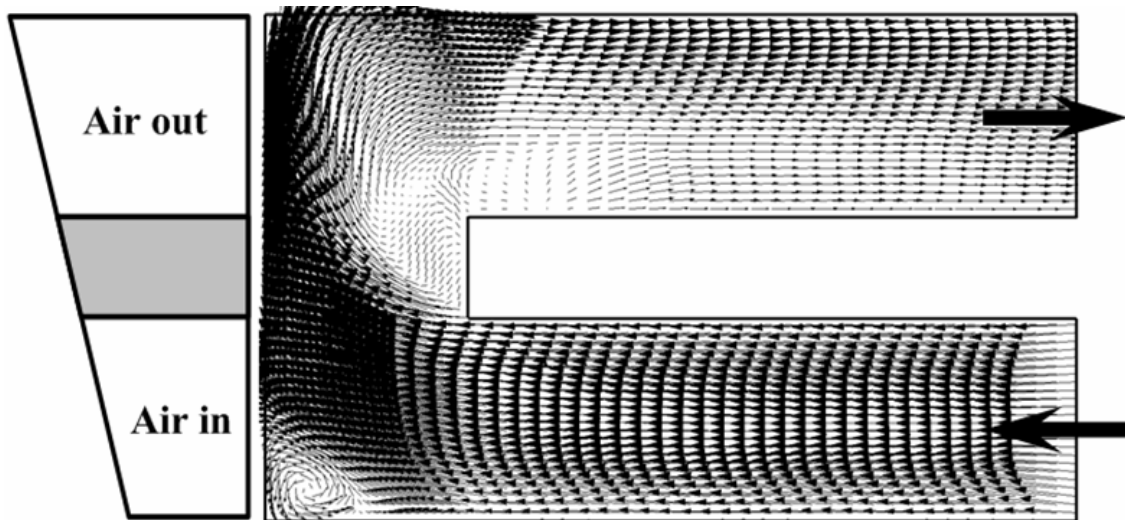
(a) Streamwise velocity vector for inlet at smaller section
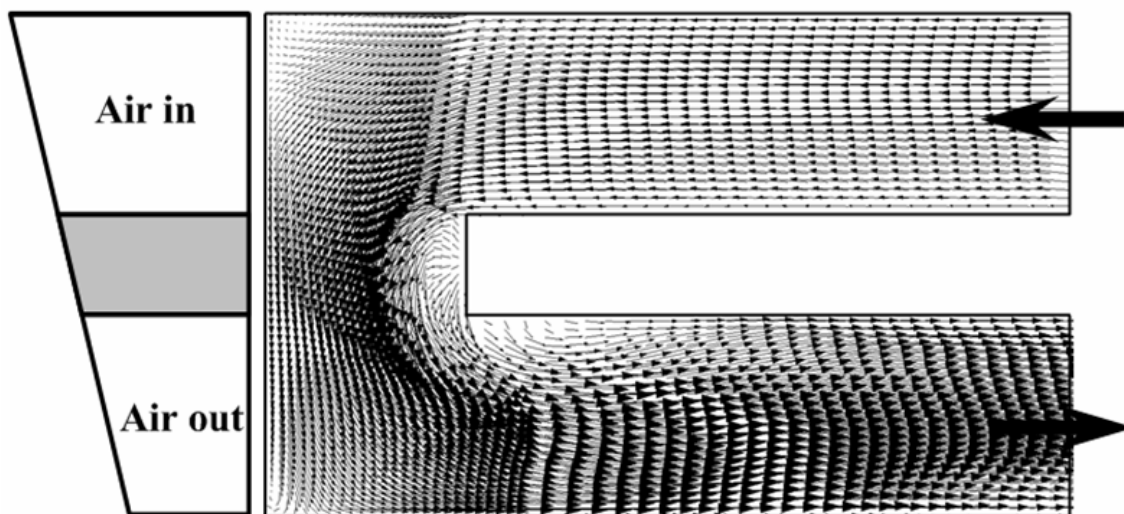
(b) Streamwise velocity vector for inlet at larger section

Fig. 9.5 Streamwise velocity vector midway between the top and bottom walls with

60° V-shaped ribs

were observed. In the center of the channel, the flows beyond the ribs and directing to ribbed surfaces to reattach were intense and these flows became weaker near outer and inner wall. In the square and rectangular channel, the walls are symmetric and two pairs of symmetric counter-rotating vortices are created. However, in the trapezoidal channel, the walls are not symmetric and all four vortices have different sizes and the strength.

Fig. 9.5 shows the streamwise velocity vector distributions at the mid-plane between the top and bottom walls with 60° V-shaped ribs at Re = 31,800 for inlet at smaller cross section and for inlet at larger cross section. For the inlet at the smaller cross section (Fig. 9.5(a)), the velocity profiles were flat before the turn. As the flow approached the turn region, flow accelerations occurred near the divider wall and a flow deceleration occurred near the outer wall due to the favorable and adverse pressure gradients along the divider and outer wall, respectively. Flow deceleration took place at the outer wall and was followed by flow separation, which results in a zone of recirculating flow in the upstream corner in the first passage. There were no separation bubbles near the divider wall tip in the turn region. However, large bifurcating zone existed near the divider wall in the second passage. For the inlet at the larger cross section (Fig. 9.5(b)), the flow had a similar pattern but bifurcating zone was smaller. Because the flow was accelerated by decreasing cross area through the turn, the streamwise velocity was much faster than the vertical velocity. In both case, there were weak flow impingements onto the end and outer wall due to the combined effects of the secondary flow induced by V-shaped ribs and the presence of the 90° ribs in the turn. Fig. 9.6, 9.7, 9.8 and 9.9 show streamwise velocity and turbulence intensity in the planes

midway between the inner (divider) and outer walls with 60° V-shaped ribs at Re = 31,800 for inlet at smaller cross section and for inlet at larger cross section. As the flow near the top and bottom wall passes over the ribs, the flow separates from the walls. This separation results in relatively low heat transfer, due to a relatively hot cell being trapped in the recirculation. However, when the flow reattaches to the wall between the ribs, this is an area of relatively high heat transfer. This pattern of separation and recirculation continues through the channel with a pattern of repeating 60° V-shaped ribs. Like the 60° ribs, the reversal flow occurred immediately behind the ribs on the both the top and bottom wall. However, there were no separations in immediately upstream of the ribs. For the smaller inlet case (Fig.9.6), in the center of the channel, the flows beyond the ribs and directing to ribbed surfaces to reattach were intense and these flows became weaker near outer and inner wall. In the turn, one large vortex occurred near the bottom, and a small vortex was observed near the top wall like the 60° ribs. It was also observed that the magnitude of the flow velocity over the ribs near the top wall was larger than that near the bottom wall. The reason was that the secondary flows induced by the ribs near the top wall were stronger than that near the bottom wall. Fig. 9.6(b) shows the turbulence intensity distributions in the first passage for the smaller inlet case. The turbulence intensities were as high as 28% immediately downstream of the ribs on the top wall and 25% immediately downstream of the ribs on the bottom wall, and diminished gradually toward the center of the channel around 10%. The highest turbulence intensity was 35% immediately downstream of the rib on the top wall just before the turn. Near the end wall the turbulence intensity was relatively low about 33%
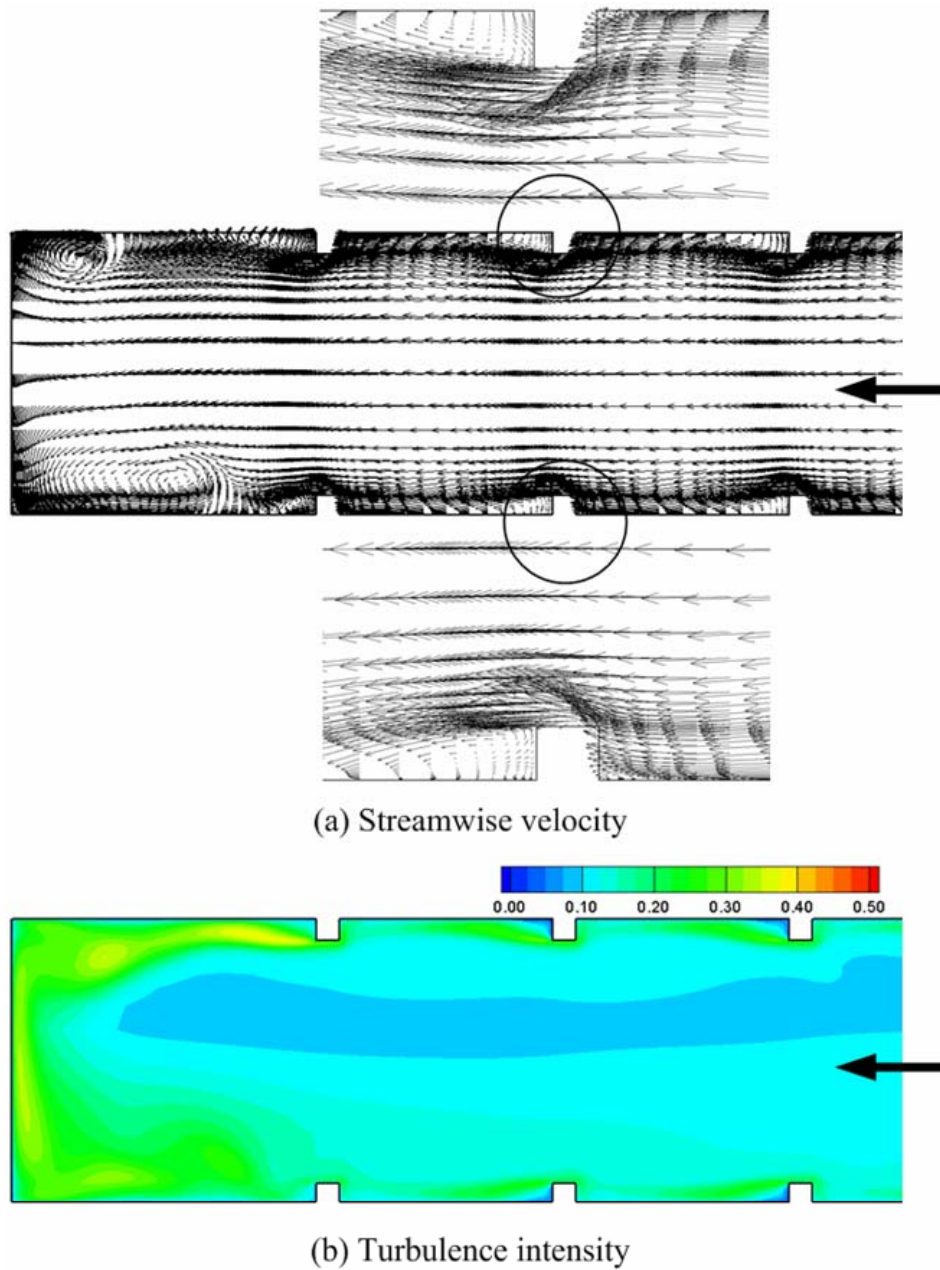
(a) Streamwise velocity

(b) Turbulence intensity

Fig. 9.6 Streamwise velocity and turbulence intensity midway between the inner and

outer walls with 60° V-shape ribs in the first passage for inlet at smaller cross section

(a) Streamwise velocity

(b) Turbulence intensity
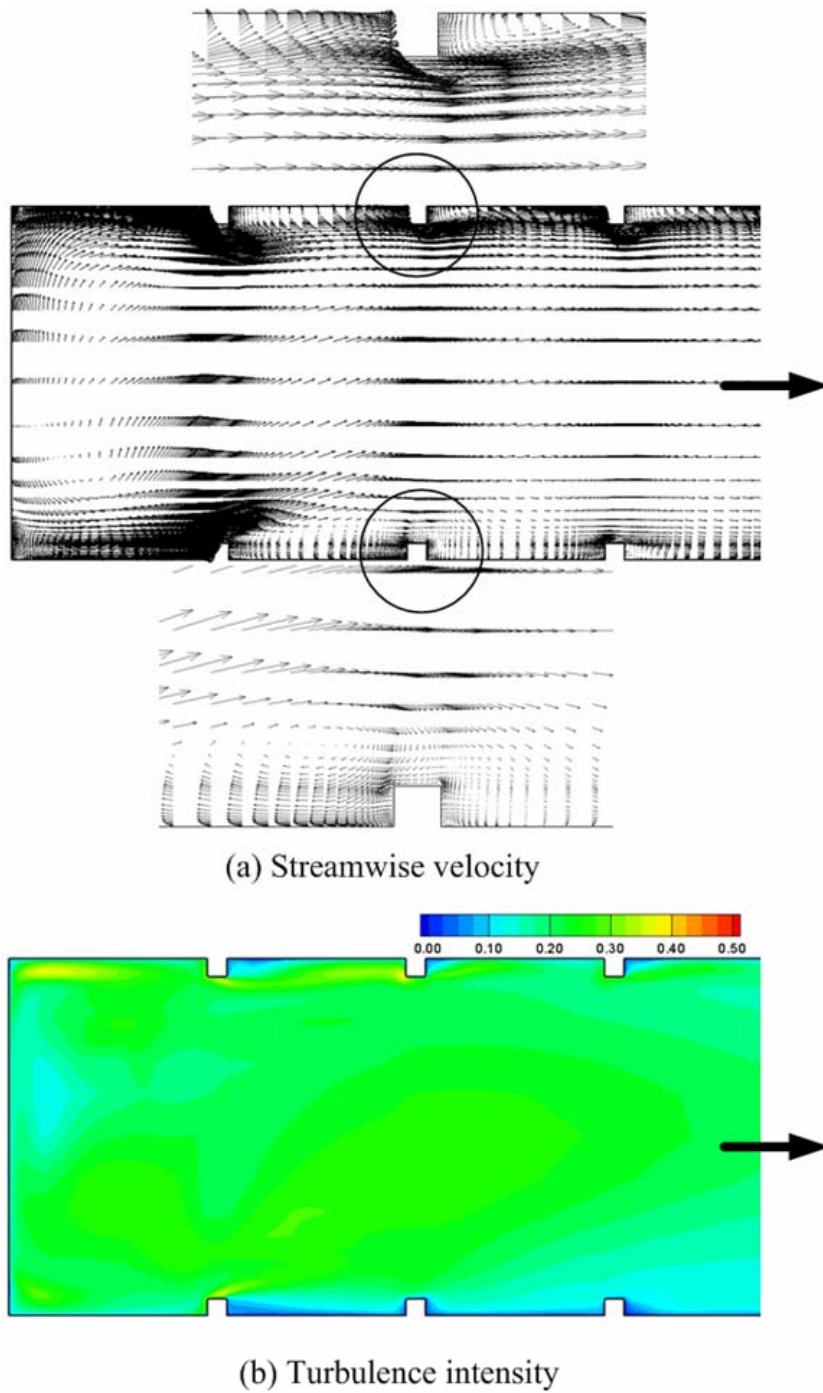
Fig. 9.7 Streamwise velocity and turbulence intensity midway between the inner and

outer walls with 60° V-shape ribs in the second passage for inlet at smaller cross section
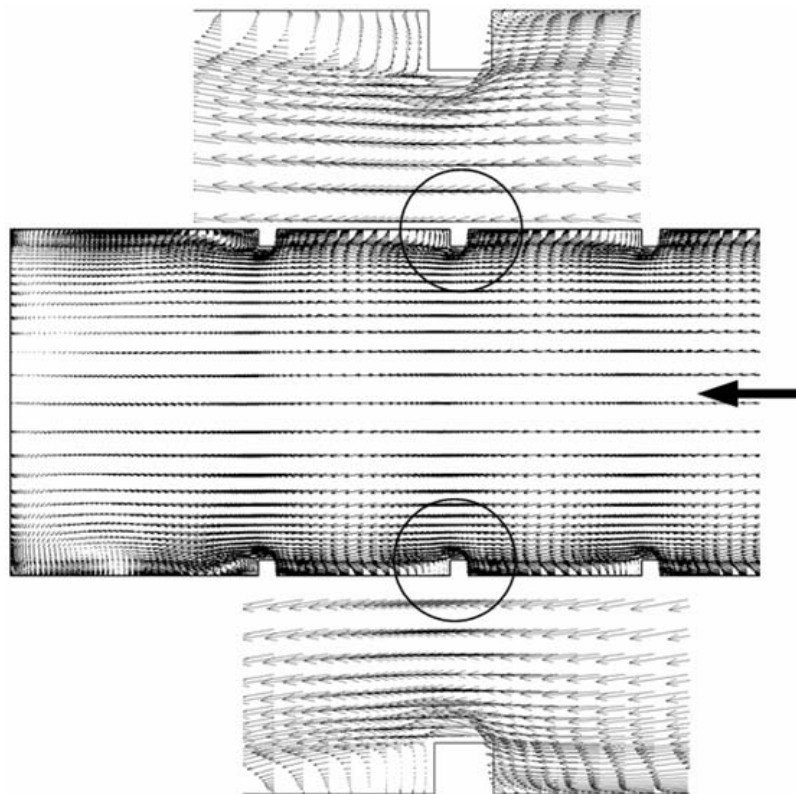
(a) Streamwise velocity
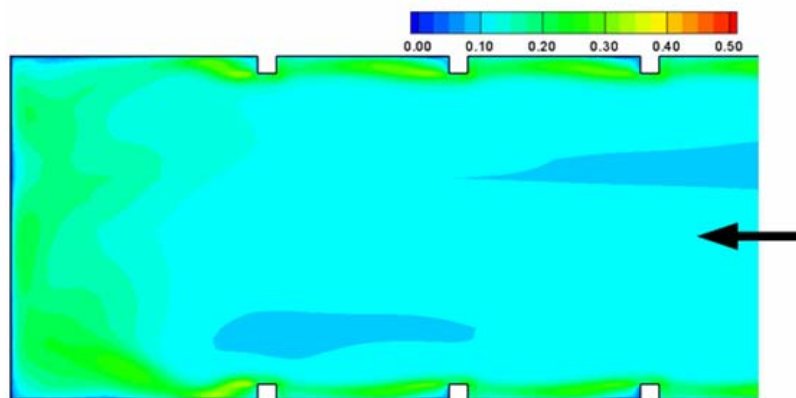
(b) Turbulence intensity

Fig. 9.8 Streamwise velocity and turbulence intensity midway between the inner and

outer walls with 60° V-shape ribs in the first passage for inlet at larger cross section
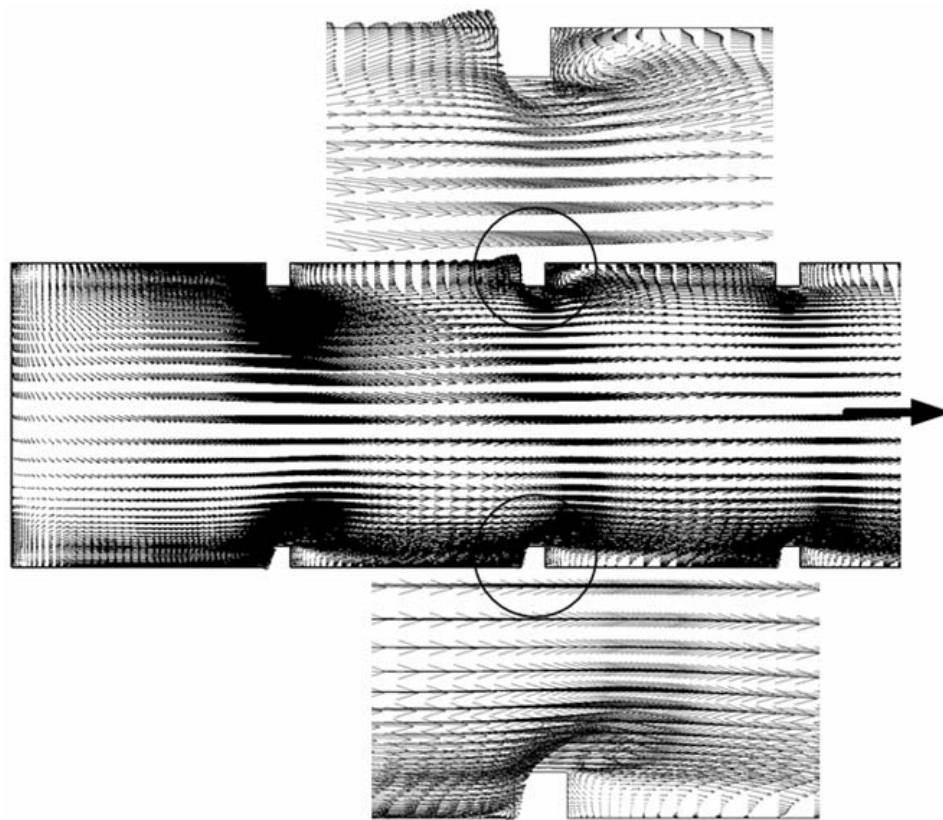
(a) Streamwise velocity
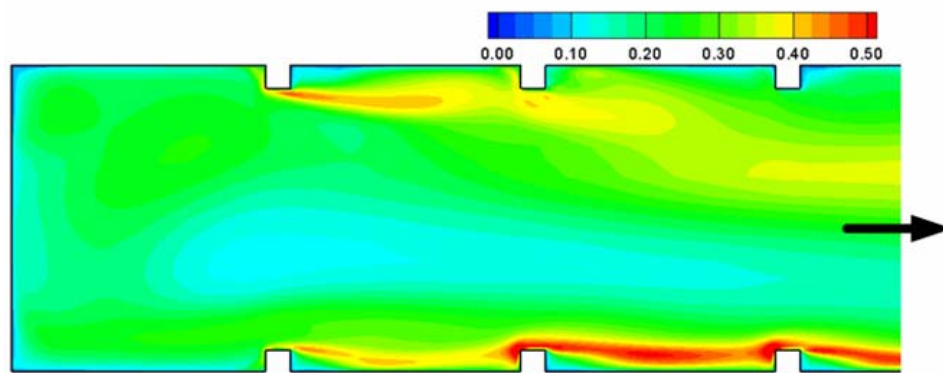
(b) Turbulence intensity

Fig. 9.9 Streamwise velocity and turbulence intensity midway between the inner and outer walls with 60° V-shape ribs in the second passage for inlet at larger cross section

due to less flow impingement. Due to the same reason mentioned above, the higher turbulence intensity occurred near the top wall. Fig 9.7 shows the streamwise velocity and turbulence intensity in the second passage in the planes midway between the inner and outer wall for inlet at smaller cross section. Through the turn, the flow was decelerated due to increase of the cross section area. Since the velocity magnitude and rib height-to-hydraulic diameter ratio (e/ $D_{h,large}$) were smaller than those in the first passage, the effects of the angled ribs were much less. After the turn, there no flow reattachments between ribs due to a large flow separation on the rib just after the turn (Fig. 9.7(a)). The main flow was deflected toward the top wall and then a strong flow impingement occurred on the top wall. However, the turbulence intensity had low values in the second passage. The turbulence intensities were as high as 24% immediately downstream of the ribs on the top wall and 14% immediately downstream of the ribs on the bottom wall.

Figure 9.8 and 9.9 show streamwise velocity and turbulence intensity for the larger inlet case. Since the velocity magnitude and rib height-to-hydraulic diameter ratio (e/ $D_{h,large}$) were smaller than those of the smaller inlet case, the effects of the ribs were much less. In the turn, two small vortices occurred near the bottom and the top wall due to weak impingements. Unlike the smaller inlet case, the flow over the ribs near the bottom and top wall was had almost same magnitude of the velocity due to weak secondary flow induced by the ribs. The turbulence intensities were as high as 27% immediately downstream of the ribs on the bottom wall and 28% immediately downstream of the ribs on the top wall, and diminished gradually toward the center of

the channel around 10% (Fig. 9.8(b)). In the second passage, after the turn, the strong flow impingement occurred on the bottom walls unlike the smaller inlet case. As the flow goes through the turn, the flow is accelerated by decreasing the cross section area. Therefore, a larger momentum of the flow from the larger inlet makes the strong flow impingements on the walls and increases turbulence intensities in the second passage of the channel. The level of turbulence intensity was about 50% near the bottom wall. Near the top wall 46% turbulence intensity only on the rib just after the turn was observed and further downstream turbulence intensity level decreased to 26%. The highest turbulence intensity was 59% on upstream of the second rib on the bottom wall just after the turn due to the strong flow impingement.

9.4 Secondary Flow Development

To better understand the complex three-dimensional flow fields in the trapezoidal channel with 60° V-shaped ribs, the secondary flow was presented here. Fig 9.11 shows the secondary flow vectors before the heating section in the first passage for the smaller inlet case. Fig. 9.12, 9.13, 9.14 and 9.15 show the secondary flow vectors at selected planes as denoted in Fig. 9.10. The secondary flow vectors of Fig. 9.11, 9.12 and 9.14 were viewed from the inlet, while the secondary flow vectors of Fig. 9.13 and 9.15 were viewed from the outlet. As mentioned earlier, 60° V ribs induced the fast secondary flow that moves parallel to the ribs from the center of the channel to two side walls. Due to the existence of the outer and inner wall, each separated flow along the ribs hit the wall

and returned to the centerline making a counter-rotating vortex. Therefore, four counter-rotating vortices are induced by the 60° V rib. In the center of the channel, the secondary flows are strong and these flows become weaker near the two side walls. From the Fig. 9.11, near the inlet, four vortices were almost same in the size and strength. One can notice that along the streamwise direction, the upper and left side vortex, and lower and right side vortex became stronger and bigger, while other two vortices became weaker and smaller since the magnitude of the vertical component velocity of those secondary flow was bigger than that of other two vortices due to the characteristics of the trapezoidal cross section. Near the heating section, the stronger and bigger two vortices became one large vortex extended diagonally, and the direction of the rotation was counterclockwise. For the smaller inlet case (Fig. 9.12 & 13), one can clearly see that the ribs induced three counter-rotating vortices that impinge on the top and bottom wall in the first passage (Fig. 9.12). One can also notice that along the streamwise direction, the size of two vortices oscillated from the largest in the middle of each inter-rib distance to the smallest on the ribs like the angled ribs. In the turn region (Fig. 9.12(4)), two counter-rotating vortices were observed, and the vortex on the bottom rib was larger and stronger than that on the top wall, which was distorted by the combined effects of centrifugal induced vortex and rib-induced vortex upstream. Along the tip of the divider wall, the magnitudes of vertical velocity were very high. In the second passage (Fig. 9.13), one large counterclockwise rotating vortex occupied almost entire cross area and smaller clockwise rotating vortex was seen near upper and right side (Fig. 9.13(6)). The velocity magnitudes were not high compared to those in the first passage because the
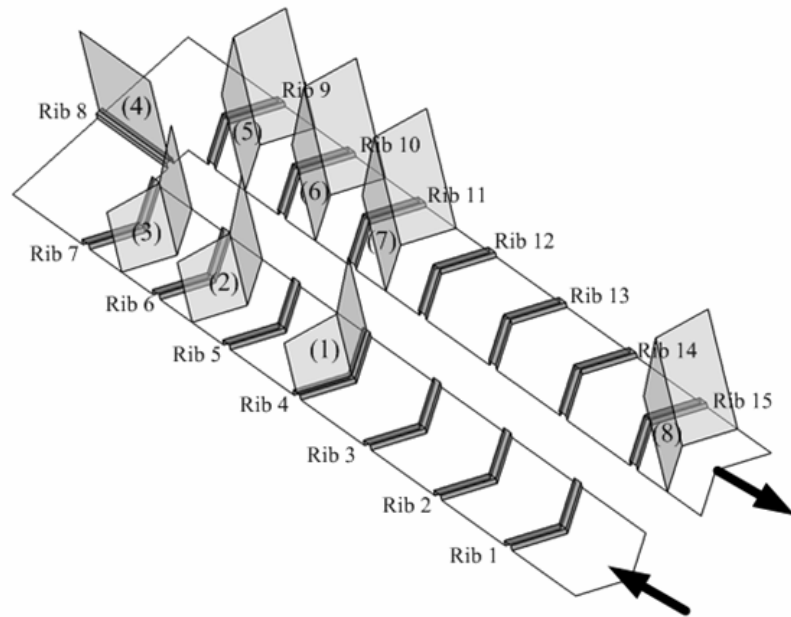
(a) Secondary flow location for smaller inlet
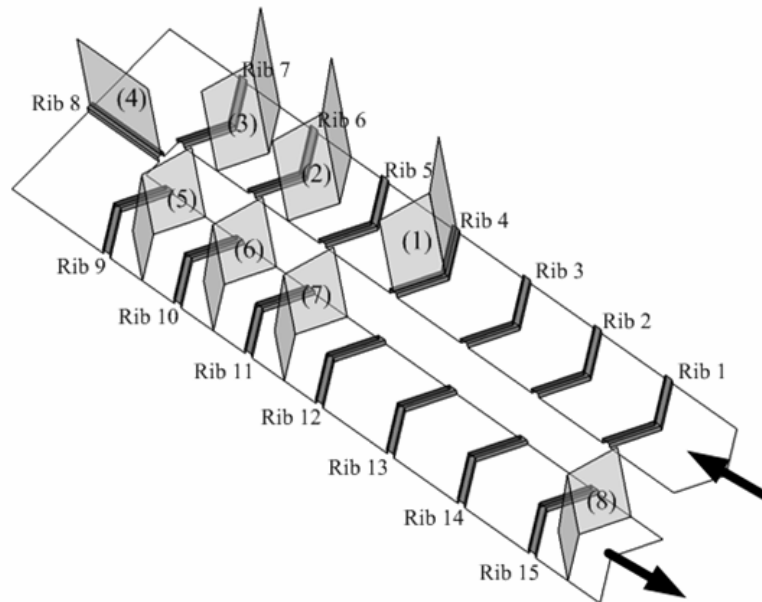
(b) Secondary flow location for larger inlet

Fig. 9.10 Secondary flow locations for trapezoidal channel with 60° V-shaped ribs
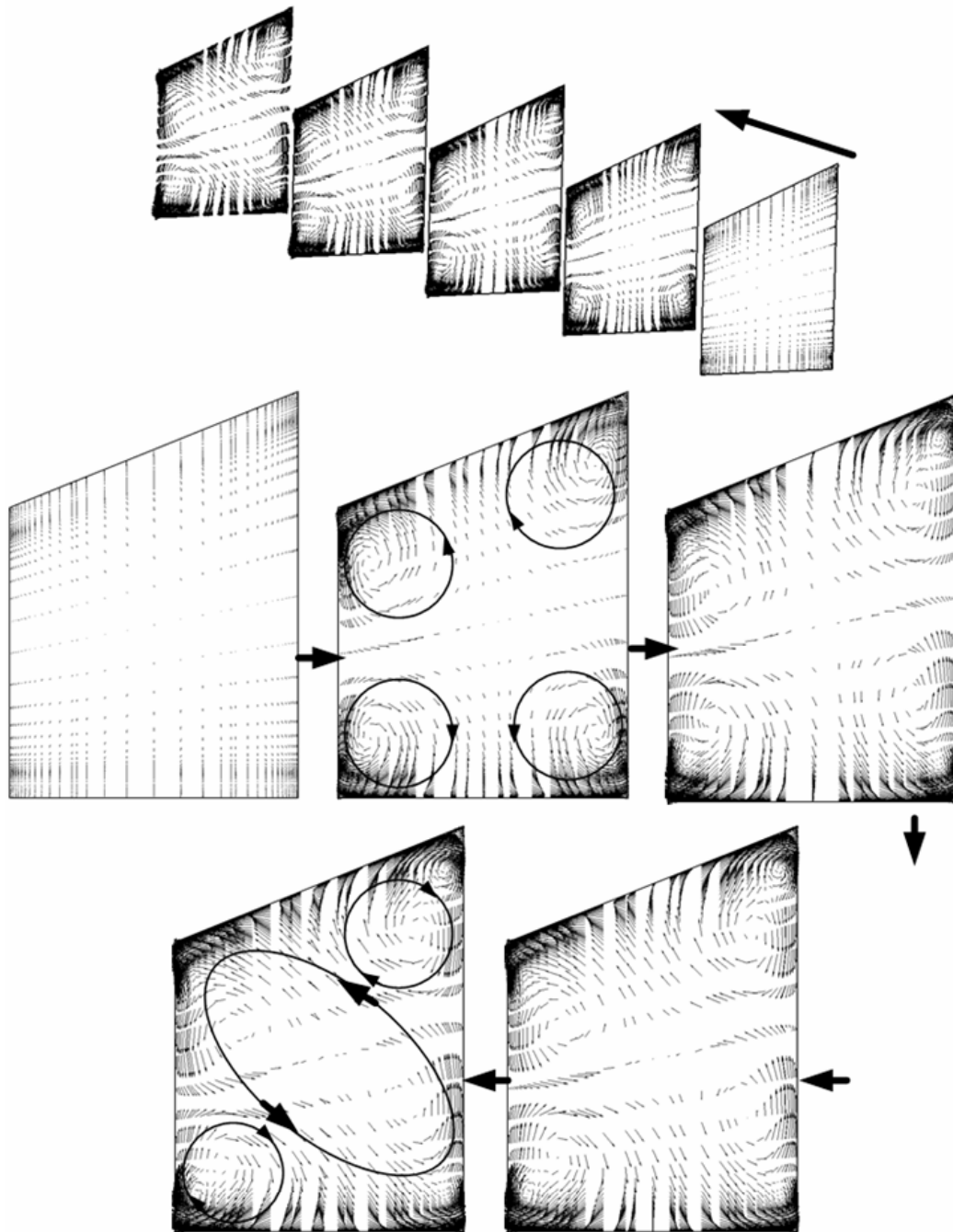
Fig. 9.11 Secondary flow developments on the entrance region of trapezoidal channel

with 60° V-shaped ribs in the first passage for inlet at smaller cross section
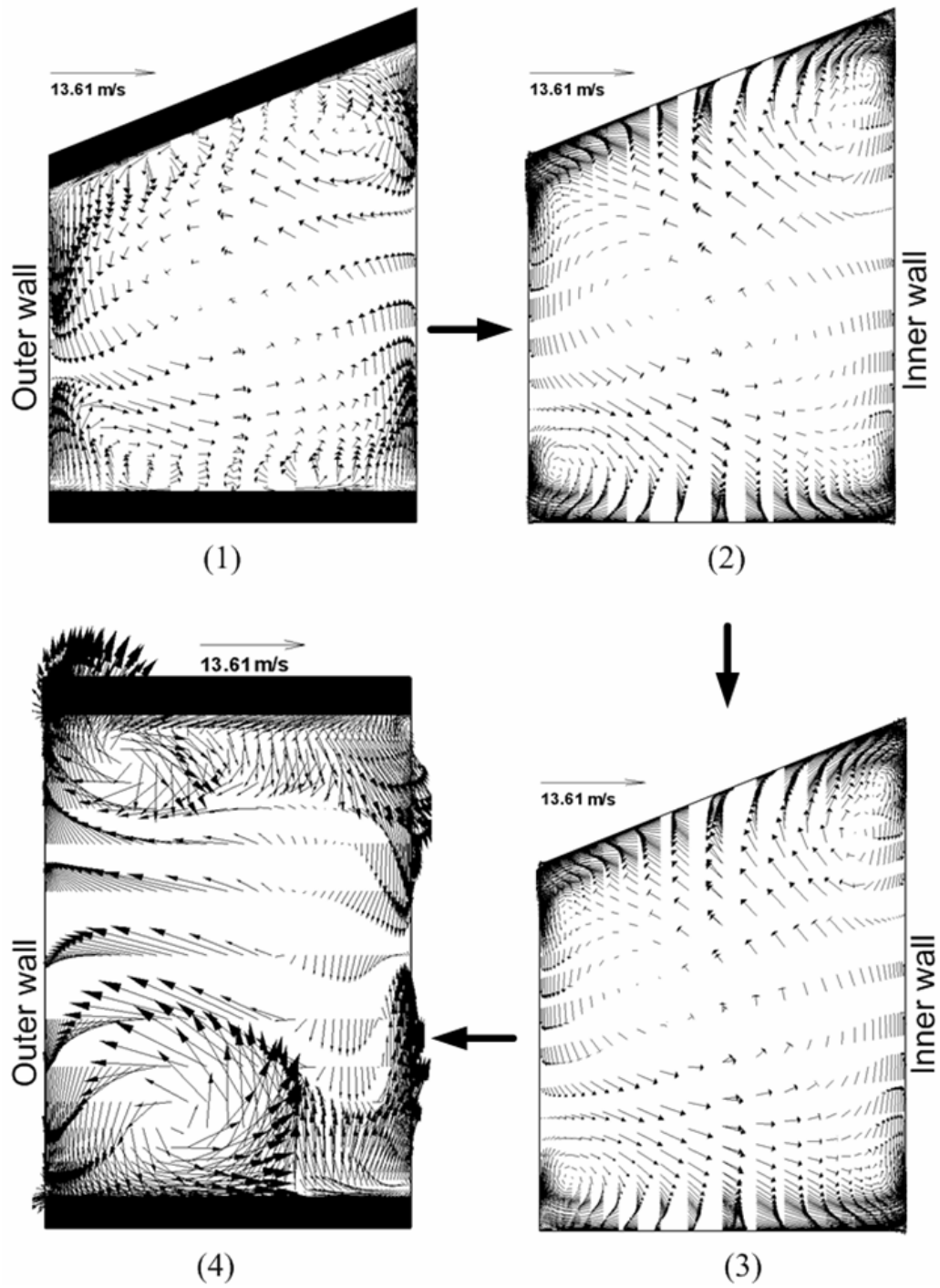
Fig. 9.12 Secondary flow developments of trapezoidal channel with 60° V-shaped ribs

in the first passage for inlet at smaller cross section
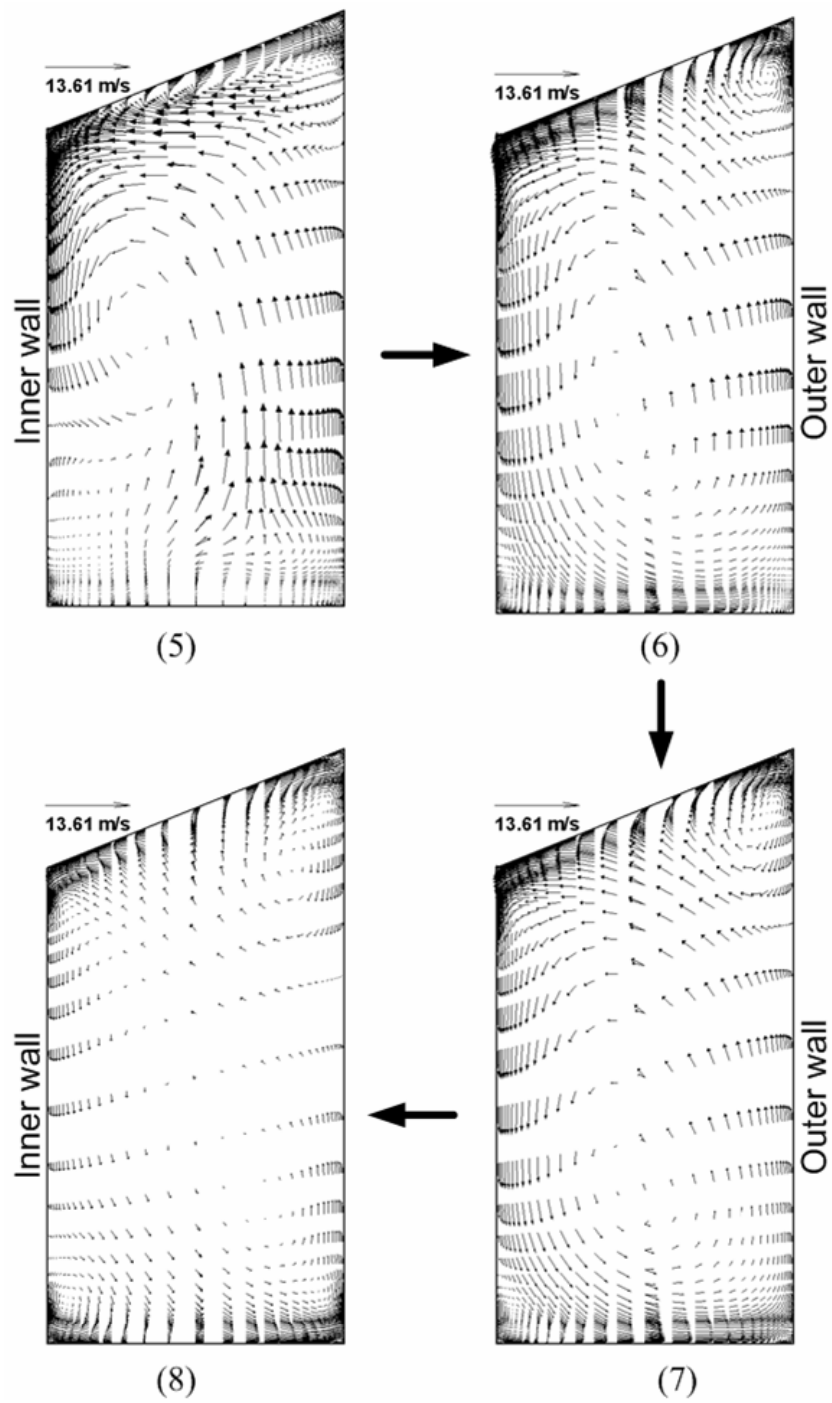
Fig. 9.13 Secondary flow developments of trapezoidal channel with 60° V-shaped ribs

in the second passage for inlet at smaller cross section

flow was decelerated through the turn. In the second passage, the bulk mean velocity was decreased from 13.61 m/s to 9.08 m/s. The rib height-to-hydraulic diameter ratio ($e/D_{h,large}$) was also decreased since the same ribs were installed but channel height was increased. Therefore, the effect of the ribs on the flow of channel was mush less and the secondary flow induced by the turn was dominant in the second passage. Along the inner wall, flow impingements were intense. Therefore, it was expected that neat the inner wall more heat transfer enhancements occur. Near the end of the heating section (Fig. 9.13(8)), as the effect of the turn reduced, the secondary flow induced by the ribs seemed to start to develop, and three counter-rotating vortices were observed like the first passage.

Fig. 9.14 and 9.15 show secondary flow developments for the larger inlet case. Unlike the smaller inlet case, in the first passage (Fig. 9.14) the four vortices induced by the ribs were almost symmetric due to the enough space to maintain rotating shapes. It seemed that four vortices were less interacted with each other due to the enough space. In the turn (Fig. 9.14(4)), a small vortex was observed on the bottom rib and was less strong due to a relatively low velocity from the large cross section. Downward flow from the top wall was strong along the tip of the divider wall. In the second passage (Fig. 9.15), the secondary flow induced by the turn was dominant just after the turn due to the flow acceleration through the decrease of cross sectional area. Therefore, the downward flow along the outer wall was much strong and a large counterclockwise rotating vortex was created (Fig. 9.15(5)). Two small vortices also observed. From the location (6), the vortices induced by the ribs with the relatively high rib height-to-hydraulic diameter
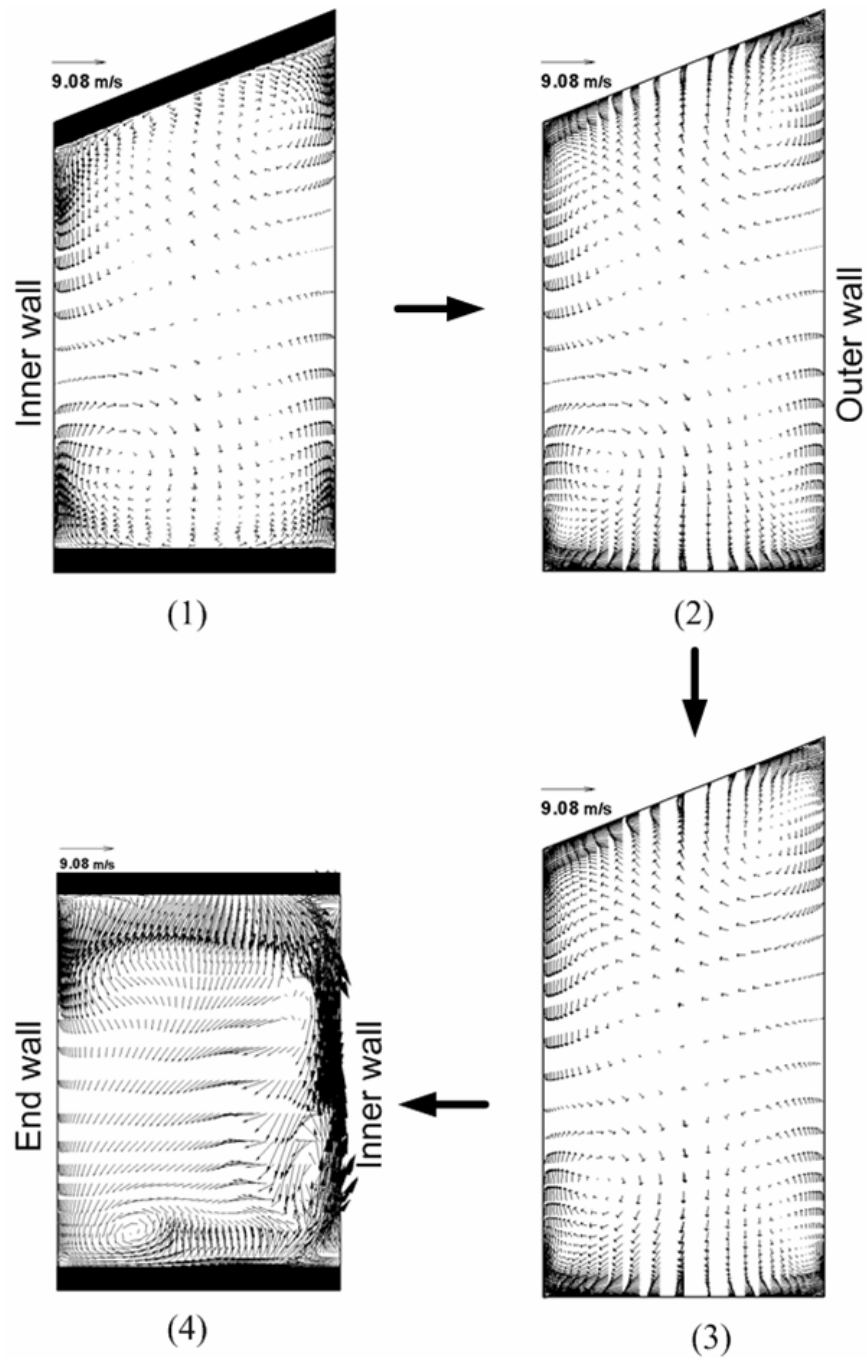
Fig. 9.14 Secondary flow developments of trapezoidal channel with 60° V-shaped ribs

in the first passage for inlet at larger cross section

Fig. 9.15 Secondary flow developments of trapezoidal channel with 60° V-shaped ribs

in the second passage for inlet at larger cross section

ratio (e/ $D_{h,small}$) seemed to start overcome the secondary flow by the turn. Therefore, like in the first passage for smaller inlet case, three vortices were observed near exit of the heating section (Fig. 9.15(8)).

9.5 Heat (Mass) Transfer Distribution

The experiments were conducted to measure the regional average heat (mass) transfer in a two-pass trapezoidal channel with 60° V-shaped ribs on two opposite walls by naphthalene sublimation technique, and the analogy of heat and mass transfer was applied to convert the mass transfer coefficients to heat transfer coefficients. The regional average Sherwood number ratios were determined for four Reynolds numbers of 9,400, 16,800, 31,800 and 57,200. Also the numerical study was performed to compare the experimental results and the numerical predictions at Re = 31,800.

Fig. 9.16 shows calculated Nusselt number ratio distributions by the RSM. V-shaped ribs originated from the concept that angled ribs can act as longitudinal vortex generator and provide heat transfer enhancement. It is assumed that V-shaped ribs can principally double the high heat transfer region and provide even higher heat transfer augmentation. The Nusselt number ratios on the rib roughened wall had a significant spanwise variation, with low levels near the outer and inner walls of the channel, and high levels at the central area where the V-shaped ribs meet. The temperature boundary layer was thin and the heat transfer was high in the downwash regions and low in the upwash region. The longitudinal vortex of the flow guaranties that the heat taken up a

flow particle at the wall is transported away from the wall and downstream. By the time it returns close to the wall, it has been cooled by the bulk temperature and then can again take up heat from the wall. The streamwise distribution of heat transfer can be explained by the flow reattachment and redevelopment. Depending on the downstream distance to the next ribs, the recirculating flow cells developing downstream reattach at the wall, and the flow then commences to develop again. Due to redevelopment of a boundary layer and enhancement of turbulence near this reattachment point, the heat transfer is enhanced. For the smaller inlet case (Fig. 9.16 (a)) in the first passage, heat transfer distributions between ribs appeared periodic because the ribs periodically interrupted the boundary layers on the bottom wall. The secondary flows induced by each angled side of the V-shaped rib moved away from the center of the channel. A high heat transfer enhancement region was obtained along the centerline of the channel. Nusselt number ratios were lower immediately downstream of each rib due to flow separation from the rib. The 90° rib in the turn region produced high heat transfer enhancement immediately downstream of the rib. In the turn region, Nusselt number ratios were very high due to the combination of the 180° sharp turn and the 90° rib. The large vortex impinged on the end wall resulting in the high heat transfer. Due to the presence of the rib and deceleration of the flow, the centrifugal effect was reduced. The contracted but strengthened vortex in the turn region pressed down the separated flow by the rib, causing strong reattachment immediate downstream of the rib in the turn. Unlike smooth wall case, near outer wall in the turn region heat transfer enhancement was mush less because the presence of the 90° rib and the flow deceleration reduced the effect of

$$Nu / Nu_o$$
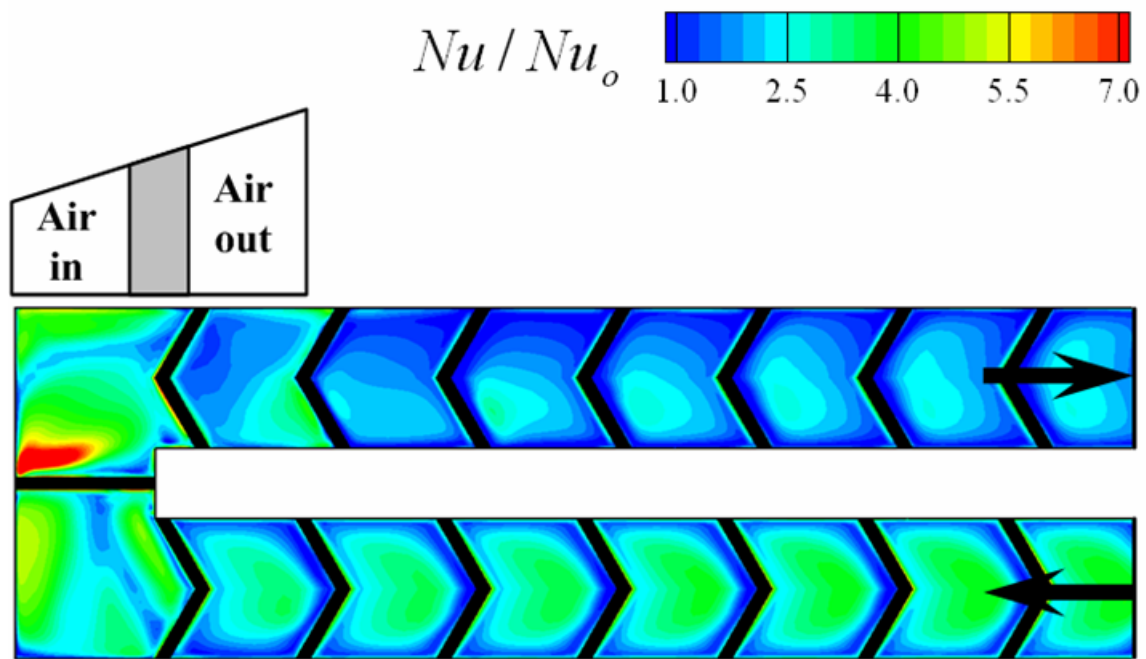
(a) Smaller inlet case
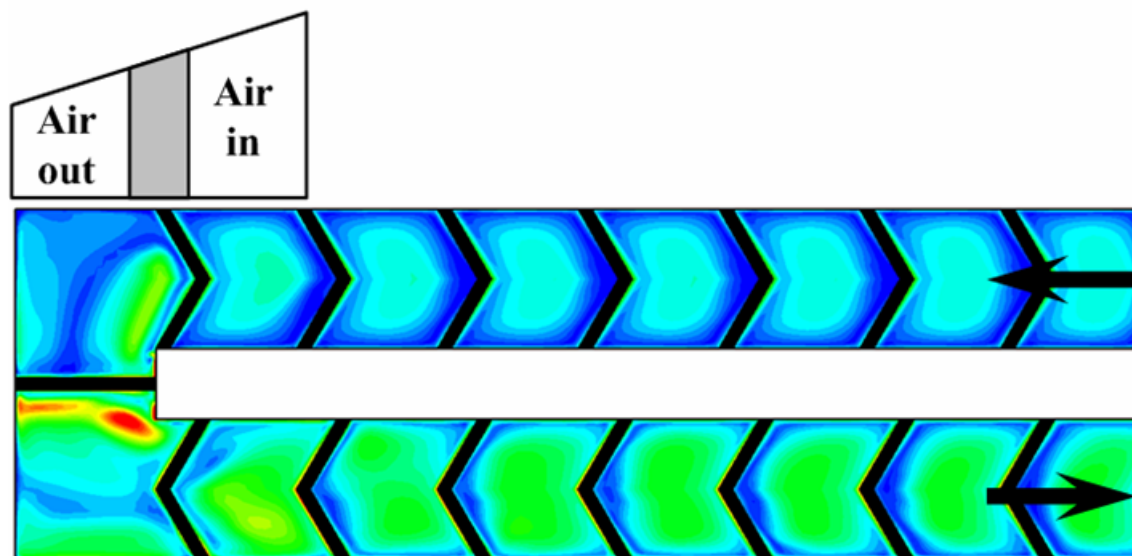
(b) Larger inlet case

Fig. 9.16 Detailed Nusselt number ratio distributions of trapezoidal channel with

60° V-shaped ribs at Re = 31,800 by RSM

centrifugal force, and caused lesser impingement on the outer wall. In the second passage, the secondary flow near the inner wall had higher momentum due to the secondary flow induced by the turn rotating counterclockwise direction, whereas the secondary flow near the outer wall had lower momentum. A relatively high heat transfer region was produced closer to the inner wall. Further downstream, the effect of the turn reduced and the secondary flow induced by the ribs increased. Therefore, the Nusselt number ratios monotonically increased. The sharp 180° turn negatively affected on the heat transfer enhancement on the bottom because when the flow was pushed by the centrifugal forces at the turn toward the outer wall and the flow was then deflected onto the top wall. Further downstream heat transfer enhancements were slightly increasing since the turning effects were reduced and the secondary flow induced by the bottom ribs seemed to overcome the secondary flow by the turn. Every Nusselt number ratio was lower than that in the first passage because bulk mean velocity was relatively lower. For the larger inlet case (Fig. 9.16 (b)), heat transfer distribution between the ribs in the first passage was periodic, and the Nusselt number ratios were higher in the central area and decreased toward two side walls in the spanwise direction. In the turn region, the heat transfer enhancements near the tip of divider wall were higher than those near the end wall downstream of the 90° rib due to strong downward flow impingements along the tip of the divider wall. In the second passage, just after the turn the relatively high heat transfer was occurred due to very strong flow impingement with high magnitude of the flow velocity that was accelerated through the turn. Unlike the smaller inlet case, the heat transfer distributions were almost periodic.
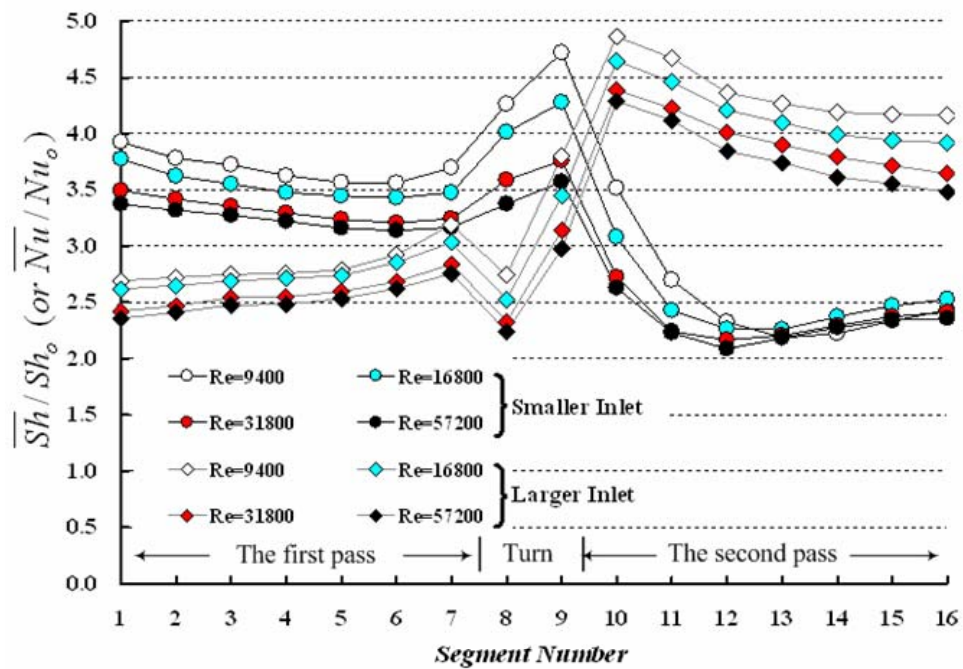
Fig. 9.17 Segmental average mass transfer distributions along the trapezoidal channel

with 60° V-shaped ribs

Fig. 9.17 shows the streamwise distributions of the regional average Sherwood number ratios ($\overline{Sh}/Sh_0$) along the trapezoidal channel for air flow entering the smaller straight section and those for air flow entering the larger straight section. It is clear that the greatest mass transfer enhancement occurred at the lowest Reynolds number of 9,400. As the Reynolds number increased, the Sherwood number ratios decreased. The general trends of Sherwood number ratios were similar for all four Reynolds numbers. For the

smaller inlet case, Sherwood number ratios gradually decreased before the turn in the first passage. On wall segment no.9 in the turn in the second passage, the $\overline{Sh}/Sh_0$ value was highest due to the secondary flow impingements induced by the turn. In the second passage, after the turn, mass transfer enhancement abruptly decreased due to the lower magnitude of the flow velocity. After that, the $\overline{Sh}/Sh_0$ value gradually decreased. However, from the wall segment no.12, the $\overline{Sh}/Sh_0$ value was slightly increasing by developing the secondary flow induced by the V-shaped ribs. For the larger inlet case, unlike the smaller inlet case, Sherwood number ratios gradually increased before the turn in the first passage. The reason was that the secondary flow induced by the ribs was slightly growing near the bottom along the streamwise direction of the channel and the flow was already fully developed. It is clear that the mass transfer was the highest downstream of the turn, as the flow that left the turn with very high turbulence entered the smaller exit section. The highest mass transfer enhancement occurred on wall segment no.10. After that, Sherwood number ratios gradually decreased since the turning effects were diminished.

The Reynolds stress model (RSM) showed well flow field and heat transfer distribution. However, when the comparison between the numerical prediction and measured regional average were considered, the prediction can not agree well with the experimental data (Fig.9.3). The RSM underpredicted heat (mass) transfer enhancements for the both cases. The maximum relative error was 28.9% and the average relative error was 22.1% for the smaller inlet case. The maximum relative error was 31.9% and the average relative error was 23.5% for the larger inlet case.

CHAPTER X

OVERALL THERMAL PERFORMANCE

The combined effects of the rib angle, rib orientation, and the sharp 180° turn significantly affect the heat (mass) transfer distributions. The average Sherwood number ratios and the friction factor ratios for 60° V-shaped ribs had the highest values, then came the case of (+) 60° ribs, and the Sherwood number ratios and the friction factor ratios for (–) 60º ribs were the lowest. The case of (–) 60º ribs with the smaller inlet produced highest thermal performance.

10.1 Channel Average Mass Transfer Ratios

The first comparisons were conducted for the channel (overall) average mass transfer ratios. Fig. 10.1 shows the channel average Sherwood number ratios for (+) 60° rib, (–) 60º rib and 60° V-shaped rib in the trapezoidal channel, and the channel average Sherwood number ratios ($\overline{Sh}/Sh_0$) for the smooth wall and 90° rib in the trapezoidal channel conducted by Lee et al (2007) also were included to compare with the results of the smooth wall case at four Reynolds numbers. The channel average Sherwood number ratios were obtained by averaging the sixteen segmental mass transfer active surfaces on the bottom wall. The $\overline{Sh}/Sh_0$ gradually decreased with increasing the Reynolds number. The channel average Sherwood number ratios for 60° V-shaped rib with the larger inlet
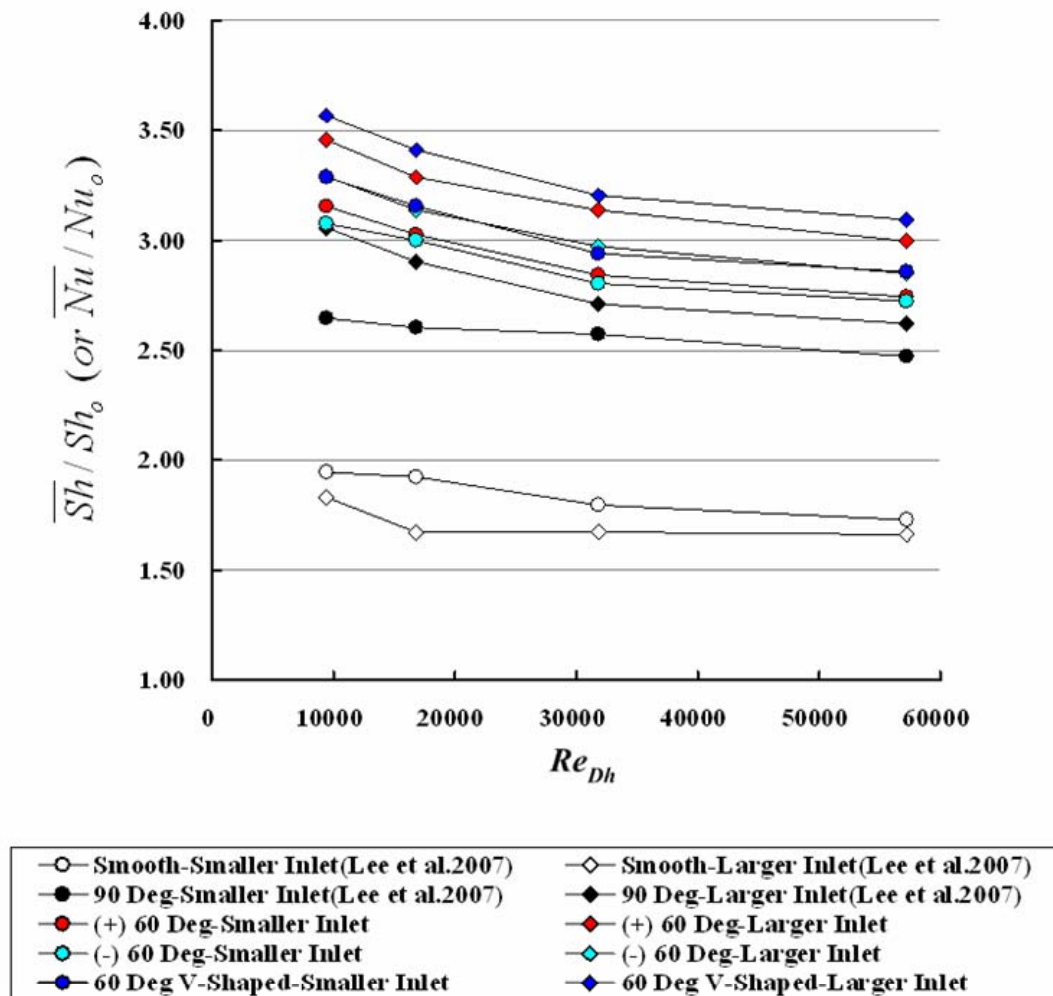
Fig. 10.1 Channel average mass transfer ratios in the trapezoidal channel

had highest $\overline{Sh}/Sh_0$ values ranging from 3.09 to 3.57, which were 86.2 to 104.0% higher

than the corresponding values for the smooth wall with the larger inlet case, and 8.1 to

9.0% higher than the corresponding values in the case with the flow direction reversed.

The $(-)$ 60º rib case with the smaller inlet had lowest $\overline{Sh}/Sh_0$ values ranging from 2.72 to

3.08. However, $\overline{Sh}/Sh_0$ values of the $(-)$ 60º rib case with the smaller inlet were slightly

higher than those of the 90° rib case with the larger inlet by 0.7 ~ 3.9% due to the secondary flow induced by the angled ribs. In general, the results show that the values of $\overline{Sh}/Sh_0$ for the larger inlet cases were always higher than those for the smaller inlet cases in the ribbed trapezoidal channel. When the flow goes through the turn from the larger cross section, the flow was accelerated due to the reduction of cross section of the channel. This accelerated flow can cause more flow mixing and higher turbulence intensity.

10.2 Pressure Drops Across the Turn

The pressure drop across the turn was defined as the difference between the static pressures at two streamwise stations near the turn in the two straight sections of the trapezoidal channel. To obtain the pressure drop across the turn, two pressure taps were installed on the top wall and the outer side wall, respectively, in each of the two straight sections of the test channels [see Fig. 2.6]. These pressure taps were located on the center point between two ribs located 4th and 5th from the end wall. The pressure drop results are presented in terms of a friction factor ratio, f/f_0 which gives the average pressure gradient around the turn relative to that for fully developed turbulent flow at the same Reynolds number in a smooth straight channel with a hydraulic diameter equal to that of the cross section at the turn clearance. In Fig. 10.2, the pressure drops across the turn are presented for flows at four different Reynolds number through the trapezoidal channel. The results show that the friction factor ratio increased with increasing

Reynolds number in all of the cases studied. According to Lee et al (2007), the f/f_0 values of the smooth wall for the smaller inlet case range from 6.54 to 10.16 and the f/f_0 values for the larger inlet case range from 9.42 to 15.40 as Reynolds number was increased from about 9,400 to 57,200. Thus, the acceleration of the flow around the turn as the flow cross section decreases appears to cause about 50% higher pressure drop than when the flow direction is reversed.
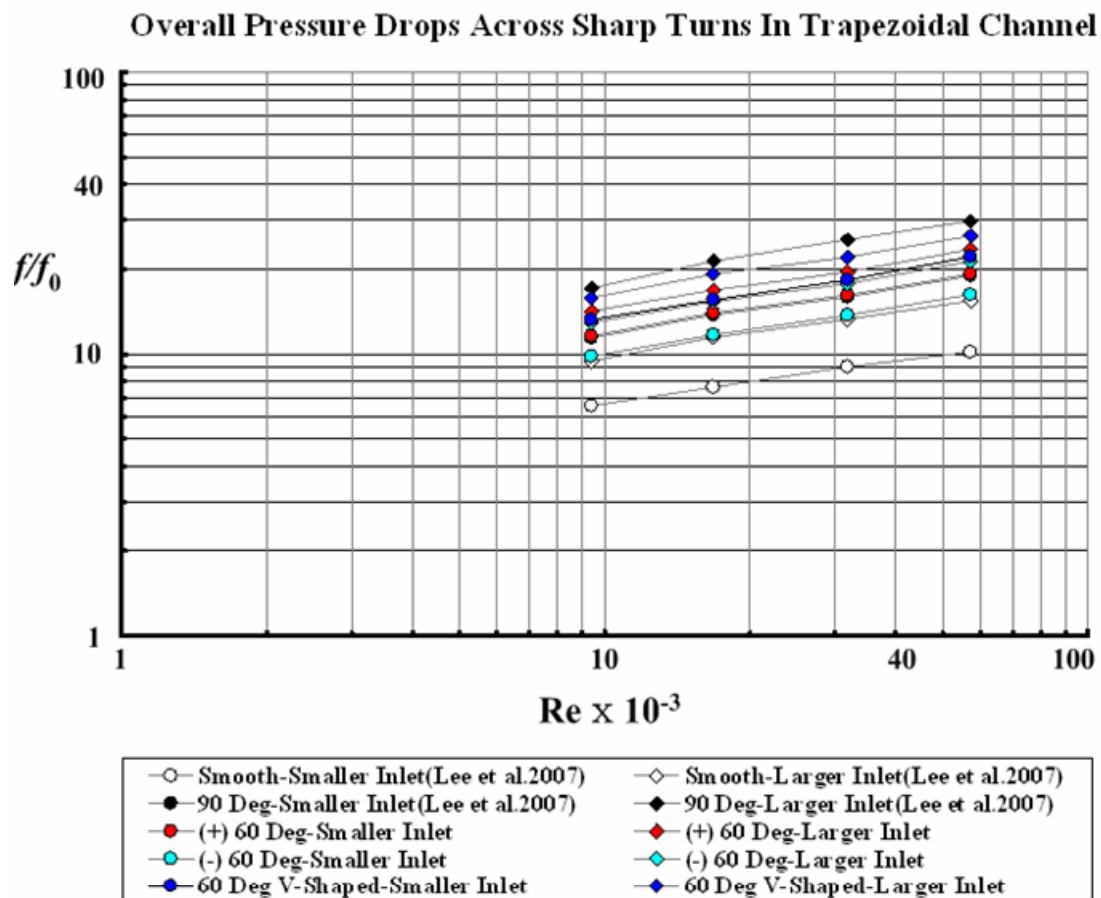
Fig. 10.2 Pressure drops across the turn in the trapezoidal channel

In the present study, the pressure drop across turn for 60° V-shaped ribs with the larger inlet had highest f/f_0 values ranging from 15.8 to 26.24, which were 141 to 158% higher than the corresponding values for the smooth wall with the smaller inlet case, and 19 to 24% higher than the corresponding values in the case with the flow direction reversed. The (–) 60º rib case with the smaller inlet had lowest f/f_0 values ranging from 9.80 to 16.23. When the (+) 60° rib case and the (–) 60º rib case were compared, the f/f_0 values of the (+) 60° rib case were higher than those of the (–) 60º rib case. The direction of the secondary flow created in the first passage by the (–) 60º ribs coincides with that of the secondary flow formed in the turn, while that created by the (+) 60° ribs gives the opposite circulation to the secondary flow in the turn. Changing the direction of the circulation causes energy loss through the flow mixing resulting in an extra pressure drop. This is the reason why the pressure drop was higher for the (+) 60° rib case.

10.3 Thermal Performance

The thermal performance obtained by considering both the heat (mass) transfer augmentation and the friction loss increment is presented based on the constant pumping power condition. As shown in Fig. 10.3, the thermal performance was decreased with an increase in the flow Reynolds number. Considering the performance comparisons of the (+) 60° ribs, the (–) 60º ribs, and 60° V-shaped ribs for the smaller inlet cases, the highest thermal performance was produced by the (–) 60º ribs, and the 60° V-shaped ribs and the (+) 60° ribs had almost same levels of the thermal performance since the 60° V-

shaped ribs produced highest heat (mass) transfer enhancement but also produced highest pressure drops.
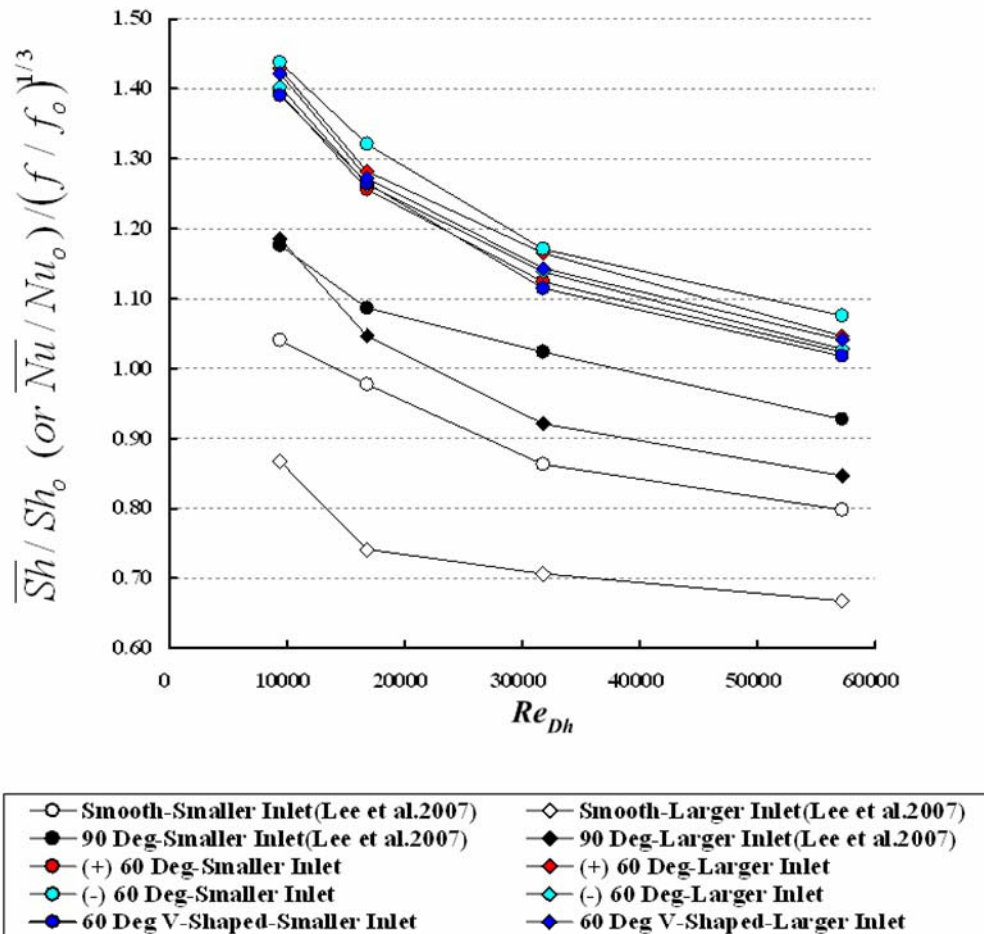
Fig.10.3 Thermal performance in the trapezoidal channel

For the larger inlet cases, the (+) 60° ribs produced the highest values, then came the case of the 60° V-shaped ribs, and the thermal performance for the (–) 60º ribs was the lowest.

CHAPTER XI

SUMMARY AND CONCLUSION

Experimental and numerical study was conducted to investigate heat (mass) transfer characteristics in a two-pass trapezoidal channel simulating the cooling passage of a gas turbine blade. Three different rib configurations were tested at four different Reynolds numbers of 9,400, 16,800, 31,800, and 57,200. (+) 60º ribs, (−) 60º ribs and 60º V-shaped ribs were attached on both the top and bottom walls in parallel sequence. Naphthalene sublimation technique was used, and the heat and mass transfer analogy was applied to convert the mass transfer coefficients to heat transfer coefficients. Numerical predictions of three-dimensional flow and heat transfer also were performed for the trapezoidal channel with and without 90º ribs tested by Lee et al. [35]. Reynolds stress turbulence model (RSM) in the FLUENT CFD code was used to calculate the heat transfer coefficients and flow fields. The Reynolds number was fixed at 31,800 for the numerical study. Therefore, all results of the flow filed and detailed heat transfer distributions calculated by RSM were at Re = 31,800. Based on experiments and numerical predictions, the results may be summarized as follows:

For the square channel and trapezoidal channel with smooth wall

1. The Nusselt number ratios predicted by the present RSM were in very good agreement with the experimental data.

2. The sharp 180° turn produced two counter-rotating vortices which transported cooler flow from the core toward the outer surface and higher heat transfer are observed near outer wall in the square channel.

3. In the trapezoidal channel with smooth walls, for the smaller inlet case, it was observed that the secondary flow near the bottom wall was large and well formed a vortex flow but the secondary flow near the top wall was smaller and slightly distorted in the turn. Just after turn, four counter rotating vortices were observed. One large counterclockwise rotating vortex occupied in the center of the channel, and two small vortices were near the top wall and one small vortex was near the outer and bottom wall. Further downstream of the turn, only one large counterclockwise rotating vortex was left and other vortices were diminished.

4. In the trapezoidal channel with smooth walls, for the larger inlet case, two counter-rotating vortices were produced, and the upper vortex was slightly bigger than a lower vortex in the turn. Downstream of the turn, two large strong vortices occupied almost entire cross sectional area and a small vortex near the inner and bottom wall was observed. Further downstream, the small vortex was diminished and the two large vortices predominated entire cross sectional area. Finally the weaker vortices were merged into one large counterclockwise vortex and relatively weaker vortex occupied the whole cross section.

5. The heat transfer was higher near the end wall and the downstream outer wall in the turn, and was relatively low in two regions near the upstream outer wall and downstream edge of the divider wall in the turn.

For the trapezoidal channel with 90° ribs

1. The reversal flow occurred immediately downstream and upstream of the ribs. The separation resulted in relatively low heat transfer, due to a relatively hot cell being trapped in the recirculation. However, when the flow reattached to the wall between the ribs, this was an area of relatively high heat transfer.

2. The ribs also increased turbulent mixing. The relatively hot flow near the wall was continuously mixing with the relatively cooler core flow near the center of the channel. This mixing also served to increase the heat transfer from the channel.

3. For the smaller inlet case, in the 90° turn, a strong vortex was generated near the top of the rib on the bottom wall, and smaller and slightly distorted one occurred the near the near the top of rib on the top wall due to the combined effect of centrifugal induced vortex in the turn and rib induced vortex in the upstream. Just after the turn, one large counterclockwise rotating vortex occupied almost entire cross area and smaller clockwise rotating vortex was seen near outer and bottom wall.

4. For the larger inlet case, in the 90° turn, the strong vortex pair appeared due to the centrifugal force action. These vortices were not distorted unlike

smaller inlet case. Just after turn, two large counter rotating vortices were generated and four small corner vortices were observed.

5. Heat transfer distributions between ribs appeared periodic because the ribs periodically interrupted the boundary layers on the bottom wall. In the second passage the periodic heat transfer patterns were not seen due to the turning effect.

For the trapezoidal channel with (+) 60° ribs and (−) 60º ribs

1. Angled ribs produced significantly higher heat transfer enhancement than 90° ribs due to two counter-rotating vortices induced by the angled ribs.

2. The reversal flow occurred immediately downstream of the ribs but there were no separations immediately upstream of the ribs.

3. The vortex induced by the ribs near the top wall was much stronger than the one near the bottom wall for (+) 60° ribs and the vortex induced by the ribs near the bottom wall was much stronger than the one near the top wall for (−) 60º ribs.

4. The Nusselt number ratios decreased from the inner wall to outer wall in the spanwise direction and the (−) 60º rib case had the reverse results.

5. As the Reynolds number increased, the heat (mass) transfer enhancements were decreased, and the general trends of Sherwood number ratios were similar for all four Reynolds numbers.

6. The (+) 60° ribs produced higher Sherwood number ratios than the (−) 60º ribs.

7. The (+) 60° ribs produced higher pressure drop across the turn than the (−) 60° ribs since the direction of the secondary flow created in the first passage by the (−) 60° ribs coincided with that of the secondary flow formed in the turn, while that created by the (+) 60° ribs gave the opposite circulation to the secondary flow in the turn.

For the trapezoidal channel with 60° V-shaped ribs

1. The 60° V-shaped ribs produced four counter-rotating vortices parallel to the ribs. In the center of the channel, the flows beyond the ribs and directing to ribbed surfaces to reattach were intense and these flows became weaker near the outer and inner walls.

2. Near the inlet, four vortices were almost same in the size and strength. Along the streamwise direction, the upper and left side vortex, and lower and right side vortex became stronger and bigger, while other two vortices became weaker and smaller. Near the heating section, the stronger and bigger two vortices became one large vortex extended diagonally.

3. The Nusselt number ratios had a significant spanwise variation, with low levels near the outer and inner walls of the channel, and high levels at the central area where the V-shaped ribs meet.

4. Since the 60° V-shaped rib was half of the 60° angled rib, the boundary layer thickness for the flow that moved parallel to one side of the 60° V-shaped rib was thinner than that produced by the 60° angled rib.

5. Unlike smooth wall case, near outer wall in the turn region heat transfer enhancement was mush less.

For the overall thermal performance

1. The average Sherwood number ratios and the pressure drops across the turn for 60° V-shaped rib had the highest values, then came the case of (+) 60° rib, and the Sherwood number ratios and the friction factor ratios for (–) 60º rib were the lowest.

2. For the smaller inlet cases, the highest thermal performance was produced by the (–) 60º ribs, and the 60° V-shaped ribs and the (+) 60° ribs had almost same levels of the thermal performance.

3. For the larger inlet cases, the (+) 60° ribs produced the highest values, then came the case of the 60° V-shaped ribs, and the thermal performance for the (–) 60º ribs was the lowest.

4. In general, the results show that the values of $\overline{Sh}/Sh_0$ for the larger inlet cases were always higher than those for the smaller inlet cases.

5. The Reynolds stress model (RSM) showed well flow fields and heat transfer distributions but underpredicted average Nusselt number ratios.

The results of this study show that the combined effects of the rib angle, rib orientation, and the sharp 180° turn significantly affect the heat (mass) transfer distributions in a two-pass trapezoidal channel. The secondary flows induced by the sharp 180° turn and the angled or V-shaped ribs play a very prominent role in heat

(mass) transfer enhancements. More detailed experimental and numerical investigations for the very complex flow field in the trapezoidal channel are needed. The detailed local heat (mass) transfer distributions on the all walls also should be measured to understand the heat transfer characteristics.

REFERENCES

1. Han, J.C., Dutta, S., and Ekkad, S.V., 2000, *Gas Turbine Heat Transfer and Cooling Technology*, Taylor and Francis, New York, NY, pp. 287-370 and pp. 439-497.

2. Han, J.C., Glicksman, L.R., and Rohsenow, W.M., 1978, "An Investigation of Heat Transfer and Friction for Rib Roughened Surfaces," Int. J. Heat and Mass Transfer **21**, pp. 1143-1156.

3. Han, J. C., Park, J. S., and Lei, C. K., 1985, "Heat Transfer Enhancement in Channels with Turbulence Promoters," Journal of Engineering for Gas Turbines and Power **107** (1), pp. 628–635.

4. Liou, T., and Hwang, D., 1992, "Turbulent Heat Transfer Augmentation and Friction in Periodic Fully Developed Channel Flows," Journal of Heat Transfer **114**, pp. 56-64.

5. Acharya, S., Dutta, S., and Baker, R., 1993, "Periodically Developed Flow and Heat Transfer in a Ribbed Duct," International Journal of Heat and Mass Transfer **36**, pp. 2069-2082.

6. Han, J.C. and Park, J.S., 1988, "Developing Heat Transfer in Rectangular Channels with Rib Turbulators," Int. J. Heat Mass Transfer **31**, pp. 183-195.

7. Park, J. S., Han, J. C., Huang, Y., and Ou, S., 1992,"Heat Transfer Performance Comparisons of Five Different Rectangular Channels with Parallel Angled Ribs," International Journal of Heat and Mass Transfer **35** (11), pp. 2891–2903.

8. Han, J. C., Zhang, Y. M., Lee, C. P., 1991, "Augmented Heat Transfer in Square Channel with Parallel, Crossed and V-Shaped Angled Ribs," Journal of Heat Transfer **113**, pp. 590-596.

9. Lau, S.C., Kukreja, R.T., and McMillin, R.D., 1991, "Effects of V-Shaped Rib Arrays on Turbulent Heat Transfer and Friction of Fully Developed Flow in a Square Channel," Int. J. Heat and Mass Transfer **34**, pp. 1605-1616.

10. Ekkad, S. V., and Han, J. C., 1997, ''Detailed Heat Transfer Distribution in Two-Pass Square Channels With Rib Turbulators,'' Int. J. Heat Mass Transf **40**, pp. 2525–2537.

11. M. E. Taslim, T. Li, and D. M. Kercher, 1996, "Experimental Heat Transfer and Friction in Channels Roughened with Angled, V-Shaped, and Discrete Ribs on Two Opposite Walls," J. Turbomachinery **119**, pp. 381–389.

12. Han, J.C., Chandra, P.R., and Lau, S.C., 1988, "Local Heat/Mass Transfer Distributions around Sharp 180º Turns in Two-Pass Smooth and Rib-Roughened Channels," ASME J. Heat Transfer **110**, pp. 91-98.

13. Chandra, P. R., Han, J. C., and Lau, S. C., 1988, "Effect of Rib Angle on Local Heat/Mass Transfer Distribution in a Two-Pass Rib-Roughened Channel," Journal of Turbomachinery **110**, pp. 233–241.

14. Han, J. C., and Zhang, P., 1989, "Pressure Loss Distribution in Three-Pass Rectangular Channels with Rib Turbulator," Journal of Turbomachinery **111** (4), pp. 515–521.

15. Han, J. C., and Zhang, P., 1991, "Effect of Rib Angle Orientation on Local Mass Transfer Distribution in a Three-Pass Rib-Roughened Channel," Journal of Turbomachinery **113**, pp. 123–130.

16. Cho, H. H., Wu, S. J., and Kwon, H. J., 2000, "Local Heat/Mass Transfer Measurements in a Rectangular Duct with Discrete Ribs," Journal of Turbomachinery **122**, pp. 579–586.

17. Rhee, D.H., Lee, D.H., Cho, H.H., and Moon, H.K., 2003, "Effects of Duct Aspect Ratios on Heat/Mass Transfer with Discrete V-Shaped Ribs," ASME Paper No. GT2003-38622.

18. Taslim, M.E., Bondi, L.A., Kercher, D.M., 1991. "An Experimental Investigation of Heat Transfer in an Orthogonally Rotating Channel Roughened with 45 Deg Criss-cross Ribs on Two Opposite Walls," J. Turbomach. **113**, 346–353.

19. Park, C.W., Lau, S.C., Kukreja, R.T., 1998. "Heat/Mass Transfer in a Rotating Two-psss Square Channel with Transverse Ribs," AIAA J. Thermophys. Heat Transfer **12**, 80–86.

20. Han, J.C., Zhang, Y.H., Kalkuehler, K., 1993. "Uneven Wall Temperature Effect on Local Heat Transfer in a Rotating Two-pass Square Channel with Smooth Walls," J. Heat Transfer **115**, 912–920.

21. Parsons, J.A., Han, J.C., Zhang, Y., 1994. "Wall Heating Effect on Local Heat Transfer in a Rotating Two-pass Square Channel with 90º Rib Turbulators," Int. J. Heat Mass Transfer **37** (9), 1411–1420.

22. Wright, M. L., Fu, W. L., and Han, J. C., 2004, "Thermal Performance of Angled, V-Shaped, and W-Shaped Rib Turbulators in Rotating Rectangular Cooling Channels (AR=4:1)," Journal of Turbomachinery **126**, pp. 604–614.

23. Lee, E., Wright, L. M., and Han, J. C., 2005, "Heat Transfer in Rotating Rectangular Channels with V-Shaped and Angled Ribs," Journal of Thermophysics and Heat Transfer **19** (1), pp. 48–56.

24. Jang, Y. J., Chen, H. C., and an, J. C., 2000, "Computation of Flow and Heat Transfer in a Two-Pass Channel with 60° ribs," AIAA Paper No. 2000-1036.

25. Jang, Y. J., Chen, H. C., and Han, J. C., 2001,"Flow and Heat Transfer in a Rotating Square Channel with 45-Degree Angled Ribs by Reynolds Stress Turbulence Model," Journal of Turbomachinery **123** (1), pp. 124–132.

26. Bonhoff, B., Parneix, S., Leusch, J., Johnson, B. V., Schabacker, J., and Bolcs, A., 1999, ''Experimental and Numerical Study of Developed Flow and Heat Transfer in Coolant Channels with 45deg Ribs,'' Int. J. Heat Fluid Flow **20**, pp. 311–319.

27. Iacovides, H. and Raisee, M., 1999, "Recent Progress in the Computation of Flow and Heat Transfer in Internal Cooling Passages of Turbine Blades," International Journal of Heat and Fluid Flow **20**, 320–328.

28. Sleiti, A.K., Kapat, J.S., 2006, "Comparison Between EVM and RSM Turbulence Models in Predicting Flow and Heat Transfer in Rib-roughened Channels," Journal of Turbulence **7** (29), pp. 1 – 21.

29. Al-Qahtani, M., Jang, Y. J., Chen, H. C., and Han, J. C., 2002, "Prediction of Flow and Heat Transfer in Rotating Two-Pass Rectangular Channels with 45-Degree Rib Turbulators," Journal of Turbomachinery **124**, pp. 242–250.

30. D. L. Rigby, 1998, "Prediction of Heat and Mass Transfer in a Rotating Ribbed Coolant Passage with a 180 Degree Turn," in Proc. ASME TURBO EXPO, Stockholm, Sweden, ASME 98-GT-329.

31. Su, G., Teng, S., Chen, H. C., and Han, J. C., 2004, "Flow and Heat-Transfer Computations in Rotating Rectangular Channels with V-Shaped Ribs," Journal of Thermophysics and Heat Transfer **18** (4), pp. 534-547.

32. Taslim, M.E., Li, T., and Spring, S.D., 1995, "Experimental Study of the Effects of Bleed Holes on Heat Transfer and Pressure Drop in Trapezoidal Passages with Tapered Turbulators," ASME J. Turbomachinery **117**, pp. 281-289.

33. Taslim, M.E., Li, T., and Spring, S.D., 1998, "Measurements of Heat Transfer Coefficients and Friction Factors in Passages Rib-Roughened on All Walls," ASME J. Heat Transfer **120**, pp. 564-570.

34. Moon, S.W., Endley, S., and Lau, S.C., 2002, "Local Heat Transfer Distribution in a Two-Pass Trapezoidal Channel with a 180° Turn via the Transient Liquid Crystal Technique," J. Energy, Heat and Mass Transfer **24**, pp. 103-121.

35. Lee, S.W., Ahn, H.S., and Lau, S.C., 2007, "Heat (Mass) Transfer Distribution in a Two-Pass Trapezoidal Channel With a 180 deg Turn," Journal of Heat Transfer **129**, pp. 1529-1537.

36. Ambrose, D., Lawrenson, I.J., and Sprake, C.H.S., 1975, "The Vapor Pressure of Naphthalene," J. Chemical Thermodynamics **7**, pp. 1172-1176.

37. Goldstein, R.J. and Cho, H.H., 1995, "A Review of Mass Transfer Measurements Using Naphthalene Sublimation," Experimental Thermal and Fluid Science **10**, pp. 416-434.

38. Eckert, E.R.G., 1976, "Analogies to Heat Transfer Processes," *Measurements in Heat Transfer*, E.R.G. Eckert and R.J. Goldstein, eds., Hemisphere Publishing Corp., New York, NY, pp. 397-423.

39. Coleman, H.W. and Steele, W.G., 1989, *Experimentation and Uncertainty Analysis for Engineers*, John Wiley & Sons, New York, NY.

APPENDIX A

EXPERIMENTAL DATA BY MASS TRANSFER

Table 1 Segmental average Sherwood number ratios for square channel with smooth wall at Re =34,500, trapezoidal channel with smooth walls and 90º ribs at Re = 31,800 conducted by Lee et al. [35].

Segment	$\overline{Sh}/Sh_o$ ($\overline{Nu}/Nu_o$)				
	Square channel with smooth walls	Trapezoidal channel with smooth walls		Trapezoidal channel with 90º ribs	
		Smaller inlet	Larger inlet	Smaller inlet	Larger inlet
1	1.45	1.76	1.37	3.04	1.99
2	1.19	1.48	1.11	2.93	1.90
3	1.14	1.42	1.07	2.89	1.89
4	1.12	1.37	1.03	2.76	1.85
5	1.11	1.34	1.02	2.77	1.83
6	1.13	1.35	1.01	2.75	1.83
7	1.21	1.45	1.07	2.73	1.92
8	2.17	2.64	2.14	3.18	2.56
9	2.42	2.71	2.43	3.76	2.97
10	2.40	2.69	2.58	2.48	4.07
11	2.29	2.58	2.29	2.05	3.93
12	2.09	2.24	2.11	1.88	3.57
13	1.84	1.79	2.03	1.86	3.47
14	1.63	1.46	1.94	1.96	3.29
15	1.44	1.27	1.85	2.06	3.19
16	1.32	1.19	1.71	2.07	3.10
Avg.	1.62	1.80	1.67	2.57	2.71

Smaller inlet   Larger inlet

Table 2 Segmental average Sherwood number ratios for (+) 60º ribs, (–) 60º ribs and 60º V-shaped ribs in smaller inlet cases

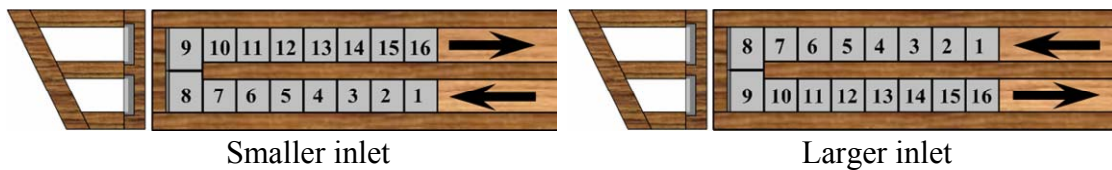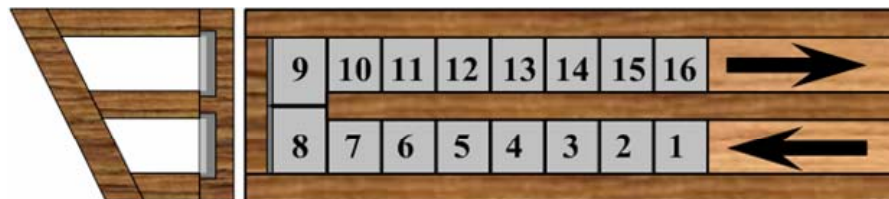| Segment	$\overline{Sh}/Sh_o$ $(\overline{Nu}/Nu_o)$											
	Re=9,400			Re=16,800			Re=31,800			Re=57,200		
	(+) 60°	(–) 60°	60° V	(+) 60°	(–) 60°	60° V	(+) 60°	(–) 60°	60° V	(+) 60°	(–) 60°	60° V
1	3.77	3.94	3.93	3.64	3.81	3.78	3.37	3.52	3.50	3.28	3.39	3.37
2	3.64	3.91	3.78	3.51	3.80	3.62	3.33	3.51	3.42	3.23	3.40	3.32
3	3.61	3.92	3.72	3.50	3.81	3.55	3.31	3.51	3.36	3.23	3.36	3.27
4	3.58	3.91	3.63	3.47	3.81	3.48	3.27	3.52	3.30	3.20	3.36	3.22
5	3.56	3.93	3.57	3.42	3.81	3.45	3.21	3.52	3.24	3.13	3.37	3.16
6	3.55	3.89	3.56	3.38	3.76	3.43	3.16	3.49	3.21	3.12	3.32	3.14
7	3.50	3.93	3.70	3.30	3.79	3.48	3.11	3.49	3.24	3.08	3.33	3.17
8	3.43	3.19	4.26	3.32	3.04	4.01	3.10	2.64	3.59	3.02	2.44	3.38
9	4.14	4.18	4.72	3.93	3.99	4.28	3.55	3.51	3.76	3.39	3.33	3.57
10	3.44	2.80	3.52	3.18	2.72	3.08	2.97	2.57	2.73	2.82	2.64	2.63
11	2.96	2.36	2.70	2.78	2.31	2.43	2.60	2.19	2.24	2.46	2.14	2.23
12	2.45	2.00	2.33	2.32	1.96	2.26	2.19	1.93	2.17	2.06	1.94	2.09
13	2.28	1.77	2.19	2.23	1.76	2.26	2.14	1.75	2.21	2.02	1.79	2.18
14	2.20	1.73	2.22	2.15	1.77	2.37	2.08	1.79	2.29	1.97	1.83	2.28
15	2.19	1.81	2.34	2.15	1.87	2.47	2.05	1.89	2.37	1.95	1.91	2.35
16	2.17	1.95	2.44	2.13	1.98	2.53	2.02	2.00	2.41	1.92	2.02	2.36
Avg.	3.15	3.08	3.29	3.03	3.00	3.16	2.84	2.80	2.94	2.74	2.72	2.86

Smaller inlet

Table 3 Segmental average Sherwood number ratios for (+) 60º ribs, (–) 60º ribs and 60º V-shaped ribs in larger inlet cases

Segment	$\overline{Sh}/Sh_o$ $(\overline{Nu}/Nu_o)$											
	Re=9,400			Re=16,800			Re=31,800			Re=57,200		
	(+) 60°	(–) 60°	60° V	(+) 60°	(–) 60°	60° V	(+) 60°	(–) 60°	60° V	(+) 60°	(–) 60°	60° V
1	2.64	2.60	2.69	2.55	2.54	2.62	2.41	2.39	2.42	2.33	2.33	2.36
2	2.65	2.57	2.72	2.57	2.52	2.65	2.43	2.37	2.47	2.37	2.32	2.41
3	2.66	2.61	2.75	2.58	2.56	2.69	2.46	2.42	2.54	2.38	2.36	2.48
4	2.69	2.64	2.76	2.61	2.59	2.72	2.51	2.47	2.55	2.43	2.40	2.48
5	2.73	2.70	2.79	2.64	2.63	2.74	2.55	2.52	2.60	2.45	2.42	2.53
6	2.78	2.75	2.93	2.70	2.66	2.86	2.57	2.52	2.68	2.48	2.45	2.62
7	3.05	3.01	3.19	2.84	2.81	3.03	2.70	2.60	2.84	2.58	2.48	2.76
8	2.75	2.67	2.74	2.63	2.46	2.53	2.47	2.24	2.33	2.34	2.09	2.24
9	3.88	3.81	3.80	3.60	3.42	3.45	3.32	3.14	3.14	3.11	2.89	2.98
10	4.49	4.12	4.86	4.24	3.84	4.65	4.07	3.75	4.39	3.87	3.53	4.29
11	4.40	4.37	4.67	4.15	4.10	4.46	3.99	3.98	4.23	3.82	3.76	4.12
12	4.19	3.93	4.36	3.99	3.79	4.21	3.88	3.59	4.01	3.68	3.49	3.85
13	4.16	3.76	4.27	3.95	3.63	4.10	3.78	3.45	3.90	3.58	3.36	3.75
14	4.10	3.64	4.19	3.88	3.52	3.99	3.72	3.32	3.79	3.54	3.21	3.61
15	4.08	3.68	4.18	3.85	3.54	3.94	3.68	3.36	3.72	3.52	3.22	3.55
16	4.04	3.77	4.16	3.82	3.61	3.92	3.66	3.44	3.65	3.49	3.28	3.48
Avg.	3.46	3.29	3.57	3.29	3.14	3.41	3.14	2.97	3.20	3.00	2.85	3.09
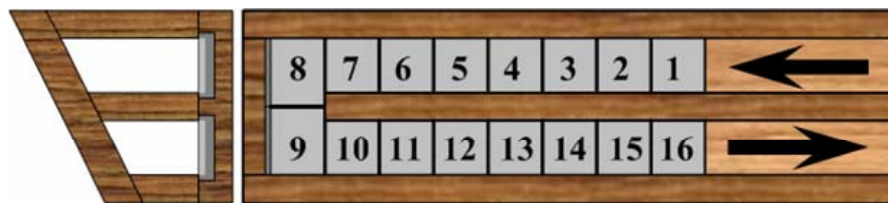
Larger inlet

Table 4 Friction factor ratios in trapezoidal channel

Smaller inlet cases					
Re	$f/f_{0,Turn}$				
	Smooth	90°	(+) 60°	(−) 60°	60° V
9,400	6.54	11.38	11.59	9.80	13.22
16,800	7.63	13.77	13.98	11.71	15.52
31,800	9.00	15.88	16.16	13.72	18.33
57,200	10.16	18.95	19.23	16.23	22.12
Larger inlet cases					
Re	$f/f_{0,Turn}$				
	Smooth	90°	(+) 60°	(−) 60°	60° V
9,400	9.42	17.14	11.59	9.80	13.22
16,800	11.46	21.36	13.98	11.71	15.52
31,800	13.28	25.45	16.16	13.72	18.33
57,200	15.40	29.68	19.23	16.23	22.12

* Smooth walls and 90° rib cases were conducted by Lee et al [35].

Table 5 Thermal performance in trapezoidal channel

Smaller inlet cases					
Re	*TP*				
	Smooth	90°	(+) 60°	(−) 60°	60° V
9,400	1.04	1.18	1.39	1.44	1.39
16,800	0.98	1.09	1.26	1.32	1.26
31,800	0.86	1.02	1.12	1.17	1.11
57,200	0.80	0.93	1.02	1.08	1.02
Larger inlet cases					
Re	*TP*				
	Smooth	90°	(+) 60°	(−) 60°	60° V
9,400	0.87	1.19	1.43	1.40	1.42
16,800	0.74	1.05	1.28	1.26	1.27
31,800	0.71	0.92	1.17	1.14	1.14
57,200	0.67	0.85	1.05	1.03	1.04

* Smooth walls and 90° rib cases were conducted by Lee et al [35].

APPENDIX B

NUMERICAL DATA BY RSM AT Re = 31,800

Table 6 Average Nusselt number ratios by RSM for square channel with smooth wall, trapezoidal channel with smooth walls and 90º ribs

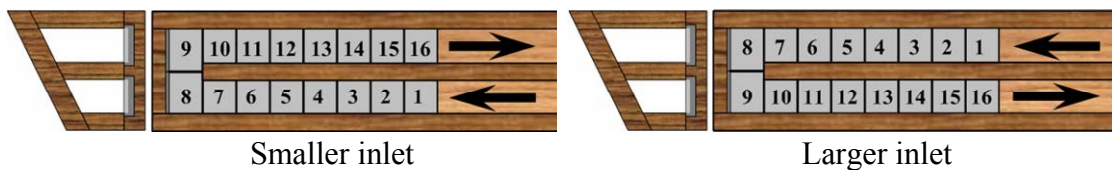| Segment	$\overline{Nu}/Nu_o$				
	Square channel with smooth walls At Re =34,500	Trapezoidal channel with smooth walls		Trapezoidal channel with 90º ribs	
		Smaller inlet	Larger inlet	Smaller inlet	Larger inlet
1	1.57	1.90	1.53	2.29	1.74
2	1.30	1.55	1.12	2.24	1.67
3	1.21	1.43	1.03	2.21	1.64
4	1.15	1.36	0.98	2.21	1.62
5	1.12	1.32	0.94	2.22	1.62
6	1.09	1.27	0.92	2.19	1.63
7	1.07	1.25	0.93	2.16	1.71
8	2.00	2.27	1.85	2.87	2.76
9	2.32	2.71	2.23	3.85	3.44
10	2.45	2.60	2.46	1.88	3.98
11	2.37	2.34	2.42	1.61	2.69
12	1.88	1.94	2.30	1.58	2.63
13	1.60	1.56	2.09	1.64	2.31
14	1.46	1.25	1.93	1.70	2.36
15	1.38	1.08	1.81	1.73	2.26
16	1.32	1.02	1.71	1.76	2.27
Avg.	1.58	1.68	1.64	2.13	2.27

Smaller inlet   Larger inlet

Table 7 Average Nusselt number ratios by RSM for (+) 60º ribs, (–) 60º ribs and 60º V-shaped ribs

Segment	$\overline{Nu}/Nu_o$					
	Trapezoidal channel with (+) 60º ribs		Trapezoidal channel with (–) 60º ribs		Trapezoidal channel with 60º V-ribs	
	Smaller inlet	Larger inlet	Smaller inlet	Larger inlet	Smaller inlet	Larger inlet
1	2.56	1.87	2.71	1.88	2.67	1.90
2	2.55	1.87	2.71	1.88	2.58	1.90
3	2.52	1.88	2.68	1.89	2.58	1.90
4	2.51	1.85	2.65	1.90	2.49	1.93
5	2.48	1.93	2.65	1.90	2.45	1.89
6	2.38	1.93	2.67	1.97	2.37	1.90
7	2.38	1.98	2.87	2.12	2.44	2.16
8	2.70	2.03	2.52	2.02	3.13	2.15
9	3.62	3.18	3.08	2.87	3.68	3.20
10	2.26	3.94	1.87	3.16	1.94	2.99
11	2.07	3.15	1.62	3.17	1.66	2.90
12	1.80	3.03	1.56	2.69	1.69	2.90
13	1.85	3.03	1.54	2.59	1.74	2.83
14	1.80	2.97	1.77	2.53	1.79	2.81
15	1.74	2.87	1.91	2.47	1.79	2.81
16	1.69	2.78	2.04	2.53	1.83	2.80
Avg.	2.31	2.52	2.30	2.35	2.30	2.44

Smaller inlet   Larger inlet
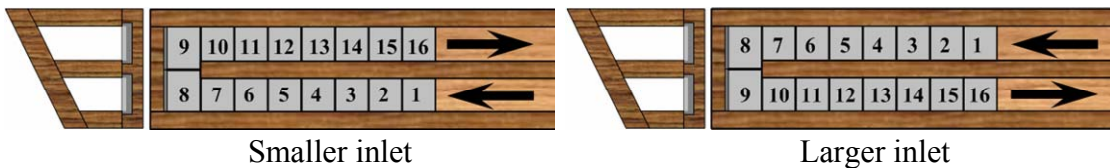
VITA

Sung Hyuk Oh received his B.En. in Mechanical Engineering from Inje University, Busan, Korea, in August 1998. He completed his M.S. in Mechanical Engineering at Texas A&M University, College Station, TX in May 2003. Mr. Oh entered the Ph.D. program in August 2003 in the Department of Mechanical Engineering at Texas A&M University, and received his Ph.D. degree in Mechanical Engineering in December 2008.

His permanent address:

Bando BoraSkyview Apt 102-1803

Oncheon 3 - dong, Dongnae-gu,

Busan

Republic of Korea